

**Geology and Geochemistry of the 25 Ma Underdown Caldera Tuffs
and the Tuff of Clipper Gap, Western Nevada Volcanic Field, North-
Central Nevada**

Kathryn J. Little

A thesis submitted to the Faculty of Graduate and Post Doctoral Affairs in partial
fulfillment of the requirements for the degree of:

Master of Science

in

Earth Sciences

Carleton University, Ottawa

© 2020

Kathryn J. Little

Abstract

The Underdown Caldera Complex is a 25.0 Ma caldera in the Western Nevada Volcanic Field formed during the mid-Cenozoic Ignimbrite Flare-up, one of the largest expressions of continental volcanism in geological time. Intracaldera and associated outflow tuffs are characteristically crystal-poor, except for one crystal-rich intracaldera tuff representing a later stage of explosive volcanism. Outflow tuffs extend to the east and west of the caldera, representing multiple phases of intracaldera tuffs. Post-deposition alteration of ignimbrites has altered Sr isotopic ratios, and caused rare earth element enrichment in the Tuff of Clipper Gap. Sr and Nd isotopic compositions of the ignimbrites show a relation to lavas collected from the margins of the caldera, and trace element ratios suggest similar origins of the lavas and ignimbrites from a mixture of mantle and crustal sources. Pb isotopes plot on mixing lines formed by a mantle-derived source and either a local sedimentary or granitoid unit.

Acknowledgements

Firstly, I would like to acknowledge my supervisor, Brian Cousens, for giving me a wonderful opportunity to learn research skills with an interesting project in an exciting field environment. Without your guidance and support, this thesis would not have been possible.

I would like to thank Dr. Christopher Henry for his invaluable help and insight in the field and throughout this project, and Evelyn Tennant for being a fantastic field partner. Thank you to Tim Mount in the Carleton University Rock Preparation Lab for preparing over one hundred thin sections and helping to prepare samples for geochemical analyses. As well, thank you to Dr. Shuangquan Zhang for all of your help in and out of the geochemistry and mass spectrometry labs. Finally, thank you to Kim Klausen for collecting and preparing samples from 2016, and thank you to Zach Pearse for geochemical work on the anomalous REE samples.

I would also like to thank the “Spice Geologists” Dr. Chris Rogers, Dr. Nico Kastek, Dr. Sarah Davey, and Matthew Trenkler for invaluable insight and advice, as well as great office memories. Thank you to all of my other close friends who have supported me throughout my time at Carleton University.

Thank you to my parents, Sue and Pat Little, and my siblings Emily and Matthew for your constant encouragement. A special thank you to Lucas Brewster, the support and patience you’ve given me the past two and a half years helped me to finish the project I

thought I never could. Finally, to my Nana, Betty McCulloch, and Grandma, Liisa Little whom we said goodbye to in the last year of work. Without you I would not be where I am today, and I will be forever grateful for all of the lessons you taught me outside of the classroom.

Table of Contents

Abstract.....	ii
Acknowledgements.....	iii
List of Figures.....	viii
List of Tables.....	xvii
List of Abbreviations.....	xviii
1.0 Introduction.....	1
2.0 Geological History of the Southwestern United States.....	3
2.1 Tectonic and Associated Magmatic Activity.....	3
2.2 Flat Slab Subduction.....	4
2.3 The Mid-Cenozoic Ignimbrite Flare-up.....	5
2.4 Basin and Range Extension.....	6
2.5 Extension Related Magmatism.....	8
3.0 Applied Concepts and Theory.....	10
3.1 Generation of Felsic Magma.....	10
3.2 Caldera Formation and Pyroclastic Flow Deposits.....	14
3.3 Introduction to Isotopes.....	21
Rb-Sr.....	21
Sm-Nd.....	23
(Pb)-(Pb) or common Pb.....	26
4.0 Regional Geology.....	29
4.1 Geological Framework.....	29
4.2 Stratigraphic Relations.....	31
4.3 Field Observations.....	35
Intracaldera tuffs and the tuff of Clipper Gap.....	35
Other tuffs and potential outflow tuff.....	40
Megabreccia blocks.....	44
Intrusions and dykes.....	48

5.0 Methods.....	49
5.1 Samples.....	49
5.2 Major and Trace element analyses.....	49
5.3 Radiogenic Isotope Methods.....	51
Pb Isotope Analysis.....	52
Sr Isotope Analysis.....	53
Nd Isotope Analysis.....	54
6.0 Results.....	56
6.1 Petrography.....	56
6.2 Geochemistry.....	66
6.2.1 Major element geochemistry.....	68
6.2.2 Trace element geochemistry.....	80
6.2.3 Isotope geochemistry.....	93
7.0 Discussion.....	108
7.1 Establishing Primary Characteristics.....	108
7.1.1 Petrographic characteristics.....	108
7.1.2 Geochemical characteristics.....	109
7.1.3 Potential alteration of isotopic ratios.....	114
7.1.4 Potential sources of the Oligocene tuffs.....	121
7.1.5 Relationship of the Underdown Tuff, tuff of Clipper Gap, and Bonita Canyon Formation.....	132
7.1.6 Identity of the Unnamed tuff.....	133
7.2 Cerium Anomalies in the tuff of Clipper Gap.....	141
7.2.1 REE chemistry of the anomalous samples.....	141
7.2.2 Major element geochemistry of the anomalous samples.....	143
7.2.3 Trace element geochemistry of the anomalous samples.....	146
7.2.4 Effects of acid washing on anomalous REE samples.....	149
7.2.5 Potential sources of Ce anomalies and REE enrichment.....	160
7.3 Other potentially related exposures.....	167

7.3.1 The tuff of Gabbs Valley.....	167
7.3.2 The tuff of Arc Dome.....	175
7.3.3 The tuff of Brunton Pass.....	176
7.3.4 The Terrill Mountains tuffs.....	181
7.3.5 Young Sierra Nevada tuffs.....	187
7.4 The Origin of Porphyritic Pumice in the Underdown Tuff.....	197
7.4.1 Field Observations and Petrography.....	197
7.4.2 Major Element Geochemistry.....	199
7.4.3 Trace Element Geochemistry.....	202
7.4.4 Source of the Porphyritic Pumice.....	206
8.0 Conclusions.....	210
8.1 The Underdown Caldera Complex.....	210
8.2 Future Work.....	211
References.....	212
Appendix I Supporting Tables.....	219
Table I: $^{40}\text{Ar}/^{39}\text{Ar}$ Ages Provided by C. Henry.....	219
Table II: Sample Locations.....	220
Table III: Thin Section Descriptions.....	224
Table IV: Major Element Oxide Abundances.....	248
Table V: Precision of Major Element analyses.....	253
Table VI: Trace Element Concentrations.....	255
Table VII: Precision of Trace Element analyses.....	267
Table VIII: Isotopic Results.....	271
Table IX: Sr Isotopic Precision.....	274
Table X: Nd Isotopic Precision.....	274
Table XI: Pb Isotopic Precision.....	275
Table XII: Partition Coefficients.....	276

List of Figures

Figure 2.1: Rollback of the subducting Farallon slab can be traced using geochronology from the north east to the southwest of Nevada.....	6
Figure 3.1: A Deep Crustal Hot Zone (DCHZ) by Annen, 2006.....	13
Figure 3.2: The evolution and collapse of a dacitic magma system and caldera over an approximately 1 million year time period (modified after Christiansen, 2005).....	16
Figure 3.3: Schematic of an idealized ignimbrite deposit, after Sparks et al., 1973.....	20
Figure 3.4: Sr vs. Nd isotopic correlation.....	26
Figure 3.5: A $^{206}\text{Pb}/^{204}\text{Pb}$ vs. $^{207}\text{Pb}/^{204}\text{Pb}$ diagram showing the differences in isotopic value of the oceanic basalt (mantle) and granites and gneiss (continental crust).....	28
Figure 4.1: Map of the western United States showing the location of the Underdown Caldera (UC) in the Western Nevada Volcanic Field (modified from Henry and John, 2013).....	30
Figure 4.2: The Underdown Caldera complex as mapped by H. F. Bonham (1970).....	33
Figure 4.3: The eastern and southern extent of the tuff of Clipper Gap, an outflow tuff from the Underdown Caldera.....	34
Figure 4.4: Field photos of cooling joints of the Underdown Tuff from Barrett Canyon (A) and a cross section slab of a cooling joint (B).....	37
Figure 4.5: The tuff of Clipper Gap exposed at Moore's Canyon Road.....	38
Figure 4.6: (A) A large outcrop of Bonita Canyon Formation in Barrett Canyon.....	39
Figure 4.7: (A) The Unnamed tuff showing its highly porphyritic texture.....	40
Figure 4.8: (A) Outcrop photo of the tuff of Gabbs Valley (geologists for scale).....	42
Figure 4.9: Hand sample and outcrop photographs of TgV2 and TgV3 from Fissure Ridge.....	43
Figure 4.10: (A) The Terrill Mountains tuffs are exposed as a lower, grey, poorly to moderately welded unit, and an upper, brown, moderately welded cooling unit, separated by a vitrophyre.....	44

Figure 4.11: (A) A Pablo Formation outcrop in Barrett Canyon (geologists for scale).....	46
Figure 4.12: (A) Large spires of a quartz-feldspar-biotite tuff deposited on the Bonita Canyon Formation which are megabreccia blocks of the tuff of Arc Dome from the caldera wall that fell inwards into the caldera during collapse.....	47
Figure 6.1: Photomicrographs of major ignimbrites showing commonly observed textures.....	64
Figure 6.2: Photomicrographs of major ignimbrites showing hydrous phases (hornblende and biotite).....	65
Figure 6.3: Total alkalis-silica diagram (Le Maitre et al., 1989) of all data from the Underdown Caldera Complex.....	67
Figure 6.4: Average chondrite normalized rare earth element patterns of the Tuff of Clipper Gap samples with no Ce anomalies and those with Ce anomalies (normalization factors of Sun and McDonough, 1989).....	68
Figure 6.5: Total alkalis-silica diagram (Le Maitre et al., 1989) showing the fields of all units collected within and outside of the Underdown Caldera.....	74
Figure 6.6: Total alkalis-silica diagram (Le Maitre et al., 1989) showing the major ignimbrite units (Underdown Tuff, tuff of Clipper Gap, Bonita Canyon Formation, and Unnamed tuff - without Ce anomaly or high LOI samples), mafic to intermediate basement rocks (Pablo Formation), dacite dyke, and rhyolite intrusions collected from the Underdown Caldera.....	75
Figure 6.7: Total alkalis-silica diagram (Le Maitre et al., 1989) showing the other ignimbrite units (tuff of Gabbs Valley, tuff of Arc Dome, tuff of Brunton Pass) and the Terrill Mountains tuffs that are close in age to the Underdown tuff.....	76
Figure 6.8: Major element variation diagrams of the Pablo Formation.....	77
Figure 6.9: Major element variation diagrams of the major ignimbrites and the rhyolite intrusions of the Underdown Caldera complex.....	78
Figure 6.10: Major element variation diagrams of the other tuffs (tuff of Gabbs Valley, tuff of Arc Dome, and tuff of Brunton Pass) and the Terrill Mountains tuffs.....	79

Figure 6.6: Trace element variation diagrams of the Pablo Formation and the dacite dyke.....84

Figure 6.12: Trace element variation diagrams of the major ignimbrites and the rhyolite intrusions of the Underdown Caldera complex.....85

Figure 6.13: Trace element variation diagrams of the other tuffs (tuff of Gabbs Valley, tuff of Arc Dome, and tuff of Brunton Pass) and the Terrill Mountains tuff.....86

Figure 6.14: Chondrite normalized (Sun and McDonough, 1989) rare earth element diagrams for the Pablo Formation and the dacite dyke.....87

Figure 6.15: Chondrite normalized (Sun and McDonough, 1989) rare earth element diagrams for the major ignimbrites of the Underdown Caldera complex (Underdown Tuff, tuff of Clipper Gap, Bonita Canyon Formation and the Unnamed tuff) and the rhyolite intrusions.....88

Figure 6.16: Chondrite normalized (Sun and McDonough, 1989) rare earth element diagrams for the slightly older Oligocene tuffs (tuff of Gabbs Valley, tuff of Arc Dome, tuff of Brunton Pass) and the Terrill Mountains tuffs.....89

Figure 6.17: Primitive mantle normalized (Sun and McDonough, 1989) trace element diagram for the Pablo Formation and dacite dyke.....90

Figure 6.18: Primitive mantle normalized (Sun and McDonough, 1989) trace element diagram for the major ignimbrites of the Underdown Caldera complex (Underdown Tuff, Tuff of Clipper Gap, Bonita Canyon Formation, and Unnamed tuff) and the rhyolite intrusions.....91

Figure 6.19: Primitive mantle normalized (Sun and McDonough, 1989) trace element diagram for the other tuffs (tuff of Gabbs Valley, tuff of Arc Dome, and tuff of Brunton Pass) and the Terrill Mountains tuff.....92

Figure 6.20: (A) ϵ_{Nd} versus $^{87}Sr/^{86}Sr$ with all Underdown Caldera complex data. (B) Same as in (A), but samples with negative Ce anomalies have been removed. (C) Same as in (B), but high LOI (> 6%) samples have been removed. (D) Same as in (C), but acid-washed tuff of Clipper Gap samples are plotted for comparison.....96

Figure 6.21: “Fresh” and acid-washed data plotted on an initial ϵ_{Nd} versus $^{87}Sr/^{86}Sr$ diagram without the Pablo Formation.....99

Figure 6.22: Initial $^{87}\text{Sr}/^{86}\text{Sr}$ versus $1/\text{Sr}$ (ppm) plot showing the relation between Sr concentration and $^{87}\text{Sr}/^{86}\text{Sr}$ isotopic ratios.....	100
Figure 6.23: Initial $^{87}\text{Sr}/^{86}\text{Sr}$ versus SiO_2 content showing the relationship between Sr isotopic values and increasing SiO_2 content.....	101
Figure 6.24: Initial ϵNd versus $1/\text{Nd}$ (ppm) showing the relation between epsilon Nd values and Nd concentration.....	102
Figure 6.25: Initial ϵNd versus SiO_2 weight percentage showing the comparison between epsilon Nd values and increasing SiO_2 content.....	103
Figure 6.26: Initial $^{207}\text{Pb}/^{204}\text{Pb}$ versus $^{206}\text{Pb}/^{204}\text{Pb}$	104
Figure 6.27: Initial $^{208}\text{Pb}/^{204}\text{Pb}$ versus $^{206}\text{Pb}/^{204}\text{Pb}$ showing the correlation between increasing $^{206}\text{Pb}/^{204}\text{Pb}$ and increasing $^{208}\text{Pb}/^{204}\text{Pb}$	105
Figure 6.28: Initial $^{208}\text{Pb}/^{204}\text{Pb}$ versus SiO_2 weight percentage showing the comparison between $^{208}\text{Pb}/^{204}\text{Pb}$ and increasing SiO_2 content.....	106
Figure 6.29: Initial $^{208}\text{Pb}/^{204}\text{Pb}$ versus Pb (ppm) showing the comparison between Pb isotopic values and Pb concentration.....	107
Figure 7.1: Initial Sr and Nd isotopic data showing the comparison between the high LOI samples and the “fresh” samples.....	117
Figure 7.2: Initial Pb isotopic diagrams showing the comparison between the high LOI samples and the “fresh” samples.....	118
Figure 7.3: Initial Sr and Nd isotopic diagrams showing the comparison between the anomalous REE samples, their acid-washed equivalents, and the “fresh” samples.....	119
Figure 7.4: Initial Pb isotopic diagrams showing the comparison between the anomalous REE samples, their acid-washed equivalents, and the “fresh” samples.....	120
Figure 7.5: Age corrected $^{87}\text{Sr}/^{86}\text{Sr}$ vs. primitive mantle normalized Gd/Yb comparing the “fresh” Oligocene tuffs and the acid-washed tuff of Clipper Gap samples with the Miocene lavas.....	123
Figure 7.6: ϵNd vs. $^{87}\text{Sr}/^{86}\text{Sr}$ after Allègre (2008) showing the “fresh” samples, acid-washed tuff of Clipper Gap samples, and Miocene lavas.....	125

Figure 7.7: Primitive mantle normalized (Sun and McDonough, 1989) Th/La versus SiO₂ content of the “fresh” Oligocene tuffs, acid-washed tuff of Clipper Gap samples, and Miocene lavas showing potential crustal addition with increasing magma evolution.....126

Figure 7.8: Initial ²⁰⁷Pb/²⁰⁴Pb versus ²⁰⁶Pb/²⁰⁴Pb diagram modified after Allègre (2008).....128

Figure 7.9: Initial ²⁰⁷Pb/²⁰⁴Pb vs. ²⁰⁶Pb/²⁰⁴Pb for the Underdown Caldera ignimbrites compared to mixing between a Miocene lava (red square) (17-SML-11) and an average of selected Paleozoic sedimentary rocks (blue square) (Stepner, 2017).....130

Figure 7.10: Initial ²⁰⁷Pb/²⁰⁴Pb vs. ²⁰⁶Pb/²⁰⁴Pb for the Underdown Caldera ignimbrites compared to mixing between a Miocene lava (red square) (17-SML-11) and a late Eocene pluton from the Northern Shoshone Range (blue square) (Cousens et al., 2019).....131

Figure 7.11: Total alkalis-silica diagram (Le Maitre et al., 1989) of the Unnamed tuff and the Tuff of Toiyabe (with data from John, 1974).....134

Figure 7.12: Major element variation diagrams comparing the Unnamed tuff with the Tuff of Toiyabe (with data from John, 1974), as well as the Underdown Tuff and Bonita Canyon Formation for reference.....135

Figure 7.13: Trace element variation diagrams comparing the Unnamed tuff with the Tuff of Toiyabe (with data from John, 1974), as well as the Underdown Tuff and Bonita Canyon Formation for reference.....137

Figure 7.14: Primitive mantle normalized trace element diagram (Sun and McDonough, 1989) of the average trace element concentrations of the Tuff of Toiyabe, Unnamed tuff, Unnamed pumice, and Underdown Tuff, using a limited amount of trace element data available from John (1974).....138

Figure 7.15: Initial ⁸⁷Sr/⁸⁶Sr versus 1/Sr concentration (A) and SiO₂ content (B) showing the Sr isotope data for the Tuff of Toiyabe and Unnamed tuff (with isotope data from John, 1974).....139

Figure 7.16: (A) Chondrite normalized rare earth element diagram for the anomalous REE samples.....142

Figure 7.17: Total alkalis-silica diagram (Le Maitre et al., 1989) of the anomalous-REE samples from the Tuff of Clipper Gap shows the samples plotting in a trend from the rhyolite to trachyte fields, with the whole rock samples plotting exclusively in the rhyolite field and the porphyritic pumice samples plotting in both the trachyte field and rhyolite field.....144

Figure 7.18: Major element oxides plotted versus SiO₂ show that the trachyte samples plot as a cluster in half of the comparisons (CaO, K₂O, and Na₂O) and a scatter in the other half (Al₂O₃, Fe₂O₃, P₂O₅, and TiO₂).....145

Figure 7.19: Trace element variation diagrams for the anomalous REE samples from the tuff of Clipper Gap, as well as the non-anomalous Underdown Tuff and tuff of Clipper Gap samples for comparison.....148

Figure 7.20: A line diagram showing the effect of acid washing on the major element oxides of the anomalous REE samples and non-anomalous REE samples.....151

Figure 7.21: Chondrite normalized REE diagrams for the acid-washed samples before (A) and after acid washing (B).....153

Figure 7.22: A line diagram showing the change in trace element concentration after the acid washing process.....154

Figure 7.23: Initial ⁸⁷Sr/⁸⁶Sr ratios plotted against Sr concentration for acid-washed and unwashed anomalous REE samples.....156

Figure 7.24: Initial εNd plotted against Nd concentration for the acid-washed and unwashed anomalous REE samples from the tuff of Clipper Gap.....157

Figure 7.25: Initial ²⁰⁸Pb/²⁰⁴Pb vs. ²⁰⁶Pb/²⁰⁴Pb showing the change in isotopic ratio after acid washing.....158

Figure 7.26: Initial ²⁰⁸Pb/²⁰⁴Pb isotopic ratios plotted against Pb concentrations showing the change in isotopic ratio and Pb concentrations of the anomalous REE samples after acid washing.....159

Figure 7.27: The fractionation of amphibole before and after the acid washing process. Dy/Yb is used to represent the formation of amphibole as amphibole preferentially partitions Dy into its structure, but takes in much less Yb.....162

Figure 7.28: (A) Chondrite normalized REE and (B) primitive mantle normalized trace element diagrams comparing TgV2 (“tuff of Gabbs Valley”) and the tuff of Arc Dome.....169

Figure 7.29: (A) Chondrite normalized REE and (B) primitive mantle normalized trace element diagrams comparing all samples from TgV2 (“tuff of Gabbs Valley”) and two samples (17-SM-14, 16-SM-09) from the tuff of Arc Dome.....170

Figure 7.30: (A) Chondrite normalized REE and (B) primitive mantle normalized trace element diagrams comparing TgV3 (“tuff of Gabbs Valley” porphyritic pumice) to the Underdown porphyritic pumice samples.....171

Figure 7.31: Chondrite normalized rare earth element plot (A) and primitive mantle normalized trace element plot (B) comparing TgV3 with the Bonita Canyon Formation and the Underdown Tuff (porphyritic pumice).....172

Figure 7.32: Nd isotopic diagrams showing the difference in initial ϵ_{Nd} values between TgV2 and TgV3.....174

Figure 7.33: Chondrite normalized rare earth element diagram (A) and primitive mantle normalized trace element diagram (B) showing the comparison between the Tuff of Arc Dome and the megabreccia block sampled from the Underdown Caldera.....176

Figure 7.34: Chondrite normalized REE (A) and primitive mantle normalized trace element (B) diagrams showing similar patterns in both the Underdown Tuff and the tuff of Brunton Pass.....178

Figure 7.35: Chondrite normalized REE diagram showing the comparison between the anomalous REE Clipper Gap whole rock and porphyritic pumice samples to the tuff of Brunton Pass.....179

Figure 7.36: Primitive mantle normalized Th/La vs. SiO_2 content indicating crustal addition into the Oligocene tuffs and Miocene lavas.....180

Figure 7.37: (A) Chondrite normalized REE and (B) primitive normalized trace element diagrams showing the comparison between the Underdown Tuff (whole rock samples), the Terrill Mountains tuffs and the Terrill Mountains pumice.....182

Figure 7.38: Primitive mantle normalized Th/La vs. SiO_2 content indicating crustal addition into the Oligocene tuffs and Miocene lavas.....183

Figure 7.39: (A) Initial ϵNd versus $^{206}\text{Pb}/^{204}\text{Pb}$ and (B) initial $^{208}\text{Pb}/^{204}\text{Pb}$ versus $^{206}\text{Pb}/^{204}\text{Pb}$ showing the comparison between the Terrill Mountains tuffs and the other Oligocene tuffs from the Underdown Caldera complex.....185

Figure 7.40: Total alkalis-silicate diagram (Le Maitre et al., 1989) comparing the Young Sierra Nevada tuffs to the Underdown Tuff.....188

Figure 7.41: Major element variation diagrams comparing the Young Sierra Nevada tuffs with the Underdown Tuff.....189

Figure 7.42: Trace element bivariate diagrams comparing the Young Sierra Nevada tuffs to the Underdown Tuff.....191

Figure 7.43: (A) Chondrite normalized REE and (B) primitive mantle normalized trace element diagrams comparing the Young Sierra Nevada tuffs with the Underdown Tuff.....192

Figure 7.44: Primitive mantle normalized Th/La vs. SiO_2 content indicating crustal addition into the Oligocene tuffs and Miocene lavas.....193

Figure 7.45: (A) Chondrite normalized REE and (B) primitive mantle normalized trace element diagrams showing the comparison between the Young Sierra Nevada tuffs and the Bonita Canyon Formation.....194

Figure 7.46: Map of the Western Great Basin, showing the location of the Underdown Tuff (light blue dashed circle) and the placement and flow direction of paleovalleys...196

Figure 7.47: Field photograph of a porphyritic pumice from the Underdown Tuff.....198

Figure 7.48: Total alkalis-silica diagram (Le Maitre et al., 1989) of the Underdown Tuff, porphyritic pumice and white pumice.....200

Figure 7.49: Major element oxide versus SiO_2 content diagrams for the Underdown Tuff.....201

Figure 7.50: Trace element bivariate diagrams showing the compatibility of trace elements in the Underdown Tuff whole rock, porphyritic pumice and white pumice...204

Figure 7.51: (A) Chondrite normalized rare earth element plot and (B) primitive mantle normalized trace element plot of the average Underdown Tuff whole rock, average porphyritic pumice, and white pumice samples (normalizing data from Sun and McDonough, 1989).....205

Figure 7.52: (A) Chondrite normalized rare earth element plot and (B) primitive mantle normalized trace element plot of the average Underdown Tuff whole rock sample, most evolved porphyritic pumice sample (16-SM-29A), least evolved porphyritic pumice sample (17-SM-17C), and white pumice sample (16-SM-29B) (normalizing data from Sun and McDonough, 1989).....206

Figure 7.53: Porphyritic pumice in the Tuff of Campbell Creek. The observation of porphyritic pumice in a crystal poor ash flow tuff outside of the Underdown Caldera suggests that the presence of porphyritic pumice in the Western Nevada Volcanic Field may be more common than previously thought.....209

List of Tables

Table 7.1: Samples selected for the acid washing process, including porphyritic pumice, white pumice, whole rock and vitrophyre samples.....	149
---	-----

List of Abbreviations

HREE: Heavy rare earth element

LREE: Light rare earth element

MASH: melting, assimilation, storage, and homogenization

REE: Rare earth element

TAS: Total alkalis-silica

WNVF: Western Nevada Volcanic Field

1.0 Introduction

Western North America was shaped by a complex history of subduction, extension, and magmatism through geologic time. One of the largest expressions of continental volcanism in geological history (Best et al., 2013; Best et al., 2016, and references therein), the mid-Cenozoic Ignimbrite Flare-up, formed an extensive field of caldera complexes and outflow tuffs which, in western Nevada, remain largely unstudied. Recent work to understand the petrogenesis of these large volume caldera forming ignimbrites is providing a better understanding of their origins (Henry and John, 2013; Best et al., 2013; Watts et al., 2016; Steiner, 2017; Cousens et al., 2019).

The 36-18 Ma Ignimbrite Flare-up is responsible for the formation of the Western Nevada Volcanic field (WNVF), a belt of calderas extending across the state of Nevada, USA. The belt was formed as a result of a sweep of magmatic activity caused by the rollback of the shallowly subducting Farallon plate beneath North America (Best et al., 2013; Henry and John, 2013; Best et al., 2016; Timmermans, 2015). During rollback, intrusions of mantle-derived magmas stalled in the thick continental crust, partially melting the continental crust, and ultimately erupting as caldera forming ignimbrite magmas (Hildreth and Moorbath, 1988; Annen and Sparks, 2002; Clemens and Stevens, 2012). The currently accepted model for the generation of subduction-related arc magmas begins with the intrusion of mantle-derived basaltic magmas into the lower crust. Mixing of the mantle-derived magmas and partial melts from the continental crust, followed by fractional crystallization and segregation of remaining melt, results in

the generation of felsic magma (Smith, 1979; Hildreth 1981; Hildreth and Moorbath, 1988; Annen et al., 2006; de Silva, 2008). The input of mantle and crustal components into the final magma can be modelled using radiogenic isotopes, providing more information on the petrogenesis of evolved magmas (Davidson, 1985; Aitchison et al., 1995; Siebel et al., 2001).

The Great Basin Ignimbrite province, formed as a result of the Ignimbrite Flare-up, is divided into three fields which are delineated by the limit of exposed outflow tuffs (Henry and John, 2013; Best et al., 2016). From west to east these fields are the Western, Central, and Indian Peak-Caliente volcanic fields, of which the WNVF is the least studied in terms of geochemistry and petrology. This study focuses on the Underdown Caldera complex, a 25.0 Ma caldera in the WNVF which was mapped for the Nevada Bureau of Mines (Bonham, 1970), but has no petrographic or geochemical analyses of the intracaldera and extracaldera tuffs. The aim of this work is to utilize petrographic analyses, as well as major element, trace element, and radiogenic isotope data to characterize the intracaldera and extracaldera tuffs from the Underdown Caldera complex. The use of Sr, Nd, and Pb isotopic data in comparison with Miocene lavas from the margins of the Underdown Caldera will be used to identify potential melt source(s) for the Underdown Caldera ignimbrites.

2.0 Geological History of the Southwestern United States

The Underdown Caldera is one of many caldera complexes in the Southwestern United States that formed during the mid-Cenozoic Ignimbrite Flare-up, one of the largest Mesozoic-Cenozoic ignimbrite events unrelated to continental breakup (Best et al., 2013; Best et al., 2016, and references therein). An overview of the tectonic and magmatic history of the southwestern United States will be discussed in this section.

2.1 Tectonic and Associated Magmatic Activity

The basement of the western United States consists of Precambrian basement to the east (Dickinson, 2006) and Phanerozoic oceanic terranes to the west, forming the basement of the future WNVF (DeCelles, 2004; Henry and John, 2013, Best et al., 2016). Prior to the Mesozoic, a plate boundary existed along the western edge of North America where the Mezcalera plate bordered the continental plate, but changed to a subduction zone by the Late Jurassic (DeCelles, 2004). In the early Late Jurassic, the Farallon plate was subducting underneath consolidated accreted terranes along the Pacific margin of the North American Plate (DeCelles, 2004). Continental arc magmatism and periods of east-vergent shortening formed the Cordilleran orogeny as the slab continued to subduct beneath North America (DeCelles, 2004), culminating in the Laramide orogen (McKee, 1971). At the end of the Mesozoic, subduction of the Farallon Plate beneath North America became more rapid, and changed geometry from a typical dipping subduction zone to flat slab subduction (DeCelles, 2004; Humphreys, 2009;

Henry and John, 2013; Best et al., 2013; Best et al., 2016). Magmatism ceased where the slab came in full contact with the underside of North America, and the arc shifted into more central regions of the North American continent (Lipman, 1992).

2.2 Flat Slab Subduction

Flat-slab subduction began as the dip of the subducting slab shallowed between 90 - 50 Ma, which replaced the asthenospheric mantle wedge with a relatively cold oceanic lithospheric plate, and prevented melting within the asthenosphere (Henry and John, 2013; Best et al., 2016, and references therein). Shallowing of the Farallon slab dip is hypothesized to have been caused by a number of factors including: (1) rapid convergence between North America and the Farallon slab (Engebretson et al., 1985; Jarrad, 1986; van Hunen et al., 2002), (2) buoyancy of the young subducting slab (Cadek and Fleitout, 2003; O'Driscoll et al., 2009), and/or (3) suction between the oceanic slab and the continental plate (Cadek and Fleitout, 2003; O'Driscoll et al., 2009). The interaction of the flat-subducting Farallon slab with the overlying continent hydrated the mantle lithosphere, and caused crustal thickening and the formation of the Nevadaplano on which the Central Nevada and Indian-Peak Caliente volcanic fields would eventually form (Best et al., 2016). During the hiatus of arc magmatism in what is now the Great Basin, magmatic activity consisted of the emplacement of S-type granitic plutons, partially melted from meta-sedimentary rocks from the miogeoclinal wedge (Best et al., 1974; Lee and Christiansen, 1983; Farmer and DePaolo, 1983).

2.3 The Mid-Cenozoic Ignimbrite Flare-up

Steepening, or rollback, of the Farallon slab beneath the continent triggered a sweep of magmatic activity from the northeast to the southwest of Nevada between 45 and 3 Ma (Henry and John, 2013; Cousens et al., 2008). The interaction of the re-established hot mantle wedge with the hydrated, fertile mantle lithosphere generated large volumes of basaltic magma through partial melting. This was the driving force behind caldera-forming explosive silicic volcanism, with the most voluminous silicic volcanism occurring between 36 - 18 Ma (Best et al., 2016). The sweep of magmatic activity followed the northeast to southwest rollback of the Farallon slab which can be traced using geochronological data (Henry and John, 2013; Best et al., 2016) (Fig. 2.1). This magmatic event, recognized by Lipman et al. (1972) and Noble (1972), was termed the Ignimbrite Flare-up by Coney (1978). The sweep of large volume silicic magmatism stopped at the Walker Lane, a zone of transpressional strike-slip deformation located on the southwestern edge of Nevada, while mafic to intermediate magmatism including stratovolcanoes and lava domes continued across the Walker Lane into the Sierra Nevada Mountains (Henry and John, 2013). While silicic and andesitic volcanism dominated the Ignimbrite Flareup, basaltic magmatism occurred after 20 Ma (Best et al., 2016).

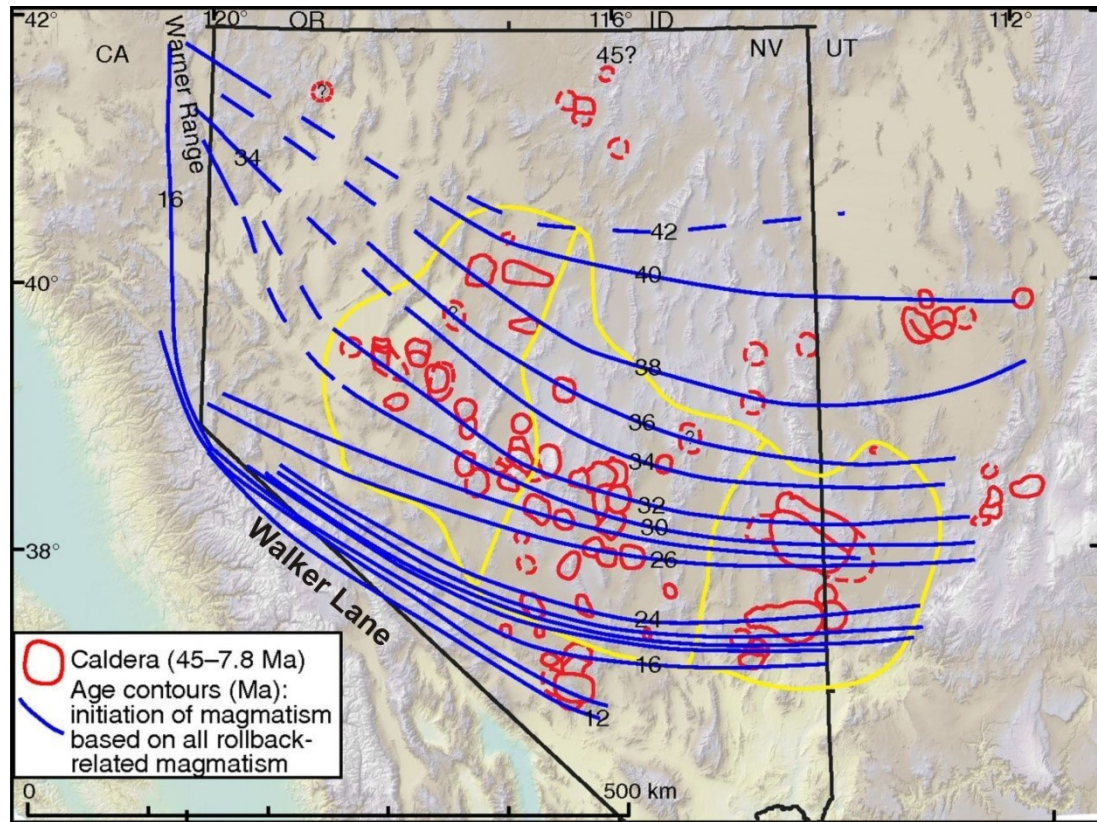


Figure 2.1: Rollback of the subducting Farallon slab can be traced using geochronology from the northeast to the southwest of Nevada. Migration of magmatism began in the northeast of Nevada and tracked to the southwest over time before stopping at the Walker Lane (Henry and John, 2013).

2.4 Basin and Range Extension

In the late Cenozoic, widespread high angle normal faulting and resulting crustal extension formed the Basin and Range Province which consists of alternating elongate mountain ranges and alluvial basins (McKee, 1971). While the terms Basin and Range Province and Great Basin are often used interchangeably when describing the North-South trending mountain ranges in Nevada, it is important to note the differences between these two terms. The Great Basin is an endoheric watershed which drains

internally, as it has no connection to an ocean, and is contained within the Basin and Range Province which extends from the Pacific Northwest to Mexico for almost 2500 km. The Basin and Range Province is characterized by faulted mountain chains and flat, alluvial valleys which were formed from extensional processes. Subsequent to the Ignimbrite Flare-up, the Great Basin underwent two extensional events (Dickinson, 2006).

Rapid Miocene extension in the Basin and Range Province began at 17-16 Ma and continued only a few million years until 12-10 Ma. Until this time, the Basin and Range province was believed to be held together by the fully subducted Farallon slab beneath the continent. The collapse of the Nevadaplano is thought to have occurred after the last piece of the Farallon slab delaminated from beneath the continent (Armstrong and Ward, 1991; Colgan and Henry, 2009). The mechanisms aiding in the extension in the mid Miocene were potentially a combination of (1) shear along the transform San Andreas Fault system, (2) gravitational collapse of the Nevadaplano, and/or (3) magmatic activity including mantle upwelling of the Yellowstone plume, formation of the northern Nevada Rift, and the main phase of the Columbia River flood basalt eruption (Atwater, 1970; Camp et al., 2015). The San Andreas transform fault system was present along the continental margin by the Early Miocene (Dickinson, 2006) and it is believed that shear interaction along the fault system caused transtensional motion of the Sierra Nevada continental block. The Basin and Range region accommodated for the movement of the Sierra Nevada block to the northwest by extension (Atwater, 1970).

Contrary to extension in the Basin and Range Province, Cenozoic extension in the Great Basin is believed to be unrelated to the formation of the transform fault system, as the subduction of the Farallon slab was still occurring during the time of extension (Dickinson, 2006). The first stage of Cenozoic extension in the Great Basin involved the denudation of metamorphic core complexes which were subjected to 50-100% strain (Parsons et al., 1996; Colgan and Henry, 2009; Camp et al., 2015). The second extensional event involved high angle block faulting which produced the basin and range topography characteristic of the Basin and Range Province. The second event began around 17 Ma and involved 100% extension along normal faults which resulted in stacked, tilted fault blocks separated by valleys in between where sedimentation could occur (Proffett, 1977; Chamberlin, 1983). Tilting of the fault blocks was varied, but was between 5-8 degrees in the southern Shoshone range, the field area for this project.

2.5 Extension Related Magmatism

Some have postulated that the deformation of the continental block and formation of the Basin and Range Province during the Miocene triggered the rejuvenation of magmatism in the Great Basin, particularly basaltic-andesitic magmatism (Dickinson, 2006). However, after the inception of the Great Basin at ca. 17 Ma, rollback continued through the late Miocene, Pliocene, and Quaternary, producing mostly basalts to andesites rather than calderas, and no clear distinction between extension-related lavas and arc-related lavas has been determined (Cousens et al., 2012). The arrival of the Yellowstone plume is believed to have formed the large volume Columbia River flood

basalts. Presently, the plume is centred beneath Yellowstone (Colgan and Henry, 2009, and references therein), however the plume arrived in northern Nevada between 16-17 Ma and early volcanic activity consisted of caldera formation and the eruption of rhyolitic tuffs (Geist and Richards, 1993) and emplacement of mafic dykes and felsic domes of the northern Nevada rift (John et al., 2000; Camp et al., 2015). Large volume, middle Miocene basaltic magmatism occurred during a volcanic maximum for the Yellowstone hotspot with the eruptions of the Steens and Columbia River basalts which cover a large portion of Oregon, Washington, and northwestern Nevada. The relation of the Yellowstone plume to the extension in the Basin and Range Province has been debated by some authors who believe the beginning of Basin and Range extension pre-dates the arrival of the Yellowstone plume (e.g., Colgan et al., 2013).

3.0 Applied Concepts and Theory

3.1 Generation of Felsic Magma

The generation of basaltic magma from partial melting of the mantle is a known and accepted concept. However, the process by which an evolved magma is formed has been under debate, as its origins are far more complex. Multiple processes are believed to occur to evolve from a basaltic magma to a rhyolitic or granitic magma end member. This section will discuss these potential magma forming processes as well as an accepted model for felsic magma generation.

Hutton (1794) first proposed that the intrusion of mafic magma and fusion of pre-existing rocks formed silicic melts, however further research into the generation of felsic magmas in arc settings has resulted in a more complex picture of the mechanisms of felsic magma generation in subduction zones, including the interactions between mantle and crustal material, and crustal anatexis (Perry et al., 1993; Annen and Sparks, 2002; de Silva, 2008; Clemens and Stevens, 2012). In a continental arc setting, a combination of partial melting and mixing of a variety of sources can contribute to the generation of silicic magma, including the subducted oceanic crust and sediments, the mantle wedge, the continental crust, crustal underplates, and the subcontinental lithospheric mantle (Winter, 2001). In a subduction zone, the dehydration of the subducting oceanic plate releases volatiles which induce flux melting of the lithospheric mantle to produce mafic magma. The mafic magma ascends and pools at the mantle-

crust boundary where it partially melts the continental crust and is believed to assimilate crustal material.

De Paolo (1981) proposed that the assimilation of crustal rocks by a basaltic magma was an important factor in the generation of felsic magmas, and mathematically demonstrated the combined effects of assimilation of wall rock and fractional crystallization (AFC). While other authors also believe that the assimilation of wall rock plays a role in the generation of silicic magmas, it is not believed to be a large contributor to pluton-wide compositional variations due to energy constraints and the inevitable crystallization and cooling of the intruding magma during assimilation (Clemens and Stevens, 2012). In addition, partial melting of a basaltic parent and/or the extensive fractional crystallization of a primitive, tholeiitic melt does yield felsic magma. However, this process would produce a volume of magma too small to form the large volume silicic volcanism observed in the Ignimbrite Flare-up. Therefore, pure crustal melting and pure fractional crystallization from a basaltic parent are discounted as major mechanisms behind the production of an evolved magma (Perry et al., 1993; Clemens and Stevens, 2012).

It is proposed that felsic magmas found in arc systems are likely formed by a combination of fractional crystallization of a mantle wedge derived magma, and partial melting of older crust (Annen and Sparks, 2002; Clemens and Stevens, 2012). In this model basaltic magma is fluxed into the crust episodically over time. Heat and volatiles transferred from the crystallizing basaltic magma induces partial melting of the pre-

existing crust. Melt generation in the crust is controlled by multiple factors including the magma intrusion rate, the water content and composition of the pre-existing crust, and the water content and temperature of the intruding basalt. For example, a dry basaltic magma intrusion into fertile crustal rocks is capable of producing a large volume of melt (Annen and Sparks, 2002).

It is in this deep crustal area that a combination of magma modification processes occurs simultaneously to produce large volumes of intermediate to felsic magma (Annen and Sparks, 2002; Clemens and Stevens, 2012). This zone was proposed by Hildreth and Moorbath (1988) as the MASH (melting, assimilation, storage, and homogenization) zone. Basaltic magma is intruded into the deep crust in a MASH zone where it undergoes differentiation by crystallization and crustal anatexis to produce a variety of magma compositions. Annen et al. (2006, 2008) and Solano et al., (2012) expanded the idea of the MASH zone model and proposed a Deep Crustal Hot Zone (DCHZ) at 20-50 km depth where episodic intrusions of basaltic magma through sills progressively elevates the temperature of the lower crust (Fig. 3.1). Basaltic injections that remain partially molten due to the increased temperature are able to mix with residual melts as they accumulate in the hot zone. Crustal melting and re-melting of intrusions will occur with the increasing temperature of the lower crust provided by the injection of basaltic magma. The resulting andesite-dacite magma will evolve to a more silicic melt through differentiation after cooling and degassing during ascent.

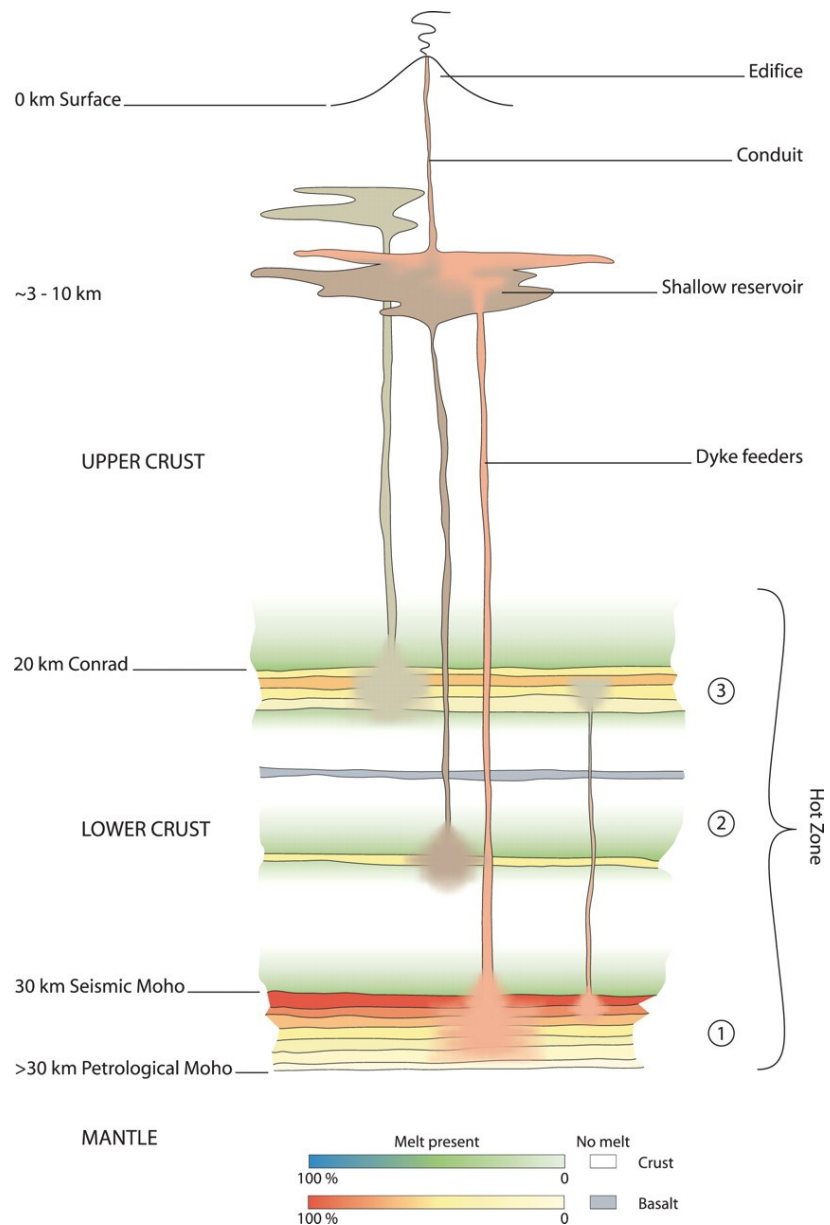
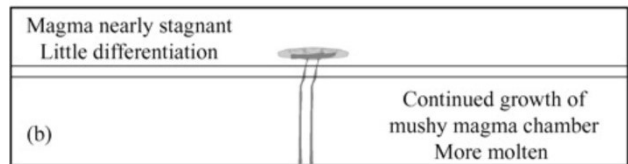
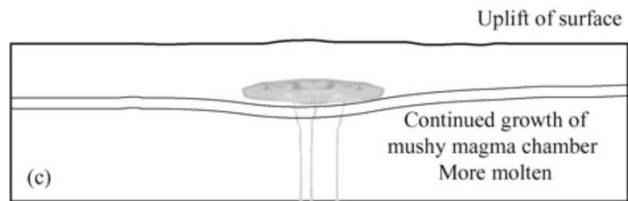
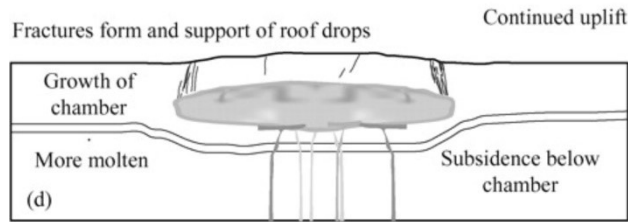
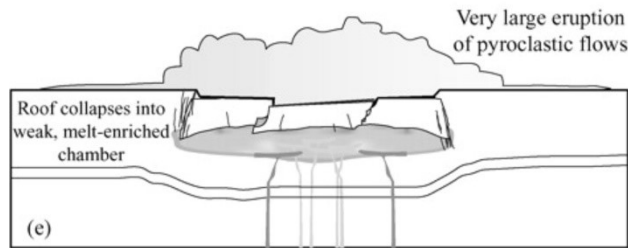
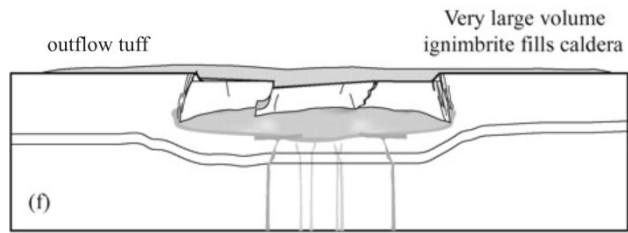


Figure 3.1: A Deep Crustal Hot Zone (DCHZ) by Annen, 2006. Basaltic magma is intruded at depth in episodic injections which heat the surrounding crust. The heated crust allows later injections of basaltic magma to accumulate and mix with other melts in the hot zone. Crustal melting and magma mixing produces an intermediate magma which differentiates into a silicic magma as it is ascending.

3.2 Caldera Formation and Pyroclastic Flow Deposits

A caldera is a volcanic depression which is formed during volcanic eruptions. Two mechanisms for caldera formation include the collapse of a volcano into an emptying magma chamber below or the removal of the top of a volcano by exploding volcanic gases, the former of which will be discussed in more detail. The collapse of a basaltic caldera involves the foundering of caldera blocks into an underlying lava lake, displacing the magma upwards. The formation of a silicic caldera can be much more violent, as fractures through the overlying blocks reach down to the magma chamber, reducing pressure in the magma chamber by rapid vesiculation, and allowing for the escape of magma. As support for the overlying roof disappears with the emptying of the magma chamber, the roof blocks collapse into the void below. Magma escaping through the fractures and the formation of gas bubbles causes a violent eruption that produces pyroclastic materials and caldera-filling ignimbrites.



10 km

Evolution of a large-volume dacitic magma system

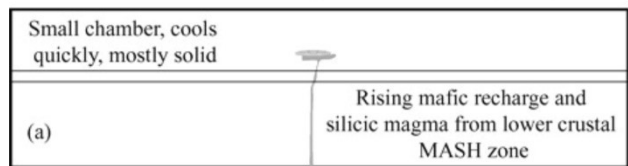


Figure 3.2: The evolution and collapse of a dacitic magma system and caldera over an approximately 1 million year time period (modified after Christiansen, 2005). (A) Basaltic magma pools in a lower crustal MASH zone where it forms a small, quickly crystallized magma chamber. (B) and (C) Repeated injection of basaltic material into the lower crust allows the growth of the magma chamber and the change from a crystallized to a mushy state. (D) Fractures form in the roof of the caldera over a large magma chamber. Fractures allow a conduit for the magma to travel upwards as it rapidly degasses and explosively erupts. (E) Support for the roof fails as the magma chamber is emptied and the roof collapses downwards as an explosive pyroclastic eruption occurs. (F) Large volume silicic ignimbrites fill the caldera.

A main product of these caldera forming eruptions are pyroclastic deposits which are formed from the fragmented material exploded from the vent during the eruption. Pyroclastic deposits are composed of pyroclasts (hot fragments) and can be divided into three categories; pyroclastic falls, pyroclastic flows, and surge deposits (sometimes considered flow deposits). Pyroclastic fall deposits are formed from the fallout of ash from a vertical eruption column, formed from a plinian-style eruption. During these highly explosive eruptions, pyroclasts (hot fragments) are propelled upwards by explosion and/or buoyant convecting gases from the vent and are carried by wind. As the forces carrying the particles dissipate, they fall back down to the Earth and form pyroclastic fall deposits. Ash particles are held the longest in air; however denser particles will fall sooner, resulting in fall deposits that are well sorted and are graded. Grain size of a fall deposit fines upwards and away from the vent. Because they are formed by fallout of relatively cool particles, pyroclastic fall deposits mantle topography and rarely become welded after deposition. The size, shape, and particle size of a pyroclastic fall deposit depends on multiple factors including the rate of explosion, the volume of erupted material, the force of the pyroclastic eruption, and the speed and direction of prevailing winds which carry the eruption column and pyroclasts.

Pyroclastic flow deposits are commonly formed from the collapse of a plinian eruption column due to the density of the suspended material and volcanic gases. However, they can also be formed by a lateral blast from a volcano (e.g. Mount St. Helens), the boiling over of a gas rich magma from a vent, or the collapse of a lava dome. Pyroclastic flows

are composed of ash, pumice, crystals and lithic fragments that have been blasted off of surrounding rock during an explosive volcanic eruption. Trapped gases within and below the pyroclastic flow cause it to be fluidized. Pyroclastic flows are hot and fast moving, flowing downwards with topography and travelling far away from their source vent in some cases. As the flow loses momentum, the hot pyroclasts suspended in the flow will be deposited, with concentrated deposits occurring in topographic lows. Pyroclastic deposits are referred to as ignimbrites, which have varied textures depending on the nature of the flow and eruption. When sorting does occur in an ignimbrite, it can be characterized by the concentration of dense, lithic fragments at the base of the flow, and lighter blocks of pumice at the top of the flow (Fig. 3.3). Heat of the deposited pyroclasts and weight of overlying material can cause lower parts of the ignimbrite deposit to become welded and foliated. Pumice blocks from these welded sections are flattened, turning the pumice into black obsidian which is then referred to as fiamme.

Pyroclastic surge deposits are erupted from the vent at a very high velocity and contain fewer particles than a pyroclastic flow. The speed and low density of a surge deposit causes the deposits to both mantle topography and concentrate in topographic lows as the deposit hugs the ground when it is erupted from the vent. Surge deposits lose momentum quickly and therefore are deposited close to the vent. Typically, surge deposits show stratification and are cross bedded. A deposit from a pyroclastic eruption may be a product of all three deposit types, based on factors such as the distance from the vent and magnitude of the eruption. In addition, pyroclastic eruptions often occur in

distinct episodes which can be reflected by the nature of the pyroclastic deposit
(Winter, 2001).

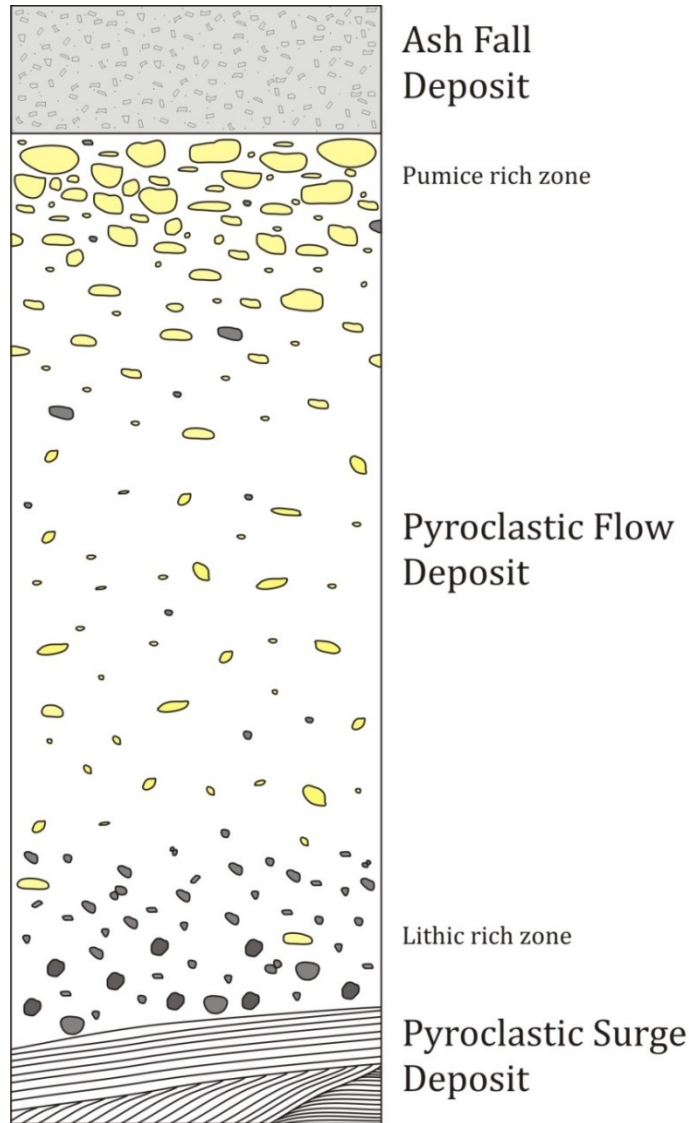


Figure 3.3: Schematic of an idealized ignimbrite deposit, after Sparks et al., 1973. The base of the ignimbrite deposit marks a high velocity, low density eruption of fine material called a pyroclastic surge deposit. The deposit can often display cross-bedding structures indicative of its eruption energy. The pyroclastic flow deposit is characterized by a concentration of dense lithic fragments at the base of the deposit and lighter pumice blocks at the top of the deposit. The pyroclastic flow deposit commonly occurs after the collapse of the plinian eruption column and concentrates in topographic lows. The ash fall deposit lies on top of the pyroclastic flow deposit and is composed of the lightest material (ash, lapilli, and pumice) which fall back down to Earth from the ash cloud and settle on the land surface last. Ash fall deposits mantle topography and extend in the direction of the prevailing winds.

3.3 Introduction to isotopes

Rb-Sr

The basic radioactive decay equation used in radiogenic isotopic analysis is:

$$D = D_0 + N(e^{\lambda t} - 1)$$

Where D is the number of daughter isotope atoms, D_0 is the initial number of daughter atoms, N is the number of parent isotope atoms, t is the amount of time passed, and λ is the decay constant. Based on this equation, the amount of daughter isotope in a closed system is a function of the amount of time passed (t) and the ratio of parent to daughter isotopes in the system at the time of closure (Dickin, 2005).

The rubidium (Rb) - strontium (Sr) isotopic system was one of the first isotopic systems originally developed for geochronometry, but is now commonly used in source identification of igneous rocks, due to the behavioural differences of the parent and daughter isotopes during partial melting. Rb has two naturally occurring isotopes, ^{85}Rb and ^{87}Rb , whose abundances are 72.1654 and 27.8346 percent, respectively. While ^{85}Rb is a stable isotope, ^{87}Rb is radioactive. Strontium has four isotopes ^{84}Sr , ^{86}Sr , ^{87}Sr , and ^{88}Sr . Of these four, ^{87}Sr is the only radiogenic isotope and is produced by the beta decay of ^{87}Rb with a half-life of ^{87}Rb ($t_{1/2}$) = 4.88×10^{10} y, and a decay constant of $\lambda = 1.42 \times 10^{-11} \text{y}^{-1}$. Sr isotopic data are reported as $^{87}\text{Sr}/^{86}\text{Sr}$ ratios; a comparison of the radiogenic daughter, ^{87}Sr , relative to a stable non-radiogenic isotope, ^{86}Sr , whose abundance does

not change. Thus, when considering the Rb-Sr isotopic system, the radioactive decay equation becomes:

$$^{87}\text{Sr}/^{86}\text{Sr} = ^{87}\text{Sr}/^{86}\text{Sr}_{t=0} + ^{87}\text{Rb}/^{86}\text{Sr} * (e^{\lambda t} - 1)$$

Therefore, in a system of cogenetic samples which crystallized at the same time, the variation in $^{87}\text{Sr}/^{86}\text{Sr}$ will only be a function of the time since closure, or crystallization, and the parent to daughter ratio at the time of crystallization.

Rubidium is typically a highly incompatible element in igneous rocks, due to its large ionic radius and +1 charge, and is found in micas, amphibole and K-feldspar in minor amounts. In contrast, Sr has a smaller ionic radius and +2 charge, and is relatively compatible in felsic igneous systems as it readily replaces Ca^{2+} in plagioclase. The chemical differences between the parent, Rb, and the daughter, Sr, can result in large differences in the Rb/Sr ratio in rocks and minerals which can vary by several orders of magnitudes. In addition to its usefulness in dating, the Rb-Sr isotopic system is particularly useful when inferring the source of a melt and magmatic differentiation processes, as the mantle has a relatively low, uniform $^{87}\text{Sr}/^{86}\text{Sr}$ ratio and the continental crust has a higher, more variable $^{87}\text{Sr}/^{86}\text{Sr}$ ratio. These differences can result in magmatic reservoirs that have distinctly different isotopic ratios (Dickin, 2005).

However, isotopic systems can reopen and the isotopic values can be changed, particularly for relatively mobile Rb and Sr. Weathering and hydrothermal activity can cause affected rocks to become contaminated with Rb and Sr removed from other

rocks, altering the isotopic values in the rocks after crystallization. Opening of the isotopic system can also occur during metamorphic events, when the temperature exceeds the closure temperature of the Rb-Sr system which will cause isotopic rehomogenization (Dickin, 2005).

$^{87}\text{Sr}/^{86}\text{Sr}$ isotopic ratios can be used to determine the source of a melt, as the continental crust and mantle have different isotopic ratios. This can be attributed to the previously mentioned chemical differences in Rb and Sr. As Rb is more incompatible than Sr, it will partition into a melt more than Sr during a differentiation event. This results in reservoirs that are enriched in incompatible elements which, over time, will evolve to have a higher $^{87}\text{Sr}/^{86}\text{Sr}$ ratio than reservoirs with depleted incompatible elements. Characteristically, the continental crust has higher $^{87}\text{Sr}/^{86}\text{Sr}$ and Rb/Sr ratios, while the mantle has a lower $^{87}\text{Sr}/^{86}\text{Sr}$ and Rb/Sr ratios (Dickin, 2005).

Sm-Nd

Samarium (Sm) and Neodymium (Nd) are both light rare earth elements, as well as lithophile and refractory elements. ^{143}Nd is produced by the alpha decay of ^{147}Sm with a half-life of $1.06 \times 10^{11}\text{y}$ and a decay constant $\lambda=6.54 \times 10^{-12}\text{y}^{-1}$. Nd has a slightly larger ionic radius than Sm, and as a result is slightly more incompatible than Sm. This results in higher Sm/Nd ratios in reservoirs that are depleted in incompatible elements, such as the mantle, as Nd is preferentially removed during partial melting. This enrichment of Sm relative to Nd results in a higher $^{143}\text{Nd}/^{144}\text{Nd}$ ratio in the mantle than in the crust. Isotopic studies using the Sm-Nd system must be done precisely, as the elements are

chemically similar and little fractionation occurs between them, such that the isotopic difference between mantle and crust are smaller than in the Rb-Sr system. Despite this, Nd and Sm are relatively immobile which makes them less susceptible to the effects of weathering and metamorphic events, unlike the Rb-Sr system. Using the isochron-type decay equation, the age can be determined using:

$$^{143}\text{Nd}/^{144}\text{Nd} = ^{143}\text{Nd}/^{144}\text{Nd}_{t=0} + ^{147}\text{Sm}/^{143}\text{Nd} * (e^{\lambda t} - 1)$$

Conventionally, Nd-isotopes are reported as a $^{143}\text{Nd}/^{144}\text{Nd}$ ratio, which is the ratio of the radiogenic daughter isotope ^{143}Nd , to a non-radiogenic, stable isotope ^{144}Nd . Epsilon (ϵ) notation, more commonly used to report Nd isotopes, is the measure of deviation of $^{143}\text{Nd}/^{144}\text{Nd}$ from the Earth's chondritic $^{143}\text{Nd}/^{144}\text{Nd}$ ratio, and is calculated using:

$$\epsilon\text{NdT} = \left[\frac{\frac{^{143}\text{Nd}}{^{144}\text{Nd}}_{T_{\text{sample}}}}{\frac{^{143}\text{Nd}}{^{144}\text{Nd}}_{T_{\text{CHUR}}}} - 1 \right] \times 10^4$$

where CHUR represents the Chondritic Uniform Reservoir assuming a chondritic Nd isotopic composition for the bulk silicate Earth at time T. The present day values for CHUR are $^{143}\text{Nd}/^{144}\text{Nd} = 0.51263$ and $^{147}\text{Sm}/^{144}\text{Nd} = 0.196$ (Bouvier et al., 2008). The ϵNd value can be used as an indicator of source, as positive ϵNd indicates a depleted source and a negative ϵNd indicates an enriched source. Most terrestrial rocks have an ϵNd value between -20 and +10, while chondritic meteorites have an ϵNd of 0 (Dickin, 2005).

Sr and Nd isotopic data can be used together as a useful way to determine the source for a suite of rocks due to the differences between the isotopic systems. This includes inverse parent-daughter compatibility which results in differences in their presence in crustal and mantle source reservoirs. On an ϵNd versus $^{87}\text{Sr}/^{86}\text{Sr}$ diagram, source can be inferred using the known isotopic values of other important reservoirs, such as mid-ocean ridge basalts (MORB), ocean island basalts (OIB), and the isotopic value of the bulk Earth (Fig. 3.4). In this diagram, the mantle array is defined by the location of MORB at the top of the array which represents the melting product of the modern depleted mantle, and has the highest ϵNd and lowest $^{87}\text{Sr}/^{86}\text{Sr}$ values of all young igneous rocks. OIBs are the melting product of a more enriched mantle and have lower ϵNd values than MORB, but can have $^{87}\text{Sr}/^{86}\text{Sr}$ values verging towards continental rocks. Continental granites characteristically have low ϵNd and high $^{87}\text{Sr}/^{86}\text{Sr}$ values; however these values are much more variable (Dickin, 2005).

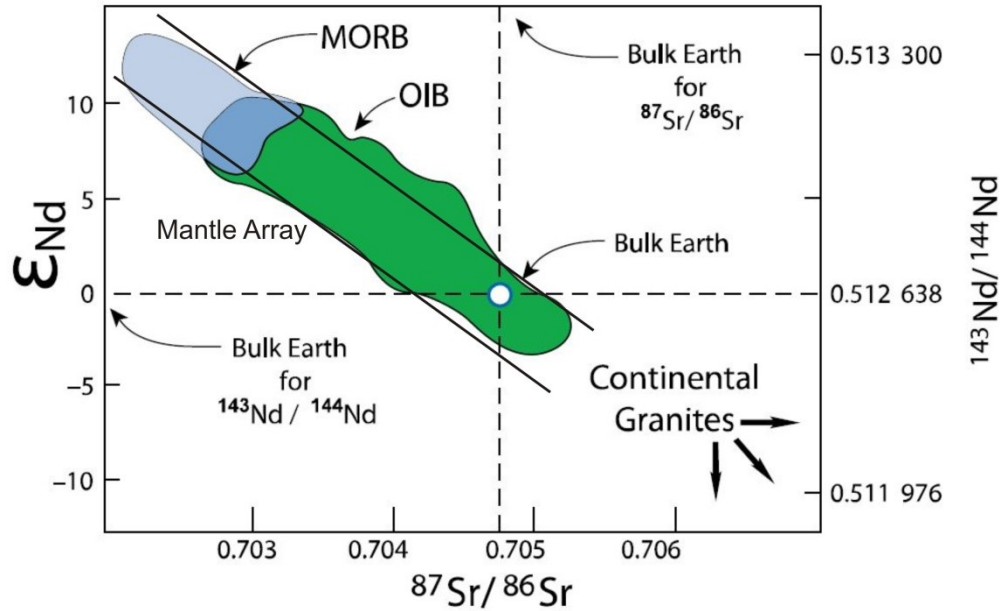


Figure 3.4: Sr vs. Nd isotopic correlation. MORB and OIB define a tightly trending correlation referred to as the mantle array. Continental granites have ϵ_{Nd} values < 0 , and have a much wider range in isotopic values than MORB and OIB. Modified after Stepmner (2017) and Allègre (2008).

(Pb)-(Pb), or common Pb

Lead (Pb) is a volatile, chalcophile element that is present as a trace element throughout the Earth. The Pb isotopic system is a much more complex decay system than Rb-Sr and Sm-Nd, and begins with the decay of radioactive uranium (U) and thorium (Th). These radioactive decay chains begin with ^{238}U , ^{235}U , and ^{232}Th , and end in the production of radiogenic daughter isotopes ^{206}Pb , ^{207}Pb , and ^{208}Pb , respectively. Intermediate members of the decay chain series are short lived and therefore will not be discussed. The half-lives of the radioactive U and Th parents vary. Whereas the half-life of ^{238}U is ~ 4.47 Ga (comparable to the age of the Earth) and the half-life of ^{232}Th is 14.01 Ga

(comparable to the age of the universe), the half-life of ^{235}U is 0.704 Ga (Dickin, 2005). Thus, little ^{207}Pb is produced today compared to ^{206}Pb and ^{208}Pb . Conventionally, the radiogenic Pb isotopes are measured relative to ^{204}Pb , a stable, non-radiogenic Pb isotope (Dickin, 2005).

Due to the high incompatibility of the radioactive parents, U and Th, compared to Pb, the Pb isotopic system is arguably the best indicator of a crustal source in a rock. The incompatibility of U and Th has caused these elements to concentrate in melts which primarily become incorporated in the crust. As a result, high Pb isotopic ratios and high concentrations of Pb exist in the continental crust relative to the mantle (Fig. 3.5). The isotopic signature of the crust is easily picked up during the assimilation of crustal rocks by mantle derived magma, and can therefore be a strong indicator of crustal contamination (Dickin, 2005).

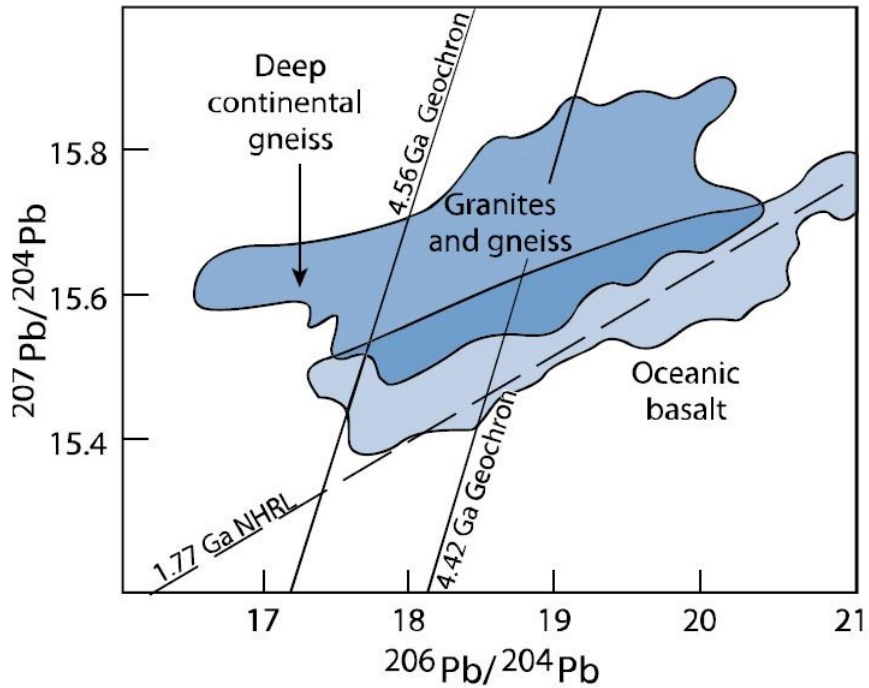


Figure 3.5: A $^{206}\text{Pb}/^{204}\text{Pb}$ vs. $^{207}\text{Pb}/^{204}\text{Pb}$ diagram showing the differences in isotopic value of the oceanic basalt (mantle) and granites and gneiss (continental crust). $^{207}\text{Pb}/^{204}\text{Pb}$ isotopic values for the continental crust are typically higher than the mantle, which can be used as a good indicator of crustal source. The Northern Hemisphere Reference Line (NHRL) represents the isotopic evolution of the conducting mantle beneath the northern hemisphere. The slope of the NHRL is equal to an age of 1.77 Ga. Two geochrons, 4.56 and 4.42 Ga, represent the approximate evolution of the Pb isotopic evolution of the bulk Earth over time. From Stepner (2017), modified after Allègre (2008).

4.0 Regional Geology

4.1 Geological Framework

The Underdown Caldera is one of 37 calderas located within the WNVF of the Great Basin, 23 of which are well identified and 14 of which are hypothesized based on dated outflow tuffs (Fig. 4.1) (Henry and John, 2013). More specifically, the Underdown Caldera is located in the Shoshone Mountains of north-central Nevada. The intracaldera tuffs of the Underdown Caldera are confined to the Shoshone Mountain range; however outflow tuff has previously been identified extending to the east of the caldera, stretching nearly to the Nevada-Utah border (Best et al., 2013). Our work indicates that at least two outflow units exist west of the Underdown Caldera. The Underdown Tuff, the main intracaldera tuff in the Underdown Caldera, has 23 km of exposure along the eastern edge of the Shoshone Mountains which indicates a minimum length of the caldera; however the entire north-south extent of the caldera has not been mapped. The Underdown Caldera is located just to the west of the initial $^{87}\text{Sr}/^{86}\text{Sr} = 0.706$ isopleth in central Nevada, and separates the Precambrian basement to the east from the Phanerozoic igneous and sedimentary basement to the west (Henry and John, 2013; Best et al., 2013).

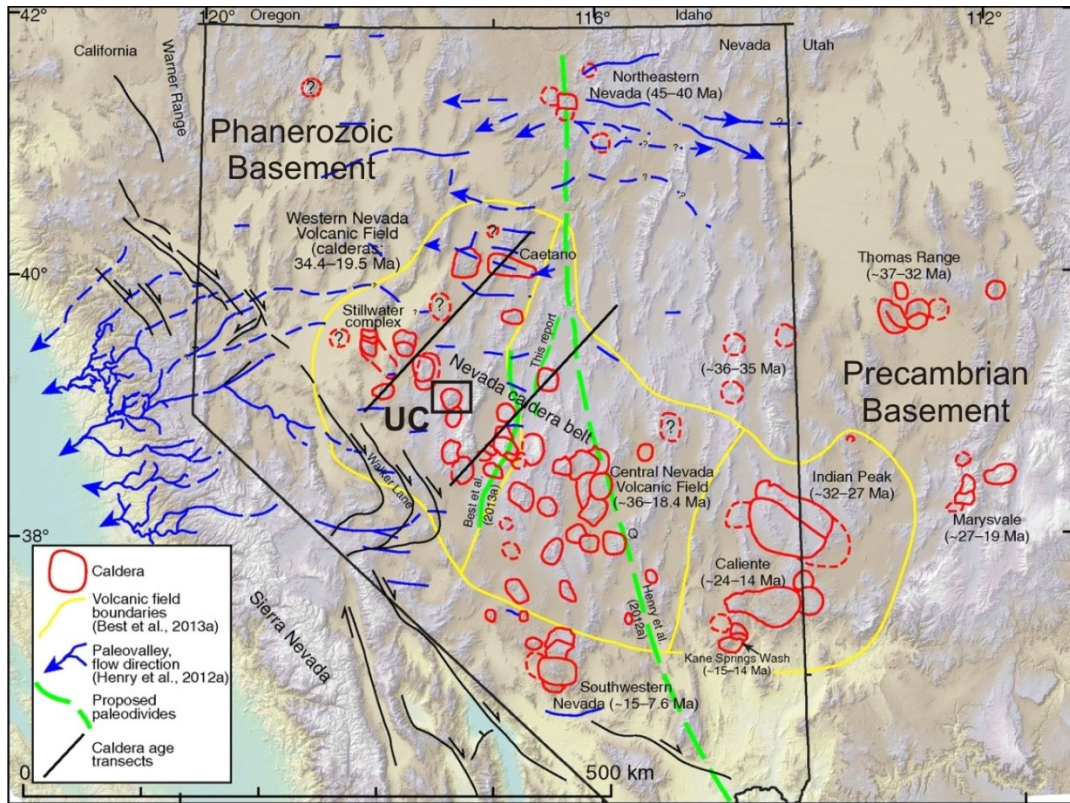


Figure 4.1: Map of the western United States showing the location of the Underdown Caldera (UC) in the Western Nevada Volcanic Field (modified from Henry and John, 2013). Dashed green lines represent proposed paleodivides that mark the highest elevation during the Eocene. Blue lines are paleovalleys (eroded channels) that outflow tuffs commonly follow. Yellow outlines separate the Western Nevada Volcanic Field, Central Nevada Volcanic Field, and Indian Peak-Caliente Volcanic Field.

4.2 Stratigraphic Relations

The Underdown Caldera is contained within a single, mildly (< 10 degrees) west-tilted fault block. In 1970, H. F. Bonham mapped the Underdown Caldera complex, identifying andesite basement rocks (the Pablo Formation), three Oligocene rhyolitic tuff packages (the Underdown Tuff, the Bonita Canyon Formation, and the Tuff of Toiyabe), rhyolite to intermediate intrusions, and basaltic lava flows (Fig. 4.2). According to Bonham (1970), the Underdown Tuff is at least 490 m thick and was deposited against a ridge of basement rocks of the Pablo Formation. The thick exposure has two cooling units, the lower of which exhibits columnar jointing and laminar flow structures (including stretched, folded and lineated pumice) in densely welded sections. The Underdown Tuff is overlain by an epi- and volcanoclastic unit up to 500 m thick; the Bonita Canyon Formation. Overlying the Bonita Canyon Formation, a similarly thick (460 m) unit of phenocryst rich tuff was identified by Bonham as the Toiyabe Quartz Latite (or Tuff of Toiyabe). The 960 m thick deposit of reworked and welded tuffs above the Underdown Tuff is interpreted as post-collapse fill of the caldera after the eruption of the Underdown Tuff (Best et al., 2013).

The rocks of the Underdown Caldera area have been dated by ^{40}Ar - ^{39}Ar dating of bulk-rock (mafic lavas), plagioclase crystals (Pablo Formation) and sanidine crystals (felsic rocks) (Appendix I, Table I). The oldest unit sampled in the Underdown Caldera is the andesite basement rocks of the Pablo Formation which have a metamorphic age of 87.6 ± 0.06 Ma (likely Mesozoic in age; C. Henry, pers. comm., 2018). The stratigraphically

lowest Oligocene tuff unit, the Underdown Tuff, has ages of 24.90 ± 0.04 - 0.07 Ma, and 24.96 ± 0.05 Ma (C. Henry, pers. comm., 2018; Best et al., 2013, respectively). The 24.999 ± 0.043 Ma Bonita Canyon Formation (C. Henry, pers. comm., 2018) unconformably overlies the Underdown Tuff, and is overlain by a densely welded tuff unit, believed by Bonham to be the Tuff of Toiyabe (Best et al., 2013; Henry and John, 2013). However, this unit is likely misidentified by Bonham (1970) due to differences between the age of this tuff and the true Tuff of Toiyabe exposed elsewhere in the Western Nevada Volcanic Field, as well as differences in the paleomagnetic polarity (Best et al., 2013). This unit will henceforth be referred to as the Unnamed tuff. The Unnamed tuff is dated as 24.755 ± 0.037 Ma (C. Henry, pers. comm., 2018) while the Tuff of Toiyabe is dated at 23.31 ± 0.05 Ma (Henry and John, 2013). The intermediate and rhyolitic intrusions within the caldera have been dated at 24.954 ± 0.043 Ma and 24.774 ± 0.051 Ma respectively (C. Henry, pers. comm., 2018). Basaltic lava flows located on the margin of the caldera have been dated at ca. 18.4 Ma (Tennant, 2018).

The tuff of Clipper Gap, the outflow tuff from the Underdown Caldera, is exposed primarily to the east of the caldera and has been dated at 24.87 ± 0.10 Ma and 24.981 ± 0.036 Ma (Henry and John, 2013; C. Henry, pers. comm., 2018, respectively). Exposures of the tuff of Clipper Gap extends across Nevada nearly to the Utah border (Fig. 4.3) and crosses the topographic barrier in central Nevada where most of the outflow tuffs of the Central Nevada volcanic field terminate. The total estimated volume of the Underdown Tuff and tuff of Clipper Gap is at least 180 km^3 (Best et al., 2013).

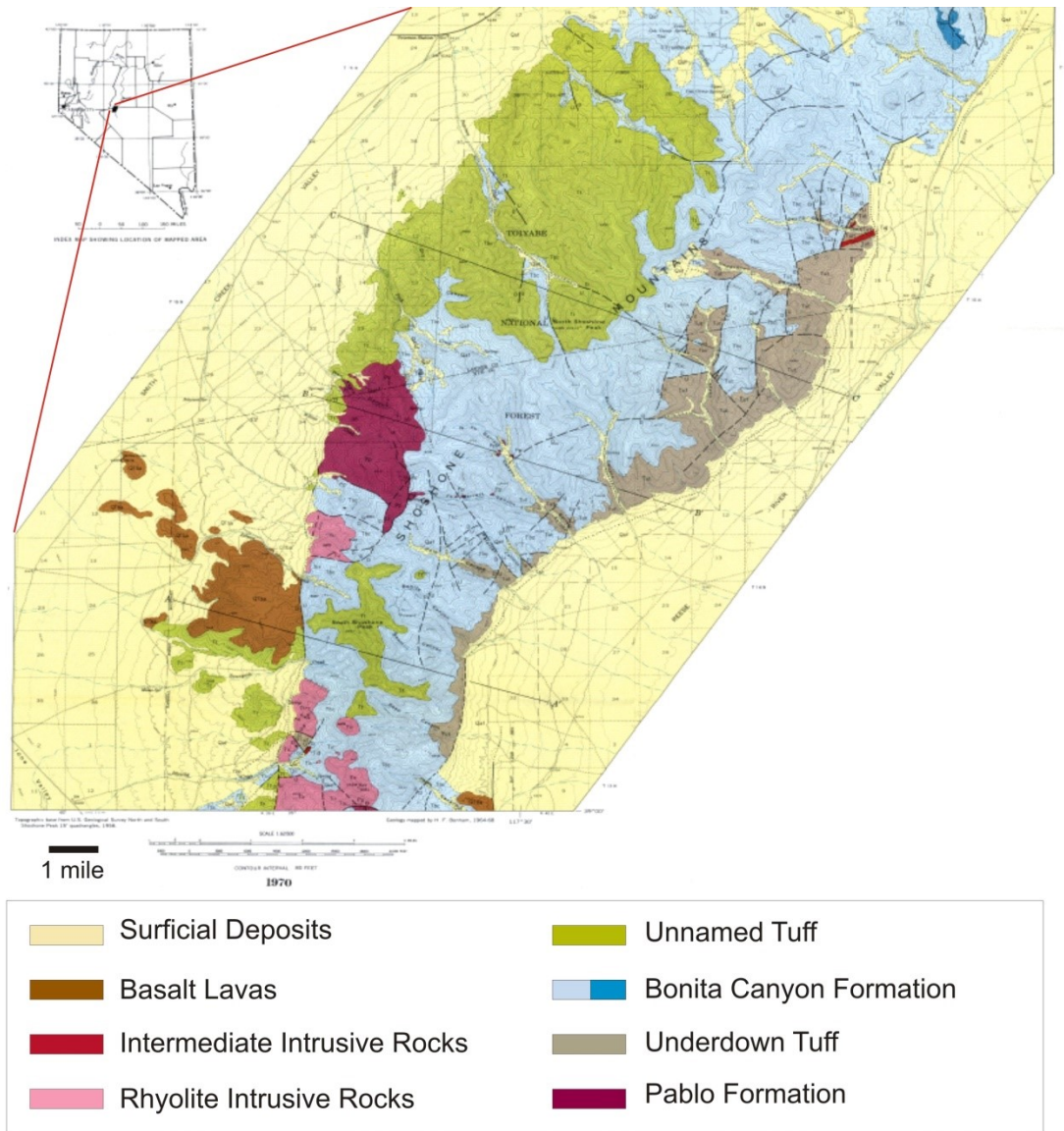


Figure 4.2: The Underdown Caldera complex as mapped by H. F. Bonham (1970). Bonham mapped three Oligocene rhyolitic tuff packages; the Underdown Tuff, the Bonita Canyon Formation, and the Tuff of Toiyabe. The Tuff of Toiyabe will henceforth be referred to as the Unnamed tuff, as this unit was incorrectly assumed to be correlative with the true Tuff of Toiyabe. Bonham also mapped andesite basement rocks (the Pablo Formation), rhyolite and intermediate intrusive rocks, and basaltic lavas.

4.3 Field Observations

Sample locations of the Underdown Caldera complex samples are listed in Appendix I, Table II.

Intracaldera tuffs and the tuff of Clipper Gap

The main caldera forming tuff, the Underdown Tuff, was identified in the field by its crystal poor texture and phenocryst assemblage of two feldspars, quartz and minor biotite. Exposures of Underdown Tuff typically consisted of two main cooling units; a poorly welded base, and a moderately to densely welded upper unit. Thick sections of the Underdown Tuff in Barrett and Underdown Canyons exhibited cooling joints in the moderately welded middle of the section (Fig. 4.4). Two types of pumice were observed in the Underdown Tuff; rare large purple porphyritic pumice and common small, white aphyric pumice. The identification of the tuff of Clipper Gap was aided by its similarities to the Underdown Tuff in phenocryst assemblage, crystal poor texture, and the two pumice types. Columnar jointing was also observed in the tuff of Clipper Gap at Butler Ranch in Monitor Valley. This section had a lower poorly welded unit and a moderately welded upper unit separated by a vitrophyre. However, in a section of tuff of Clipper Gap on Moore's Canyon Road most of the section was unwelded and porphyritic pumice was only found in a small welded section at the very top of the exposure (Fig. 4.5).

The Bonita Canyon Formation was distinguishable from the Underdown Tuff by its local sedimentary textures, as well as its poorly welded, light coloured matrix. The base of the

Bonita Canyon Formation contains abundant lithic material ranging in size from cm-size fragments to large blocks, and some lithics in the base of the formation were identified as possible Underdown Tuff and tuff of Arc Dome (Fig. 4.6). Megabreccia blocks of older tuff units (Tuff of Arc Dome) and Pablo Formation are found in the Bonita Canyon Formation. Moving up section, the Bonita Canyon Formation grades into a pumice rich tuff, where lithic material is rare. Pumice in the Bonita Canyon Formation is brown and aphyric, and no porphyritic pumice was observed. The poorly to unwelded matrix typically contained a small proportion of quartz and feldspar phenocrysts, however no biotite was observed in the field in this unit.

The Unnamed tuff was easily distinguished from the Underdown Tuff and tuff of Clipper Gap by its highly porphyritic texture, despite their similar phenocryst assemblages (Fig. 4.7). Pumice in the Unnamed tuff was typically grey and aphyric, but no purple porphyritic pumice characteristic of the Underdown Tuff and tuff of Clipper Gap were observed. Both columnar jointing and rosette jointing were observed in a thick section of Unnamed tuff in Gold Park Canyon. No vitrophyre was found in Peterson Canyon, War Eagle Canyon, or Gold Park Canyon where the Unnamed tuff was also sampled.

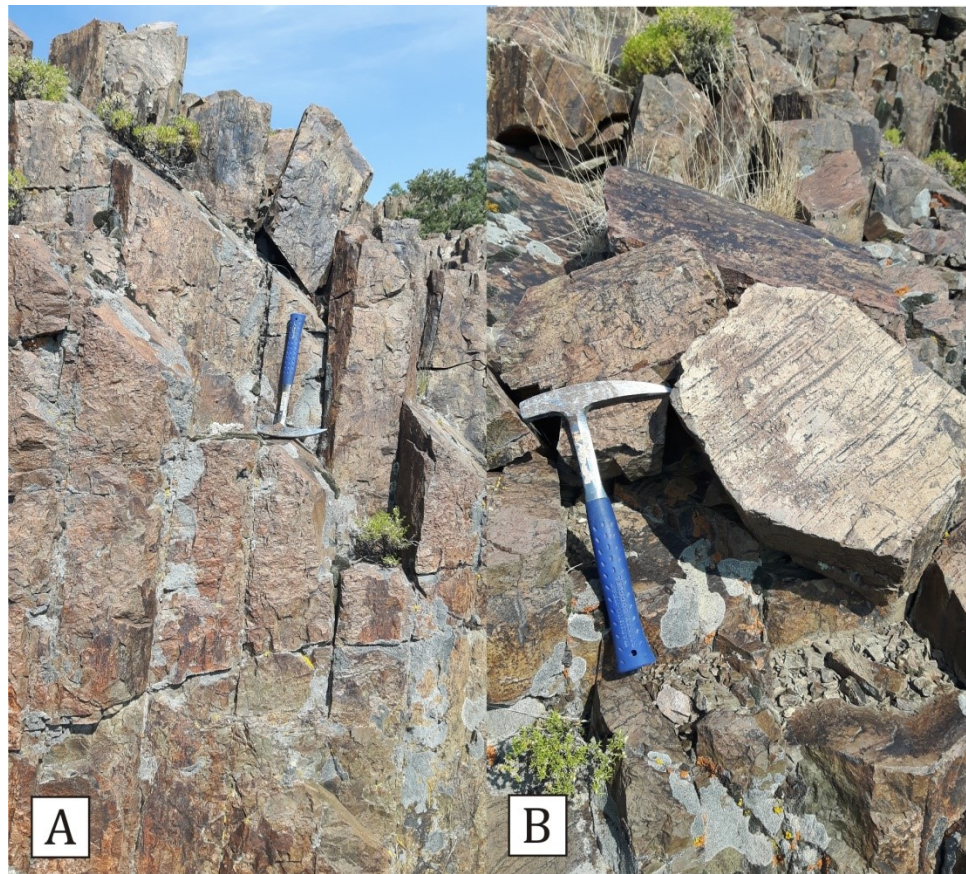


Figure 4.4: Field photos of cooling joints of the Underdown Tuff from Barrett Canyon (A) and a cross section slab of a cooling joint (B). Black streaks in the slab are flattened pumice propagating perpendicular to the elongation of the cooling joint (hammer for scale).

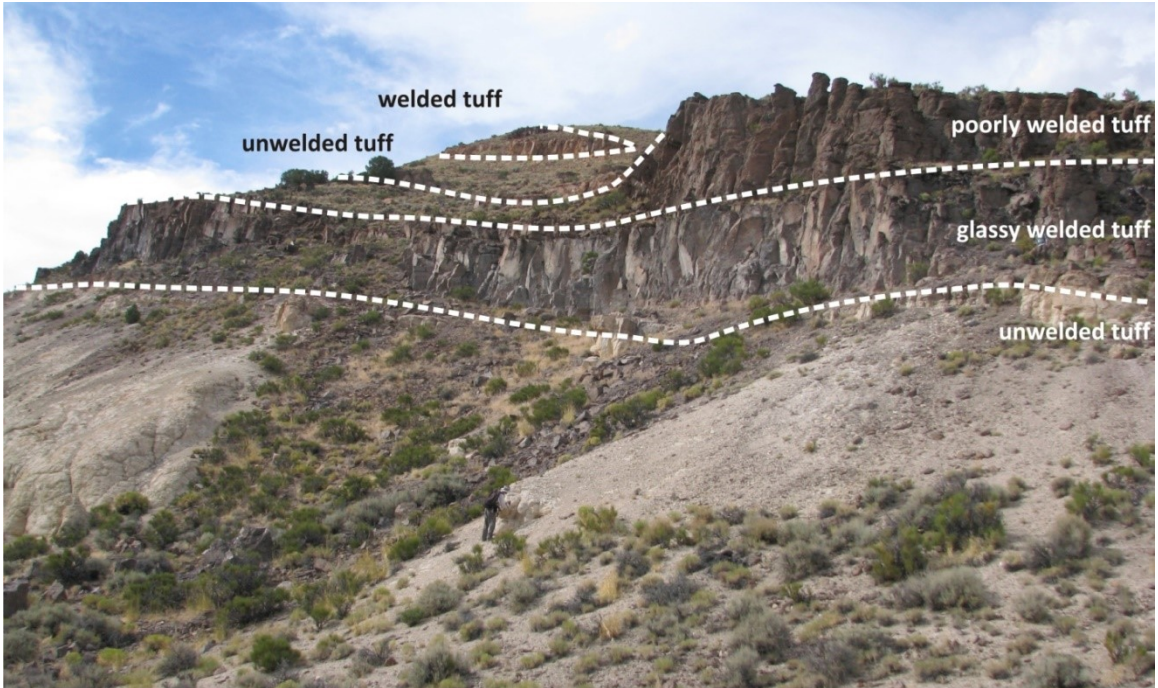


Figure 4.5: The tuff of Clipper Gap exposed at Moore’s Canyon Road. The exposure of tuff of Clipper Gap was unusual based on its thick sections of unwelded to poorly welded material. A section of glassy, welded tuff separates the basal unwelded section from the poorly welded section in the upper section of the cliff. Unwelded tuff sits on top of the poorly welded unit, and welded tuff is exposed at the very top of the section (geologist for scale in lower centre of the photo).



Figure 4.6: (A) A large outcrop of Bonita Canyon Formation in Barrett Canyon. (B) A lithic fragment of Underdown Tuff in the lithic rich base of the Bonita Canyon Formation (hammer for scale). (C) The lithic rich base of the Bonita Canyon Formation and a large tuff of Arc Dome lithic fragment (hammer for scale). (D) The lithic poor upper section of the Bonita Canyon Formation (hammer for scale).



Figure 4.7: (A) The Unnamed tuff showing its highly porphyritic texture. (B) The Unnamed tuff with small grey fiamme (photos from Brian Cousens, hammer for scale).

Other tuffs and potential outflow tuff

Other units such as the tuff of Gabbs Valley (25.15 ± 0.06 Ma; Henry and John, 2013), the tuff of Arc Dome (25.18 ± 0.06 Ma; Henry and John, 2013), and the tuff of Brunton Pass (24.89 ± 0.05 Ma, 25.12 ± 0.06 Ma; C. Henry, pers. comm., 2018; Henry and John, 2013, respectively) were sampled outside of the Underdown Caldera. Similar to the Underdown Tuff, the tuff of Gabbs Valley was crystal poor; however the unit contained three different types of pumice; white, dark, and banded, all of which were crystal poor (Fig. 4.8). At Fissure Ridge, previously mapped tuff of Gabbs Valley was sampled as potentially being tuff of Clipper Gap. This exposure consisted of three different tuff units of differing ages, the top two of which are similar in age to the Underdown Caldera magmatic event. The first of these two units, TgV2 (25.11 ± 0.08 Ma; C. Henry, pers. comm., 2018), had a poorly welded base with large banded pumice and a phenocryst assemblage of quartz, feldspar and biotite. Welding of the unit increased moving up

section as the tuff became highly porphyritic and pumice disappeared. The uppermost unit, TgV3 (24.875 ± 0.048 ; C. Henry, pers. comm., 2018), was separated from TgV2 by the basal vitrophyre of TgV3 (24.898 ± 0.009 ; C. Henry, pers. comm., 2018). The crystal poor texture of TgV3 made it more similar in appearance to the Underdown Tuff and tuff of Clipper Gap. TgV3 was densely welded and contained very large porphyritic pumice (Fig. 4.9).

A similar aged ash flow tuff to the tuff of Gabbs Valley is the tuff of Arc Dome which was identified outside of the Underdown Caldera by its crystal rich texture, and phenocryst assemblage of quartz, feldspar and biotite. A highly porphyritic vitrophyre sampled from the Reese River Butte contained ~50% feldspar and quartz phenocrysts. The tuff of Arc Dome is separated by a fault from the tuff of Brunton Pass at the Brunton Pass locality. The tuff of Brunton Pass was identified by its tan matrix and abundant grey fiamme, as it has a crystal poor texture and phenocryst assemblage of quartz, feldspar and biotite, similar to the other Oligocene tuff units.

Potential Underdown Caldera outflow tuff was collected west of the caldera in the Terrill Mountains. Similar to the tuff of Clipper Gap, these tuffs are exposed in two distinct cooling units separated by a vitrophyre. The poorly to moderately welded basal unit is grey in colour, crystal poor, and contains three different types of pumice; white, banded, and black fiamme (Fig. 4.10). The basal unit was observed to have a gradational contact with the overlying basal vitrophyre of a moderately welded upper cooling unit.

The brown, upper tuff unit is also crystal poor, contains small black and white pumice, and contains minor amounts of quartz and feldspar.

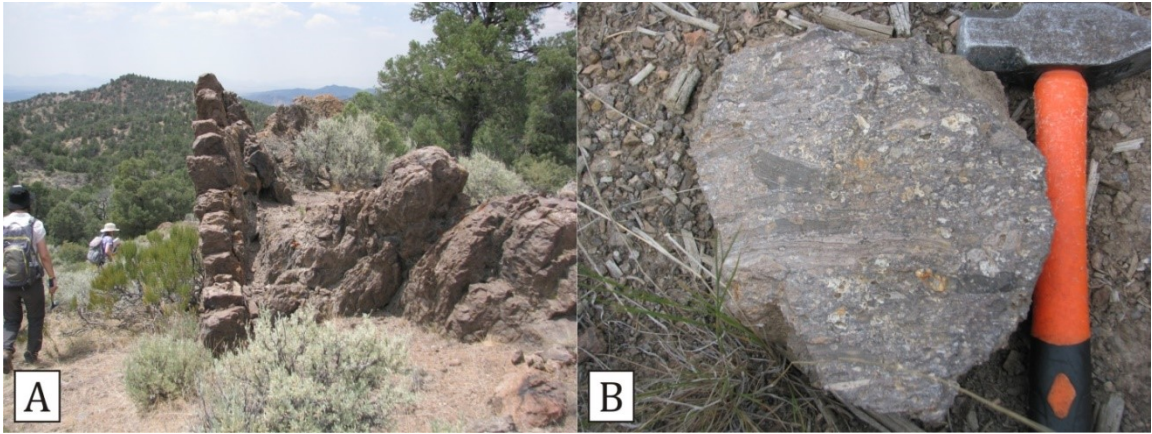


Figure 4.8: (A) Outcrop photo of the tuff of Gabbs Valley (geologists for scale). (B) Hand sample photograph of the tuff of Gabbs Valley showing the large banded pumice typical of the unit (photos from Brian Cousens, hammer for scale).



Figure 4.9: Hand sample and outcrop photographs of TgV2 and TgV3 from Fissure Ridge. (A) Hand sample photograph of the poorly welded TgV2 base (thumb for scale). (B) Hand sample photograph of the moderately welded middle of TgV2 (thumb for scale). (C) Hand sample of the densely welded top of TgV2. (D) Outcrop photograph of a large, porphyritic pumice in TgV3 (photos from Brian Cousens, hammer for scale).

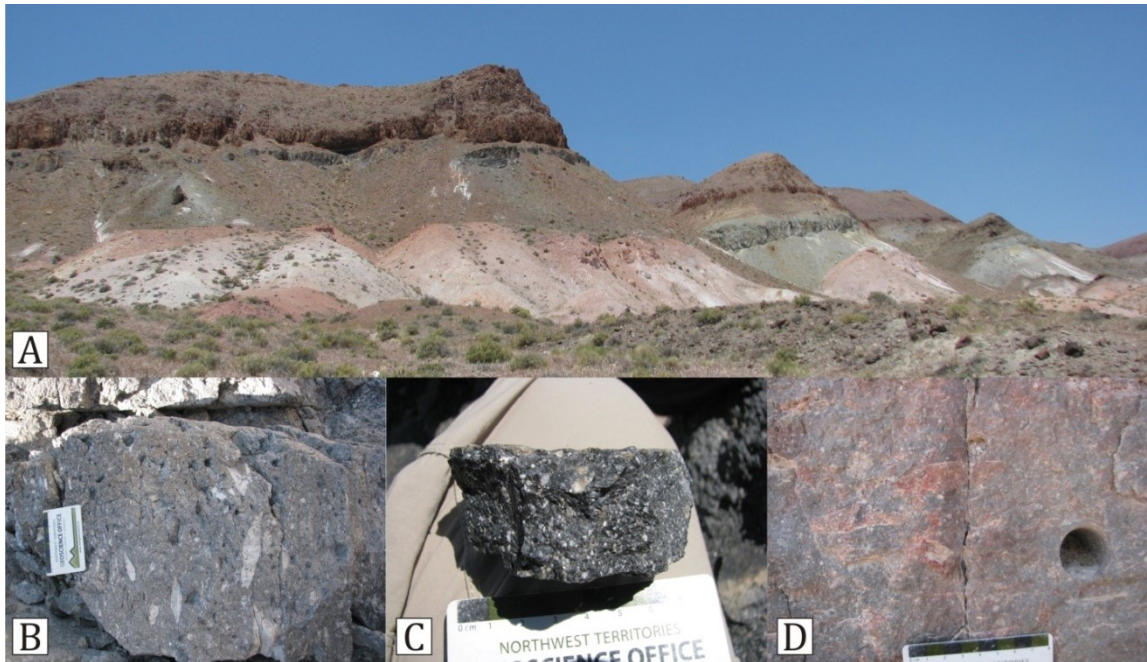


Figure 4.10: (A) The Terrill Mountains tuffs are exposed as a lower, grey, poorly to moderately welded unit, and an upper, brown, moderately welded cooling unit, separated by a vitrophyre. (B) A sample of the lower cooling unit showing the white pumice and black fiamme. (C) A hand sample of the porphyritic vitrophyre. (D) An outcrop shot of the upper cooling unit and paleomagnetic drill hole (photos from Brian Cousens).

Megabreccia blocks

The Pablo Formation is commonly exposed as large blocks in the Underdown Caldera (Fig. 4.11). These large blocks sit unconformably on top of the Bonita Canyon Formation in Barrett and War Eagle Canyon. The Pablo Formation was easily distinguishable from other units within the caldera by its dark grey colour and plagioclase-hornblende matrix. Large blocks of the Pablo Formation typically appear to be brecciated and some have epidote alteration. Some of the large blocks mapped as Pablo Formation in Barrett

Canyon by Bonham (1970) were targeted during field work to verify their identity. While all of these blocks in Barrett Canyon were mapped as Pablo Formation by Bonham, one block near the base of a large exposure of Bonita Canyon Formation was determined to be a large conglomerate block containing cobble to boulder sized material. The tuff of Arc Dome was also found in large blocks and spires in canyons within the caldera margin. Similar to the Pablo Formation, spires of the tuff of Arc Dome unconformably lie on the Bonita Canyon Formation. These spires of megabreccia material were identified as possible tuff of Arc Dome by their phenocryst assemblages (quartz-feldspar-biotite) and crystal rich texture (Fig. 4.12).



Figure 4.11: (A) A Pablo Formation outcrop in Barrett Canyon (geologists for scale). The Pablo Formation was often present as blocks and spires sitting unconformably on top of the Bonita Canyon Formation. (B) A close-up photo of the Pablo Formation outcrop (hammer for scale). The unit was variably altered and brecciated (photos from Brian Cousens).

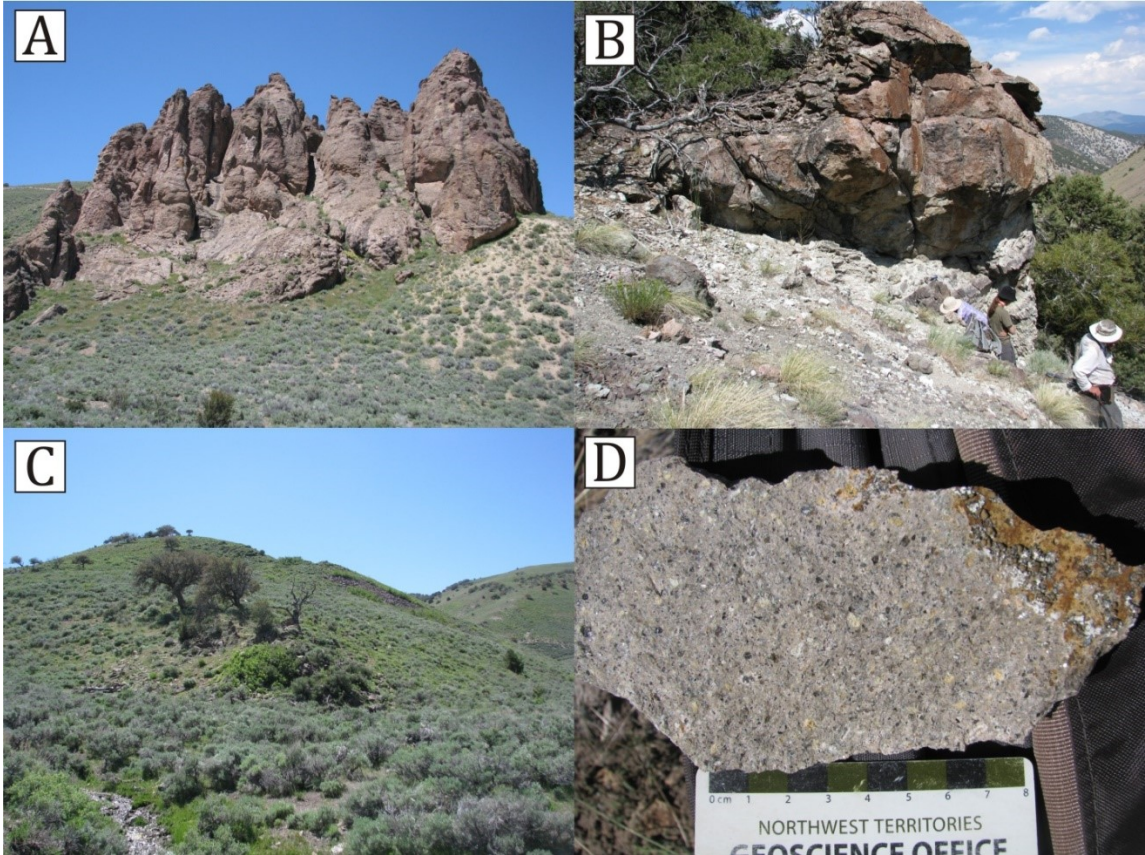


Figure 4.12: (A) Large spires of a quartz-feldspar-biotite tuff deposited on the Bonita Canyon Formation which are megabreccia blocks of the tuff of Arc Dome from the caldera wall that fell inwards into the caldera during collapse. (B) A large block of tuff of Arc Dome overlying the Bonita Canyon formation in the Barrett Canyon (geologists for scale). (C) A small outcrop of the quartz-feldspar-biotite tuff from where a megabreccia sample was taken. (D) A sample of porphyritic quartz-feldspar-biotite tuff proposed to be megabreccia from the wall rock of the caldera collected from the small outcrop (C) (photos from Brian Cousens).

Intrusions and dykes

A dacite porphyry dyke was sampled in Devil's Gate Canyon and was distinguished by its high proportion of feldspars (30-40%) and minor biotite. Fine grained intrusions were observed within the porphyritic texture of the intermediate dyke. The contact of the dacite dyke with the Underdown Tuff trends east to west. Rhyolite intrusions sampled in Idlewild Canyon had a similar mineral assemblage as the surrounding Bonita Canyon Formation and Unnamed tuff (quartz, feldspar and biotite).

5.0 Methods

5.1 Samples

41 rock samples were collected in July 2017 and prepared for petrographic, geochemical and isotopic analysis. Unaltered, non-weathered in-situ pumice and whole rock samples were collected, where possible, from intracaldera and potential outflow tuff units. Pumice fragments were collected in locations where the pumice could be separated from the matrix, and whole rock samples were collected with an effort to minimize the amount of lithic fragments. These samples were added to an existing collection of 70 samples from the same region collected by K. Klausen, B. Cousens, and C. Henry (Nevada Bureau of Mines and Geology) in June 2016. These samples from 2016 were previously prepared as thin sections by K. Klausen.

Polished thin sections were produced from 37 of the 41 collected samples at the Carleton University Thin Section Laboratory. The thin sections were analyzed using a Leica petrographic transmitted light microscope, and photomicrographs were taken using a petrographic microscope with a Nikon camera and Jenoptik software.

5.2 Major and Trace element analyses

Sample preparation was done at the Carleton University rock preparation lab. A diamond-bladed rock saw was used to cut samples into slabs and remove any weathered surfaces and lithic fragments. Pumice was removed from the whole rock matrix where possible. A Bico Chipmunk jaw-crusher was used to crush each sample

until the particle size was reduced to (<1 mm). A small amount of sample was used to pre-contaminate the jaw-crusher before each sample was crushed, that was discarded after crushing, reducing the possibility of contamination from the steel plates. The steel plate and inside of the jaw-crusher was scrubbed with a wire brush and cleaned with ethanol and compressed air between each sample. A Rocklabs ring mill with a chrome-steel head was used to reduce each sample to a fine powder. The ring mill was cleaned between samples with water, compressed air, and ethanol. The ring mill was then pre-contaminated with a small amount of crushed sample which was then discarded. The steel head only adds Cr to the crushed powder, based on comparison analyses between tuffs crushed in an agate and the steel head.

Whole rock major and trace element concentrations were determined at the ALS Laboratory in North Vancouver, British Columbia. Major element concentrations were obtained using inductively coupled plasma atomic emission spectroscopy (ICP-AES), and trace element concentrations were measured by inductively coupled plasma mass spectrometry (ICP-MS). ICP-AES measures concentrations in weight percent (wt. %) for the following oxides; Al₂O₃, BaO, CaO, Cr₂O₃, Fe₂O₃, K₂O, MgO, MnO, Na₂O, P₂O₅, SiO₂, SrO and TiO₂. The loss-on-ignition (LOI), which is the weight loss of volatiles (H₂O, CO₂, S, and other trace gases) during fusion, was also measured. Trace element concentrations were determined by ICP-MS for the following elements; Ag, Ba, Cd, Ce, Cs, Cu, Dy, Er, Eu, Ga, Gd, Hf, Ho, La, Li, Lu, Mo, Nb, Nd, Pb, Pr, Rb, Sm, Sn, Sr, Ta, Tb, Th, Tm, U, W, Y,

Yb, and Zr. Concentrations of the metals Co, Cr, Ni, Pb, Sc, V, and Zn were determined by ICP-OES (inductively coupled plasma optical emission spectrometry).

Analysis of the rare earth element (REE) characteristics of some samples showed that their REE abundances have been modified. In an attempt to determine if the REE addition to some samples was due to alteration, five grams of powder was acid-washed in 2.5N HCl on a hotplate at 80°C for five days, then rinsed several times in ultrapure H₂O. A fraction of the acid-washed sample was sent to ALS Laboratories for major and trace element analysis, and isotopic determinations were performed on the acid-washed powder.

5.3 Radiogenic Isotope Methods

22 samples were chosen for Sr and Nd isotopic analysis by thermal ionization mass spectrometry (TIMS) and Pb isotopic analysis by multi-collector inductively coupled plasma mass spectrometry (MC-ICP-MS) at the Isotope Geochemistry and Geochronology Research Centre (IGGRC), Carleton University. Approximately 100 mg of powdered sample was dissolved in 15 mL Savillex Teflon beakers using 3 mL of a concentrated HF:HNO₃ mixture (at an approximately 1:2 ratio). The beakers were left on a 130°C for 2 days before being opened and evaporated until dry. The dried precipitate was re-dissolved using 1-2 drops of concentrated HNO₃ and dried down once more. 6N HCl was then added to the dried residue and the closed Sallivex beakers were placed on a 130°C hotplate. After 2 days, the lids were removed from the beakers and the samples were left to evaporate, before 1N HBr was added to the dried sample for Pb column

chromatography. Elemental separation from the same dissolution was in the order Pb, Sr, and Nd.

Pb Isotope Analysis

Pb separation was completed using a 2 pass procedure. Samples dissolved in 3.0 mL of 1.0N HBr were loaded using a pipette into Bio-Rad 10-mL polyethylene Econo columns containing 0.6 mL of cleaned and conditioned AG1-8X anion resin. After adding the sample to the column, a 2.0 mL wash of HBr was added to the column and both were collected in clean Teflon beakers for Sr and Nd chemistry. 2.0 mL of 1.0N HBr and 0.5 mL of 2.0N HCl were passed through the columns and discarded. 5.0mL of 6.0N HCl was used to elute the Pb into clean snap-cap Teflon beakers which was then dried completely. 0.5mL of 1.0N HBr was added to the dried Pb in preparation for the second column pass. The dissolved sample was pipetted into columns loaded with 0.2 mL of conditioned AG1-8X anion resin. 2.0 mL of 1.0N HBr and 0.3 mL of 1.5N HCl were added sequentially to the columns, and the Pb separate was eluted using 3.0 mL of 6.0N HCl, and then dried down. 0.5 mL of 7.0N HNO₃ was added to the dried Pb residue to drive off any bromides. A 90% Pb yield was measured from the columns, based on calibration of Pb eluted from the column.

The Pb separate was dissolved in 10 µL of HNO₃ for 10 minutes, whereas the acid-washed samples were dissolved in 20 µL HNO₃. 2 mL of HNO₃ and 20 µL (only 15 µL for acid-washed samples) of thallium (Tl) spike were added to a clean polyethylene centrifuge tube. A fraction of the dissolved sample was then pipetted into the centrifuge

tube and the samples were centrifuged for three minutes to remove any particulate matter. The amount of sample added to the tube was calculated based on an assumed 90% column yield, and based on the following equation:

$$\mu L_{sol} = \frac{\mu L_{HNO_3} \times 0.3 \mu g}{\mu g_{sample}}$$

Where μL_{sol} is the volume of solution added to the centrifuge tube, μL_{HNO_3} is the volume of HNO_3 , and $0.3 \mu g$ represents the weight of the HNO_3 . The centrifuge tubes were loaded into the autosampler of a Thermo-Finnigan NEPTUNE multi-collector induction coupled plasma mass spectrometer (MC-ICP-MS). 7 blocks of 10 ratios were taken for each sample, and BCR-2 and NBS981 were run as standards along with the samples. All samples were corrected for mass fractionation using the Tl spike and using the NBS981 standard which has long term laboratory averages of $^{206}Pb/^{204}Pb = 16.9316 \pm 0.0015$, $^{207}Pb/^{204}Pb = 15.4853 \pm 0.0014$, and $^{208}Pb/^{204}Pb = 36.6789 \pm 0.0041$ (24 runs; August 2018-June 2019). BCR-2 has laboratory averages of $^{206}Pb/^{204}Pb = 18.7628 \pm 0.0008$, $^{207}Pb/^{204}Pb = 15.6130 \pm 0.0008$, and $^{208}Pb/^{204}Pb = 38.7218 \pm 0.0020$ (4 runs; October 2018-June 2019).

Sr Isotope Analysis

The LILE/REEs-bearing HBr solution was dried down, subsequently dissolved in 1.0 mL of 7.0N HNO_3 , and was dried down again. The dried residue was taken up in 2.5N HCl and was pipetted into borosilicate glass columns containing ~3mL Dowex AG50-X8 cation resin. The columns were washed using 18.0 mL of 2.5N HCl, and Sr was then collected

using 6.0 mL of 2.5N HCl. Rare earth elements were then eluted using 6.0N HCl. ~2.5µg of Sr, diluted using weak HNO₃, were loaded onto single tantalum filaments with 3 µL of H₃PO₄ and run in a Thermo-Finnigan TRITON thermal ionization mass spectrometer (TIMS). 10 blocks of 10 ratios were taken for each sample, for a total of 100 ratios. NBS987 was run as a standard and yielded an average value of $^{87}\text{Sr}/^{86}\text{Sr} = 0.710242 \pm 0.000013$. The long term lab average for NBS987 standard is $^{87}\text{Sr}/^{86}\text{Sr} = 0.710242 \pm 0.000014$ (17 runs; June 2018-August 2019). The long term lab average for BCR-2 is 0.704998 ± 0.000018 (5 runs; June 2018-March 2019). Initial age-corrected $^{87}\text{Sr}/^{86}\text{Sr}$ ratios were calculated using $^{40}\text{Ar}/^{39}\text{Ar}$ ages provided by C. Henry (Appendix I, Table I).

Nd Isotope Analysis

The REE-bearing fraction collected from the Sr columns was dried down and then taken up in 0.26N HCl. The solution was pipetted into Eichrom Ln spec columns containing Teflon powder coated with HDEHP (di(2-ethylhexyl)) orthophosphoric acid. 6.5 mL of 0.26 N HCl was used to wash the columns, after which the Nd was eluted using 5 mL of 0.26N HCl and was then dried down. ~0.5 µg of Nd and 1 µL of H₃PO₄ was loaded onto a double rhenium filament and run in the TRITON TIMS. Initial $^{143}\text{Nd}/^{144}\text{Nd}$ ratios were calculated using $^{40}\text{Ar}/^{39}\text{Ar}$ ages provided by C. Henry (Appendix I, Table I), Sm and Nd concentrations from the whole-rock ICP-MS analyses, and a ^{147}Sm decay constant $\lambda = 6.54 \times 10^{-12}$. Initial epsilon values (ϵNd_i) were calculated with $^{143}\text{Nd}/^{144}\text{Nd}_{\text{CHUR}} = 0.512638$ and $^{147}\text{Sm}/^{144}\text{Nd}_{\text{CHUR}} = 0.1967$. An internal laboratory standard (Nd Std) was analysed with the other samples and yielded an average ratio of $^{143}\text{Nd}/^{144}\text{Nd} = 0.511814$

± 0.000009 . The long term lab average of Nd Std is $^{143}\text{Nd}/^{144}\text{Nd} = 0.511815 \pm 0.000009$ (7 runs; June 2018-May 2019). Based on comparative analyses between the Nd Std and La Jolla standards, this average value corresponds to a La Jolla standard value of 0.511845. The average $^{143}\text{Nd}/^{144}\text{Nd}$ obtained for the BCR-2 international standard is 0.512536 ± 0.000023 (2-sigma, n = 21 runs).

6.0 Results

6.1 Petrography

Thin sections were analyzed to determine the mineral and glass phases in the samples and to characterize the textures of the units. Full thin section descriptions are listed in Appendix I, Table III.

Pablo Formation

The Pablo Formation, interpreted to be basement to the Underdown caldera (Bonham, 1970), is an andesite with a mineral assemblage of plagioclase + amphibole \pm pyroxene, and contains trace amounts of Fe-Ti oxides and biotite. One sample appears to contain secondary quartz, and pyrite is visible in one hand sample, therefore some opaque minerals are assumed to be pyrite. Pyroxene crystals are being replaced by amphibole and contain opaque inclusions. Plagioclase is the dominant mineral phase and is commonly partially altered to sericite and/or calcite. Plagioclase phenocrysts are up to 2.5 mm, while smaller grains which make up the groundmass are \sim 0.10 mm. Amphibole phenocrysts are 1.5-3.0 mm and commonly contain opaque inclusions 0.10-0.25 mm. Crystals are euhedral to subhedral in shape.

The tuff of Gabbs Valley

The tuff of Gabbs Valley is an ash flow tuff containing approximately <20% phenocrysts. The unit is composed of plagioclase + quartz + sanidine, and contains variable to trace amounts of biotite, amphibole, opaque minerals, Fe-Ti oxides and monazite. Whole rock

samples contain different proportions of plagioclase, quartz, and sanidine. Welded samples have matrices containing glass shards and banding that wraps around phenocrysts. Both banded and white pumice are observed to be phyric and contain spherulites. Plagioclase crystals show some zoning, resorption, and alteration to calcite and sericite. Plagioclase phenocrysts are variable in size, ranging from 0.30-3.0 mm in different samples. Quartz phenocrysts range in size from 0.10-2.0 mm, sanidine range in size from 0.75-2.25 mm, biotite are ~0.4-2.25 mm, amphibole are <0.2 mm, and opaque minerals are <0.5 mm. Phenocrysts are subhedral in shape.

The tuff of Arc Dome

The tuff of Arc Dome is an ash flow tuff containing 10-25% phenocrysts. Pumice is less crystal rich (10%) than the whole rock samples (15-25%). The unit is composed of plagioclase + quartz + sanidine + biotite, and contains trace amounts of amphibole, opaque minerals, Fe-Ti oxides, monazite and pyroxene. Some samples have a matrix containing spherulites, and the pumice is also spherulitic. Some feldspars and matrices show alteration to calcite. Plagioclase, quartz and sanidine have relatively equal abundances across the samples with some exceptions. No quartz was observed in whole rock 17-SM-20 which was found to contain ~15% pyroxene. Plagioclase phenocrysts are generally around 1.5-2.5 mm, but in one sample they are up to 5.0 mm. Quartz phenocrysts are 1.0-2.5 mm, and sanidine phenocrysts are generally 0.50-3.0 mm with one sample up to 4.0 mm. Biotite phenocrysts are 0.75-2.5 mm, amphibole are 1.5-2.0 mm, and opaque minerals are <0.4 mm. Phenocrysts are subhedral in shape.

The tuff of Brunton Pass

The Tuff of Brunton Pass is a crystal poor ash flow tuff with approximately <5% phenocrysts. The unit is composed of sanidine + quartz, and trace amounts of plagioclase, biotite, opaque minerals and Fe-Ti oxides. Microcrystalline lithic fragments are found in both samples. The matrices are glassy, altered, and spherulitic. Both white and banded fiamme are found in 17-SM-13A. The matrix of 17-SM-13B contains glass shards, and areas of glassy pumice are completely spherulitic. Calcite alteration is found in the matrix of 17-SM-13B. Plagioclase phenocrysts are small in both samples, 0.50-0.75 mm, while quartz and sanidine phenocrysts are 1.25-2.0 mm. Biotite phenocrysts are 0.25-0.50 mm, and opaque minerals are <0.5 mm. Phenocrysts are subhedral in shape.

Underdown Tuff

The Underdown Tuff is an ash flow tuff that contains ~5-25% phenocrysts in whole rock samples, 10-20% phenocrysts in porphyritic pumice samples, and <10% phenocrysts in white pumice samples. The Underdown Tuff contains plagioclase + quartz + sanidine, and contains minor and trace amounts of biotite, amphibole, opaque minerals, Fe-Ti oxides, and monazite. The more common white pumice contains quartz, sanidine and secondary calcite. Matrices of porphyritic pumice are dark brown, glassy and altered. Generally, porphyritic pumice has a relatively equal proportion of plagioclase, quartz and sanidine phenocrysts. Biotite and amphibole are only found in one porphyritic pumice sample and both appear to be altered to chlorite. Whole rock matrices are variably welded with some containing spherulites and banding which wraps around

phenocrysts (Fig. 6.1). Whole rock samples have variable proportions of plagioclase, quartz and sanidine, and trace amounts of biotite and hornblende that appear to be altered to chlorite (Fig. 6.2). Some matrices also show sericite alteration. Plagioclase phenocrysts in whole rock samples are 1.0-3.0 mm, quartz phenocrysts are 1.0-2.5 mm and commonly show embayments, and sanidine phenocrysts are 0.50-3.5 mm. Most biotite crystals are ~0.10 mm, amphibole phenocrysts are up to 0.50-1.50 mm, and opaque minerals are <0.1 mm. Phenocrysts are subhedral in shape.

The tuff of Clipper Gap

The tuff of Clipper Gap is an ash flow tuff that contains ~5-20% phenocrysts in whole rock samples and 15-25% phenocrysts in porphyritic pumice. White pumice contains fewer phenocrysts of quartz and sanidine than the porphyritic pumice (~3-10%). The tuff of Clipper Gap contains plagioclase + quartz + sanidine and trace amounts of biotite, amphibole, opaque minerals, Fe-Ti oxides, and monazite. The matrices of porphyritic pumice are dark brown, glassy and heavily altered, and some contain glass shards (Fig. 6.1). Whole rock matrices are glassy, altered and some contain spherulites. Unaltered samples have matrices composed of glass shards. Porphyritic pumice has no identifiable quartz and a higher abundance of sanidine than plagioclase. Whole rock samples generally also have a higher proportion of sanidine than plagioclase and quartz, and in some cases do not contain any identifiable quartz. Biotite is not present in porphyritic pumice and only exists in trace amounts in whole rock samples (Fig. 6.2). A trace amount of amphibole is present in one porphyritic pumice sample and some of the

whole rock samples. Generally, biotite and amphibole appear altered in whole rock samples. In the porphyritic pumice, plagioclase phenocrysts are 1.0-2.5 mm and sanidine phenocrysts are 1.0-4.5 mm. In whole rock samples, plagioclase phenocrysts are 0.50-2.5 mm with some smaller crystals ~0.10 mm, quartz phenocrysts are 1.0-2.0 mm, and sanidine phenocrysts are 1.0-4.0 mm. Biotite and amphibole crystals are typically 0.10-0.75 mm with some larger crystals 1.0-2.0 mm, and opaque minerals are 0.1-0.5 mm. Phenocrysts are subhedral in shape.

The Terrill Mountains tuffs

The Terrill Mountains tuffs are a series of ignimbrites with ~5% phenocrysts. The unit contains plagioclase + quartz + sanidine and trace amounts of biotite, opaque minerals, Fe-Ti oxides, and possible pyroxene. The samples have a higher abundance of quartz and sanidine than plagioclase. White and banded fiamme are aphyric and phyric, respectively, and the matrices of the samples are generally densely welded. One sample shows possible alteration in the matrix, while the others are composed of fresh glass and glass shards. Plagioclase phenocrysts are generally small, ranging from 0.25-1.0 mm, and sanidine phenocrysts are similarly sized between 1.0-1.50 mm. Quartz phenocrysts are larger and are ~1.50-1.75 mm. Biotite phenocrysts are 0.25-0.5 mm, and opaque minerals are <0.1 mm. Phenocrysts are subhedral in shape.

Bonita Canyon Formation

The Bonita Canyon Formation contains 5-15% phenocrysts. The unit is composed of plagioclase + quartz + sanidine + biotite and trace amounts of amphibole, opaque minerals, Fe-Ti oxides, and monazite. The unit also contains a large proportion of lithic fragments composed of quartz and feldspar, up to 10% in some samples. Biotite is more common than amphibole in this unit, as amphibole was only identified in one sample (Fig. 6.2). Generally, quartz is slightly more abundant in the whole rock samples, however all phenocryst phases are present in low percentages. Matrices of white pumice samples are composed of glass and glass shards, and appear heavily altered by a green alteration phase. Plagioclase phenocrysts are 0.50-2.5 mm, quartz phenocrysts are 0.50-2.5 mm and commonly show embayments (Fig. 6.1), and sanidine crystals are 0.50-2.0 mm. Biotite phenocrysts are 0.25-2.0 mm and are generally unaltered, however one phenocryst was observed to be heavily resorbed. Opaque minerals are <0.1 mm. Phenocrysts are either subhedral to anhedral in shape or are broken fragments of crystals.

Dacite Dyke

The dacite dyke is an intermediate intrusive rock composed primarily of plagioclase with small amounts of biotite, opaque minerals, Fe-Ti oxides, and monazite. Plagioclase crystals appear to be partially altered to calcite, and the matrix appears to be partially altered to sericite. Plagioclase is present in two sizes, a larger size up to 5.0 mm, and a smaller groundmass size <0.50 mm. Biotite crystals appear to be filling spaces between

plagioclase crystals and range from 0.50-1.75 mm, and opaque minerals are <0.2 mm. Crystals are subhedral to euhedral in shape.

Rhyolite Intrusions

The rhyolite intrusions are composed of plagioclase + quartz + sanidine + biotite, and trace amounts of opaque minerals, Fe-Ti oxides and monazite. Crystals tend to be present in clusters and the matrices of the samples appear partly composed of microcrystalline quartz. Plagioclase crystals are 1.5-3.0 mm, tend to be present in a lower abundance than both quartz and sanidine, and show resorption in the centre of the crystals. Quartz crystals have embayments and are 1.5-2.5 mm. Sanidine crystals are 1.75-2.5 mm and show no alteration. Biotite crystals are 0.75-2.0 mm and are commonly replaced by opaque minerals <0.25 mm. Crystals are subhedral in shape.

The Unnamed tuff

The Unnamed tuff is a sequence of ash flow tuffs with 10-30% phenocrysts. The unit contains plagioclase + quartz + sanidine + biotite + amphibole, and trace amounts of opaque minerals, Fe-Ti oxides, and monazite. Biotite is present in all samples, and amphibole is present in all but two (Fig. 6.2). Two samples contain lithic fragments composed of microcrystalline material, and most samples have a highly welded, glassy brown matrix. Aphyric fiamme are common throughout the unit, as well as large fractured phenocrysts (Fig. 6.1). Some pumice and matrix appear microcrystalline and are possibly silicified. Occasionally, fractures will radiate out from phenocrysts into the

glassy matrix. Quartz phenocrysts commonly show embayments. Generally, plagioclase, quartz, and sanidine are present in relatively equal abundances. Plagioclase phenocrysts are 1.0-1.5 mm, quartz phenocrysts are 1.5-3.0 mm, and sanidine are generally 2.0-4.0 mm. Biotite phenocrysts are ~0.25-1.75 mm, and amphibole phenocrysts are ~0.10-2.5 mm. Biotite and hornblende show possible alteration to chlorite and some phenocrysts have yellow rims of alteration. Opaque minerals are <0.25 mm. Phenocrysts are subhedral in shape.

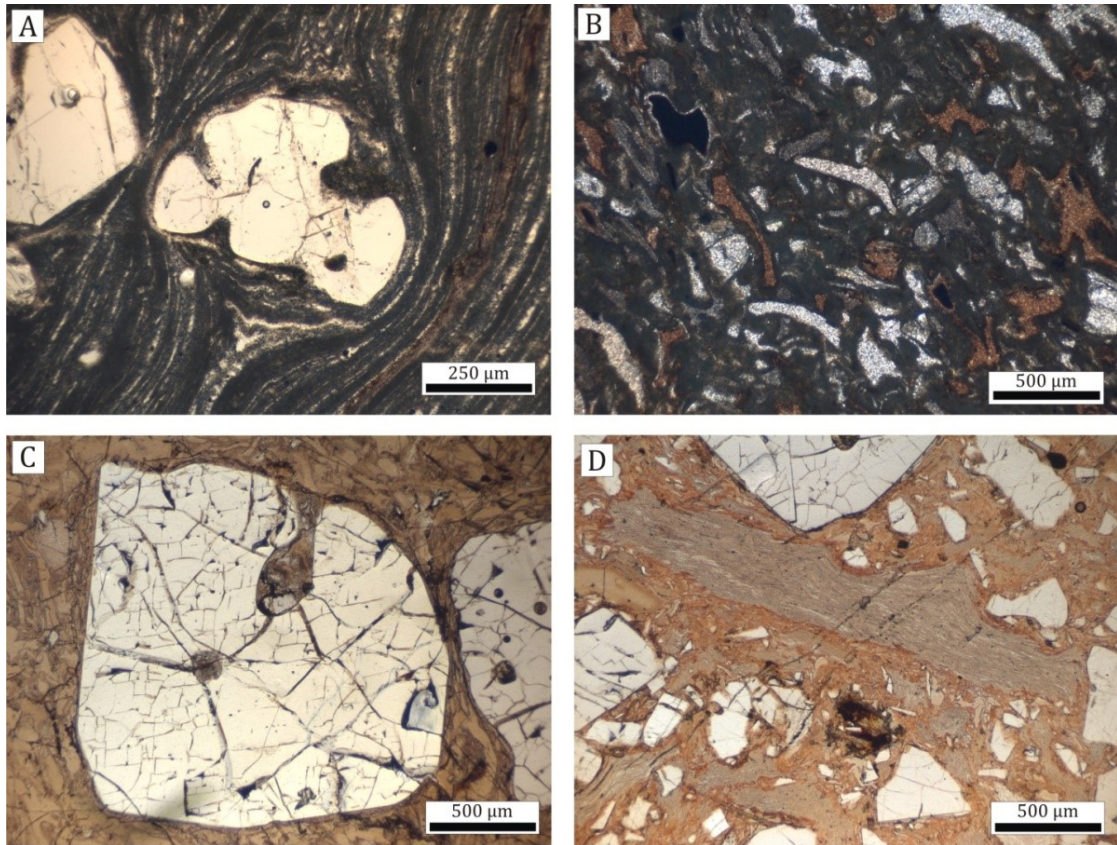


Figure 6.1: Photomicrographs of major ignimbrites showing commonly observed textures. (A) Underdown Tuff - Quartz eye phenocryst with a heavily banded matrix that wraps around the phenocrysts (sample 16-SM-50). (B) Tuff of Clipper Gap showing a densely welded matrix composed of glass shards (sample 17-SM-22). (C) Bonita Canyon Formation - a vitrophyre sample with a glassy matrix and large, fractured and embayed quartz phenocryst (sample 16-SM-03). (D) Unnamed Tuff - A typical Unnamed tuff sample shows a high degree of welding. Fractured phenocrysts can be seen alongside large flattened, aphyric pumice (sample 16-SM-06D).

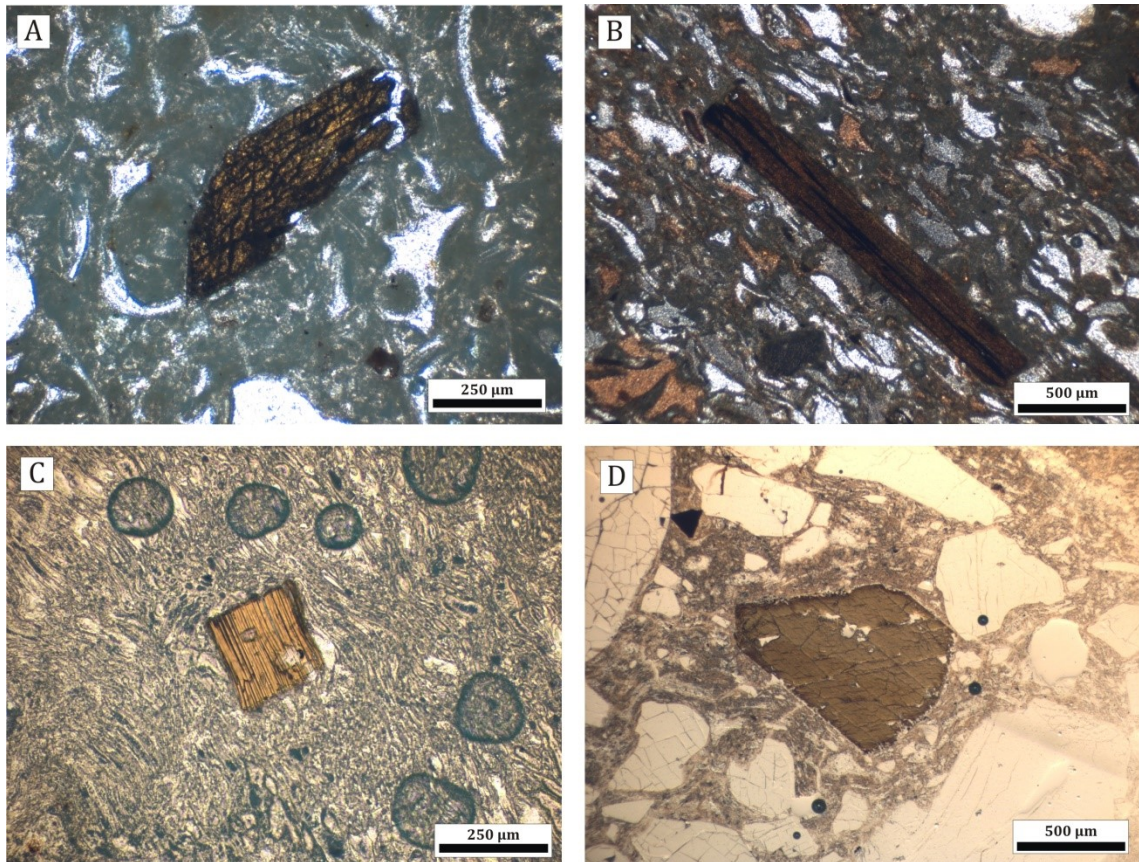


Figure 6.2: Photomicrographs of major ignimbrites showing hydrous phases (hornblende and biotite). (A) Underdown Tuff - an example of hornblende viewed in the Underdown Tuff. Distinctive cleavage can be seen on the dark brown crystal (sample 17-SM-27). (B) Tuff of Clipper Gap - A biotite crystal seen in the Tuff of Clipper Gap (sample 17-SM-22). (C) Bonita Canyon Formation - A biotite crystal in the Bonita Canyon formation. The matrix of this unit is far less welded than the vitrophyre which is typical for this unit (sample 16-SM-21B). (D) Unnamed Tuff - An amphibole crystal in the Unnamed tuff. Distinctive cleavage can be seen (sample 16-SM-39).

6.2 Geochemistry

All data from the Underdown Caldera Complex are shown in Figure 6.3, a total alkalis-silica (TAS) classification diagram (Le Maitre et al., 1989). The Oligocene tuffs plot in both the rhyolite and trachyte fields. Trachyte samples include pumice samples from the Underdown Tuff, tuff of Clipper Gap, and Bonita Canyon Formation as well as the dacite dyke sample which is likely a trachydacite. Both the Underdown Tuff and tuff of Clipper Gap plot in a trend from rhyolite to trachyte. The trachyte tuff of Clipper Gap pumice samples as well as some of the rhyolitic pumice and whole rock samples exhibit negative and positive Ce anomalies that are not observed in other samples that largely plot in the rhyolite field (Fig. 6.4). These samples, as well as the origin of the Ce anomalies will be discussed separately from the rest of the data (section 7.2). Other samples that will not be interpreted with the main group of data are samples with high loss on ignition (LOI) of over 6 weight percent. These samples have been removed from the major and trace element diagrams as they are interpreted to be altered and therefore the geochemistry does not reflect the original characteristics of the unit. The high LOI samples which have been removed include samples from the tuff of Clipper Gap, Bonita Canyon Formation, and Terrill Mountains tuffs. Acid-washed tuff of Clipper Gap samples with anomalous REEs are plotted in the isotope geochemistry section but not in the major and trace element geochemistry sections as acid washing has removed some primary phases (apatite, Fe-oxides) which alter the major and trace element geochemistry.

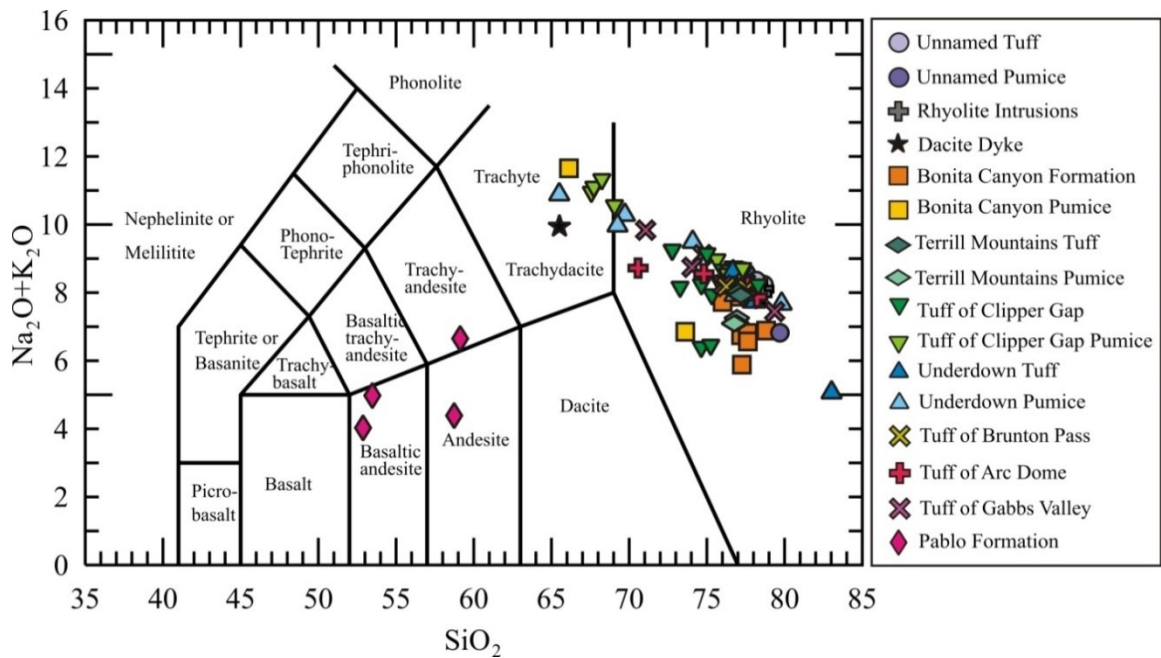


Figure 6.3: Total alkalis-silica diagram (Le Maitre et al., 1989) of all data from the Underdown Caldera Complex. Most felsic samples plot in the rhyolite field of the diagram, while a few samples plot in the trachyte field. Both the Underdown Tuff and the tuff of Clipper Gap show a trend from rhyolite towards trachyte, particularly in their pumice.

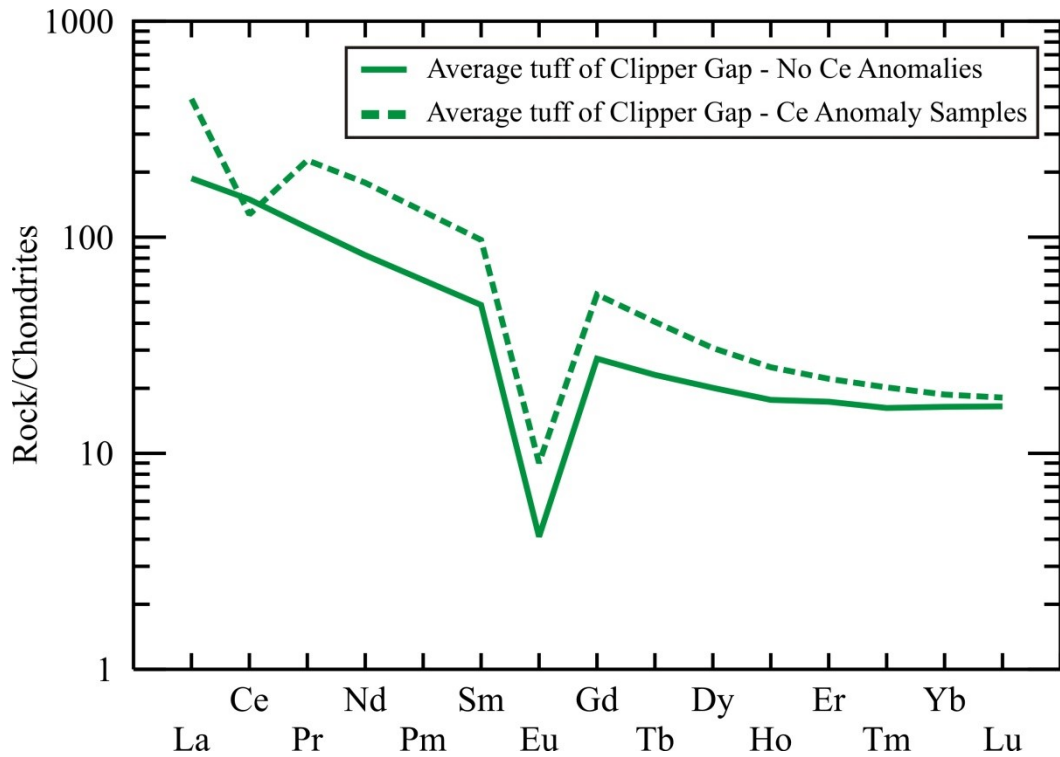


Figure 6.4: Average chondrite normalized rare earth element patterns of the Tuff of Clipper Gap samples with no Ce anomalies and those with Ce anomalies (normalization factors of Sun and McDonough, 1989).

6.2.1 Major element geochemistry

Major element compositions are reported in Appendix I, Table IV. All values are recalculated to 100% anhydrous compositions for plotting. As these are mainly felsic rocks, the concentrations of MgO and MnO were very low in all Oligocene tuffs and therefore are not presented in this section for these units. All units have been plotted as fields on a total alkalis-silica (TAS) diagram in Figure 6.5 (Le Maitre et al., 1989), and have subsequently been divided two different TAS diagrams to better view the Oligocene tuff units.

Pablo Formation

The Pablo formation is intermediate in composition and plots in the basaltic-andesite, andesite, and trachy-andesite fields of a TAS diagram (Fig. 6.6, Le Maitre, 1989). The Pablo Formation shows positive trends in Al_2O_3 and Na_2O with increasing SiO_2 content, and a negative trend in all other major elements with increasing SiO_2 content except K_2O which shows a scatter.

Oligocene tuffs

The Oligocene tuffs plot mainly in the rhyolite field of a TAS diagram (Le Maitre et al., 1989), as previously mentioned, with some samples plotting as a trend into the trachyte field. However, after the anomalous-REE tuff of Clipper Gap samples and the high LOI Bonita Canyon pumice samples have been removed, the Underdown pumice samples are the sole Oligocene tuffs which plot in the trachyte field. The tuff of Gabbs Valley and tuff of Arc Dome also show a trend towards the trachyte field but remain in the rhyolite field of the diagram (Fig. 6.6).

The Oligocene tuffs show relatively similar trends in major element oxide data when compared to increasing SiO_2 content. These trends and characteristics will be discussed in the next paragraph. However, for the tuff of Brunton Pass and the Terrill Mountains tuffs, the number of samples from each unit (two samples from each) causes there to be no observable trend in the data. The Unnamed tuff samples are also homogeneous and

plot as a cluster for all major element oxides. Major ignimbrites, including the Underdown Tuff, Bonita Canyon Formation, tuff of Clipper Gap, and the Unnamed tuff were plotted on major element bivariate diagrams on Figure 6.9. The other tuffs, including the tuff of Gabbs Valley, tuff of Arc Dome, tuff of Brunton Pass, and Terrill Mountains tuffs were plotted on Figure 6.10 along with the Underdown Tuff and Bonita Canyon Formation data for comparison.

The Oligocene tuffs show a strong negative trend in Al_2O_3 with increasing SiO_2 content. Both the major ignimbrites from the Underdown Caldera, the Tuff of Clipper Gap, and the other tuffs show a similar trend. The Underdown Tuff shows the most variation in Al_2O_3 content, with the pumice samples generally containing a higher concentration of Al_2O_3 than the whole rock samples. The Terrill Mountains tuffs, tuff of Brunton Pass, and the Unnamed tuff all plot as a cluster at the end of the trend (excluding the highest Underdown Tuff whole rock).

Many of the Oligocene tuffs show a negative trend in CaO with increasing SiO_2 content. In detail, the Underdown pumice samples with low SiO_2 contents show a negative trend while the whole rock samples and some pumice with higher SiO_2 contents plot more as a cluster. Like the Underdown tuff, the Bonita Canyon Formation tuffs show a slightly scattered negative correlation between CaO and increasing SiO_2 . The Tuff of Clipper Gap shows the most variation in CaO as the whole rock and pumice samples generally plot as a cluster near the Underdown Tuff samples, with a few whole rock samples showing a strong decrease from high CaO contents. The tuff of Gabbs Valley and tuff of Arc Dome

show negative trends similar to the Underdown Tuff, the tuff of Brunton Pass plots as a scatter, and the Unnamed tuff is clustered.

A trend of decreasing Fe_2O_3 with increasing SiO_2 is also observed in the Underdown Tuff. Similar to Al_2O_3 and CaO , the Underdown pumice plot in a strong negative correlation between decreasing Fe_2O_3 and increasing SiO_2 and the Underdown whole rock samples plot as a cluster with the Bonita Canyon Formation and the tuff of Clipper Gap. The tuff of Gabbs Valley shows the most variation in Fe_2O_3 content and plots as a scatter with little change in the Fe_2O_3 concentration. In contrast, the tuff of Arc Dome plots in a strong negative correlation between decreasing Fe_2O_3 and increasing SiO_2 , similar to the Underdown pumice. The Terrill Mountains tuffs, tuff of Brunton Pass, and the Unnamed tuff all plot as a cluster with the other clustered major ignimbrites.

The Underdown tuff shows a scattered pattern in both the whole rock and pumice samples. One outlying sample contains very little K_2O and plots along with samples from the Bonita Canyon Formation which shows a scatter. The tuff of Clipper Gap shows a slight decrease in K_2O content with increasing SiO_2 content, but with more scatter than the Underdown Tuff. Both the tuff of Gabbs Valley and tuff of Arc Dome show a very slight decrease in K_2O that is less steep than the Underdown Tuff samples. The Terrill Mountains tuffs, tuff of Brunton Pass, and the Unnamed tuff are clustered with a majority of the major ignimbrite samples.

Out of all major element oxides, Na_2O shows the most scatter among ignimbrite units. The Underdown Tuff, Bonita Canyon Formation, and tuff of Clipper Gap all plot as a

scatter with increasing SiO_2 content, and the Underdown Tuff shows the largest variation in Na_2O content. The tuff of Gabbs Valley and tuff of Arc Dome plot in similar linear trends with little Na_2O variation with increasing SiO_2 . The Terrill Mountains tuffs, tuff of Brunton Pass, and Unnamed tuff generally plot as clusters, although one Unnamed tuff sample plots as an outlier at a much lower Na_2O content than the other samples.

Negative correlations between P_2O_5 and increasing SiO_2 content exist in the Underdown Tuff, Bonita Canyon Formation and tuff of Clipper Gap. The tuff of Gabbs Valley shows a negative correlation between decreasing P_2O_5 and increasing SiO_2 content that is less steep than the Underdown Tuff, while the tuff of Arc Dome shows a strongly negative correlation between decreasing P_2O_5 and SiO_2 similar to the Underdown Tuff. The Terrill Mountains tuffs, the tuff of Brunton Pass, and the Unnamed tuff show a large scatter.

A negative correlation between decreasing TiO_2 and increasing SiO_2 is observed in the Underdown Tuff and the Bonita Canyon Formation. The Underdown tuff shows the largest variation in TiO_2 content, mostly in the pumice which forms most of the decreasing pattern. The Underdown Tuff whole rocks generally plot as a cluster, with one outlier at a high SiO_2 content. The tuff of Clipper Gap has more scatter in TiO_2 content in both the whole rock and pumice samples, but plots close to the cluster of Underdown Tuff samples. The tuff of Gabbs Valley and tuff of Arc Dome also show negative trends in TiO_2 content with increasing SiO_2 . The tuff of Arc Dome shows a correlation between TiO_2 and SiO_2 similar to the Underdown pumice samples, while the

tuff of Gabbs Valley shows more scatter between decreasing TiO_2 and increasing SiO_2 content. The Terrill Mountains tuffs, tuff of Brunton Pass, and Unnamed tuff all plot as clusters near the Underdown Tuff whole rock samples.

Intrusive Rocks

The dacite dyke is felsic in composition and plots in the trachy-dacite field on the TAS diagram (Fig 6.6, Le Maitre et al., 1989). The dacite dyke has a relatively similar concentration of all major element oxides as the Underdown Tuff pumice samples except for CaO (Fig. 6.9). For CaO, the dacite dyke has a much higher concentration (2.8 wt. %) than the Underdown Tuff pumice samples (0.14-1.4 wt. %).

The rhyolite intrusive rocks collected from the Underdown Caldera are felsic in composition and plot in the rhyolite field on a TAS diagram (Fig. 6.6, Le Maitre et al., 1989). In major element variation diagrams, the rhyolite intrusions plot as a cluster with other major ignimbrites and show the most similarity to the Unnamed tuff samples. As there are only two samples from this unit, no fractionation trends are observed in the data, however the samples typically plot in the most evolved end of the major element fractionation trends observed in the other major ignimbrites (Underdown Tuff, Bonita Canyon, tuff of Clipper Gap) (Fig. 6.9).

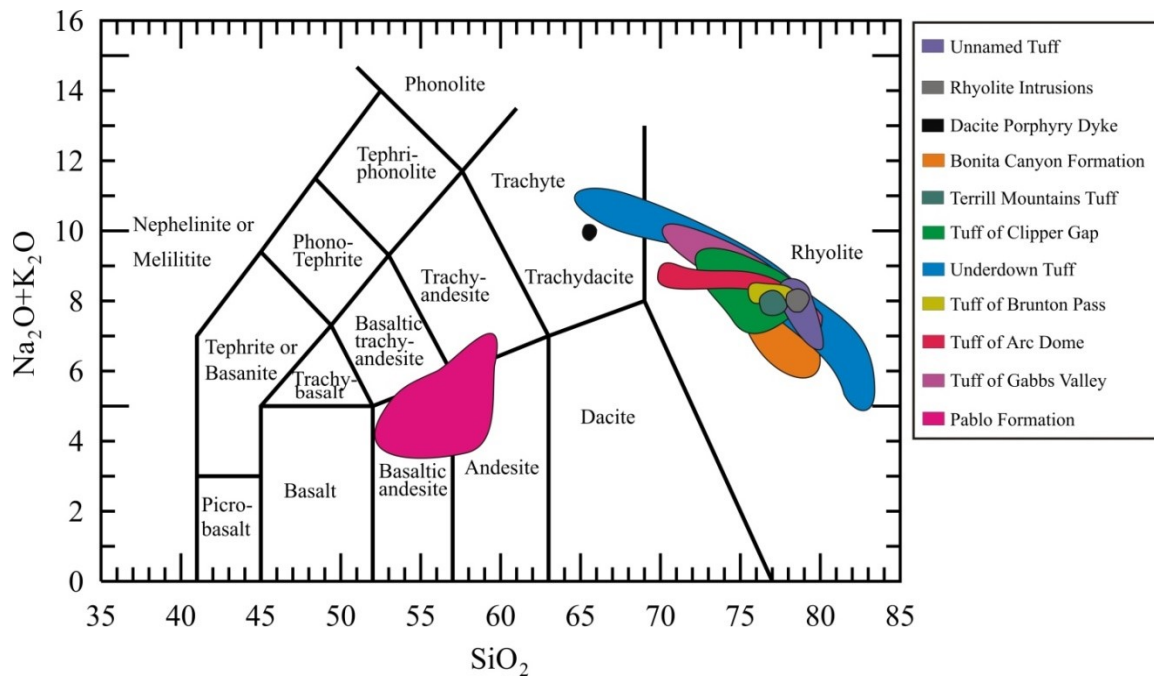


Figure 6.5: Total alkalis-silica diagram (Le Maitre et al., 1989) showing the fields of all units collected within and outside of the Underdown Caldera. The Underdown Tuff and Bonita Canyon formation show a trend of samples into the trachyte field, while other units plot within the rhyolite field. The dacite dyke plots as a point (black circle) in the trachydacite field. The Pablo Formation plots as a field extending between the basaltic andesite, andesite and trachy-andesite fields.

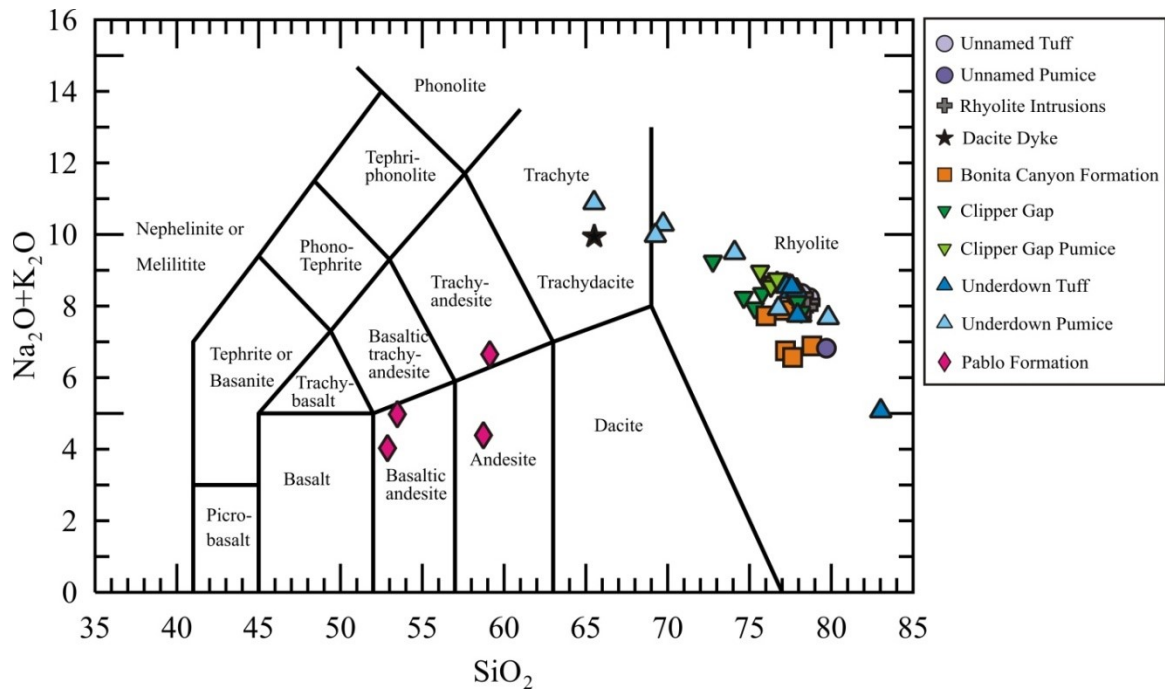


Figure 6.6: Total alkalis-silica diagram (Le Maitre et al., 1989) showing the major ignimbrite units (Underdown Tuff, tuff of Clipper Gap, Bonita Canyon Formation, and Unnamed tuff - without anomalous REE or high LOI samples), mafic to intermediate basement rocks (Pablo Formation), dacite dyke, and rhyolite intrusions collected from the Underdown Caldera. Most ignimbrite and intrusive samples are rhyolitic in composition, with some Underdown pumice samples plotting in a trend into the trachyte field.

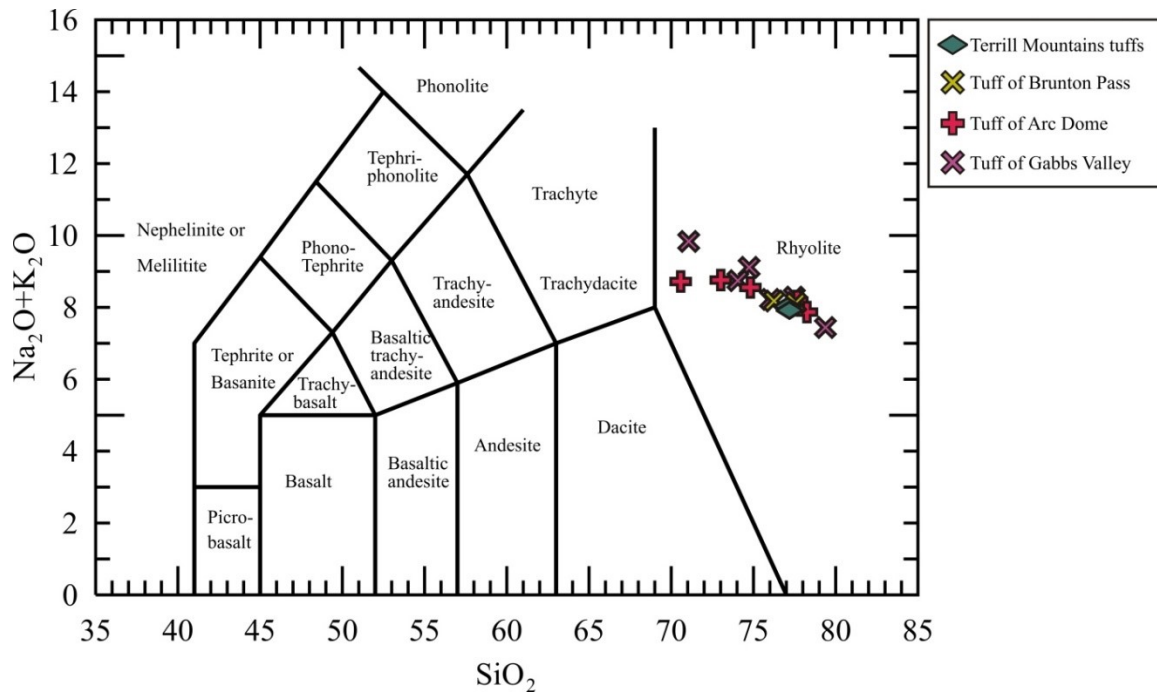


Figure 6.7: Total alkalis-silica diagram (Le Maitre et al., 1989) showing the other ignimbrite units (tuff of Gabbs Valley, tuff of Arc Dome, tuff of Brunton Pass) and the Terrill Mountains tuffs that are close in age to the Underdown tuff. All samples plot within the rhyolite field.

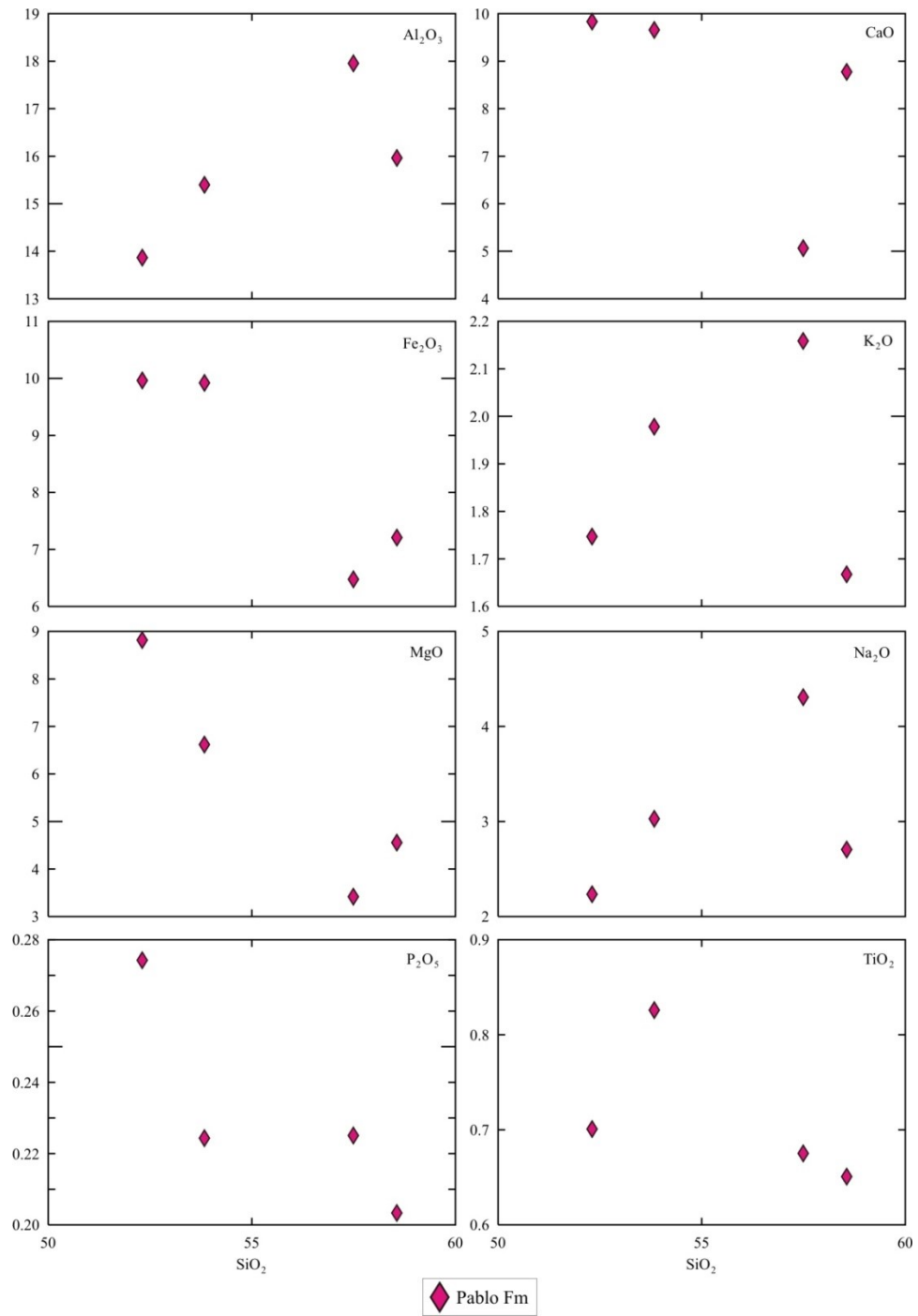


Figure 6.8: Major element variation diagrams of the Pablo Formation. CaO, Fe₂O₃, MgO, and P₂O₅ show decreasing trends with increasing SiO₂ content. TiO₂ increases between 52-54 wt.% SiO₂ and then shows a decreasing trend. Al₂O₃, K₂O and Na₂O show positive trends with increasing SiO₂ content until ~57 wt. %.

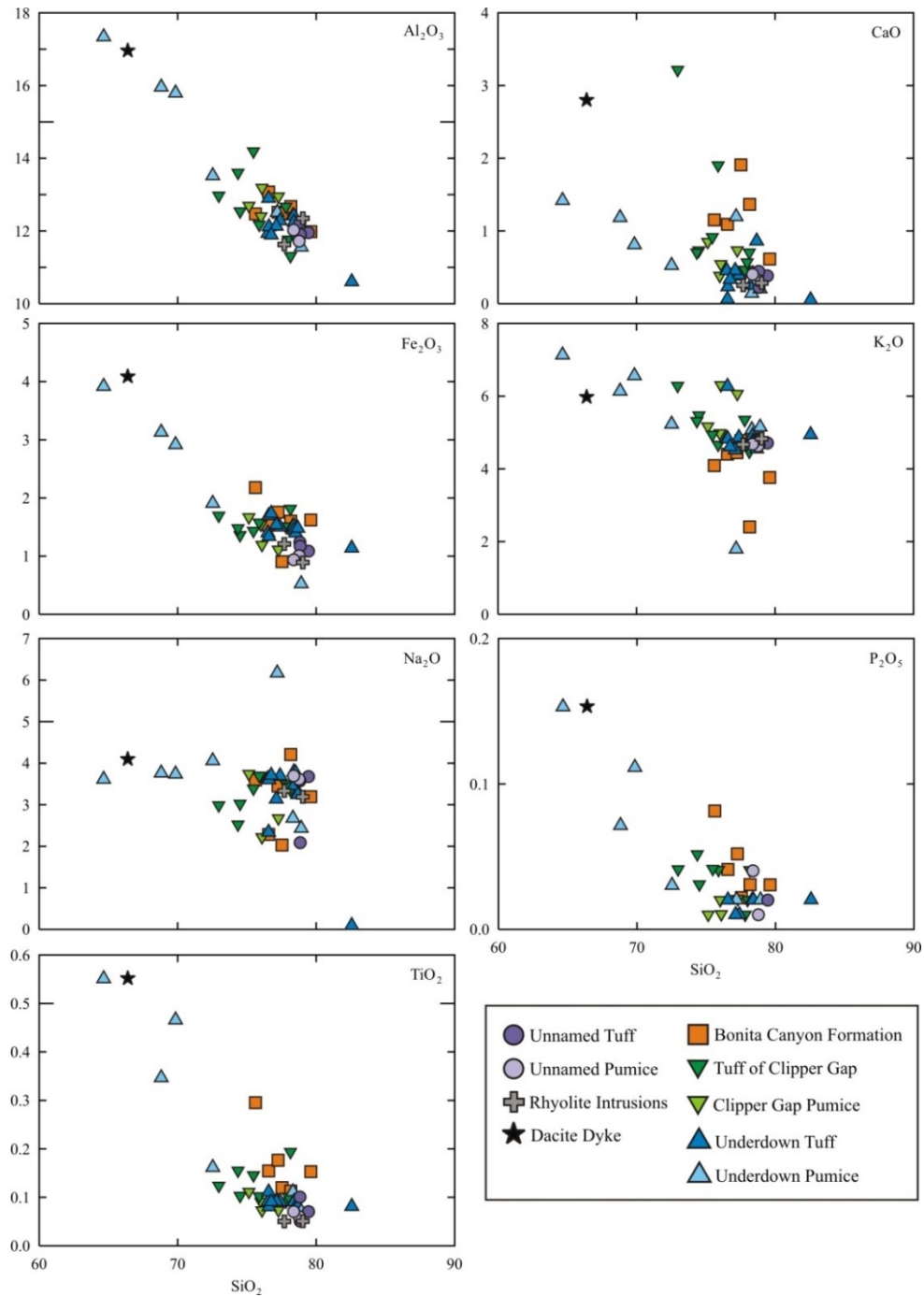


Figure 6.9: Major element variation diagrams of the major ignimbrites and the rhyolite intrusions of the Underdown Caldera complex. All major element oxides show a decreasing trend with increasing SiO_2 content except for Na_2O . Al_2O_3 and Fe_2O_3 show tight negative trends with increasing SiO_2 , while other major element oxides show more of a variation in steepness between the units.

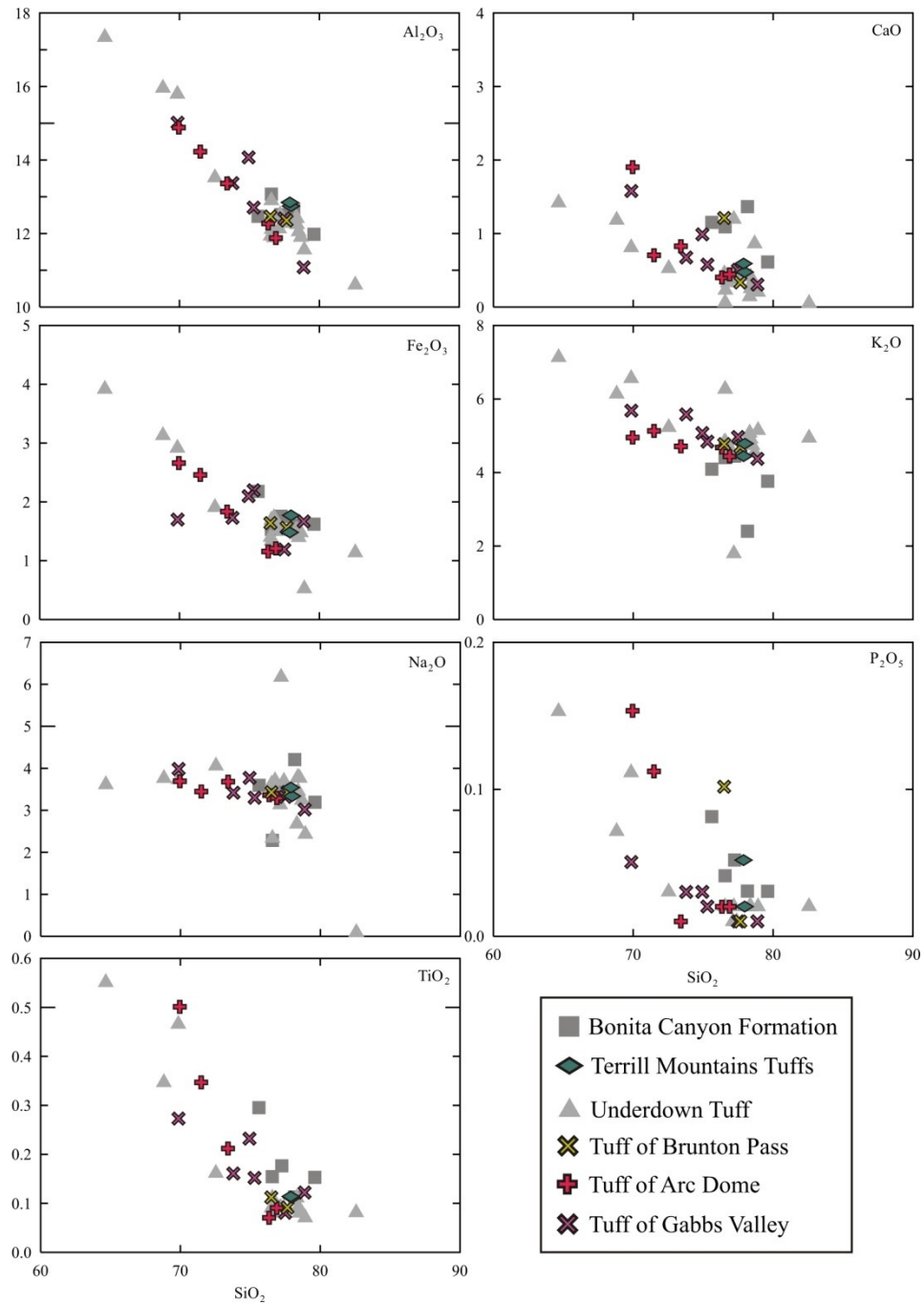


Figure 6.10: Major element variation diagrams of the other tuffs (tuff of Gabbs Valley, tuff of Arc Dome, and tuff of Brunton Pass) and the Terrill Mountains tuffs. All major element oxides show a decreasing trend with increasing SiO_2 content. K_2O , MgO and Na_2O show the weakest negative trends with increasing SiO_2 content.

6.2.2 Trace element geochemistry

Trace element results are reported in Appendix I, Table VI. Zirconium concentrations are highly variable, and therefore have been left out of the primitive mantle normalized trace element diagrams. The variation in Zr may reflect whether Zircon is a stable crystallizing phase in the ignimbrites. Zirconium abundances can be seen in the bivariate (trace element versus SiO₂ content) diagrams.

Pablo Formation

Cr, Eu, and Tb appear to be incompatible elements in the Pablo Formation as they show positive correlations with increasing SiO₂ content. Lu and Y show positive correlations until ~65 wt. % SiO₂ where the concentration appears to decrease. Other trace elements, La, Nb, Sm, Pb, Sr, Th, and Zr show scattered patterns which may be a result of sample size (Fig 6.11).

On a chondrite normalized rare earth element diagram, the Pablo Formation shows enrichment in the LREEs relative to the HREEs and a flattening pattern in the HREEs (Fig. 6.14). On a primitive mantle normalized trace element diagram, positive anomalies are observed in Ba, U, Pb and Sr, and a negative Nb-Ta anomaly is observed (Fig. 6.17).

Oligocene Tuffs

Trace element bivariate plots show which trace elements behave as compatible elements and which behave as incompatible elements. Compatible trace elements are preferentially incorporated into crystallizing phases in the rock. This is shown by a

decrease in trace element concentration with increasing magma evolution (SiO_2 content). In the Oligocene tuffs, Ba, Eu, Pb, Sr, and Zr behave as compatible elements. All of these trace elements show correlation between decreasing concentration of the trace element and increasing SiO_2 content. Nb and Th behave as incompatible elements in the Oligocene tuffs. Both of these trace elements show a positive correlation between increasing Nb and Th concentration and increasing SiO_2 content. Little correlation is observed between Y concentration and increasing SiO_2 content. Similar to the major element oxides, the sample size of the Terrill Mountains tuffs and tuff of Brunton Pass make inferring trends difficult, but their clustering also indicates more homogeneity than is observed in the other Oligocene tuffs.

Chondrite normalized rare earth element diagrams show that the Oligocene tuffs show enrichment in the LREEs relative to the HREEs, and have a flattened pattern in the HREEs. A negative Eu anomaly is observed in every Oligocene tuff unit, the largest of which exists in the Unnamed tuff and the smallest of which exists in the tuff of Gabbs Valley and tuff of Arc Dome. However, individual samples from the Underdown Tuff and the Bonita Canyon Formation also show very small negative Eu anomalies. Small positive Ce anomalies are observed in a few samples in units including the Underdown Tuff and the Unnamed tuff, and a small negative Ce anomaly is observed in one sample from the Tuff of Brunton Pass (Fig. 6.15, Fig. 6.16). Primitive mantle normalized trace element diagrams show that the Oligocene tuffs have patterns typical of convergent margin rocks. Negative anomalies are observed in Ba, Sr, and Eu in all units; however the Ba

anomaly is more variable in the tuffs of Gabbs Valley and Arc Dome. A positive anomaly is observed in Pb. Overall, the pattern shows flattening in the HREEs, similar to what was observed on the chondrite normalized REE diagram (Fig. 6.18. Fig. 6.19). Samples were normalized to chondrite and primitive mantle using data from Sun and McDonough (1989).

Intrusive Rocks

The dacite dyke is similar chemically to the major ignimbrite units, occasionally along trends of other units, such as the Underdown Tuff. For example, the dacite dyke plots close to the Underdown Tuff in Eu, Nb, Pb, Th, and Zr. The dacite dyke also contains a higher concentration of Ba and Sr than the major ignimbrites (Underdown Tuff, Bonita Canyon Formation, and tuff of Clipper Gap), and shows little relation to the major ignimbrite units in Y. Overall, the dacite dyke shows concentrations of compatible and incompatible trace elements which would be expected for a more primitive, related feeder. Similar to the major element geochemistry, the rhyolite intrusions plot similarly to the Unnamed tuff samples and typically plot at the most evolved end of compatible and incompatible trends observed in the major ignimbrites (Underdown Tuff, Bonita Canyon Formation, and tuff of Clipper Gap). The rhyolite intrusion samples are scattered in Y, similar to the other major ignimbrite units of the Underdown Caldera complex.

On a chondrite normalized REE plot, the dacite dyke shows a pattern similar to the Pablo Formation, however has a higher enrichment of LREEs. A flattening pattern is observed in the dacite dyke as well as no negative Eu anomaly, also similar to the Pablo

Formation, which distinguishes it from the ignimbrites (Fig. 6.14). A similar pattern to the Pablo Formation is also observed on the primitive mantle normalized trace element diagram for the dacite dyke (Fig. 6.17). The rhyolite intrusions show less enrichment in the LREEs than the other Oligocene tuffs, and show less decrease towards the HREEs on a chondrite normalized REE plot (Fig. 6.15). A large Eu anomaly exists in the rhyolite intrusions, however, there is also depletion in Pr, Nd, and Sm in one sample compared to the other. On a primitive mantle normalized trace element diagram, the rhyolite intrusions show a similar pattern to the Oligocene tuffs, however the negative Ba and positive Pb anomalies appear to be larger in the rhyolite intrusions (Fig. 6.16). All samples were normalized to chondrite and primitive mantle using data from Sun and McDonough (1989).

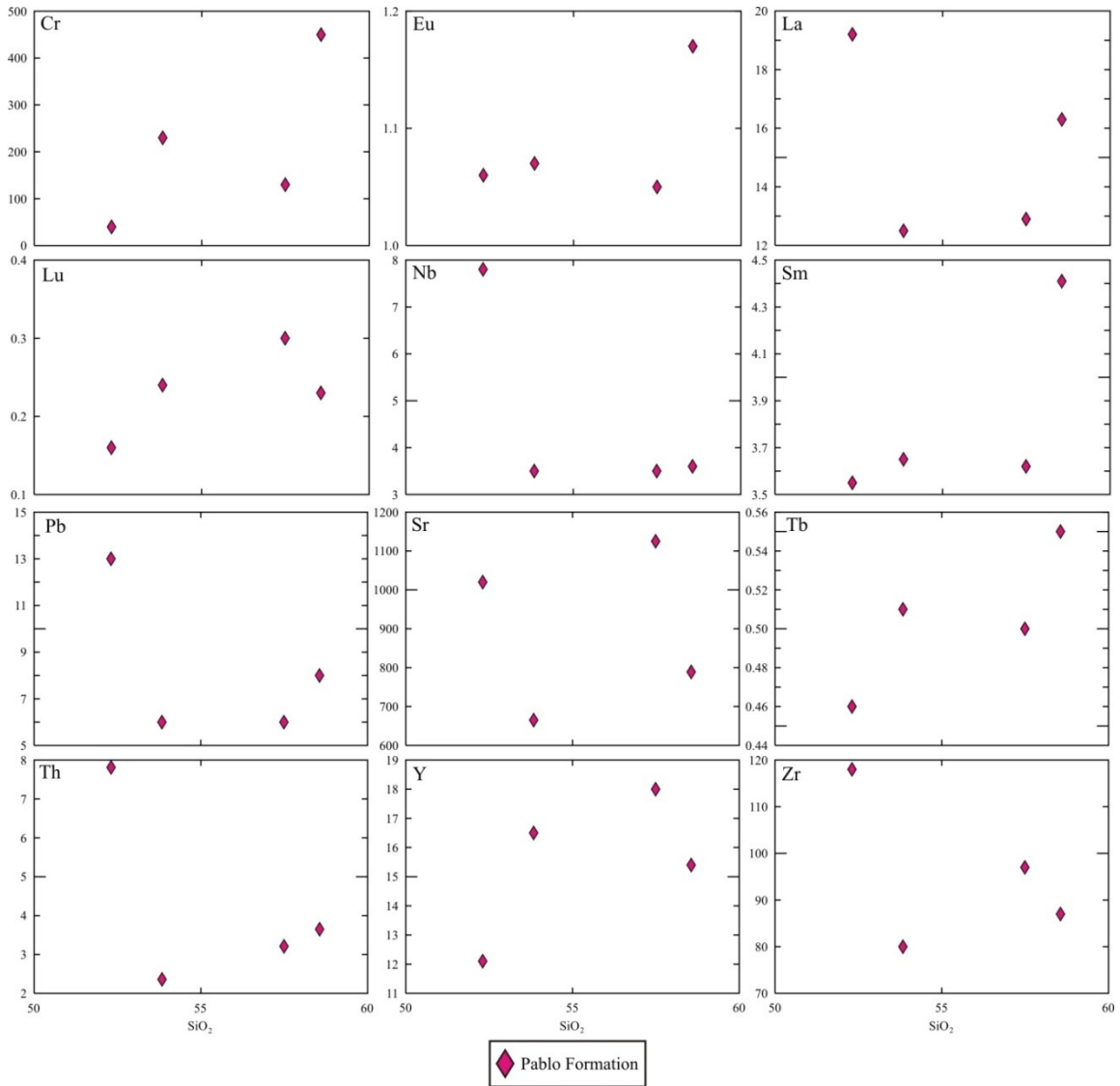


Figure 6.11: Trace element variation diagrams of the Pablo Formation and the dacite dyke. Typical compatible elements in andesite and dacite melts appear to be incompatible in these rocks, except for Sr.

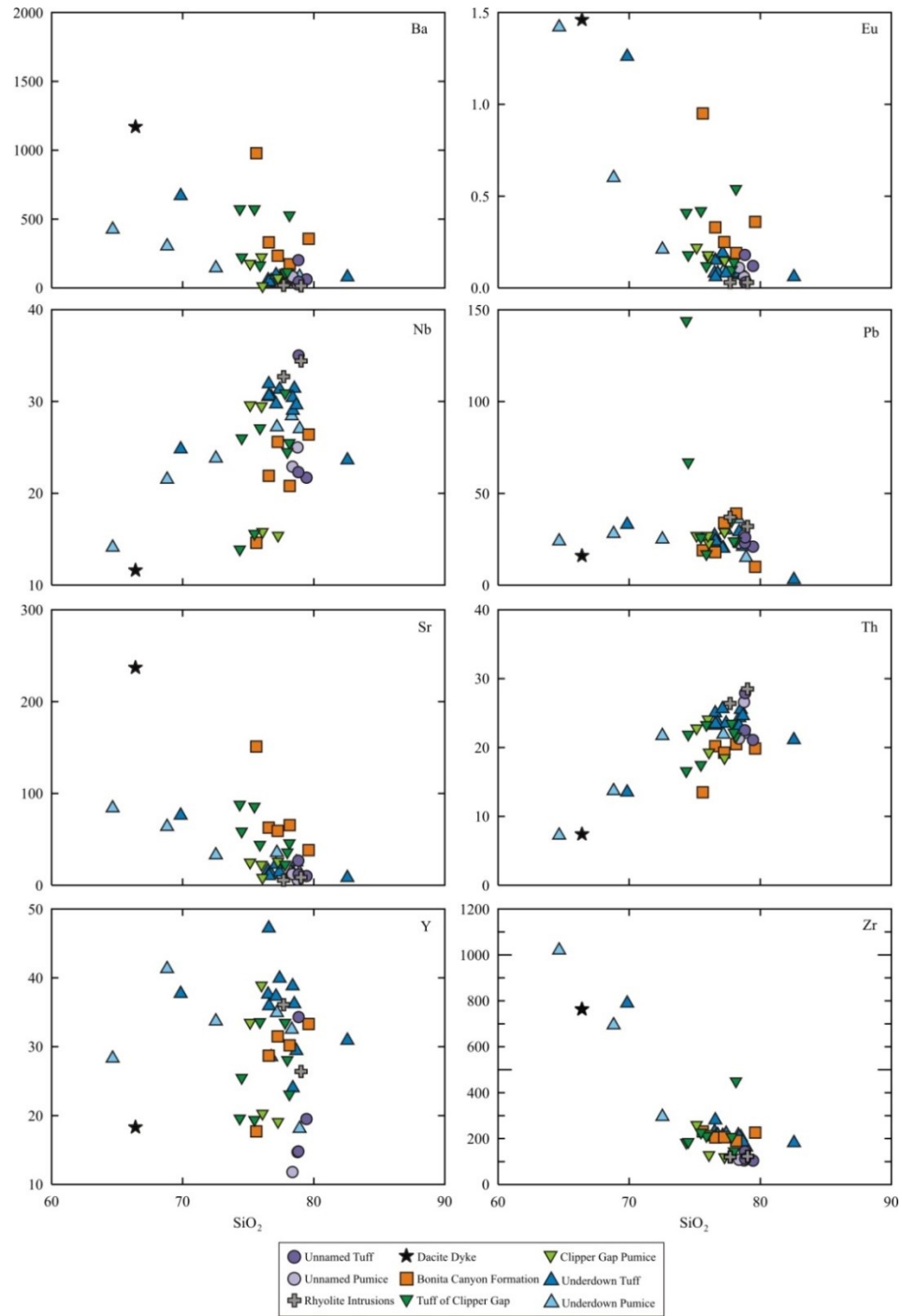


Figure 6.12: Trace element variation diagrams of the major ignimbrites and the rhyolite intrusions of the Underdown Caldera complex. Ba, Eu, Sr, and Zr are behaving as compatible elements in these units as they show a negative correlation with increasing SiO_2 content. The rhyolite intrusions show no observable trend due to the sample size.

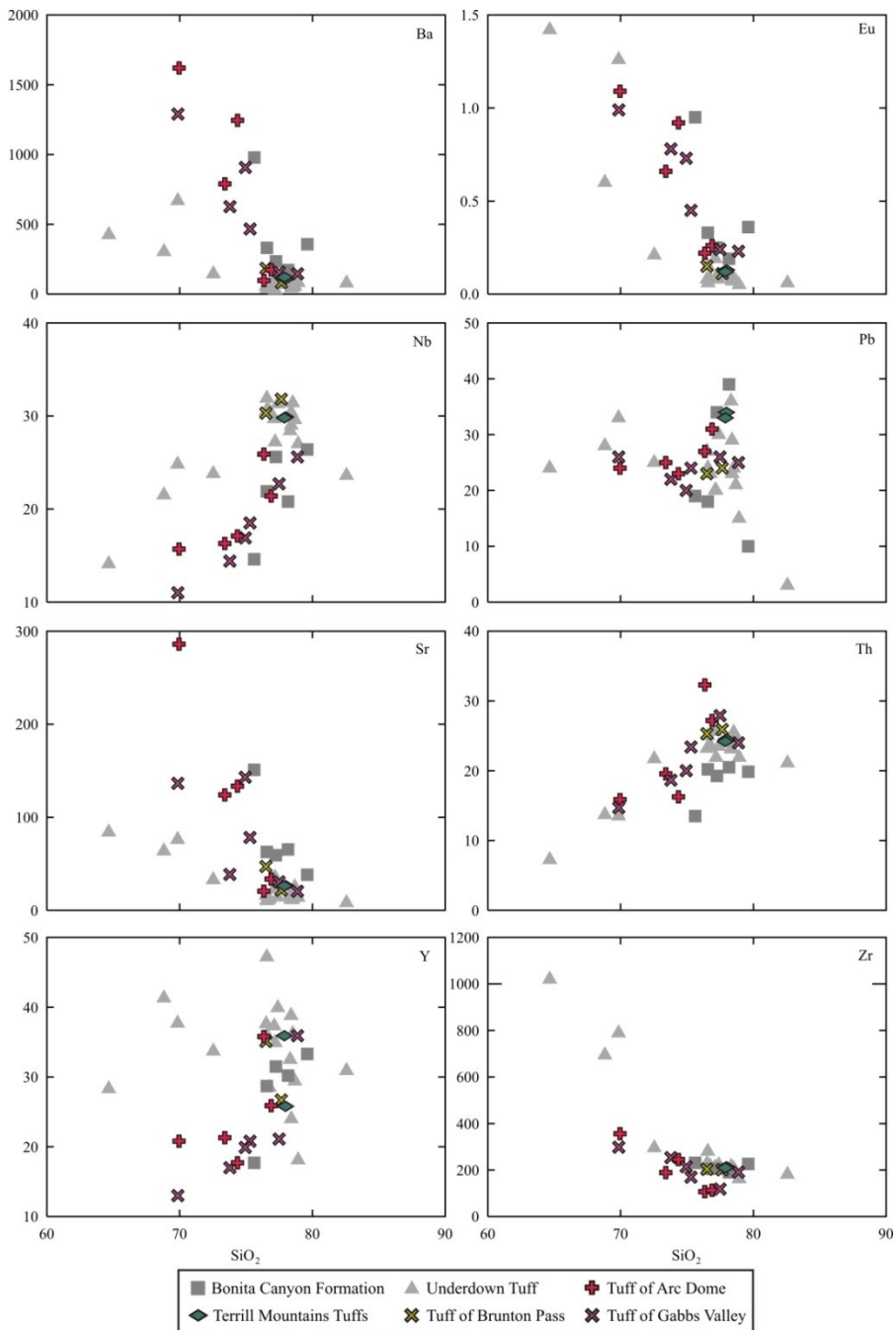


Figure 6.13: Trace element variation diagrams of the other tuffs (tuff of Gabbs Valley, tuff of Arc Dome, and tuff of Brunton Pass) and the Terrill Mountains tuff. Ba, Eu, Sr, and Zr are behaving as compatible elements in these units as they show a negative correlation with increasing SiO_2 content. Ba, Eu, and Sr show a stronger negative trend than Zr with increasing SiO_2 . The Terrill Mountains tuffs plot as a cluster in Ba, Eu, and Zr, but show a strong negative correlation between Sr and SiO_2 .

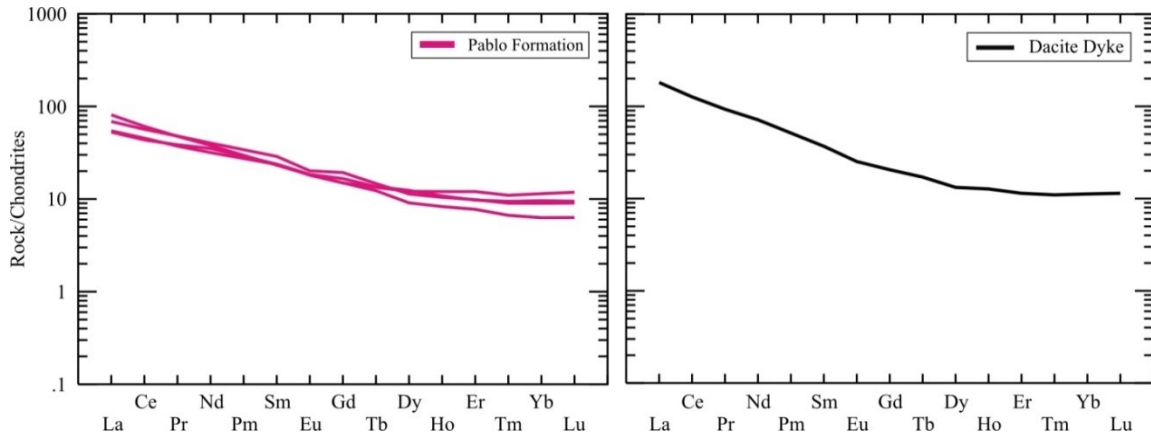


Figure 6.14: Chondrite normalized (Sun and McDonough, 1989) rare earth element diagrams for the Pablo Formation and the dacite dyke. Dacite dyke samples show a larger enrichment in LREEs relative to HREEs than the Pablo Formation. Both units show a flattening pattern in the HREEs and no negative Eu anomaly.

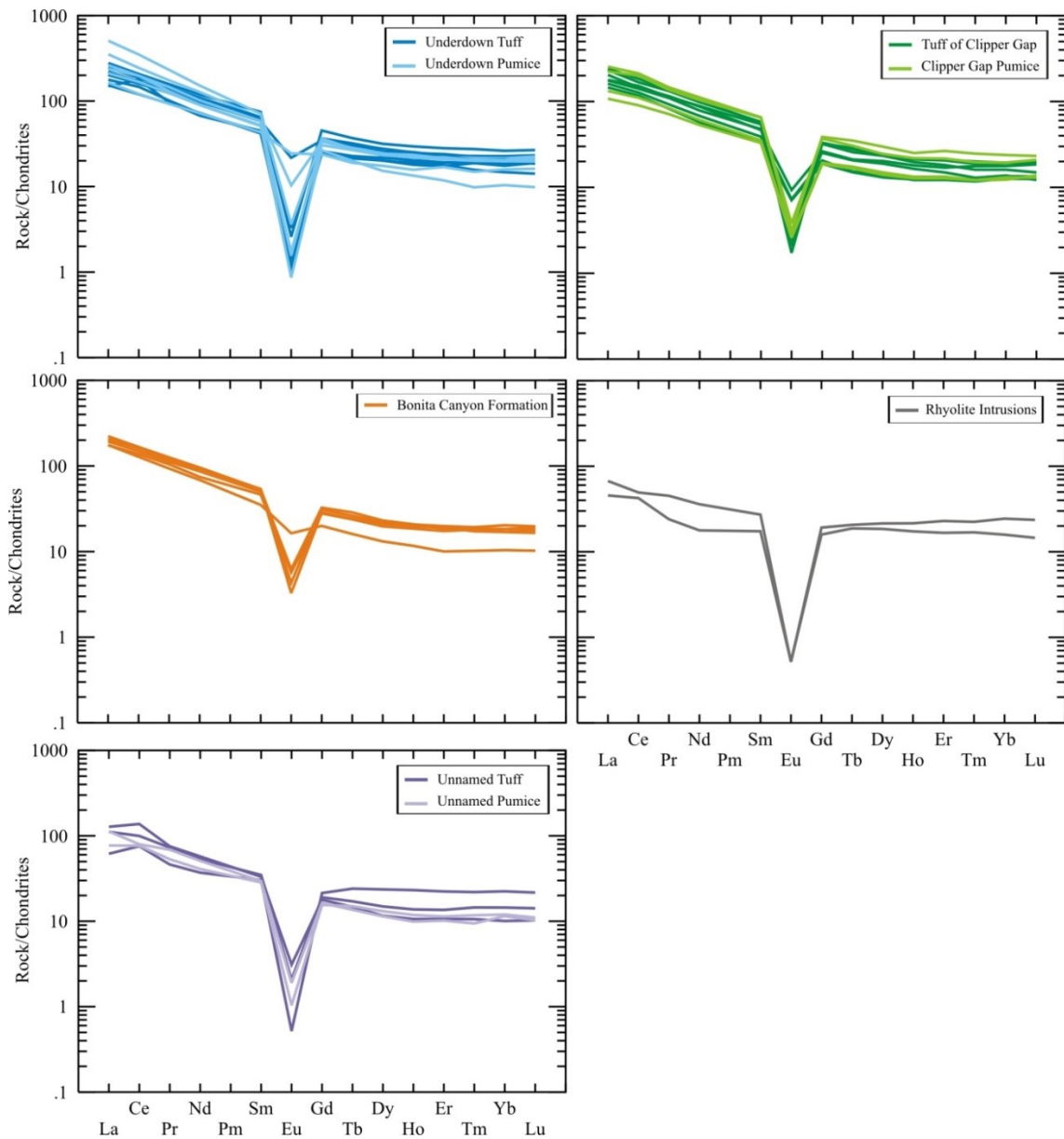


Figure 6.15: Chondrite normalized (Sun and McDonough, 1989) rare earth element diagrams for the major ignimbrites of the Underdown Caldera complex (Underdown Tuff, tuff of Clipper Gap, Bonita Canyon Formation and the Unnamed tuff) and the rhyolite intrusions. Samples show enrichment in LREEs relative to HREEs and a flattened slope in the HREEs, as well as a large negative Eu anomaly. All the major ignimbrites show a similar pattern, however the rhyolite intrusions and the Unnamed tuff show less LREE enrichment and a larger variation in the HREEs.

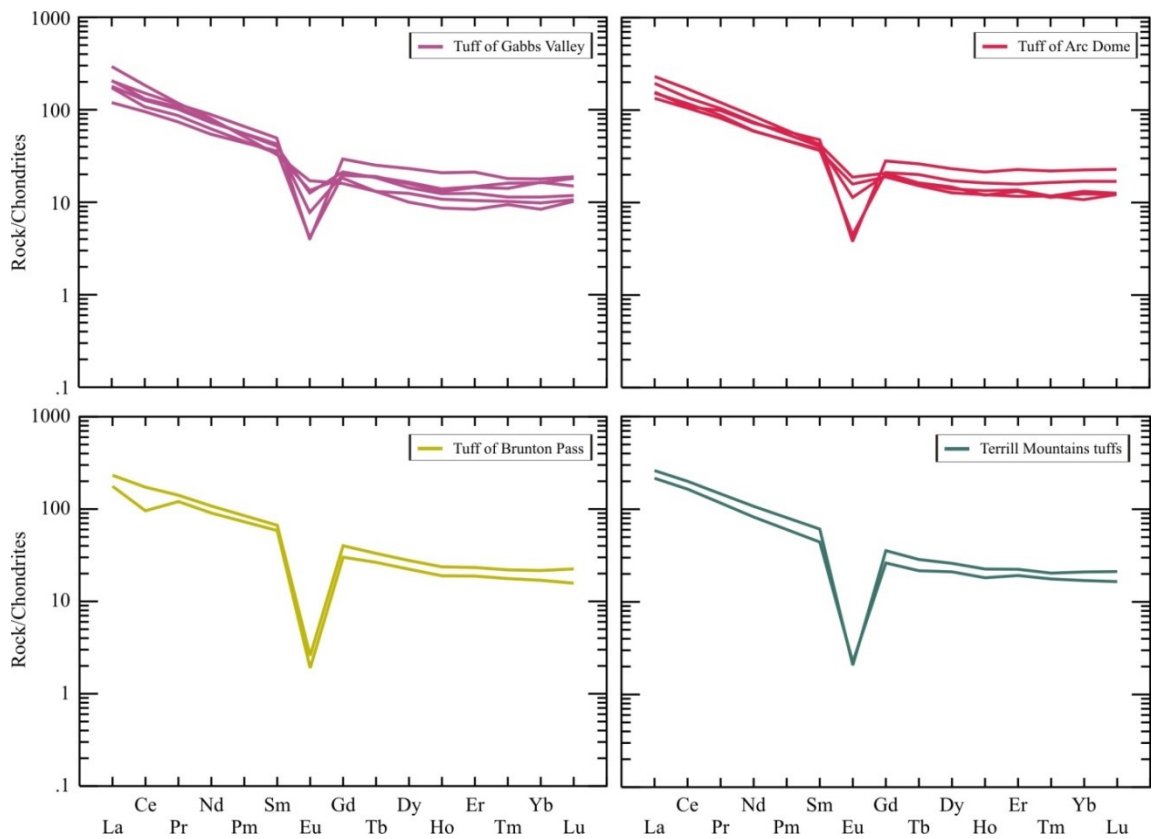


Figure 6.16: Chondrite normalized (Sun and McDonough, 1989) rare earth element diagrams for the slightly older Oligocene tuffs (tuff of Gabbs Valley, tuff of Arc Dome, tuff of Brunton Pass) and the Terrill Mountains tuffs. Samples show enrichment in LREEs relative to HREEs and a flattened slope in the HREEs, as well as a large negative Eu anomaly.

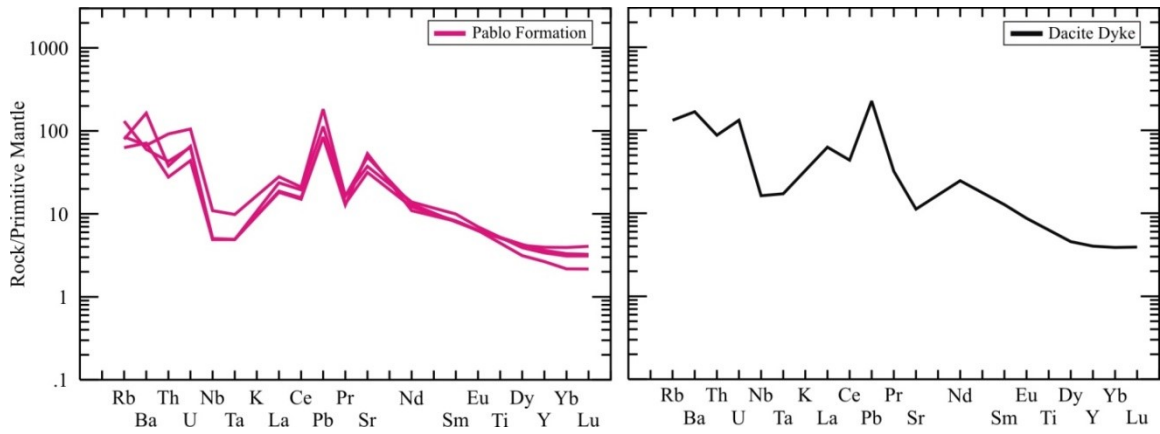


Figure 6.17: Primitive mantle normalized (Sun and McDonough, 1989) trace element diagram for the Pablo Formation and dacite dyke. In the Pablo Formation, positive anomalies exist in Pb and Sr. In the dacite dyke, there is a positive anomaly in Pb and a negative anomaly in Sr. Both units also show a Nb-Ta anomaly.

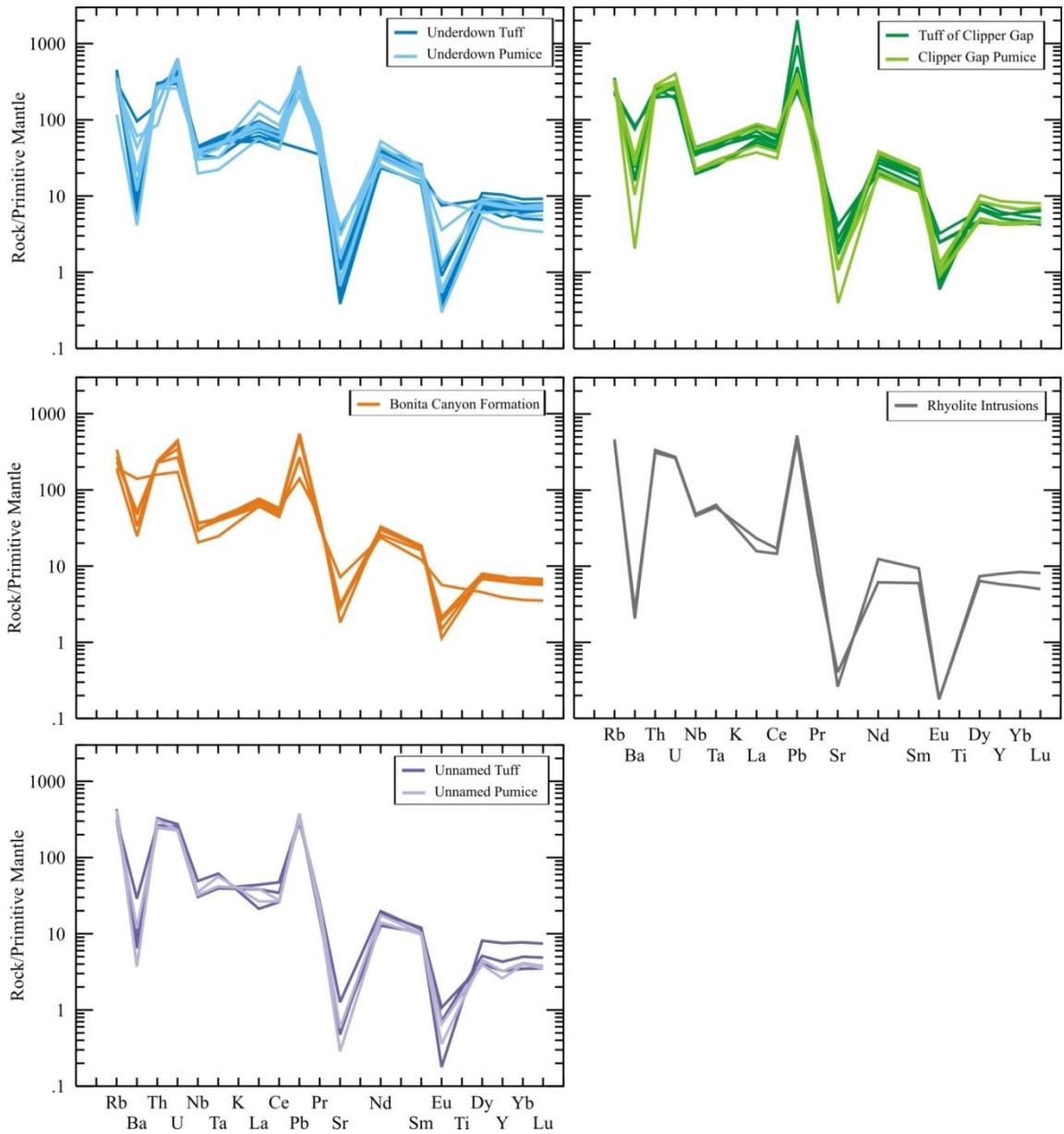


Figure 6.18: Primitive mantle normalized (Sun and McDonough, 1989) trace element diagram for the major ignimbrites of the Underdown Caldera complex (Underdown Tuff, Tuff of Clipper Gap, Bonita Canyon Formation, and Unnamed tuff) and the rhyolite intrusions. Positive anomalies exist in Th and Pb, and negative anomalies exist in Ba, Sr, and Eu.

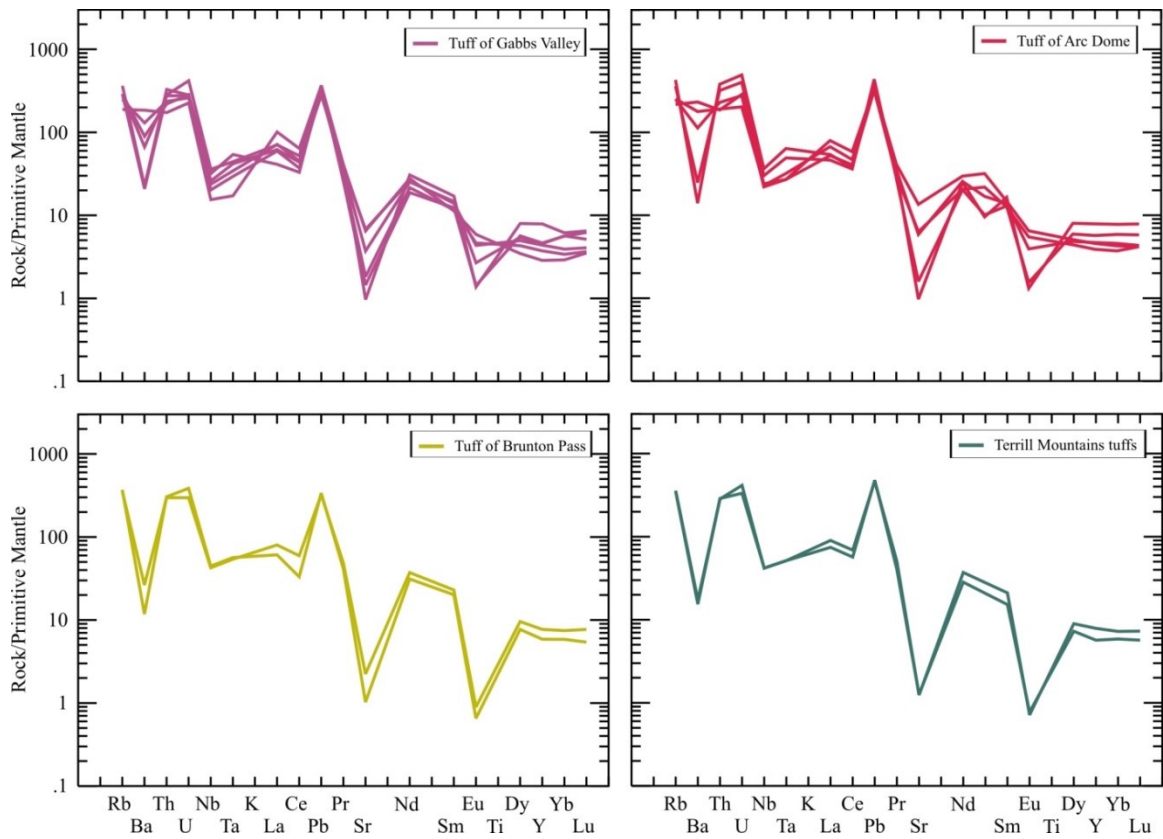


Figure 6.19: Primitive mantle normalized (Sun and McDonough, 1989) trace element diagram for the other tuffs (tuff of Gabbs Valley, tuff of Arc Dome, and tuff of Brunton Pass) and the Terrill Mountains tuff. Positive anomalies exist in Th and Pb, and negative anomalies exist in Ba, Sr, and Eu.

6.2.3 Isotope geochemistry

Isotopic results are listed in Appendix I, Table VIII. The selection of samples for isotopic analysis was limited by very low concentrations of Sr in most of the ignimbrite units. Generally, samples selected for isotopic analysis contained over 40 ppm of Sr. However, two samples have concentrations below 40 ppm; a whole rock and a pumice sample from the Unnamed tuff (26.7 and 12.2 ppm Sr, respectively). These two samples were analyzed in spite of their low Sr concentrations as they contained the highest concentrations of Sr in any of the Unnamed tuff samples. No rhyolite intrusion samples were analyzed due to their low Sr concentration (8.8 and 5.5 ppm). Samples from the tuff of Arc Dome, tuff of Gabbs Valley, and dacite dyke contained much higher Sr concentrations (above 120 ppm) than the Oligocene tuffs from the Underdown Caldera.

Radiogenic isotope analyses were completed on a range of samples including the Pablo Formation, tuff of Gabbs Valley, tuff of Arc Dome, Underdown Tuff, tuff of Clipper Gap, Bonita Canyon Formation, the dacite dyke, the Unnamed tuff, and the Terrill Mountains tuffs. The results for $^{87}\text{Sr}/^{86}\text{Sr}$, $^{144}\text{Nd}/^{143}\text{Nd}$, $^{204}\text{Pb}/^{206}\text{Pb}$, $^{207}\text{Pb}/^{206}\text{Pb}$ and $^{208}\text{Pb}/^{206}\text{Pb}$ are listed in Appendix I, Table VIII. All data plotted below are initial, age-corrected ratios unless otherwise stated. The Pablo Formation has been age corrected to 24.9 Ma for comparison with the other Underdown Caldera tuffs. Miocene-aged lavas from the Underdown Caldera margin analyzed by Tennant (2018) have been plotted with the Underdown Caldera complex data for comparison. Acid-washed tuff of Clipper Gap

samples are plotted in the isotope geochemistry section to show what is believed to be “fresh” isotopic ratios for those samples.

All isotope data are plotted in Figure 6.20A. This includes samples with REE anomalies and high LOI. The REE anomaly samples will be interpreted separately from the main group of data, and were therefore subsequently removed from the main group of data. The remaining samples were plotted on Figure 6.20B. The high LOI samples (including the tuff of Clipper Gap, Bonita Canyon Formation, and Terrill Mountains tuffs) appear to have ϵNd values that are similar to the main group of data however, the $^{87}\text{Sr}/^{86}\text{Sr}$ ratios are either higher or lower than the main group of data. In particular, the Terrill Mountains tuffs have variable $^{87}\text{Sr}/^{86}\text{Sr}$ ratios despite originating from the same unit. The Terrill Mountains whole rock sample plots to the left of the bulk earth line away from a continental signature, one pumice sample from the same unit has an $^{87}\text{Sr}/^{86}\text{Sr}$ value around 0.7050, and the second pumice sample has an $^{87}\text{Sr}/^{86}\text{Sr}$ value around 0.7075. Based on the suspect age corrected $^{87}\text{Sr}/^{86}\text{Sr}$ ratios of the high LOI samples, those samples were removed and the remaining samples were plotted on Figure 6.20C. The remaining group of data mainly plots between $^{87}\text{Sr}/^{86}\text{Sr}$ values of 0.705 to 0.706, with one outlying tuff of Clipper Gap sample which has an ϵNd value closer to zero and an $^{87}\text{Sr}/^{86}\text{Sr}$ value over 0.707. Acid-washed tuff of Clipper Gap samples were plotted for comparison in Figure 6.20D. All acid-washed tuff of Clipper Gap samples are pumice. These samples have ϵNd and $^{87}\text{Sr}/^{86}\text{Sr}$ values similar to the main group of non-acid-washed Underdown Caldera complex data and plot closer to the main group of data

than the remaining tuff of Clipper Gap sample (17-SM-07). The Miocene-aged lavas have isotopic compositions similar to the Oligocene tuffs in the ϵNd versus $^{87}\text{Sr}/^{86}\text{Sr}$ diagram. Four of the Miocene-aged lava samples plot close to the mantle array while two lava samples have higher $^{87}\text{Sr}/^{86}\text{Sr}$ values which are closer to the Underdown Tuff and dacite dyke samples. At the time of ignimbrite formation, the Pablo Formation samples plot far away from the Underdown Caldera complex data in the mantle array and do not appear to be related to the Oligocene tuffs. As a potential mantle source, the Miocene lavas appear more similar to the Oligocene tuffs of the Underdown Caldera than the Pablo Formation. The Pablo Formation has been ignored and only the Miocene aged lavas have been plotted with the Underdown Caldera data on all subsequent isotope diagrams.

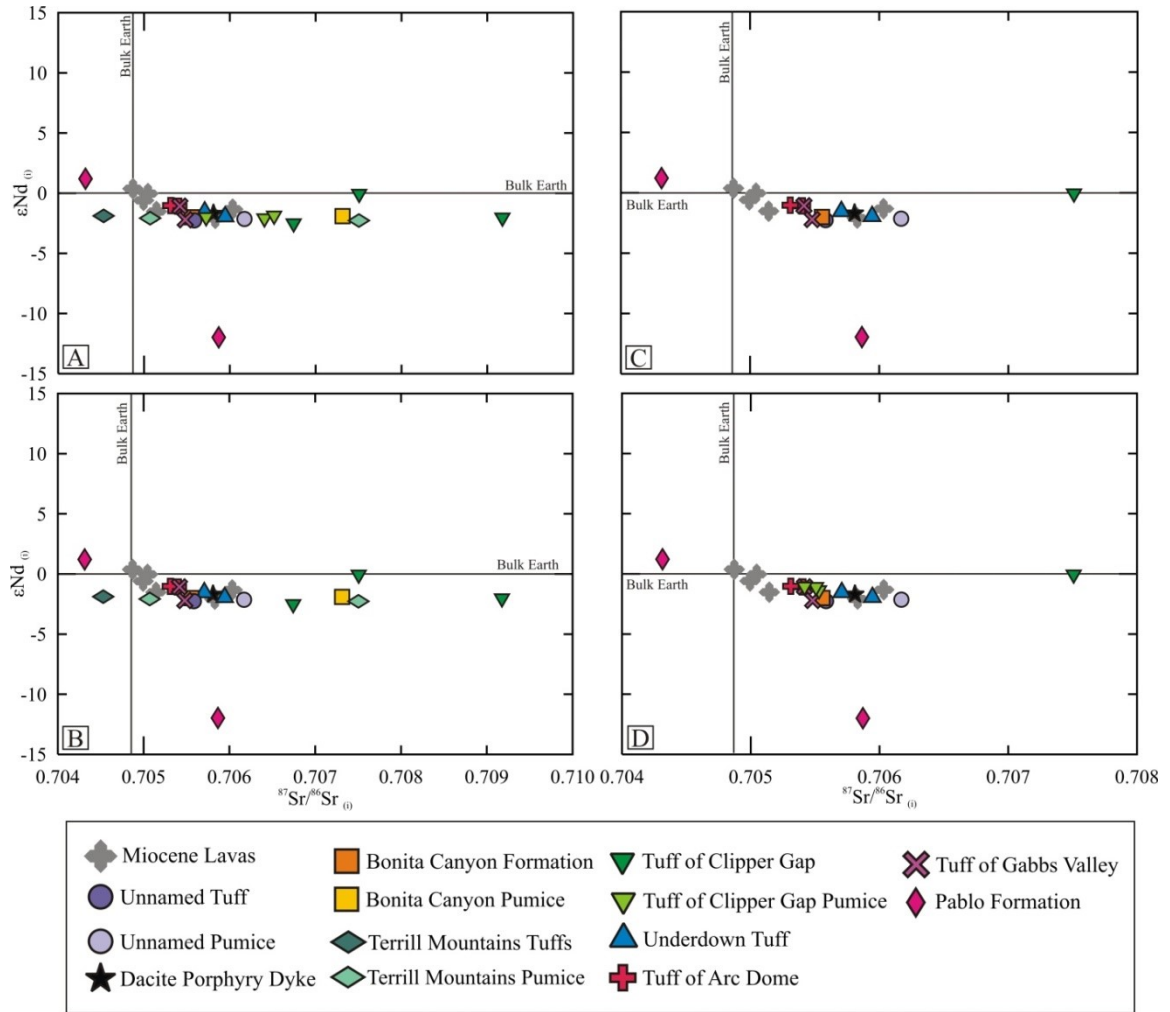


Figure 6.20: (A) Initial ϵNd versus $^{87}Sr/^{86}Sr$ with all Underdown Caldera complex data. (B) Same as in (A), but samples with negative Ce anomalies have been removed. (C) Same as in (B), but high LOI (> 6%) samples have been removed. (D) Same as in (C), but acid-washed tuff of Clipper Gap samples are added for comparison.

The removal of the Pablo Formation shows more detail on an ϵNd versus $^{87}\text{Sr}/^{86}\text{Sr}$ diagram. While there appears to be no observable trend when all of the data is plotted, the removal of the anomalous REE and high LOI samples shows a correlation between increasing $^{87}\text{Sr}/^{86}\text{Sr}$ and decreasing ϵNd in the remaining “fresh” and acid-washed samples (Fig. 6.21). In this ϵNd vs. $^{87}\text{Sr}/^{86}\text{Sr}$ diagram, the ignimbrite samples appear to be related to the Miocene-aged mafic to intermediate lavas, however the lavas collected from the Underdown Caldera margin have much higher Sr concentrations than the Oligocene tuffs. There is also a slight positive correlation between decreasing Sr concentration and increasing $^{87}\text{Sr}/^{86}\text{Sr}$ ratios in the “fresh” samples (Fig. 6.22). Sample 17-SM-07 (tuff of Clipper Gap) appears to be an outlier with a much higher $^{87}\text{Sr}/^{86}\text{Sr}$ ratio than the other Oligocene tuffs, while the acid-washed tuff of Clipper Gap samples plot with the main group of data. The Unnamed tuff has a much lower Sr concentration than the other Oligocene tuffs and there is a large difference in Sr concentration between the whole rock sample and the pumice sample of the Unnamed tuff. There appears to be no correlation between $^{87}\text{Sr}/^{86}\text{Sr}$ ratios and the SiO_2 content of the samples, as the data is scattered (Fig. 6.23). The “fresh” and acid-washed samples show little variation in $^{87}\text{Sr}/^{86}\text{Sr}$ ratios with increasing SiO_2 but show a larger amount of variation in $^{87}\text{Sr}/^{86}\text{Sr}$ ratios at high SiO_2 content.

When analyzing Nd isotopic ratios, there appears to be little to no correlation between ϵNd values and Nd concentration or SiO_2 content. On an age corrected ϵNd versus $1/\text{Nd}$ concentration diagram, the “fresh” and acid-washed samples appear to show a similar

correlation between decreasing Nd concentration and increasing ϵNd value as the Miocene lavas (Fig. 6.24). On an ϵNd versus SiO_2 diagram, there is a large scatter in the data in the “fresh” samples and the acid-washed tuff of Clipper Gap samples (Fig. 6.25).

“Fresh” and acid-washed samples plot in steep positive trends in both the $^{207}\text{Pb}/^{204}\text{Pb}$ and $^{208}\text{Pb}/^{204}\text{Pb}$ versus $^{206}\text{Pb}/^{204}\text{Pb}$ diagrams. $^{207}\text{Pb}/^{204}\text{Pb}$ versus $^{206}\text{Pb}/^{204}\text{Pb}$ shows a similar slope as the Miocene aged lavas but at a higher $^{206}\text{Pb}/^{204}\text{Pb}$ ratio (Fig. 6.26). However the Miocene aged lavas and the Oligocene tuffs plot in one tight trend when comparing $^{208}\text{Pb}/^{204}\text{Pb}$ to $^{206}\text{Pb}/^{204}\text{Pb}$ (Fig. 6.27). In the Pb isotope diagrams, 17-SM-07 is much less radiogenic than all of the other Oligocene tuffs, while the acid-washed tuff of Clipper Gap samples are some of the most radiogenic samples in the arrays. Within specific units, pumice samples tend to be more radiogenic than their whole rock equivalents. Older units such as the tuffs of Gabbs Valley and Arc Dome are some of the least radiogenic samples, but are more radiogenic than 17-SM-07. When comparing the $^{208}\text{Pb}/^{204}\text{Pb}$ ratios to increasing SiO_2 and magma evolution, the “fresh” and acid-washed samples plot in a scattered, negative trend (Fig. 6.28). When comparing $^{208}\text{Pb}/^{204}\text{Pb}$ ratios to Pb concentration, the samples show a scattered positive correlation, where higher Pb content is associated with more radiogenic Pb isotope ratios (Fig. 6.29).

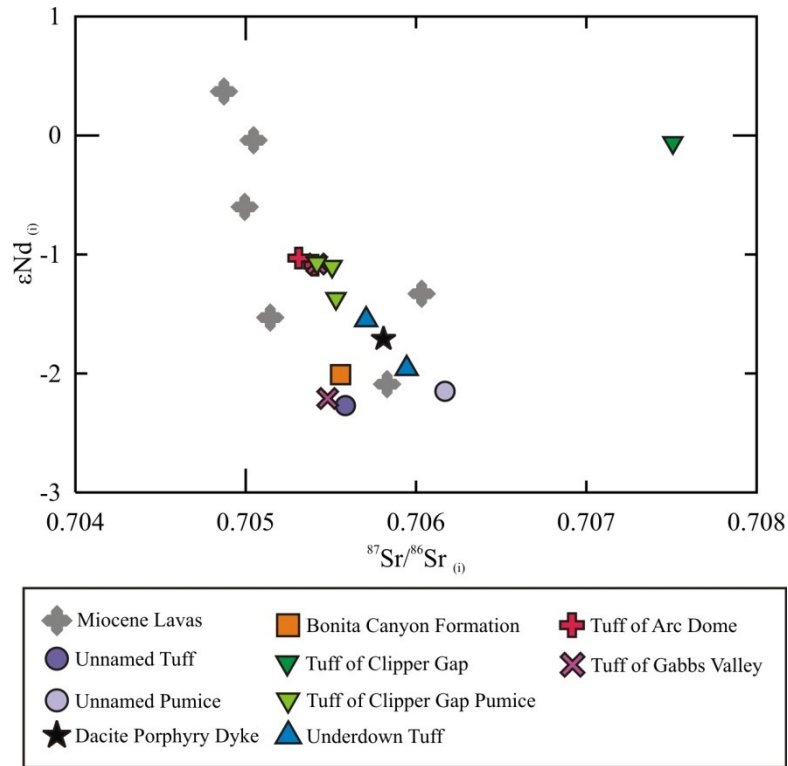


Figure 6.21: “Fresh” and acid-washed data plotted on an initial ϵNd versus $^{87}\text{Sr}/^{86}\text{Sr}$ diagram without the Pablo Formation. Samples show a negative correlation between ϵNd values and increasing $^{87}\text{Sr}/^{86}\text{Sr}$ ratios. The Miocene lavas form the low-Sr and high-Nd isotope ratio endmember. Sample 17-SM-07, a tuff of Clipper Gap whole rock, plots as an outlier at a very high $^{87}\text{Sr}/^{86}\text{Sr}$ ratio. Acid-washed tuff of Clipper Gap samples plot within the “fresh” samples without anomalous REEs.

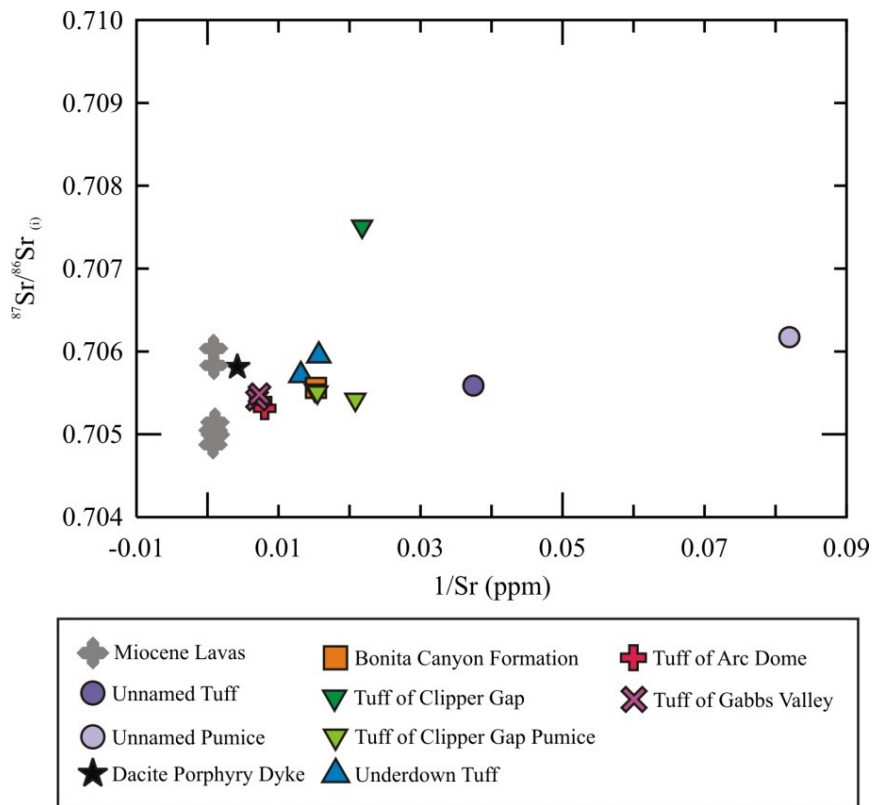


Figure 6.22: Initial $^{87}\text{Sr}/^{86}\text{Sr}$ versus $1/\text{Sr}$ (ppm) plot showing the relation between Sr concentration and $^{87}\text{Sr}/^{86}\text{Sr}$ isotopic ratios. The “fresh” samples show near-constant $^{87}\text{Sr}/^{86}\text{Sr}$ ratios that overlap with $^{87}\text{Sr}/^{86}\text{Sr}$ isotope ratios in the Miocene mafic to intermediate lavas. Similar to the previous diagram, 17-SM-07 appears to be an outlier at a much higher $^{87}\text{Sr}/^{86}\text{Sr}$ value, and the acid washed tuff of Clipper Gap data plot close “fresh” samples. The Unnamed tuff whole rock and pumice have a much lower Sr concentration than the rest of the “fresh” samples.

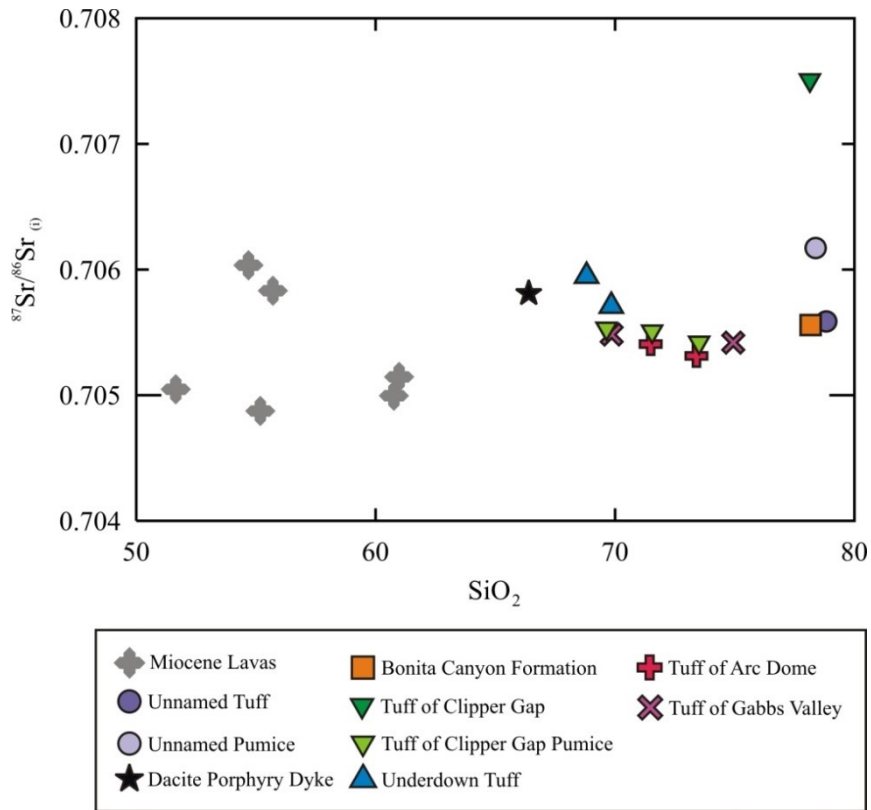


Figure 6.23: Initial $^{87}\text{Sr}/^{86}\text{Sr}$ versus SiO_2 content showing the relationship between Sr isotopic values and increasing SiO_2 content. “Fresh” samples without anomalous REEs and acid-washed samples show a scattered pattern between increasing SiO_2 content and Sr isotopic ratio. Acid-washed tuff of Clipper Gap samples plot more similarly to the “fresh” samples than the 17-SM-07 tuff of Clipper Gap sample which has a much higher $^{87}\text{Sr}/^{86}\text{Sr}$ ratio. In particular, the acid-washed samples show large similarities to the tuff of Gabbs Valley, tuff of Arc Dome, and Underdown Tuff samples. More variation in $^{87}\text{Sr}/^{86}\text{Sr}$ ratios is observed at high SiO_2 content.

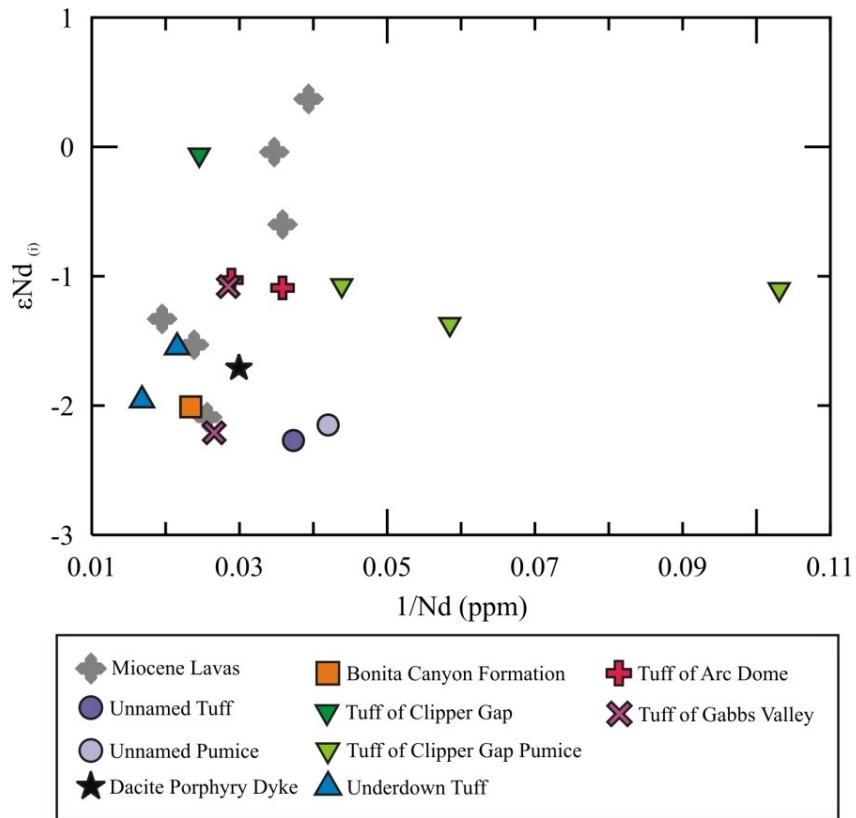


Figure 6.24: Initial ϵNd versus $1/Nd$ (ppm) showing the relation between epsilon Nd values and Nd concentration. The “fresh” samples show an increasing scatter between increasing ϵNd value and decreasing Nd concentration. Note that the Miocene lavas extend to higher ϵNd values than most of the Oligocene ignimbrites. The acid-washed tuff of Clipper Gap samples have a much lower Nd concentration than a majority of the other samples which may be a result of the acid washing process.

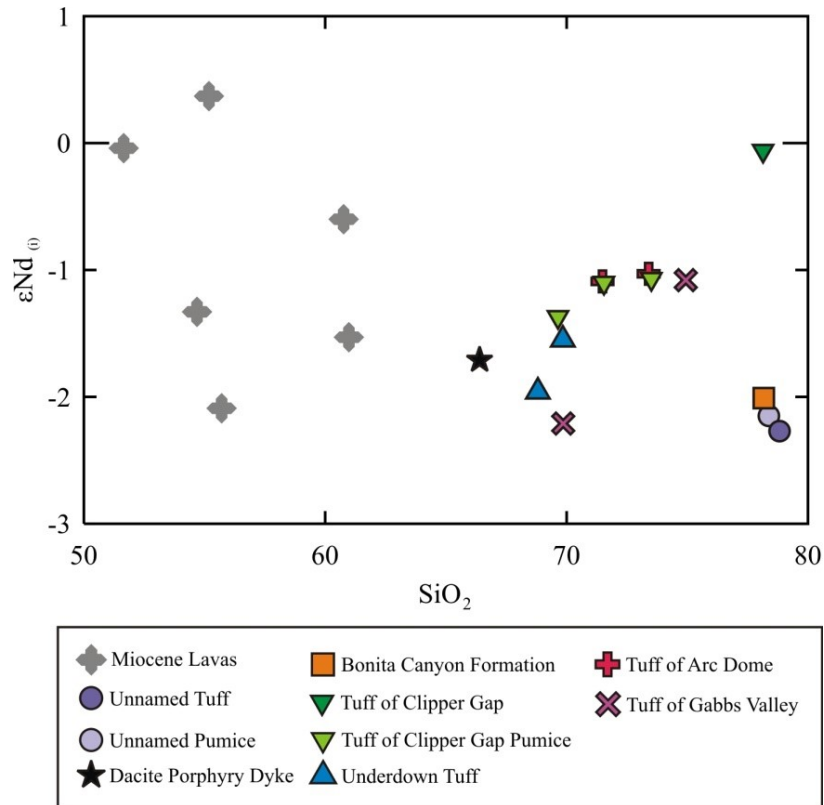


Figure 6.25: Initial ϵNd versus SiO_2 weight percentage showing the comparison between epsilon Nd values and increasing SiO_2 content. The samples appear scattered and there appears to be no correlation between increasing SiO_2 content and ϵNd value. The acid-washed tuff of Clipper Gap data plots more similarly to the “fresh” samples than 17-SM-07 (tuff of Clipper Gap) which has an ϵNd value closer to zero than any other sample.

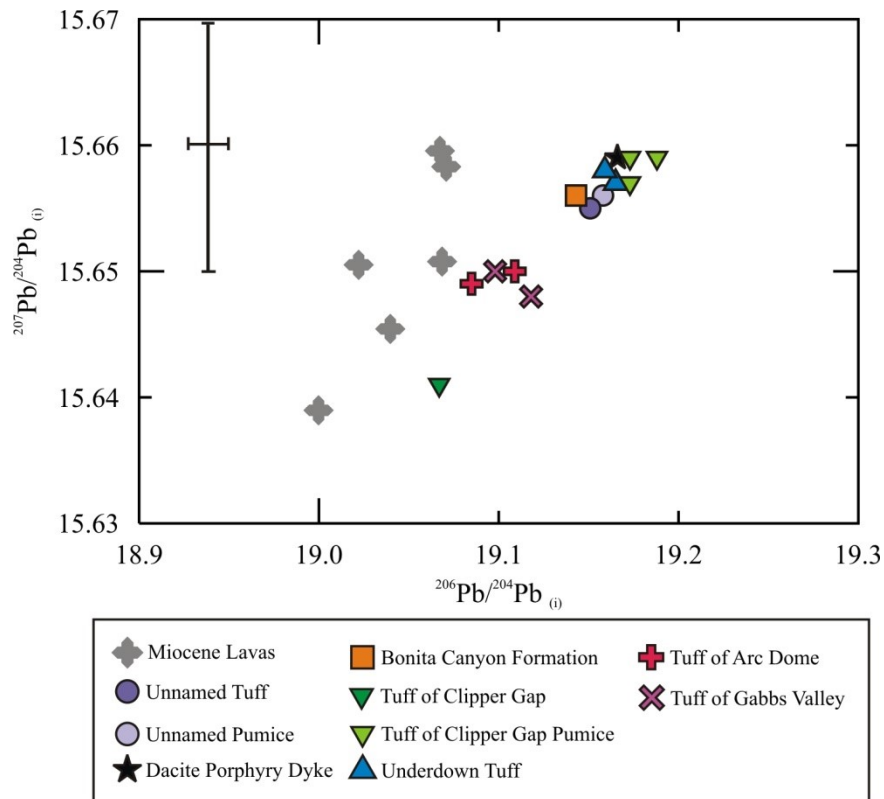


Figure 6.26: Initial $^{207}\text{Pb}/^{204}\text{Pb}$ versus $^{206}\text{Pb}/^{204}\text{Pb}$. The Underdown Caldera complex data plots as a fairly tight positive correlation that is similar to the Miocene lavas, but at a higher $^{206}\text{Pb}/^{204}\text{Pb}$ ratio (which may be explained by differences in analytic techniques). Sample 17-SM-07 (tuff of Clipper Gap) is the least radiogenic sample in the trend, while the acid-washed samples are the most radiogenic in the group. Note that the Miocene lavas were analyzed by TIMS whereas the ignimbrite samples were analyzed by MC-ICP-MS, which likely explains the greater scatter in the Miocene lava data. An error bar in the top left corner represents the error for the each Miocene lava sample. Error bars for MC-ICP-MS runs are the size of the symbols.

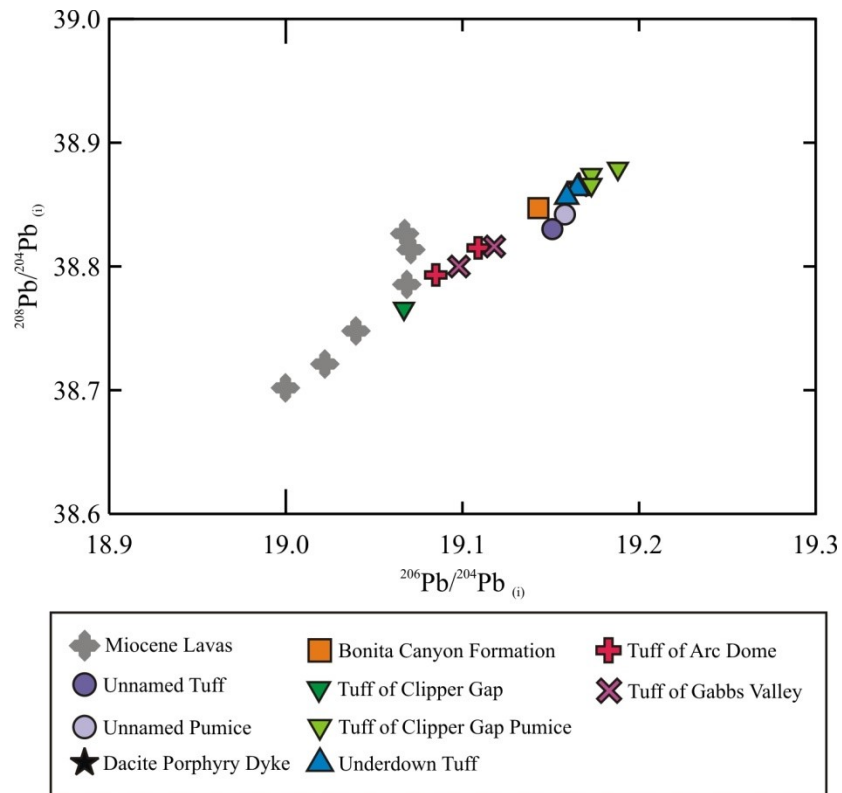


Figure 6.27: Initial $^{208}\text{Pb}/^{204}\text{Pb}$ versus $^{206}\text{Pb}/^{204}\text{Pb}$ showing the correlation between increasing $^{206}\text{Pb}/^{204}\text{Pb}$ and increasing $^{208}\text{Pb}/^{204}\text{Pb}$. Similar to the $^{207}\text{Pb}/^{204}\text{Pb}$ versus $^{206}\text{Pb}/^{204}\text{Pb}$ comparison, the acid-washed tuff of Clipper Gap samples are much more radiogenic than tuff of Clipper Gap sample 17-SM-07, which is less radiogenic than the tuff of Gabbs Valley and tuff of Arc Dome. In general, the Miocene lavas are less radiogenic than the Oligocene tuffs but generally plot in the same correlation as the Oligocene tuffs.

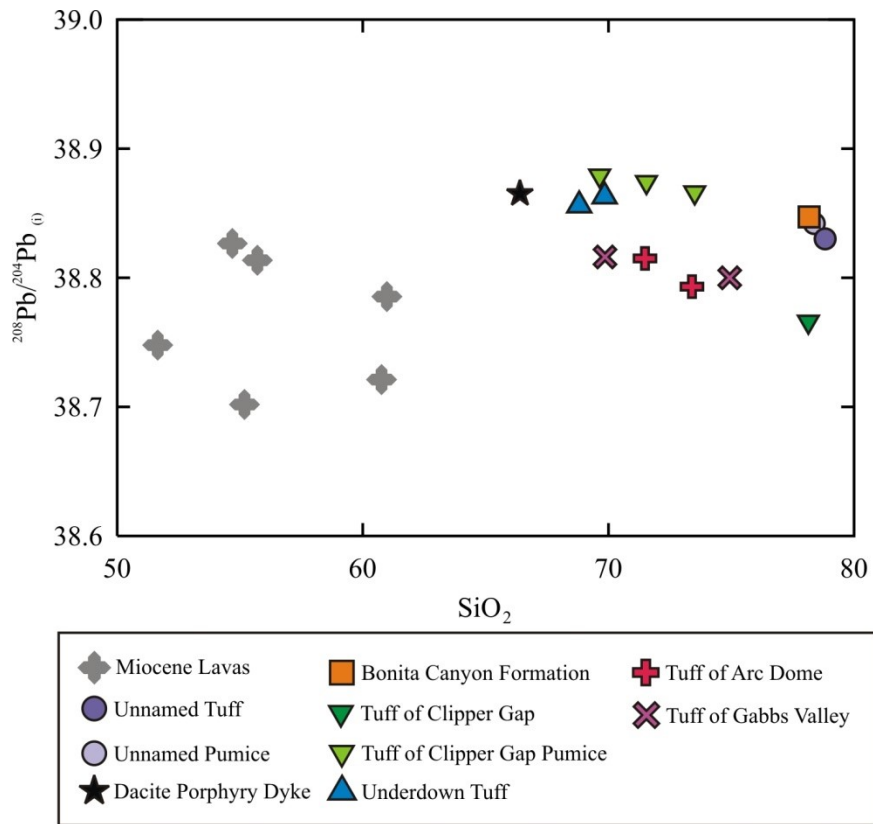


Figure 6.28: Initial $^{208}\text{Pb}/^{204}\text{Pb}$ versus SiO_2 weight percentage showing the comparison between $^{208}\text{Pb}/^{204}\text{Pb}$ and increasing SiO_2 content. The “fresh” samples and acid-washed samples show a scattered decrease with increasing SiO_2 content.

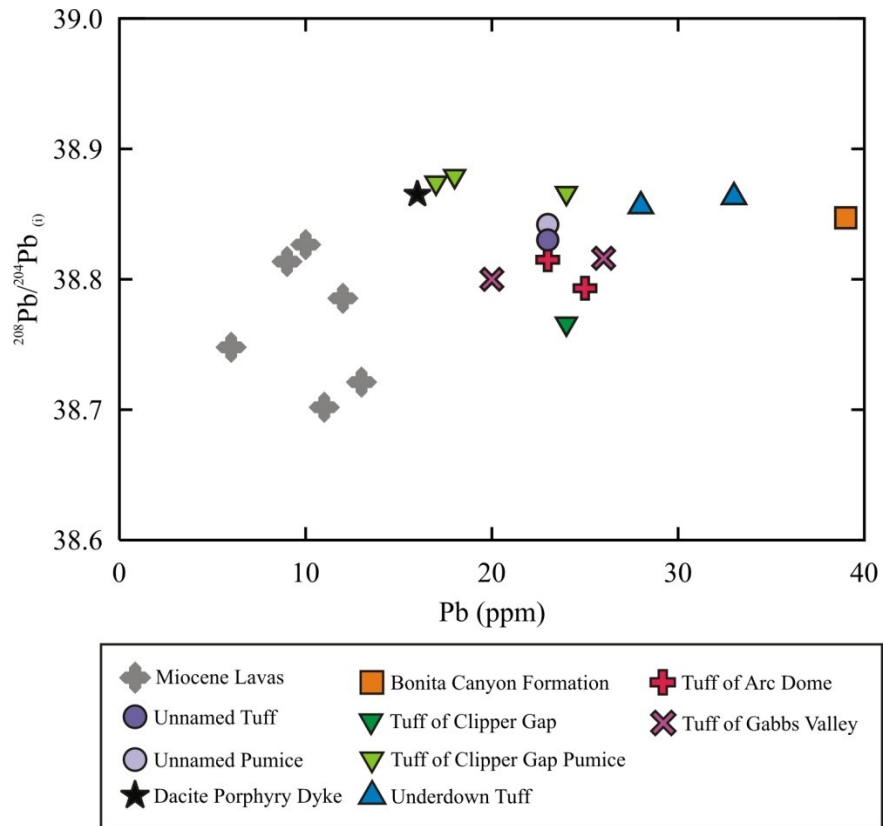


Figure 6.29: Initial $^{208}\text{Pb}/^{204}\text{Pb}$ versus Pb (ppm) showing the comparison between Pb isotopic values and Pb concentration. The “fresh” samples and acid-washed samples show a scattered positive correlation between $^{208}\text{Pb}/^{204}\text{Pb}$ ratios and Pb concentration.

7.0 Discussion

7.1 Establishing Primary Characteristics

This section discusses the petrography and geochemistry of the intracaldera tuffs of the Underdown Caldera complex and the tuff of Clipper Gap to establish the primary characteristics of the units. The isotopic results will be compared to Miocene lavas collected from the margin of the caldera to investigate possible magma sources for the Oligocene tuffs.

7.1.1 Petrographic characteristics

The Oligocene tuffs of the Underdown Caldera complex are determined to be “Great Basin” style ignimbrites due to the presence of hydrous phases; biotite, hornblende, and Fe-Ti oxides (Christiansen, 2005). A combination of one or more of these minerals was observed in every ignimbrite unit. Phenocryst assemblages of two feldspars, quartz, and biotite and/or hornblende were standard across the caldera forming and extracaldera ignimbrites. Many quartz and feldspar phenocrysts in the ignimbrites were observed to be fractured, which is likely a result of the flow of pyroclastic material at the time of eruption. Some of the quartz and feldspar phenocrysts were also observed to be partially resorbed suggesting a reaction between the phenocrysts and a melt of changing composition. As expected, the Underdown Tuff and tuff of Clipper Gap were petrographically similar. In particular, the presence of two different pumice types, purple porphyritic pumice and white aphyric pumice, made these units distinct. The

potential origin of the porphyritic pumice will be discussed in a subsequent section (section 7.4). The Bonita Canyon Formation contained the most sedimentary characteristics of any of the caldera forming ignimbrites. For example, this unit contained a higher proportion of lithic fragments than was observed in the other Oligocene tuffs. These lithic fragments are composed of quartz and feldspar, and likely originate from the Underdown Tuff or other tuffs located in proximity to the caldera. It is possible that this unit is a reworked unit of the upper Underdown Tuff or an unwelded upper section of the Underdown Tuff. The Unnamed tuff appears to be more welded than the other Oligocene tuffs from this study. This difference is highly noticeable, as the matrix of the Unnamed tuff is completely glassy in nearly all studied samples. The higher degree of welding in this sample may be a result of higher melt temperatures at the time of eruption. Many of the ignimbrite samples, particularly porphyritic pumice samples, show a high degree of weathering or alteration, despite the fact that samples appeared fresh when collected in the field.

7.1.2 Geochemical characteristics

Major element geochemistry

The Oligocene tuffs from the Underdown Caldera complex follow the same major element fractionation trends as other ignimbrites from the WNVF (Henry and John, 2013). Na_2O shows the most scatter of all major element oxides when compared to increasing SiO_2 content, likely due to the bulk partition coefficient of Na being close to 1 and/or the susceptibility of Na to weathering. As many of the samples appeared to be

weathered and/or altered under petrographic observation, it is possibly a combination of the two. The trend of Underdown and tuff of Clipper Gap samples (particularly pumice) between the rhyolite and trachyte fields on the TAS diagram is likely a result of weathering which has decreased the SiO₂ content and increasing the alkali content. A similar weathering signature was observed in the Fish Creek Mountains tuffs (Cousens et al., 2019). Therefore, this observed range in SiO₂ content is not interpreted to be a primary geochemical characteristic of these units. One Underdown Tuff sample with a SiO₂ content of approximately 83 weight percent is interpreted to have undergone post-deposition silicification. The same sample has only 0.09 weight percentage Na₂O, suggesting that it has also lost Na due to weathering.

Trace Element Geochemistry

Barium, Eu, Sr, and Zr are interpreted to behave as compatible elements in the Oligocene tuffs based on their negative correlations with SiO₂ content observed in the trace element bivariate plots. Based on partition coefficients compiled from GERM (Appendix I, Table XII), Ba is likely being preferentially included into potassium feldspar and biotite. Europium may be incorporated into plagioclase feldspar, potassium feldspar, and amphibole. Strontium is preferentially included into plagioclase feldspar, and Zr may be incorporated into zircon. Niobium appears to be an incompatible element in the Oligocene tuffs based on its correlation between increasing Nb concentration and increasing SiO₂ content. Based on its partition coefficient, biotite preferentially incorporates Nb into its structure, and biotite was observed to be present in all of the

ignimbrite units, which contradicts the observed incompatible trend. However, despite biotite being present in all units, it was not present in all individual samples, and was found in a small abundance (typically trace-2%) when present. The observed incompatibility in Nb could suggest that other minerals which don't incorporate Nb are dominating the crystallizing sequence. There may therefore be more Nb left in the melt than is incorporated into the small amount of crystallizing biotite as the magma evolves. Pb is partitioning variably into each ignimbrite unit as shown by the Pb bivariate plot which shows a clustered correlation between Pb concentration and SiO₂ content. While Pb may be incorporating into potassium feldspar, making it a compatible element, other minerals which do not incorporate Pb may be dominating the crystallizing sequence, causing it to appear incompatible in some units, similar to Nb. Thorium is also interpreted to behave as an incompatible element, and based on partition coefficient is not preferentially incorporated into any of the phenocryst phases in the ignimbrite units. The scatter of Y when compared to increasing SiO₂ content makes it impossible to determine whether the element is behaving compatibly or incompatibly. Yttrium has a positive partition coefficient for biotite, apatite, and zircon, however there is no correlation between Y and increasing magma evolution that suggests it is being preferentially incorporated into any of these phases.

The Pablo Formation and dacite dyke samples show very similar chondrite normalized REE and primitive mantle normalized trace element patterns, suggesting that the dacite dyke could be originating from a partial melt of the Pablo Formation. However, the Sr

and Nd isotopic values for these two units are quite different, making this scenario unlikely.

As observed on the chondrite normalized REE plots (Fig 6.15 and 6.16) most of the felsic units show enrichment in the LREEs compared to the HREEs, except for the rhyolite intrusions and the Unnamed tuff. Those two units show very little enrichment in the LREEs compared to the HREEs, and in the case of the rhyolite intrusions, a nearly flat pattern is observed from the LREEs to the HREEs. Similar chondrite normalized REE patterns are observed in pumice and fiamme from the base of the lower cooling unit of the Fish Creek Mountains tuff (Varve, 2013). The flatter patterns are proposed to be due to allanite fractionation, which preferentially removes the LREE from the melt (Mahood and Hildreth, 1983). The rhyolite intrusions and Unnamed tuff fiamme are interpreted to be early-erupted material from the most evolved part of the magma chamber that has undergone allanite fractionation. As magmatism continued, the eruption drew deeper into the magma reservoir, tapping less evolved magma that has not undergone allanite fractionation, causing a rotation in the REE pattern as La/Yb increases, resulting in enrichment in the LREEs compared to the HREEs.

The ~24.9 Ma Underdown Tuff, tuff of Clipper Gap, and Bonita Canyon Formation do not show the flattened pattern between the LREEs to the HREEs. The rhyolite intrusions and the Unnamed tuff were dated at 24.774 ± 0.051 and 24.755 ± 0.037 Ma, respectively (C. Henry, pers. comm., 2018). Based on their ages, the rhyolite intrusions may mark a recharge event of magma into the Underdown Caldera complex, after a time when the

magma chamber was allowed to rest and the magma evolved in composition, resulting in the emplacement of more evolved material than was erupted during the formation of the Underdown Tuff, tuff of Clipper Gap, and Bonita Canyon Formation. The rhyolite intrusions may mark the beginning of a new stage of magmatism, as their REE patterns are flatter than the Unnamed tuff which shows some small rotation to more enriched LREE patterns. However, this may also indicate that this region was a long lived center of felsic magmatism lasting from the eruption of the oldest ignimbrite (tuff of Gabbs Valley, 25.15 ± 0.06 Ma) (Henry and John, 2013) to the youngest ignimbrite (Unnamed Tuff, 24.774 ± 0.051 Ma) (C. Henry, pers. comm., 2018). It is possible that the cooling units marking the beginning of eruption of the Underdown Tuff also shows this REE signature; however the base of the Underdown Tuff is believed to be buried (Bonham, 1970). Therefore no samples were collected from the actual base of the Underdown Tuff, and no rotation in the chondrite normalized REE data is observed in the Underdown Tuff.

The crystallization of an LREE phase, such as allanite, may be responsible for the flattened chondrite normalized REE patterns in the rhyolite intrusions and the Unnamed tuff. Allanite has a high affinity for the LREEs (La-Sm), and a less high affinity for the HREEs and the high field strength elements (HFSEs), therefore the crystallization of this phase from a melt would fractionate LREEs to a high degree, and the La/Yb ratio would be lowered. The crystallization of allanite is an indication of high degrees of magma evolution (Mahood and Hildreth, 1983). Allanite exists in both the lower flows of the

24.7 Ma Fish Creek Mountains tuff and throughout the 34.0 Ma Caetano Tuff (Cousens et al., 2019; Watts et al., 2016). The very low affinity for the HFSEs (which includes Nb and Ta) in allanite compared to the LREEs would also result in the higher abundances of Nb and Ta observed in the rhyolite intrusions and the Unnamed tuff than in magmas which have not fractionated allanite (Fig. 6.18 and 6.19). The highly evolved, basal pumice from the Fish Creek Mountains tuff also shows a larger negative Eu anomaly than the pumice from the overlying cooling unit. The largest negative Eu anomalies in the felsic rocks of the Underdown Caldera complex are observed in the rhyolite intrusions and Unnamed tuff, similar to what is observed in the Fish Creek Mountains tuff.

7.1.3 Potential alteration of isotopic ratios

Samples with higher than 6 weight percent LOI were not included in the isotope diagrams of the results section due to the potential that those samples have been altered which could affect their age-corrected isotopic ratios. Sr isotopic ratios of high-LOI samples appear to show higher variance than those of the “fresh” samples, whereas ϵNd values appear to be similar to those of the “fresh” samples (Fig. 7.1). Pb isotope ratios of the high-LOI samples also are similar to the “fresh” samples, since they plot in the array of Pb isotopic ratios formed by the “fresh” samples and Miocene lavas (Fig. 7.2). Therefore any alteration on the high-LOI samples is assumed to have affected Sr isotopic ratios to a higher degree than Nd or Pb isotopic ratios.

Anomalous REE-rich samples were also withheld from the isotope diagrams of the results section based on similar suspicions of alteration. Anomalous REE samples are those which appear to have elevated overall REE abundances as well as negative and positive Ce anomalies. The isotopic data from the anomalous REE samples were plotted along with isotopic data from the same samples after acid washing, as well as the “fresh” samples (Fig. 7.3). Sr isotopic ratios of acid-washed anomalous REE samples are lower, more uniform, and more similar to the “fresh” samples than their non-acid-washed equivalents, while ϵ_{Nd} values become slightly higher and remain consistent with the “fresh” samples. Pb isotopic ratios are nearly unchanged after acid washing (Fig. 7.4). Nevertheless, the isotopic ratios of the acid-washed samples are interpreted to be more correct, i.e., closer to magmatic values, than of their un-acid-washed equivalents.

Due to the low concentration of Sr in most samples collected from the Underdown Caldera complex, it is likely that the Sr isotopic ratios have been altered, resulting in the age corrections of some samples becoming over or under age corrected. Suspect Sr isotopic ratios were also investigated in silicic ignimbrites from Gran Canaria, Canary Islands where Rb and Sr were determined to be mobile elements during low temperature, post emplacement interactions with groundwater (Cousens et al., 1993). This mobilization of Rb and Sr resulted in inaccurate initial $^{87}Sr/^{86}Sr$ isotopic ratios. It is suspected that low temperature groundwater alteration is also causing the apparent unusual range in calculated initial Sr isotopic ratios in the Underdown Caldera complex

ignimbrites. Pb and Nd have much higher concentrations in the Underdown Caldera complex rocks and it is therefore much less likely that these isotopic ratios have been altered.

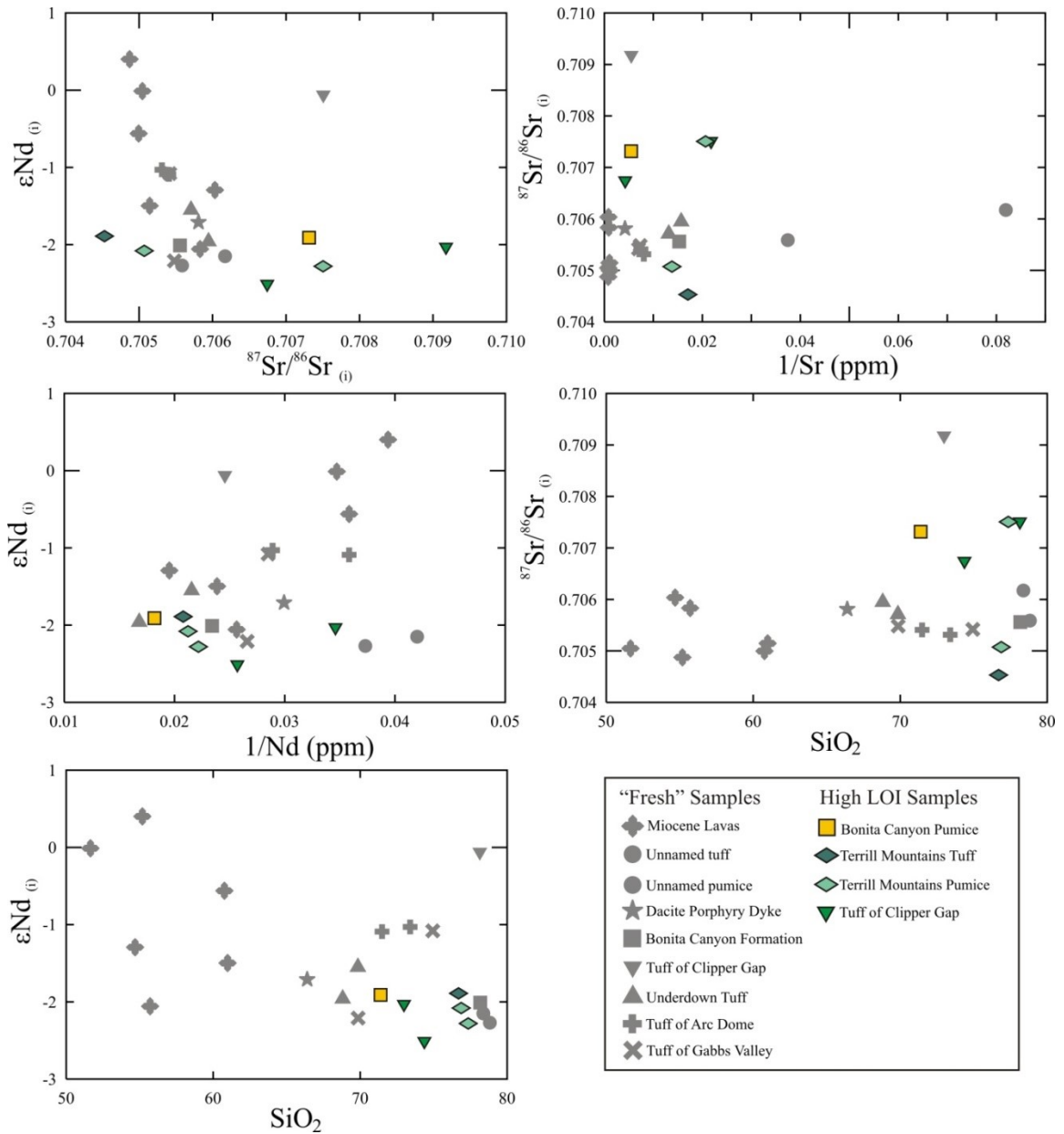


Figure 7.1: Initial Sr and Nd isotopic data showing the comparison between the high LOI samples and the “fresh” samples. High LOI samples show the most variance from “fresh” samples in their Sr isotopic data, while their ϵNd values remain similar to those of the “fresh” samples.

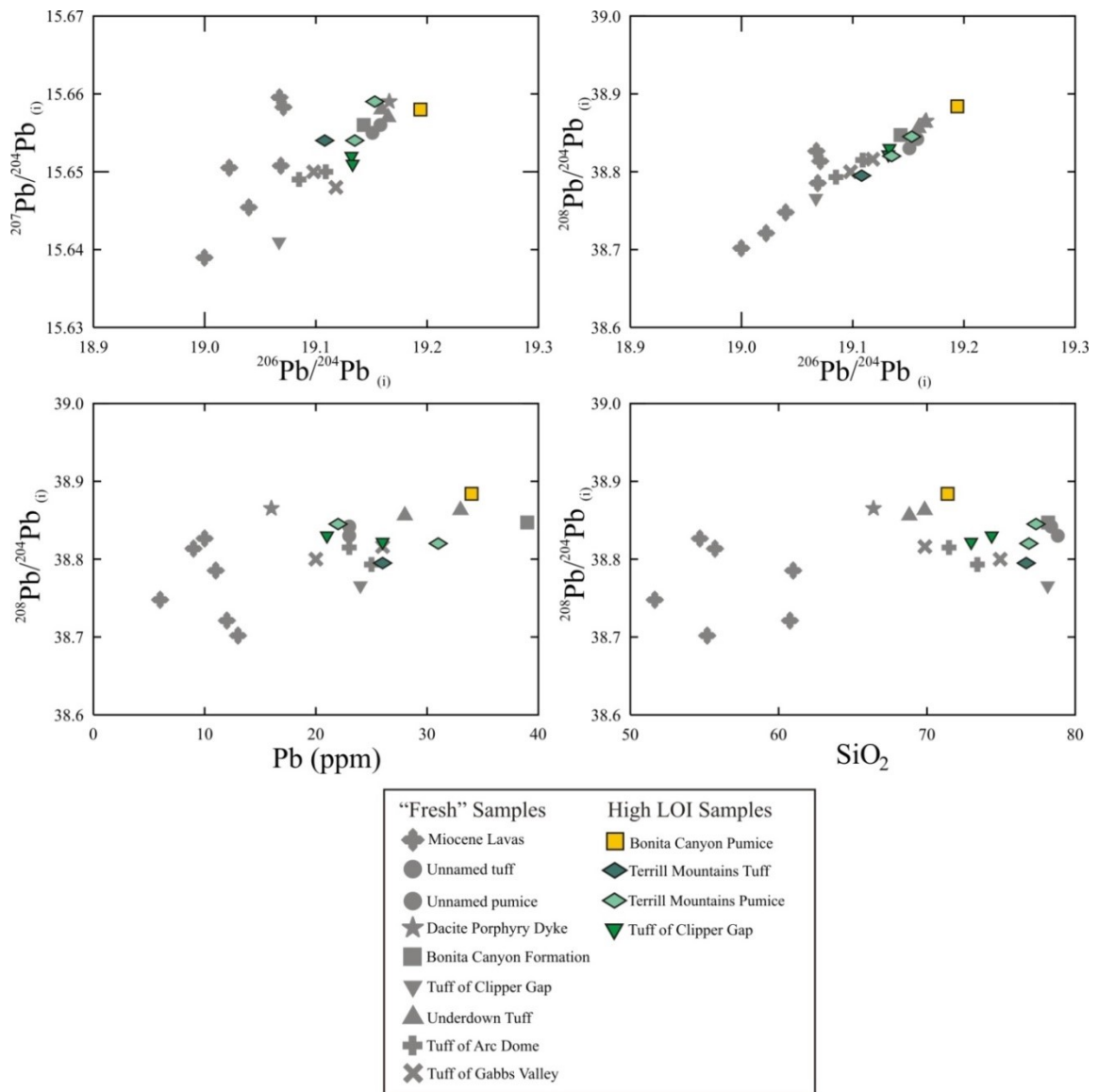


Figure 7.2: Initial Pb isotopic diagrams showing the comparison between the high LOI samples and the "fresh" samples. High LOI samples show very little difference in Pb isotopic data to the "fresh" samples, as the high LOI samples plot with the "fresh" samples in positive correlations in the $^{207}\text{Pb}/^{204}\text{Pb}$ vs. $^{206}\text{Pb}/^{204}\text{Pb}$ and $^{208}\text{Pb}/^{204}\text{Pb}$ vs. $^{206}\text{Pb}/^{204}\text{Pb}$ diagrams.

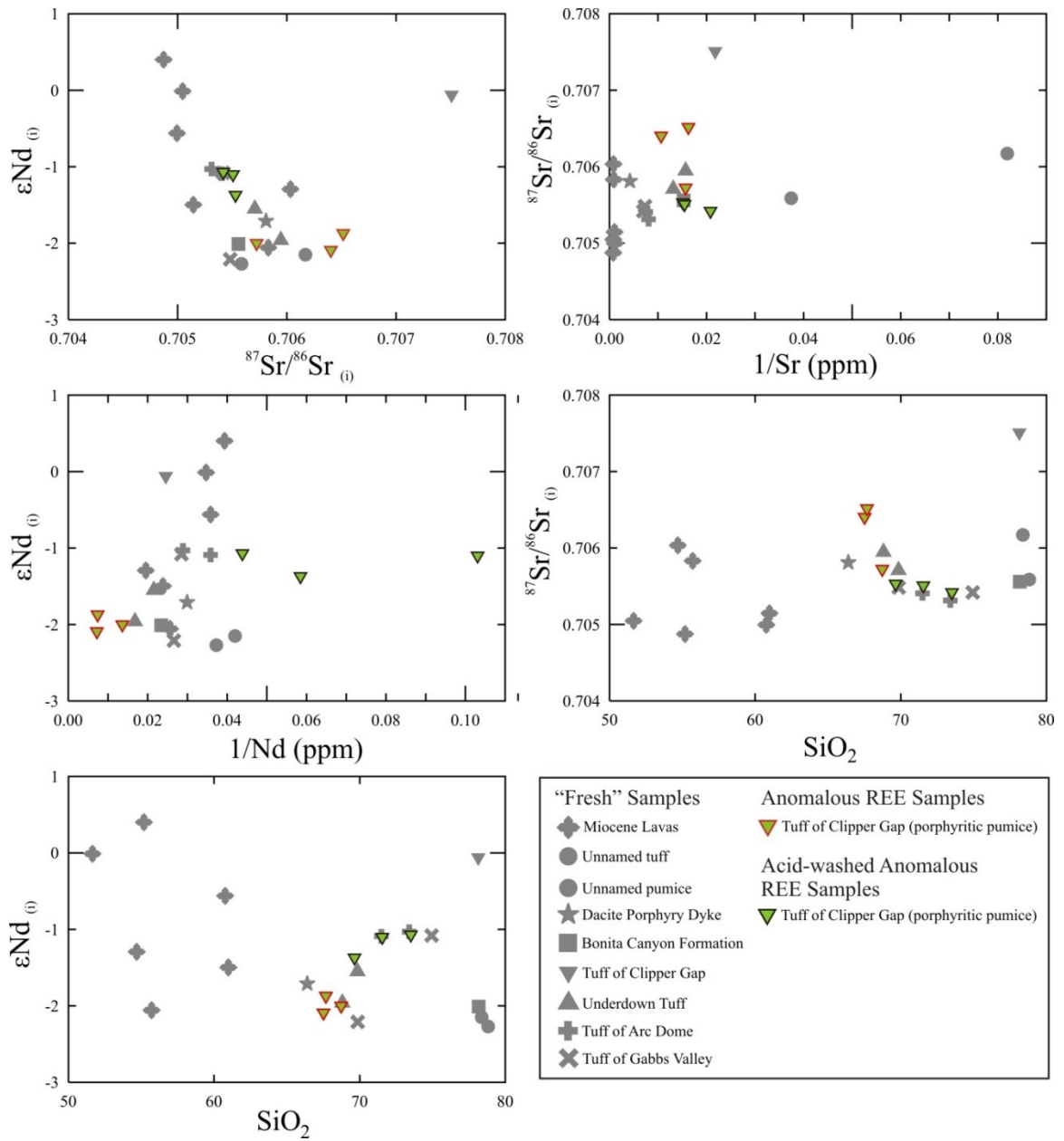


Figure 7.3: Initial Sr and Nd isotopic diagrams showing the comparison between the anomalous REE samples, their acid-washed equivalents, and the “fresh” samples. Sr isotopic ratios show less variation from the “fresh” samples than the high LOI samples, while their ϵNd values become less negative after acid washing.

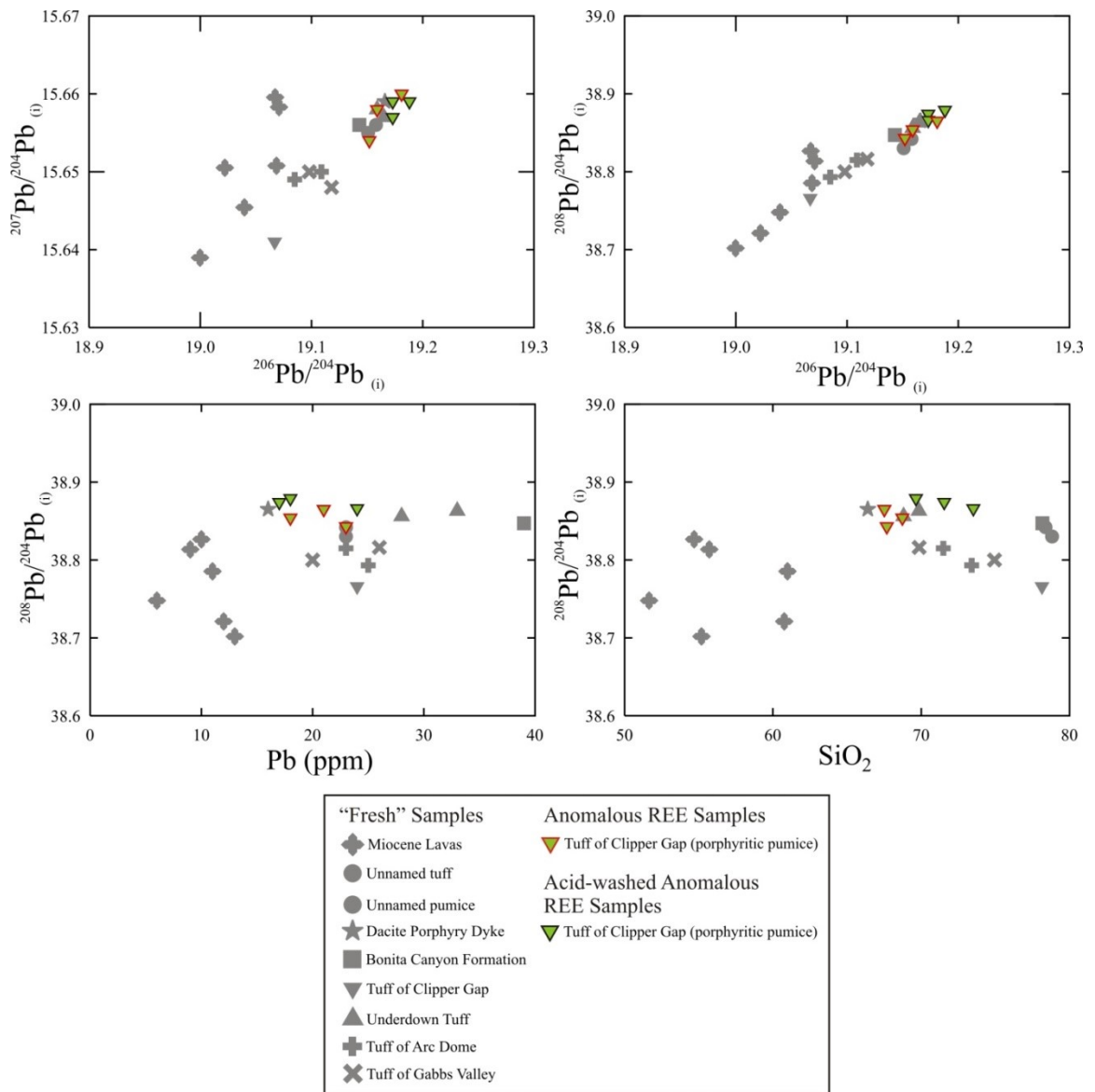


Figure 7.4: Initial Pb isotopic diagrams showing the comparison between the anomalous REE samples, their acid-washed equivalents, and the "fresh" samples. Pb isotopic ratios of the anomalous REE samples appear relatively unchanged after acid washing.

7.1.4 Potential sources of the Oligocene tuffs

The Oligocene tuffs most likely originate from a multi-component system. One component is suspected to have differentiated from a mantle derived melt, due to the similarity of the Sr and Nd isotopic compositions in the tuffs to those of the slightly younger Miocene mafic to intermediate lavas. Tennant (2018) proposed that the Miocene lavas originated from a subcontinental lithospheric mantle source, coupled with minor assimilation and/or contamination by the overlying Phanerozoic crust. Scattered relationships between isotopic ratios (Sr, Nd, and Pb) with SiO₂ content suggests that the mantle derived source was contaminated by a crustal component, as pure fractionation does not fractionate isotopes, and progressive assimilation of a crustal component would produce a tighter trend between the isotopic ratios and increasing SiO₂ content, as opposed to a scatter. During the Oligocene, the thick lithosphere of the Nevadaplano dominated what is now the Western Great Basin (Colgan and Henry, 2009). The exceptionally thick crust likely prevented most mantle derived melts from reaching the surface, causing them to pool in the crust. If the Oligocene tuffs were derived from a mostly mantle melt, pooling in a MASH (melting, assimilation, storage and homogenization) zone within the crust would allow ample opportunity for assimilation or contamination with the surrounding continental crust (Putirka and Busby, 2007).

The source of the Oligocene tuffs appears to originate from a shallower depth than the melt of the Miocene lavas which appear to originate from the garnet stability field (>80

km depth) (Winter, 2001). Primitive mantle normalized Gd/Yb represents the slope from the middle REEs to the heavy REEs, signifying the retention of heavy REEs in garnet during partial melting of the mantle. Whereas the Miocene lavas have a Gd/Yb ratio between 2 and 3, the Oligocene tuffs have a Gd/Yb ratio between 1 and 2, suggesting their source melt originates from a shallower depth (above the garnet-peridotite stability field) (Rollinson, 1993). However, the difference in Gd/Yb ratio between the two groups could also be a result of fractionation of middle to heavy REE-loving mineral phases from the melt. For example, allanite, apatite, amphibole, or zircon could be responsible for the shift in Gd/Yb ratios. Alternatively, the assimilation of a shallow crustal component containing no garnet into the melt could also be responsible for the shift in Gd/Yb ratios to lower values (Fig. 7.5).

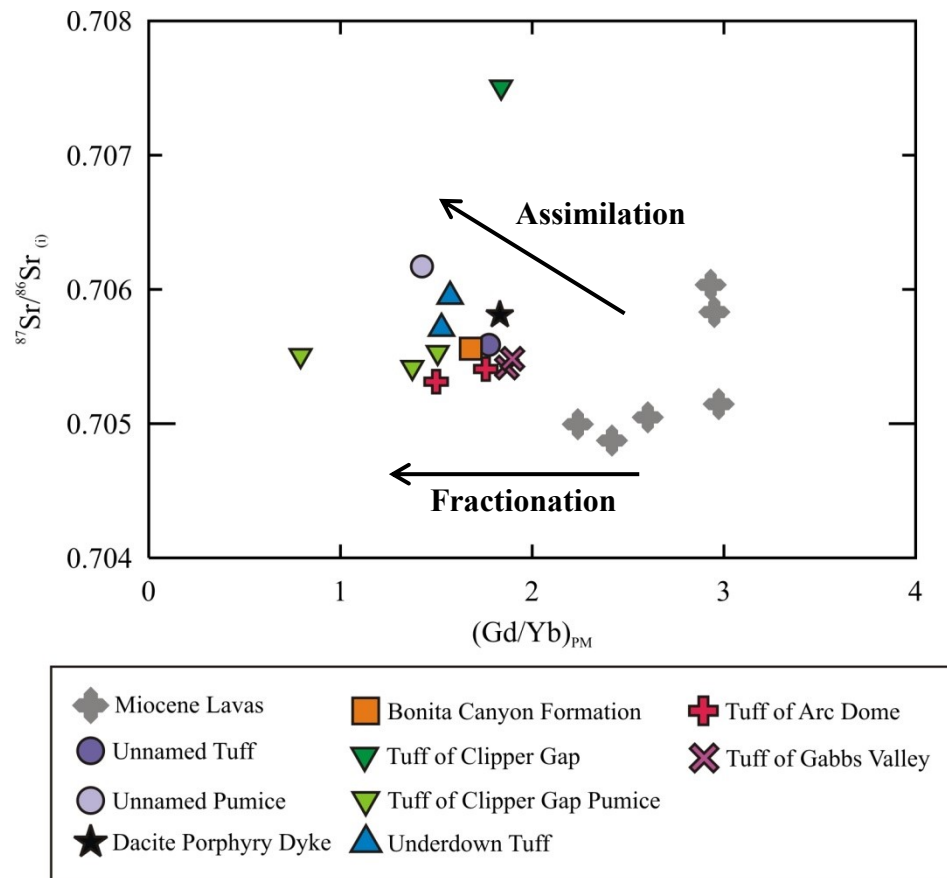


Figure 7.5: Age corrected $^{87}Sr/^{86}Sr$ vs. primitive mantle normalized Gd/Yb comparing the “fresh” Oligocene tuffs and the acid-washed tuff of Clipper Gap samples with the Miocene lavas. Gd/Yb is a slope estimate for the middle to heavy REEs which suggests a depth of melting of the source of mantle derived rocks. The Miocene lavas plot between a Gd/Yb ratio of 2-3, and the Oligocene tuffs mostly plot between a Gd/Yb ratio of 1-2. Fractionation of a middle to heavy REE-loving phase, or assimilation of a garnet-absent crustal rock into the melt could explain the shift in Gd/Yb observed from the Miocene lavas to the Oligocene tuffs.

The Miocene lavas were determined to be from two suites, a mildly alkaline suite and a sub-alkaline suite (Tennant, 2018). Miocene lavas with higher $^{87}\text{Sr}/^{86}\text{Sr}$ isotopic ratios (from the mildly alkaline suite) were interpreted to include more crustal components than those from the sub-alkaline suite which plot closer to the mantle array at lower $^{87}\text{Sr}/^{86}\text{Sr}$ ratios. The mildly alkaline samples have Sr isotopic ratios nearly identical to the Underdown Tuff and the dacite dyke (Fig. 7.6). In a plot of crustal addition (primitive mantle normalized Th/La vs. SiO_2), the Miocene lavas, “fresh” Oligocene tuffs, and acid-washed tuff samples exhibit an increase in Th/La with increasing SiO_2 content (Fig. 7.7). This suggests that as SiO_2 content increases, more Th-rich continental crust is added to the magmas. The dacite dyke sample has the lowest Th/La and has suffered the least amount of crustal assimilation out of the Underdown Caldera complex felsic samples. The Oligocene tuffs are mostly clustered in two groups; the first group between about 65-75 weight percent SiO_2 , and the second between about 75-79 weight percent SiO_2 . The Unnamed tuff samples which plot at much higher Th/La at similar SiO_2 content as the Bonita Canyon Formation and tuff of Clipper Gap are interpreted to have fractionated allanite, thus increasing the Th/La ratio (based on the Th and La concentration measured in allanite by Mahood and Hildreth (1983)). A similar fractionation trend was observed in the Caetano and Fish Creek Mountains Tuffs (Cousens et al., 2019). Based on Figure 7.7, the most assimilation of crustal material appears to occur between the high silica dacites and the low silica rhyolites.

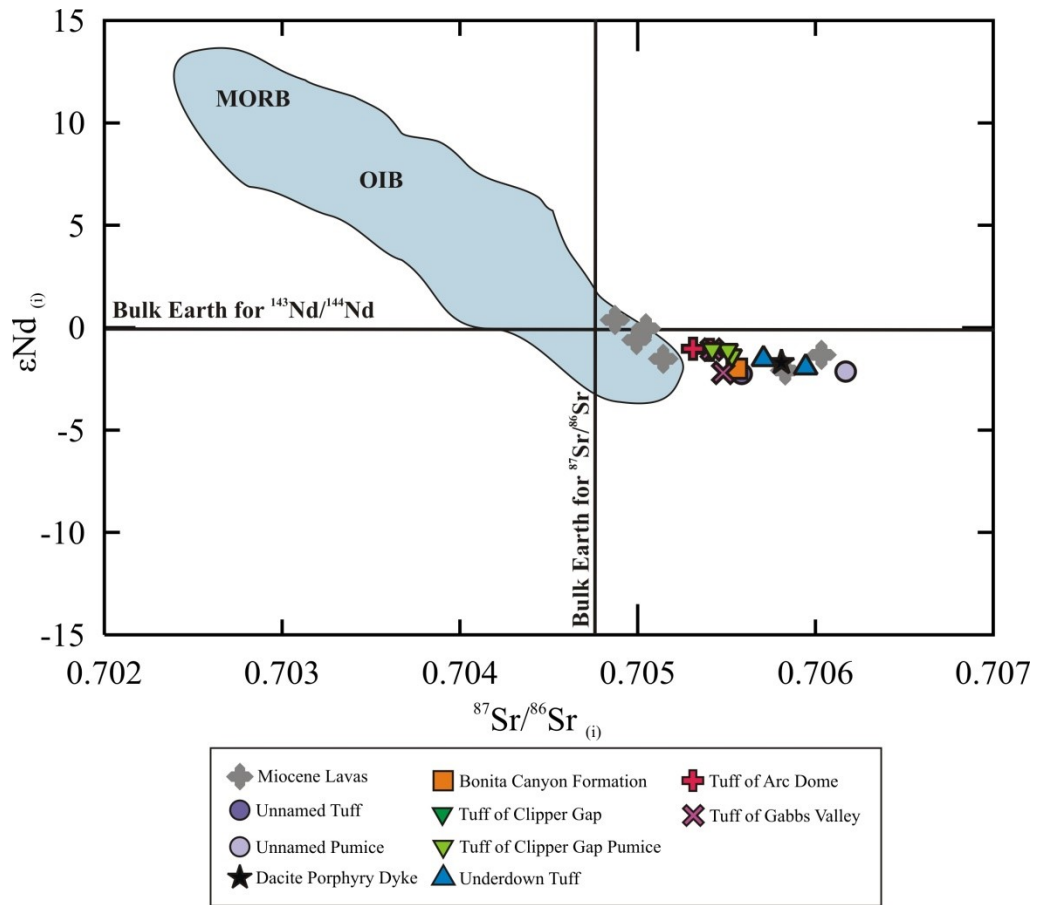


Figure 7.6: ϵNd vs. $^{87}Sr/^{86}Sr$ after Allègre (2008) showing the “fresh” samples, acid-washed tuff of Clipper Gap samples, and Miocene lavas. Miocene lavas from the subalkaline suite plot with the mantle array, while two samples from the mildly alkaline suite have higher $^{87}Sr/^{86}Sr$ ratios that are nearly identical to the dacite dyke and Underdown Tuff.

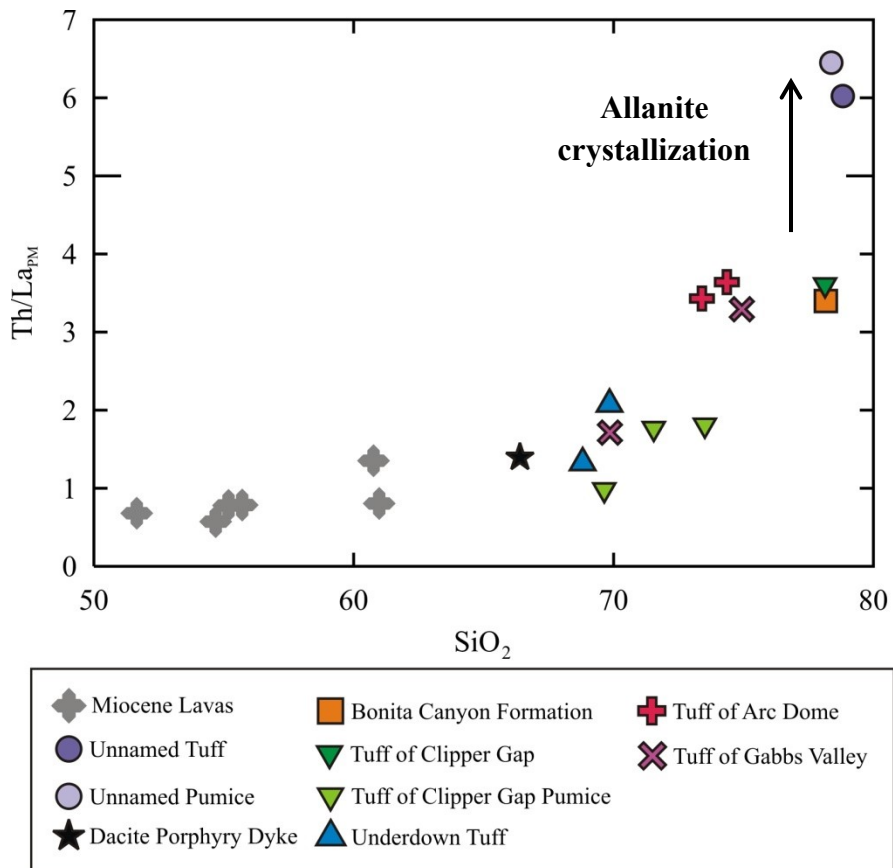


Figure 7.7: Primitive mantle normalized (Sun and McDonough, 1989) Th/La versus SiO₂ content of the “fresh” Oligocene tuffs, acid-washed tuff of Clipper Gap samples, and Miocene lavas showing potential crustal addition with increasing magma evolution. The Miocene lavas and Oligocene tuffs show a positive correlation between Th/La and SiO₂ content. The plot suggests that the Oligocene tuffs have assimilated more crustal material than the andesitic Miocene lavas. Unnamed tuff samples are interpreted to have fractionated allanite, resulting in much higher Th/La ratios.

Pb isotope diagrams also suggest crustal addition to the Underdown magmas. On a $^{207}\text{Pb}/^{204}\text{Pb}$ versus $^{206}\text{Pb}/^{204}\text{Pb}$ diagram (modified after Allègre, 2008), the Miocene lavas and Oligocene tuffs fall on the overlap between continental granites and oceanic basalts (Fig. 7.8). Both the Miocene lavas and the Oligocene tuffs plot above the Northern Hemisphere Reference Line (NHRL), a best-fit line through modern oceanic basalts from the Northern Hemisphere, indicating they do not originate from an asthenospheric source (Hart, 1984). Based on the presented geochemical data and the observed relationship between the Miocene lavas and the Oligocene tuffs, it is postulated that the lavas found around the margin of the caldera may represent a potential parental magma of the Oligocene tuffs. This would require the melting of isotopically-similar lithospheric mantle at the time of both magmatic events.

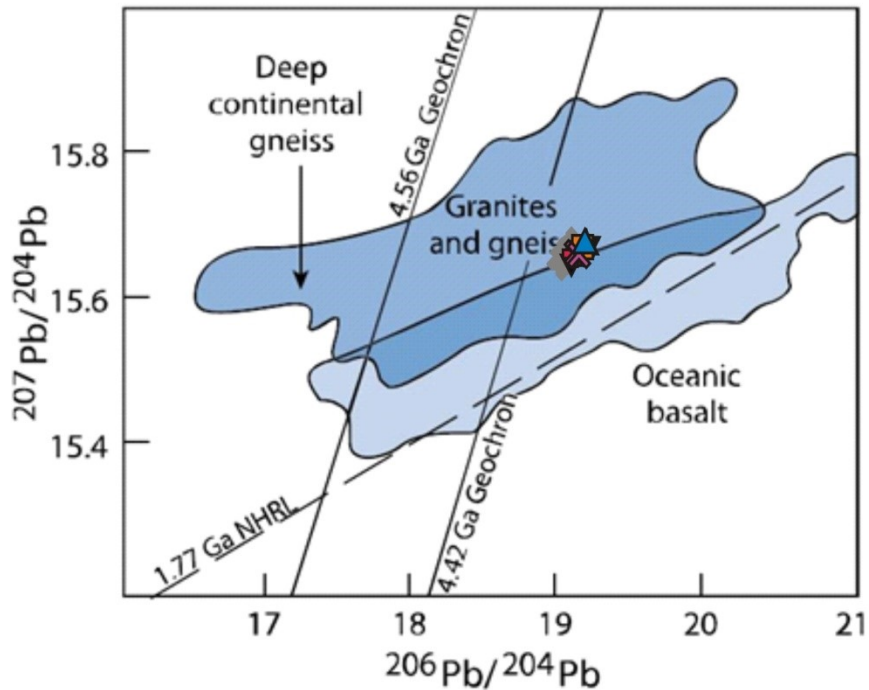


Figure 7.8: Initial $^{207}\text{Pb}/^{204}\text{Pb}$ versus $^{206}\text{Pb}/^{204}\text{Pb}$ diagram modified after Allègre (2008). The Oligocene tuffs from the Underdown Caldera complex and the Miocene lavas plot on an overlap zone between continental rocks and oceanic basalt, above the Northern Hemisphere Reference Line (Hart, 1984).

Due to suspect Sr isotopic ratios, Pb isotopes were used to model potential mixing lines for the Underdown Caldera complex ignimbrites. The primitive end-member used in the mixing line is a sample of the Miocene lavas from the caldera margin (17-SML-11) and will be referred to as the mantle derived magma. Exhaustive options for a crustal source included the upper, middle, lower, and average continental crust (Rudnick and Fountain, 1995), granitic basement from the Stillwater range (Stepner, 2017), and the Carico Lake Pluton (Watts et al., 2016). The two “crustal melt” end-members which fit the mixing line relatively well were (A) an average of Paleozoic sedimentary rocks from the Stillwater Range and Clan Alpine Mountains northwest of the Underdown region

(Stepner, 2017), and (B) a late Eocene pluton from the Northern Shoshone Range (Cousens et al., 2019). The average sedimentary samples include shale, calcareous shale, and limestone. While the mixing line utilizing the average sedimentary “crustal melt” end-member is not a perfect match to the Underdown Caldera complex ignimbrites, it suggests that the Oligocene tuffs may originate from a mix of a mafic component from the mantle beneath the caldera and a local sedimentary unit (Fig. 7.9). However, it appears as though the ignimbrites are closer in composition to the mantle-derived magma. The individual sedimentary samples used for the “crustal melt” end-member average (also plotted on the mixing line diagram) show how the Pb isotopic data varies between the sedimentary samples, and suggests that any combination of local sedimentary sources could be responsible for the crustal component in the melt. On the mixing line using the late Eocene pluton as the “crustal melt”, the samples plot in two groups; one group between 60-70% mantle component, and a second larger group between 30-40% mantle component (Fig. 7.10). Based on the proposed mixing lines and isotopic similarities to the Miocene lavas, it is possible that the Underdown Caldera ignimbrites originated from a mantle derived source beneath the caldera, and are not the product of a purely crustal melt. Mixing lines suggest that the source of the Oligocene tuffs may be a mixture between a mantle source (similar to that of the Miocene lavas) and either a local sedimentary unit, or a local granitoid.

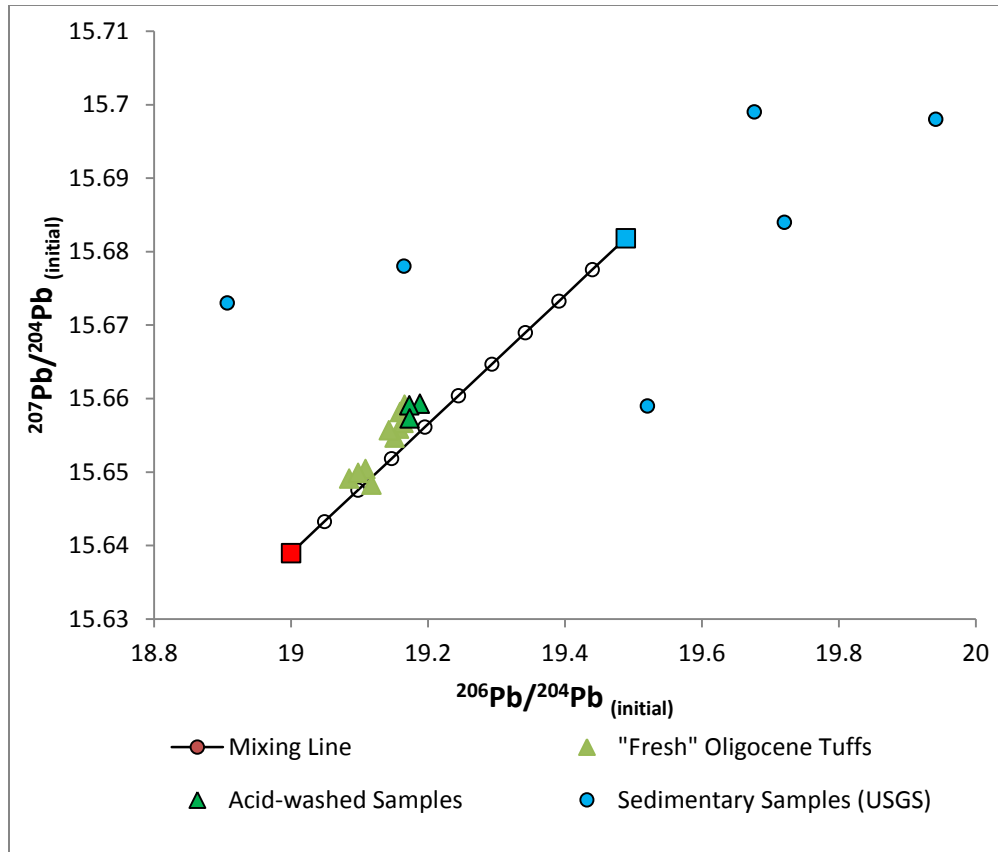


Figure 7.9: Initial $^{207}\text{Pb}/^{204}\text{Pb}$ vs. $^{206}\text{Pb}/^{204}\text{Pb}$ for the Underdown Caldera ignimbrites compared to mixing between a Miocene lava (red square) (17-SML-11) and an average of selected Paleozoic sedimentary rocks (blue square) (Stepner, 2017). The individual sedimentary rocks which make up the average sedimentary composition are plotted to show the variance in Pb isotopic data for the sedimentary samples. Each open circle represents 10% increments of mixing. The mixing line represents purely binary mixing between the “mantle derived magma” and “crustal melt” and is one of the best obtained mixing lines with available data. The ignimbrites appear to be closer in composition to the mantle derived magma end-member.

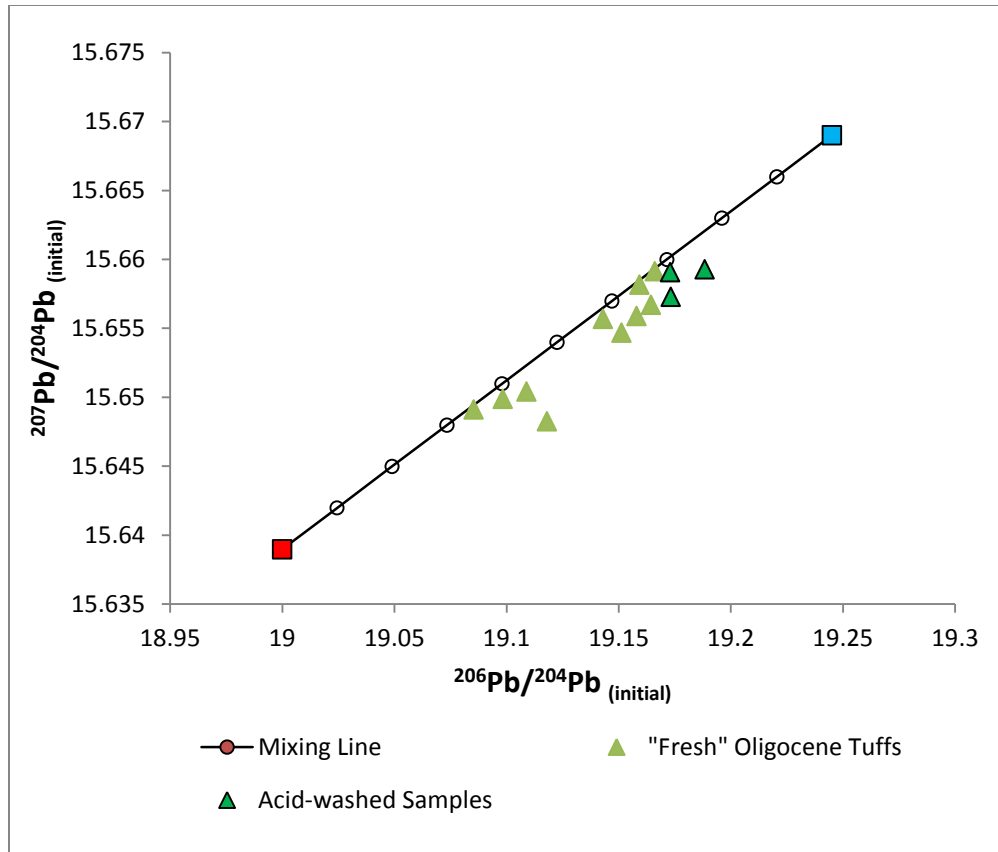


Figure 7.10: Initial $^{207}\text{Pb}/^{204}\text{Pb}$ vs. $^{206}\text{Pb}/^{204}\text{Pb}$ for the Underdown Caldera ignimbrites compared to mixing between a Miocene lava (red square) (17-SML-11) and a late Eocene pluton from the Northern Shoshone Range (blue square) (Cousens et al., 2019). Each open circle represents 10% increments of mixing. The mixing line represents purely binary mixing between the “mantle derived magma” and “crustal melt” and is the best obtained mixing line with available granitoid data. The Oligocene tuffs are assumed to originate from a melt which mixes material from a mantle derived source beneath the caldera and a local crustal unit. The ignimbrites plot in two groups along the mixing line. The first group plots between approximately 60-70% mantle component, and the second group plots between approximately 30-40% mantle component.

7.1.5 Relationship of the Underdown Tuff, tuff of Clipper Gap, and Bonita Canyon Formation

While it has been suggested that, based on its sedimentary textures, the Bonita Canyon Formation may be a reworked unit of the upper Underdown Tuff, isotopic results as well as the Th/La vs. SiO₂ plot showing potential crustal addition (Fig. 7.7) suggest that the Bonita Canyon Formation and the Underdown Tuff are separate, related units. If the Bonita Canyon Formation was composed of reworked Underdown Tuff, the isotopic results between the two units would be identical which is not observed. Sr isotopic analysis of the Bonita Canyon pumice was affected by high LOI; however, as observed in Figures 7.1 and 7.2, the Bonita Canyon pumice appears more similar to the Underdown Tuff than the Bonita Canyon whole rock sample in the Nd and Pb isotopic systems. Based on the major element, trace element, and isotopic data of “fresh” samples, the Underdown Tuff and the Bonita Canyon Formation appear to be distinct units, however, new isotopic analyses of acid-washed Bonita Canyon pumice could provide a stronger comparison.

The tuff of Clipper Gap is interpreted to be related to the Underdown Tuff phase of volcanism in the Underdown Caldera Complex. The isotopic values of the Underdown Tuff, Bonita Canyon Formation, and the acid-washed tuff of Clipper Gap appear similar in most isotopic comparisons. However, the acid-washed tuff of Clipper Gap samples are more similar to the Underdown Tuff than the Bonita Canyon Formation. These isotopic similarities, as well as the unique presence of porphyritic pumice in the Underdown Tuff

and tuff of Clipper Gap which is not observed in the Bonita Canyon Formation, supports the hypothesis that the tuff of Clipper Gap is correlative outflow of the Underdown Tuff.

7.1.6 Identity of the Unnamed tuff

The 24.755 ± 0.037 Ma Unnamed tuff (Henry, pers. comm., 2018), which as previously stated was mapped as the Tuff of Toiyabe by Bonham (1970), was compared to the true Tuff of Toiyabe with geochemical data from John (1974). A published age of the Tuff of Toiyabe is 23.31 ± 0.05 Ma (Henry and John, 2013), making the Tuff of Toiyabe notably younger than the Unnamed tuff from the Underdown Caldera complex.

While the samples from the Unnamed tuff and true Tuff of Toiyabe have similar petrographic descriptions (densely welded, phenocryst rich, phenocryst assemblage of plagioclase, sanidine, quartz and minor biotite and hornblende), and are both rhyolitic (Le Maitre et al., 1989), the Unnamed tuff has a higher SiO_2 content than the Tuff of Toiyabe (Fig. 7.11). While major element bivariate plots show that the Tuff of Toiyabe and Unnamed tuff generally plot on the same trends between major element oxides and increasing SiO_2 content, nearly all ignimbrites in the WNVF show these fractionation trends (Fig. 7.12) (Henry and John, 2013). The Tuff of Toiyabe also appears to show more compositional variation than the Unnamed tuff which generally appears relatively homogeneous.

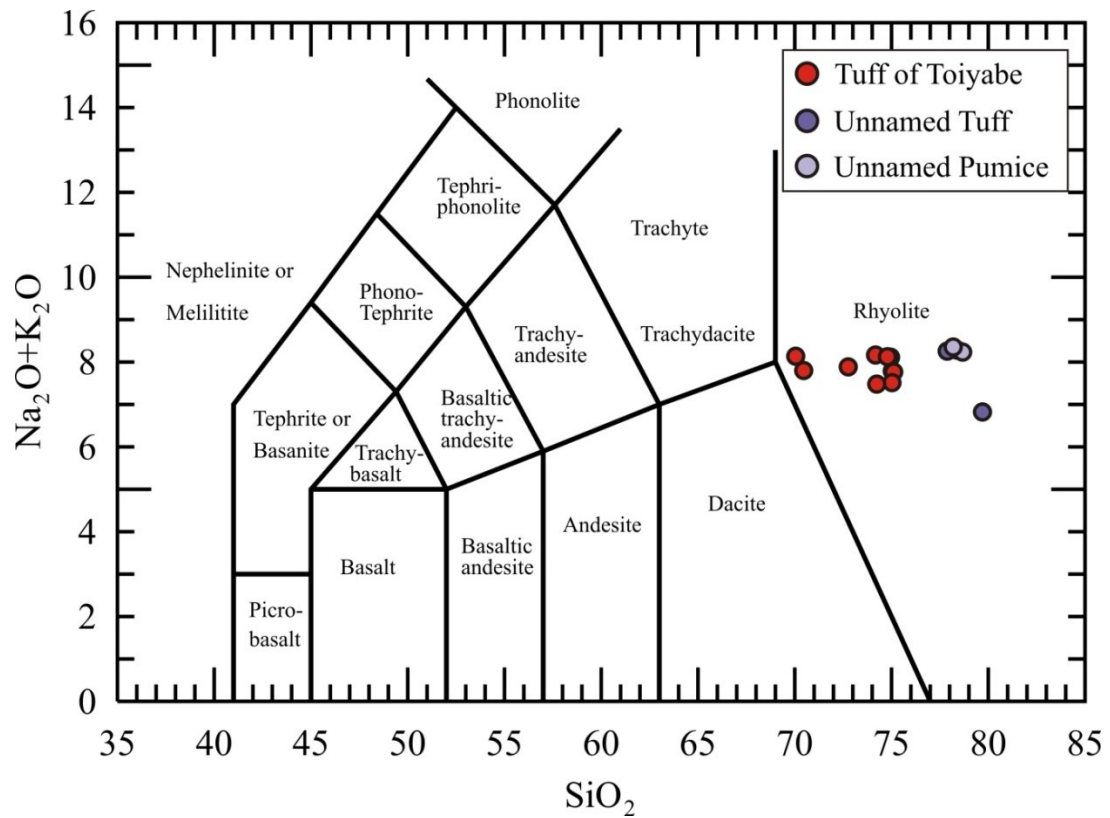


Figure 7.11: Total alkalis-silica diagram (Le Maitre et al., 1989) of the Unnamed tuff and the Tuff of Toiyabe (with data from John, 1974). Both groups of samples plot in the rhyolite field, however the Unnamed tuffs have higher SiO_2 contents than the Tuff of Toiyabe.

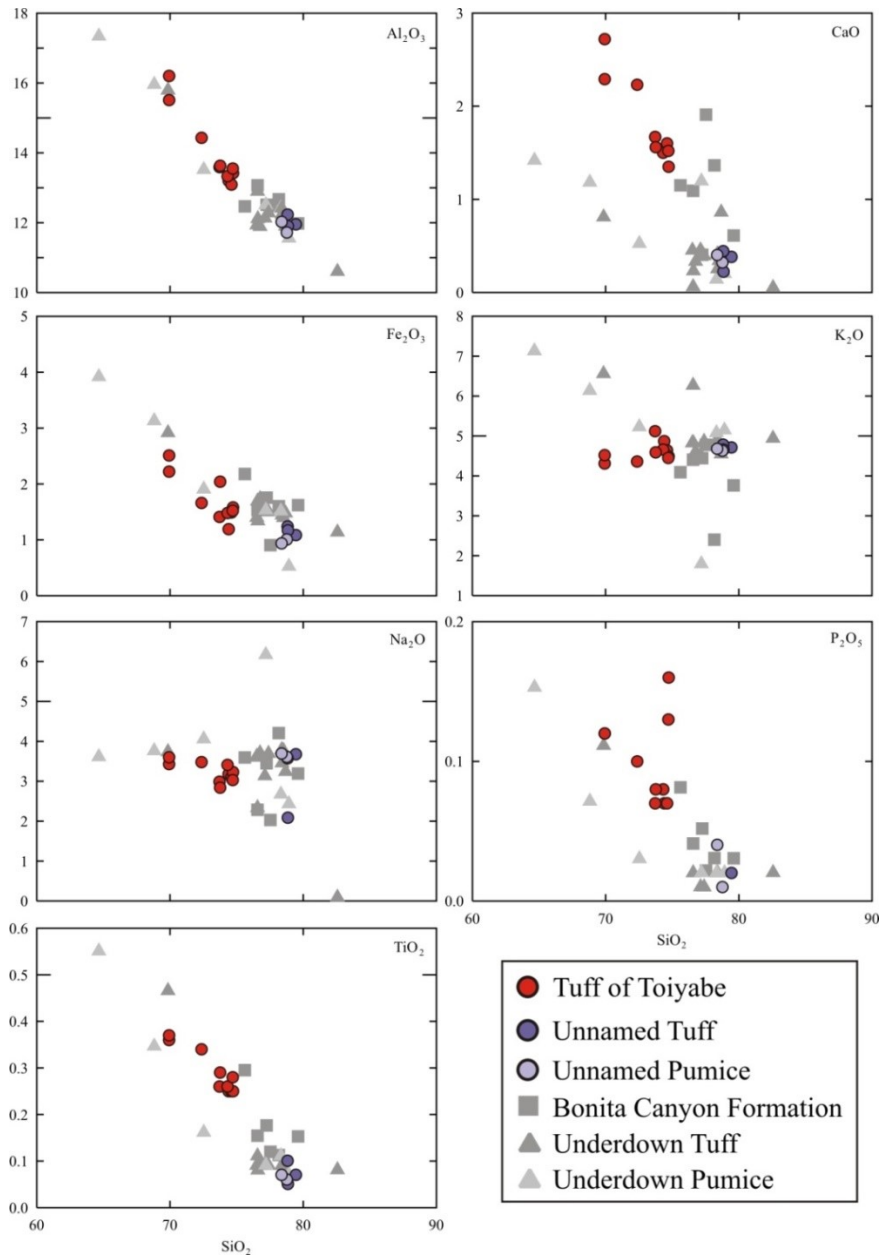


Figure 7.12: Major element variation diagrams comparing the Unnamed tuff with the Tuff of Toiyabe (with data from John, 1974), as well as the Underdown Tuff and Bonita Canyon Formation for reference. The Unnamed tuff and Tuff of Toiyabe plot in similar fractionation trends in all major element oxides, however these trends are similar for most ignimbrites in the Western Nevada Volcanic Field (Henry and John, 2013), as well as in the Underdown Tuff and Bonita Canyon Formation. The Tuff of Toiyabe appears to show more compositional variation than the Unnamed tuff in most major element oxides.

Trace element data from the Unnamed tuff shows some similarities to the Tuff of Toiyabe. Only Ba, Ce, La, Nb, Sr, Y, and Zr trace element values were published for the Tuff of Toiyabe (John, 1974) as data collection was completed using XRF (x-ray fluorescence), therefore trace element variation diagrams were made based on those elements (Fig. 7.13). With increasing SiO₂ content, Ba and Sr decrease, Nb increases, and Ce, La, Sr, Y, and Zr show a combination of scattering and clustering. For trace elements that show a trend with SiO₂, the Unnamed tuff does show trends in common with the Tuff of Toiyabe. However, due to the difference in SiO₂ content, compositional gaps exist between the two units. As observed in the major element bivariate diagrams, the Tuff of Toiyabe appears to show more compositional variation than the Unnamed tuff in Ba and Sr.

Averages of the Unnamed tuff, Unnamed tuff pumice and Tuff of Toiyabe were plotted on a primitive mantle normalized trace element diagram along with the average Underdown Tuff for comparison, with primitive mantle data from Sun and McDonough (1989) (Fig. 7.14). The primitive mantle normalized pattern of the Unnamed tuff shows more similarity to the average Underdown Tuff than the average Tuff of Toiyabe. In particular, the Tuff of Toiyabe lacks characteristic negative anomalies in Ba and Sr that are observed in all of the Underdown Caldera ignimbrites. The Unnamed tuff also has a more similar Nb concentration to the Underdown Tuff which is characteristically high in the Underdown Tuff and tuff of Clipper Gap compared to most Great Basin ignimbrite units (> 20 ppm; Henry and John, 2013).

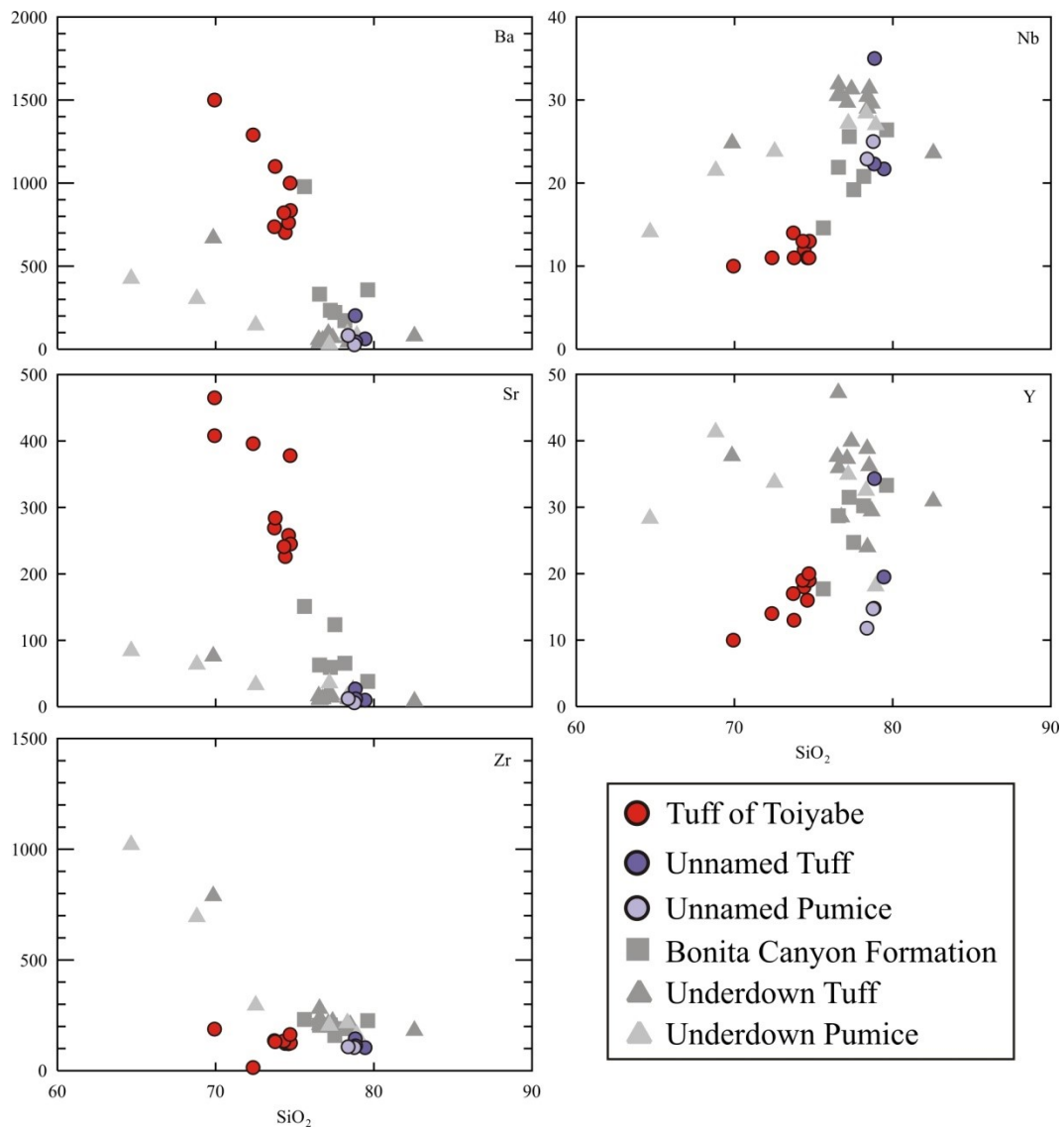


Figure 7.13: Trace element variation diagrams comparing the Unnamed tuff with the Tuff of Toiyabe (with data from John, 1974), as well as the Underdown Tuff and Bonita Canyon Formation for reference. The Unnamed tuff could plot on a fractionation trend with the Tuff of Toiyabe in Ba and Sr, but appears to plot differently in all other trace elements. The Tuff of Toiyabe shows more compositional variation in Ba and Sr.

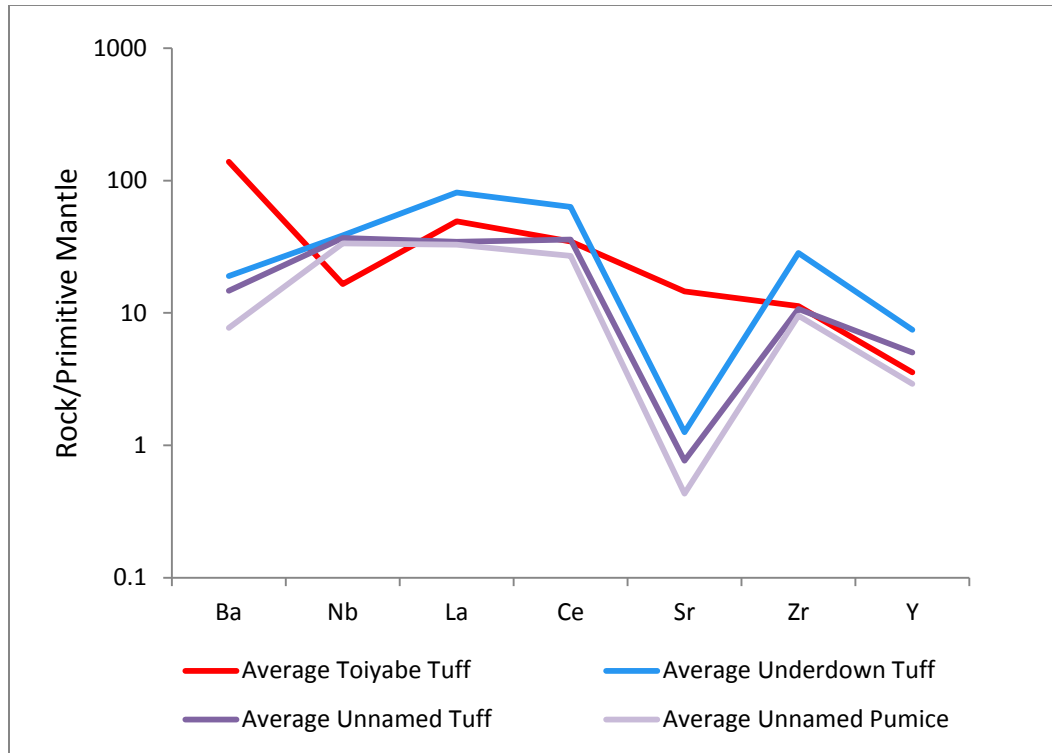


Figure 7.14: Primitive mantle normalized trace element diagram (Sun and McDonough, 1989) of the average trace element concentrations of the Tuff of Toiyabe, Unnamed tuff, Unnamed pumice, and Underdown Tuff, using a limited amount of trace element data available from John (1974). The Unnamed tuff and pumice show more similarity to the Underdown Tuff than the Tuff of Toiyabe. The average Tuff of Toiyabe lacks characteristic negative Ba and Sr anomalies in the Unnamed tuff and Underdown Tuff, and contains less Nb.

Strontium isotope data for the Tuff of Toiyabe were plotted with the “fresh” ignimbrites from the Underdown Caldera complex as well as acid-washed tuff of Clipper Gap samples and the Miocene lavas (Fig. 7.15). Only Sr isotope data were available from John (1974), therefore the data were plotted in initial $^{87}\text{Sr}/^{86}\text{Sr}$ versus $1/\text{Sr}$ concentration and initial $^{87}\text{Sr}/^{86}\text{Sr}$ versus SiO_2 content comparisons. In both diagrams, the Tuff of Toiyabe and the Unnamed tuff appear to be distinct however, both overlap the Underdown Caldera ignimbrites in when comparing $^{87}\text{Sr}/^{86}\text{Sr}$ versus SiO_2 content. Due to very low Sr concentration for the Unnamed Tuff, the isotope comparison is likely inconclusive.

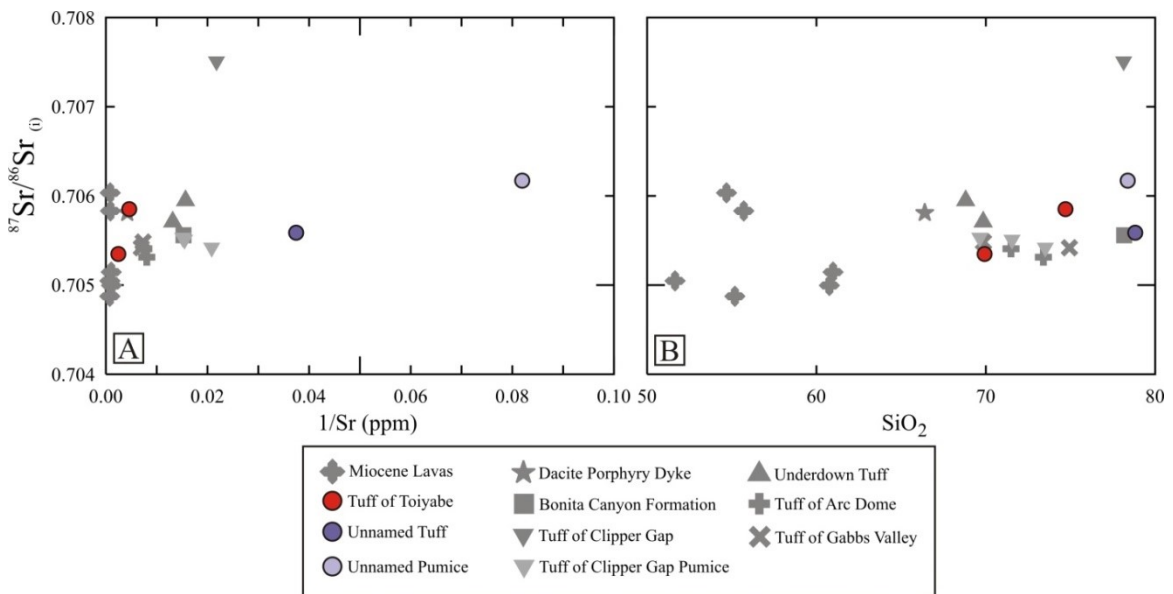


Figure 7.15: Initial $^{87}\text{Sr}/^{86}\text{Sr}$ versus $1/\text{Sr}$ concentration (A) and SiO_2 content (B) showing the Sr isotope data for the Tuff of Toiyabe and Unnamed tuff (with isotope data from John, 1974). The “fresh” ignimbrites have also been plotted along with acid-washed tuff of Clipper Gap samples and the Miocene lavas. The Sr isotopic ratios of the Unnamed Tuff do not overlap with the Tuff of Toiyabe, and appear more similar to the Bonita Canyon Formation in panel (B). However, the Unnamed tuff suffers from low Sr concentration, therefore the Sr isotopic ratios may be questionable.

Based on the differences in geochemistry, as well as the notable age difference, and the opposite paleomagnetic polarity of the Unnamed tuff to the Tuff of Toiyabe (Best et al., 2013), the Unnamed tuff is likely a distinct ash flow tuff unit of the Underdown Caldera as opposed to a unit from the Tuff of Toiyabe. While the degree of welding and the mineral assemblage of the Unnamed tuff does bear similarities to what is described in the Tuff of Toiyabe, the units are most likely two different ash flow tuff units in the WNVF.

7.2 Cerium Anomalies in the tuff of Clipper Gap

In earlier sections, samples from the tuff of Clipper Gap that have a negative or positive Ce anomaly were removed from the dataset. This section will investigate these samples and the potential cause of the Ce anomaly. Most samples that contain a Ce anomaly are from the Tuff of Clipper Gap, however, there is one sample of the tuff of Brunton Pass which also shows a negative Ce anomaly. This section will focus on samples from the Tuff of Clipper Gap as they provide a closely comparable suite of samples to study. Rock samples with Ce anomalies are termed “anomalous REE samples”, and include whole rock and porphyritic pumice samples.

7.2.1 REE chemistry of the anomalous samples

As the REEs in the anomalous samples are what make them questionable, they will be discussed first. In a chondrite normalized rare earth element plot, the anomalous REE samples show more enrichment in the LREEs relative to the HREEs than was observed in the average non-anomalous whole rock sample (Fig. 7.16A). The patterns show negative Ce anomalies in most samples, a positive Ce anomaly in one sample, and large negative Eu anomalies in all samples. Most anomalous REE porphyritic pumice samples are more enriched in LREEs than the anomalous REE whole rock samples (except one porphyritic pumice), and show a steeper slope to the HREEs than the anomalous REE whole rock and other anomalous REE porphyritic pumice sample which show flattened patterns. In an extended primitive mantle normalized trace element plot, the samples are enriched in LILEs, show large negative anomalies in Ba and Sr, and large positive anomalies in La

and Pb (Fig. 7.16B). Differences in Nb-Ta anomalies exist between the anomalous REE porphyritic pumice, anomalous REE whole rock samples, and the average non-anomalous whole rock sample.

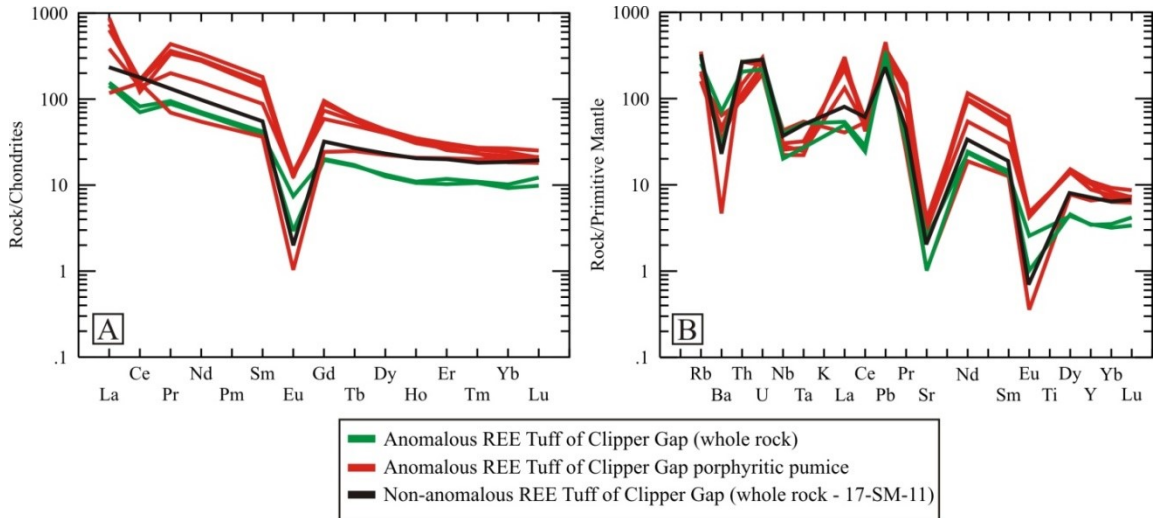


Figure 7.16: (A) Chondrite normalized rare earth element diagram for the anomalous REE samples. Either a positive or negative Ce anomaly can be seen in the whole rock and porphyritic pumice samples, as well as the typical Eu anomaly observed in the non-anomalous tuff of Clipper Gap samples. The porphyritic pumice samples with negative Ce anomalies appear to be more enriched in most REEs than the whole rock samples and porphyritic pumice sample with a positive Ce anomaly. (B) Primitive mantle normalized trace element diagram. Porphyritic pumice samples with negative Ce anomalies have much higher La concentrations than the whole rock samples and porphyritic pumice sample with a positive Ce anomaly. In both diagrams, a non-anomalous REE sample is plotted for comparison (chondrite and primitive mantle normalizing values from Sun and McDonough, 1989).

7.2.2 Major element geochemistry of the anomalous samples

In a TAS diagram, the anomalous REE samples plot in two groups in the rhyolite and trachyte fields (Fig. 7.17, Le Maitre et al., 1989). The porphyritic pumice samples with negative Ce anomalies plot in the trachyte field. The whole rock samples and porphyritic pumice sample with a positive Ce anomaly plot in the rhyolite field at higher SiO₂ and lower alkali contents than the porphyritic pumice in the trachyte field.

Major element oxides of the anomalous REE samples were plotted in comparison to the non-anomalous Underdown Tuff and tuff of Clipper Gap samples (Fig. 7.18). While the anomalous REE whole rock samples and rhyolitic anomalous REE porphyritic pumice plot with the cluster of non-anomalous whole rock samples from the Underdown Tuff and tuff of Clipper Gap, the rest of the anomalous REE porphyritic pumice generally plot with the non-anomalous Underdown pumice samples (specifically, Underdown porphyritic pumice). The anomalous porphyritic pumice samples with negative Ce anomalies plot as a cluster, except for in Al₂O₃, Fe₂O₃, and P₂O₅ where more scatter is observed.

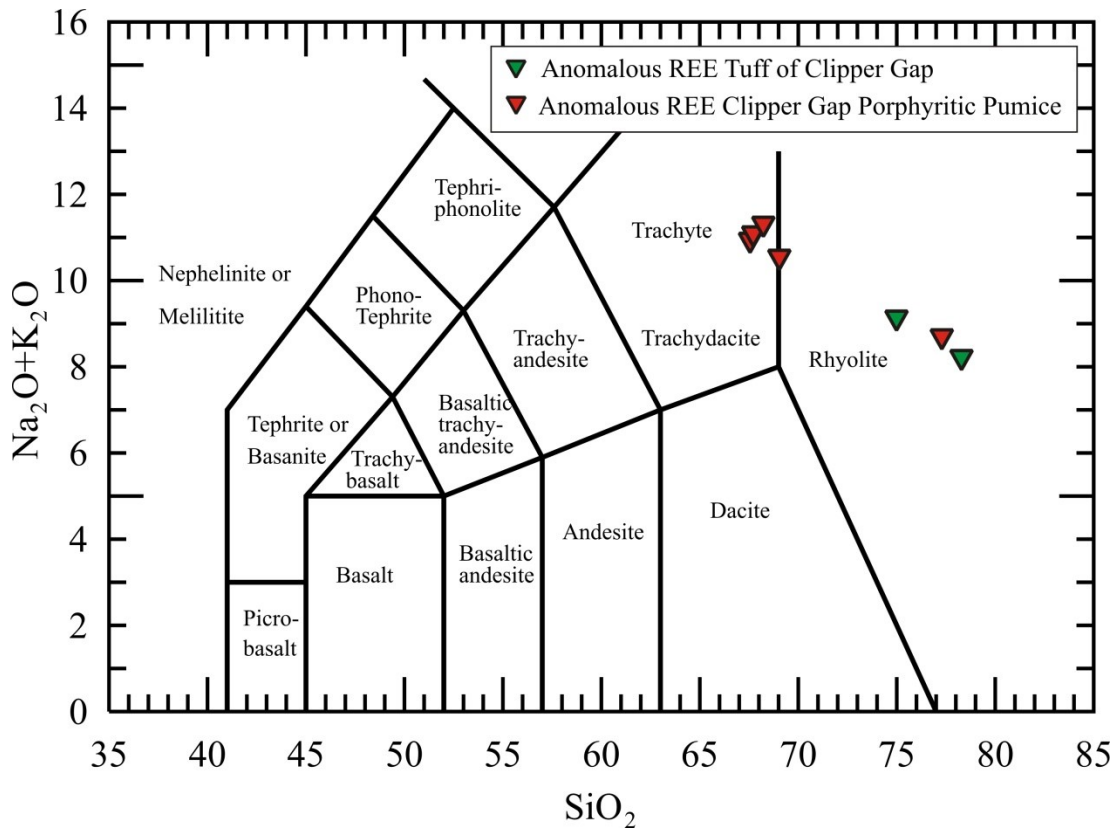


Figure 7.17: Total alkalis-silica diagram (Le Maitre et al., 1989) of the anomalous-REE samples from the Tuff of Clipper Gap shows the samples plotting in two groups in the rhyolite and trachyte fields, with the whole rock samples plotting exclusively in the rhyolite field and the porphyritic pumice samples plotting in both the trachyte and rhyolite fields. One sample of porphyritic pumice (with a positive Ce anomaly) plots in the rhyolite field with the whole rock samples while the rest of the porphyritic pumice samples (with negative Ce anomalies) plot exclusively in the trachyte field.

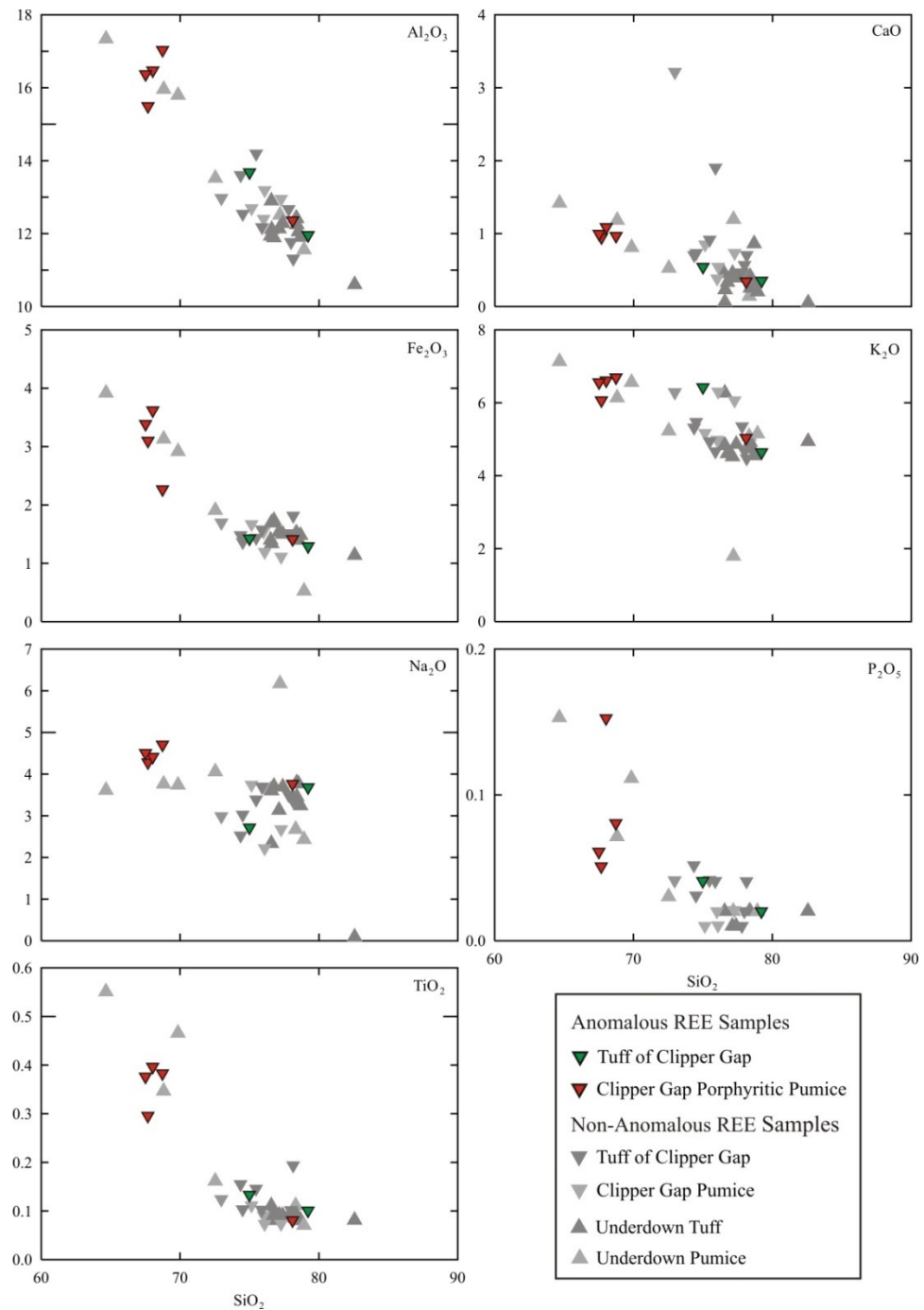


Figure 7.18: Major element oxides plotted versus SiO₂ show that the trachyte samples plot as a cluster in half of the comparisons (CaO, K₂O, and Na₂O) and a scatter in the other half (Al₂O₃, Fe₂O₃, P₂O₅, and TiO₂). The rhyolitic porphyritic pumice sample which plots more similarly to the anomalous REE whole rock samples contains a positive Ce anomaly.

7.2.3 Trace element geochemistry of the anomalous samples

The anomalous REE samples of the tuff of Clipper Gap were plotted in comparison to the Underdown Tuff and non-anomalous tuff of Clipper Gap samples on trace element bivariate diagrams versus SiO_2 . Similar to the major element oxide bivariate diagrams, the anomalous REE porphyritic pumice samples plot close to the Underdown Tuff porphyritic pumice and the anomalous REE whole rock samples and anomalous REE rhyolitic porphyritic pumice sample plot with the cluster of Underdown Tuff and tuff of Clipper Gap whole rock data (Fig. 7.19).

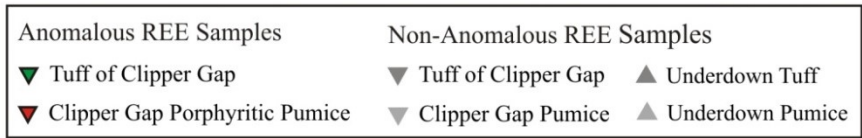
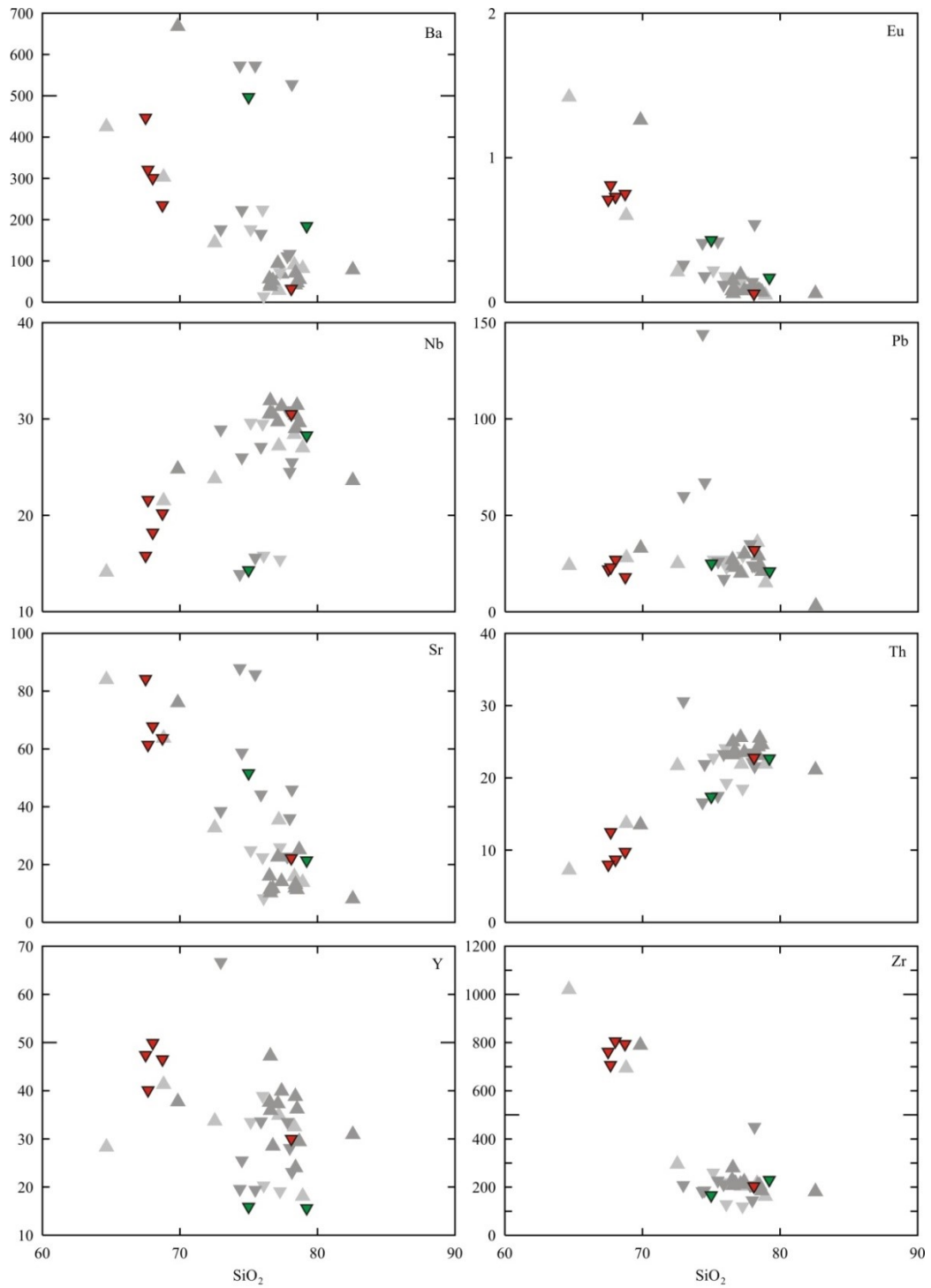


Figure 7.19: Trace element variation diagrams for the anomalous REE samples from the tuff of Clipper Gap, as well as the non-anomalous Underdown Tuff and tuff of Clipper Gap samples for comparison. Similar to the major element bivariate diagrams, the anomalous REE rhyolitic porphyritic pumice sample plots closer to the anomalous REE whole rock samples than the anomalous REE trachyte porphyritic pumice samples.

7.2.4 Effects of acid washing on anomalous REE samples

Acid washing with 2.5N hydrochloric acid (HCl) for five days at 80 degrees Celsius was performed on a selection of the anomalous REE samples to determine whether the REE enrichment and observed Ce anomalies are geochemical characteristics of the tuff of Clipper Gap or are caused by the presence of a secondary phase in the rocks. These secondary phases would be removed by the acid washing process, however it is important to note that primary phases may also be removed by acid washing (eg. apatite, Fe-Ti oxides). Three samples without anomalous REEs were included in the selection of samples along with four anomalous REE samples to compare the effect of the acid washing process on non-anomalous samples. Table 7.1 lists the samples that were acid-washed and whether they show a negative, positive, or no Ce anomaly.

Sample Number	Unit	Sample Type	Ce Anomaly
16-SM-13C	Tuff of Clipper Gap	Whole Rock	None
16-SM-14	Tuff of Clipper Gap	Porphyritic Pumice	Positive
16-SM-16	Tuff of Clipper Gap	Porphyritic Pumice	Negative
17-SM-21A	Tuff of Clipper Gap	Porphyritic Pumice	Negative
17-SM-22	Tuff of Clipper Gap	Vitrophyre	None
17-SM-26A	Tuff of Clipper Gap	White Pumice	None
17-SM-26C	Tuff of Clipper Gap	Porphyritic Pumice	Negative

Table 7.1: Samples selected for the acid washing process, including porphyritic pumice, white pumice, whole rock and vitrophyre samples. Three anomalous REE-enriched porphyritic pumice samples show a negative Ce anomaly while one shows a positive Ce anomaly. Non-anomalous samples selected for the acid washing process include a whole rock, vitrophyre, and white pumice samples.

Geochemical Results

Geochemical analyses of the acid-washed samples have been compared to the geochemical data for the same unwashed samples to show the effect of acid washing on major and trace element concentrations, as well as isotopic values.

Major Elements

Major element data for the acid-washed samples is listed in Appendix I, Table IV. Major element oxide contents in the acid-washed samples were normalized to the same major element contents in the unwashed samples and plotted by major element oxide for each sample (Fig. 7.20). This shows how the weight percentage of the major element oxide has changed due to the acid washing process. This analysis does not assume that any major element oxide is completely immobile. Major element oxides plotting at 1.0 showed no change in the concentration after acid washing.

After acid washing, Al_2O_3 , K_2O , Na_2O , and SiO_2 remained unchanged in all samples. The percentage of CaO which was removed from samples shows the most variation of all major element oxides and ranges between 10-70%. Fe_2O_3 was removed from all samples and shows a decrease of 60-70%. P_2O_5 was heavily depleted in all samples except 16-SM-13C, with decreases in concentration ranging from 70-100%. TiO_2 showed a depletion of 5-25% in the samples.

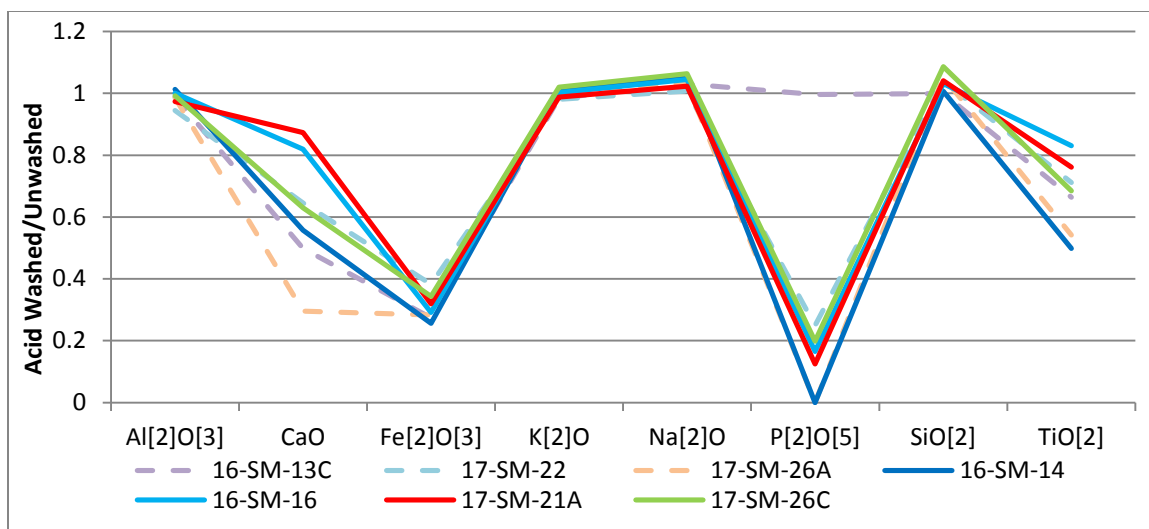


Figure 7.20: A line diagram showing the effect of acid washing on the major element oxides of the anomalous REE samples and non-anomalous REE samples. Non-anomalous REE samples are represented by dashed lines while anomalous REE samples are represented by solid lines. Al₂O₃, K₂O, Na₂O, and SiO₂ largely remained the same after acid washing. However, CaO, Fe₂O₃, and P₂O₅ show large decreases in concentration after acid washing. TiO₂ shows a small to moderate decrease in concentration after acid washing.

Trace Elements

Trace element data for the acid-washed samples is listed in Appendix I, Table VI. In a chondrite normalized REE diagram, acid washing has caused the LREEs in the acid-washed samples to become depleted relative to the LREEs in the unwashed samples (Fig. 7.21). A decreasing slope towards the HREEs still exists, however the middle REEs are being strongly depleted which has caused a concave-upward curve in the middle to heavy REEs. The negative Ce anomaly is completely removed from almost all samples after acid washing, except for sample 16-SM-16 which still shows a small negative anomaly. The positive Ce anomaly in sample 16-SM-14 has also been removed by acid washing. After acid washing, the negative Eu anomaly generally becomes smaller, and in some samples, the negative Eu anomaly has disappeared or become slightly positive. However, the actual normalized value of Eu in most samples remains unchanged from before acid washing. Certain trace element concentrations in the acid-washed samples were also normalized to the trace element concentrations of the unwashed samples and plotted on a line graph for comparison (Fig. 7.22). Neodymium, Y, Yb, Sr, Sm, U and Th show a decrease in concentration after acid washing. Zirconium and Rb show little to no decrease in concentration.

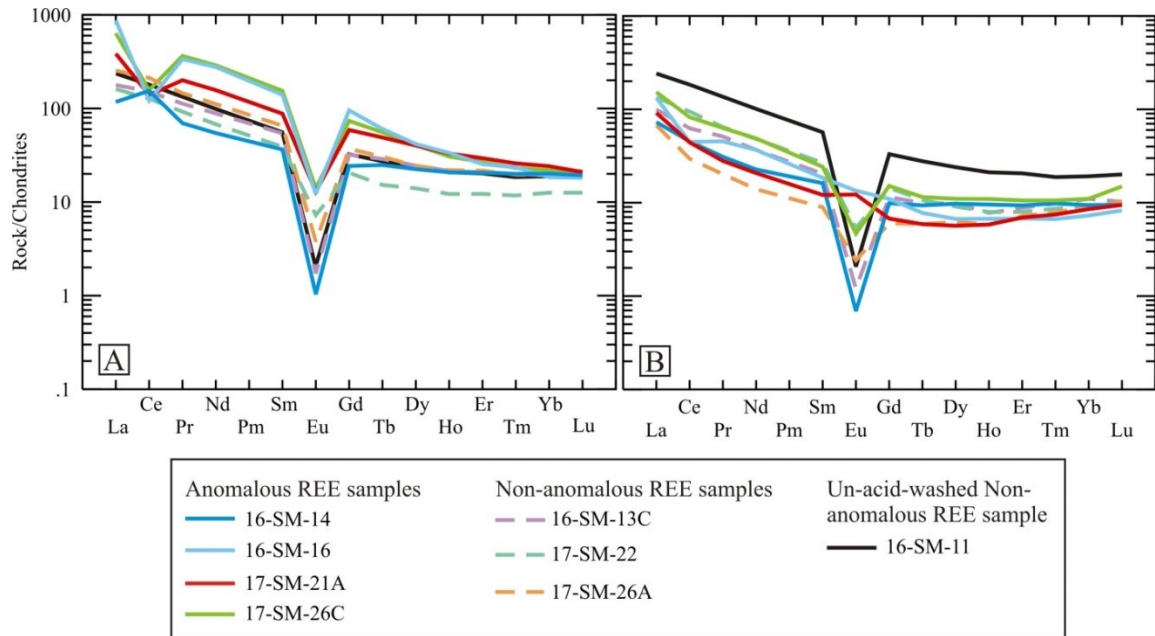


Figure 7.21: Chondrite normalized REE diagrams for the acid-washed samples before (A) and after acid washing (B). The acid washing process has removed the Ce anomaly almost entirely, except for sample 16-SM-16 which still shows a small negative anomaly. A concave-upward curvature is observed in the middle to heavy REEs, suggesting that a middle REE-loving phase is being removed during acid washing (likely apatite due to the complete loss of P_2O_5 during acid washing). The Eu anomaly also appears to become smaller after acid washing (normalizing values from Sun and McDonough, 1989).

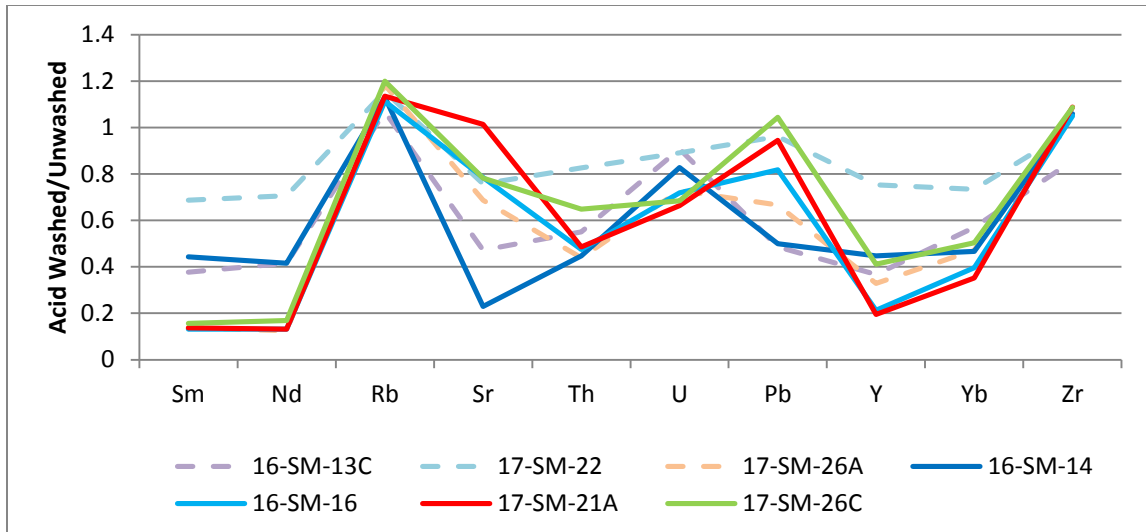


Figure 7.22: A line diagram showing the change in trace element concentration after the acid washing process. Non-anomalous REE samples are represented by dashed lines while anomalous REE samples are represented by solid lines. The anomalous REE and non-anomalous REE samples show little to no depletion of Rb and Zr. The most highly depleted trace elements in the anomalous REE samples are Sm, Nd, Y, and Yb. The anomalous REE samples are depleted to various degrees in Sr and Pb, with Sr showing the most variation between anomalous REE samples. The anomalous REE samples are moderately depleted in Th and U. The non-anomalous REE samples are moderately depleted in most trace elements, however the degree of depletion varies among individual samples. In some trace elements, the non-anomalous REE samples are depleted to the same degree as the anomalous REE samples. Of the anomalous REE samples, the three porphyritic pumice with negative Ce anomalies (16-SM-16, 17-SM-21A, 17-SM-26C) show similar patterns of trace element depletion, while sample 16-SM-14 (anomalous REE porphyritic pumice with a positive Ce anomaly) shows a different pattern of depletion.

Isotope Geochemistry

Isotopic data for the acid-washed samples is listed in Appendix I, Table VIII. Four acid-washed samples were analyzed isotopically, and the initial isotopic values were compared to the initial isotopic values for the same unwashed samples to observe any changes in isotopic ratio after acid washing. When comparing initial $^{87}\text{Sr}/^{86}\text{Sr}$ isotopic values to the concentration of Sr, there is a negative correlation seen in all samples except for 17-SM-21A in which the isotopic value decreases but the Sr concentration shows no change (Fig. 7.23). After acid washing, the samples have consistently lower initial $^{87}\text{Sr}/^{86}\text{Sr}$ isotopic ratios which decrease to approximately the same ratio for all samples. This new isotopic value is closer to the bulk earth $^{87}\text{Sr}/^{86}\text{Sr}$ ratio, and is similar to the $^{87}\text{Sr}/^{86}\text{Sr}$ ratios of non-anomalous samples from the other Oligocene tuffs.

When comparing the initial ϵNd value and the concentration of Nd, there is a strong decrease in Nd concentration and an increase in the ϵNd values after acid washing (Fig. 7.24). The ϵNd value increases to values closer to the bulk earth ϵNd value in all samples. The original Nd concentration varies between the samples, with 16-SM-16 and 17-SM-26C containing a Nd concentration of nearly double that in 17-SM-21A. However, all samples experience a decrease in Nd concentration to a relatively similar value which is more similar to Nd concentrations in non-anomalous REE samples.

Both $^{208}\text{Pb}/^{204}\text{Pb}$ and $^{206}\text{Pb}/^{204}\text{Pb}$ ratios increase after acid washing (Fig. 7.25). When comparing the $^{208}\text{Pb}/^{204}\text{Pb}$ isotopic values and the Pb concentrations for the acid-washed and unwashed samples, the change in Pb concentration is variable between the

samples (Fig. 7.26). The acid-washed samples experience much less change in Pb concentration than is observed in Sr and Nd. Sample 17-SM-26C is interpreted to not change at all, as it appears to increase by 1 ppm, however this is close to the analytical uncertainty for Pb by ICP-MS.

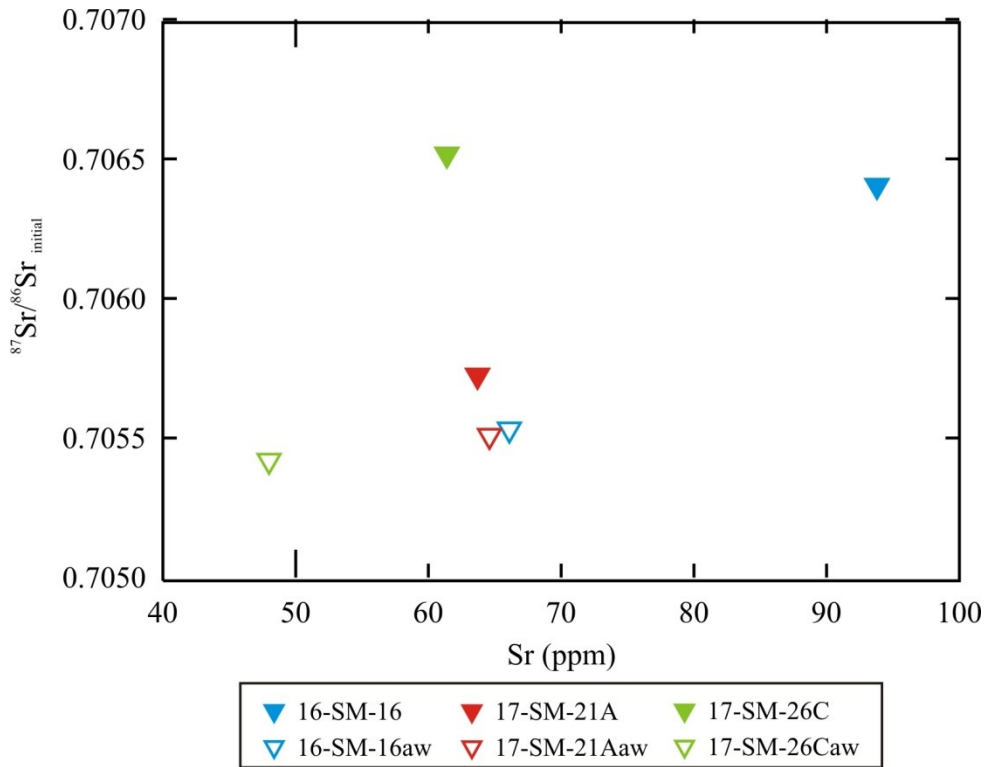


Figure 7.23: Initial $^{87}\text{Sr}/^{86}\text{Sr}$ ratios plotted against Sr concentration for acid-washed and unwashed anomalous REE samples. All samples show a decrease in both $^{87}\text{Sr}/^{86}\text{Sr}$ isotopic value and Sr concentration after acid washing except for sample 17-SM-21A which shows only small changes in both.

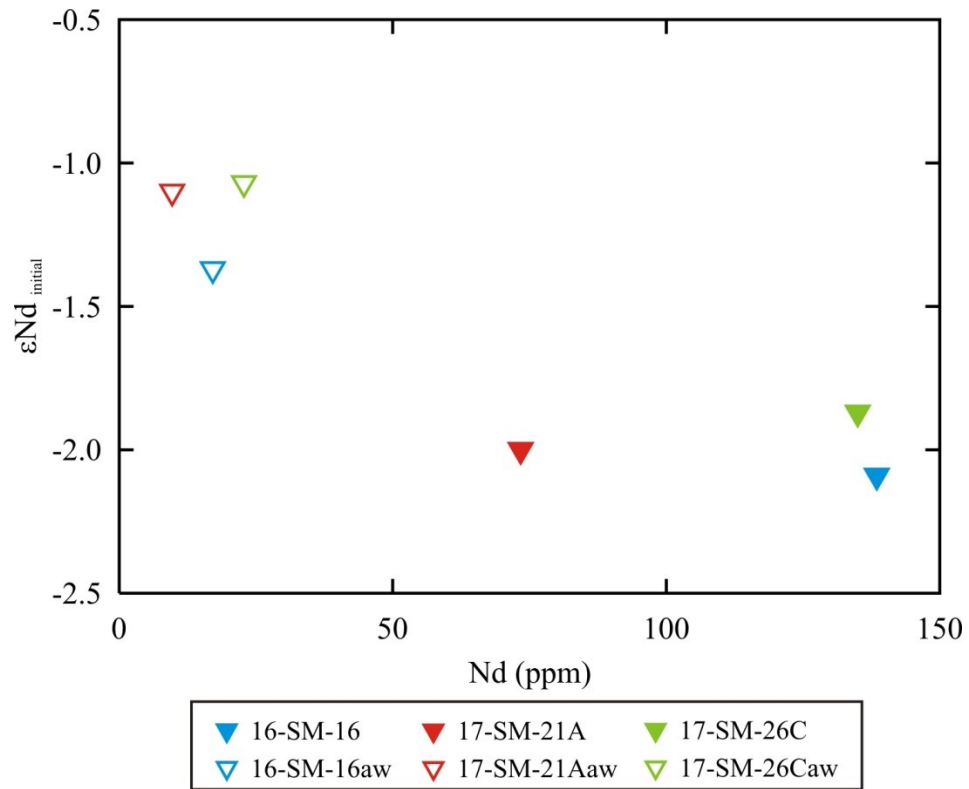


Figure 7.24: Initial ϵNd plotted against Nd concentration for the acid-washed and unwashed anomalous REE samples from the tuff of Clipper Gap. After acid washing, the samples show a decrease in both ϵNd isotopic value (less negative values) and Nd concentration.

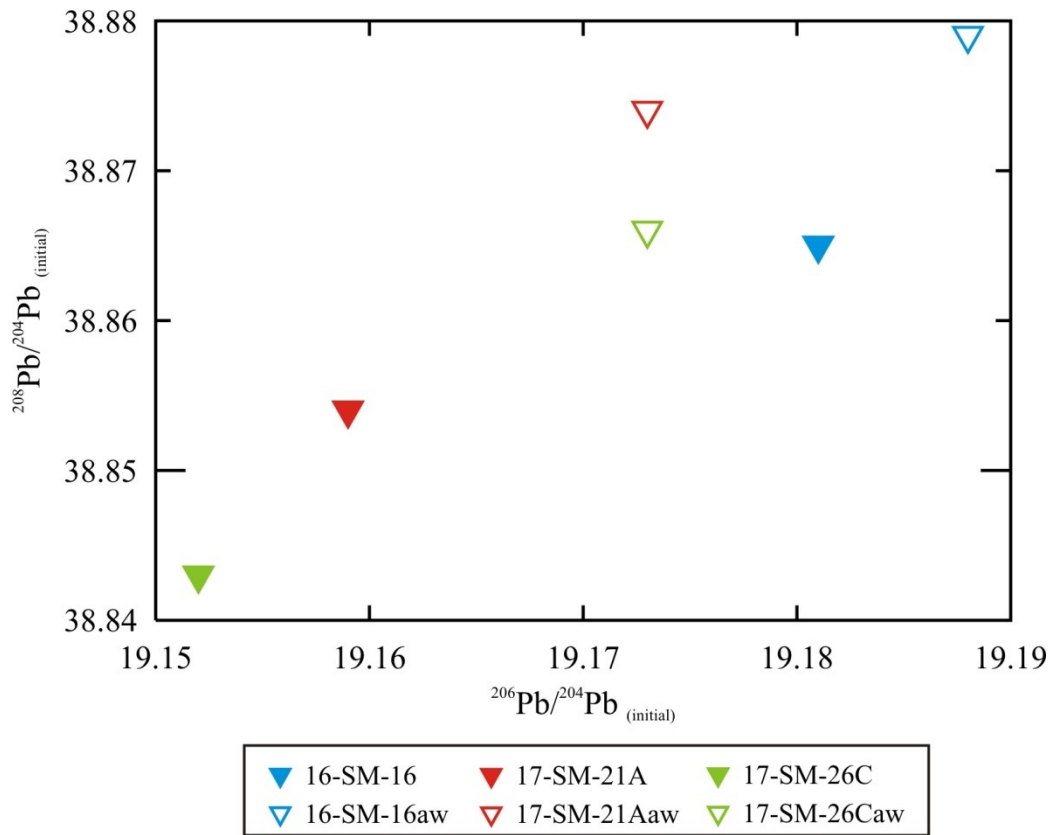


Figure 7.25: Initial $^{208}\text{Pb}/^{204}\text{Pb}$ vs. $^{206}\text{Pb}/^{204}\text{Pb}$ showing the change in isotopic ratio after acid washing. Both $^{208}\text{Pb}/^{204}\text{Pb}$ and $^{206}\text{Pb}/^{204}\text{Pb}$ ratios increase after acid washing. After acid washing, 17-SM-21A and 17-SM-26C appear to have the same $^{206}\text{Pb}/^{204}\text{Pb}$ ratios.

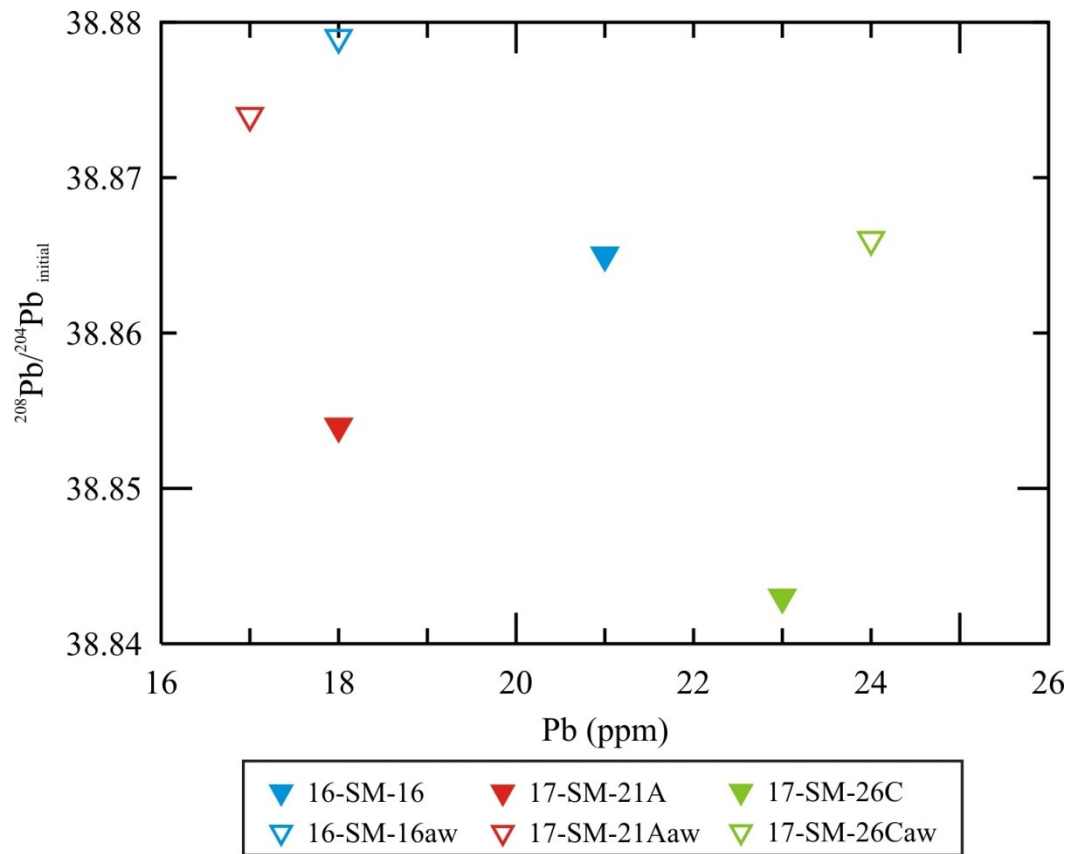


Figure 7.26: Initial $^{208}\text{Pb}/^{204}\text{Pb}$ isotopic ratios plotted against Pb concentrations showing the change in isotopic ratio and Pb concentrations after acid washing. All samples show an increase in Pb isotopic ratios after acid washing, while Pb concentrations decrease in samples 16-SM-16 and 17-SM-21A. The Pb concentration in 17-SM-26C is interpreted to experience no change as 1 ppm is close to analytical uncertainty for Pb by ICP-MS.

7.2.5 Potential sources of Ce anomalies and REE enrichment

Apatite

The effects of the acid washing process suggest that the Ce anomalies could be caused by a secondary phase, and are not a geochemical characteristic of the unit. Acid washing with HCl strips away surface bonds but leaves internal bonds, such as SiO₂ bonds, intact. As observed in the normalized major element line plots, the SiO₂ content of the samples did not change after acid washing, however major element oxides such as CaO, Fe₂O₃, P₂O₅, and TiO₂ experienced significant changes in abundance. The removal of Fe-Ti oxides from the samples accounts for the loss of both Fe₂O₃ and TiO₂. It is possible that P₂O₅ and CaO are being depleted by the removal of apatite, perhaps secondary, from the samples. Apatite, Ca₅(PO₄)₃ has a high affinity for all the REEs, and especially partitions the middle REEs. Therefore, the removal of this phase could account for the concave-upward curvature in the middle and heavy REEs observed after acid washing. Although there is only a small amount of P₂O₅ present in these samples to begin with, only a small concentration is required to crystallize apatite (Watson and Capobianco, 1981). The apatite in these rocks may be a secondary phase precipitated by fluids altering the rocks. However, the loss of apatite does not explain the loss of the Ce anomalies, since apatite does not preferentially partition Ce into its structure relative to La or Pr.

Amphibole

Amphibole also shows a high affinity for middle REEs. The fractionation of amphibole before and after acid washing was investigated in Figure 7.27. Dy/Yb was used as an indicator for the formation of hornblende, as amphibole has a high partition coefficient for Dy and a lower one for Yb (11.3 and 1.8, respectively, Appendix I, Table VII). Concentrations of these trace elements and the SiO₂ content before and after acid washing were compared to observe whether amphibole is removed during acid washing. While the concentration of Dy/Yb decreases after acid washing, the SiO₂ content in the samples increases. However, this increase is due to the low amount of SiO₂ in amphibole (~50%). The removal of apatite by acid washing would also have a similar effect on the SiO₂ abundance and concentrations of Dy and Yb, as Dy and Yb also have high partition coefficients in apatite (16.9 and 9.4, respectively, Appendix I, Table XII). As apatite has a higher affinity for heavy REEs than amphibole, it would preferentially incorporate heavy REEs relative to light REEs to a higher degree than amphibole. While this suggests that the removal of apatite or amphibole could be responsible for the observed pattern in the REEs after acid washing, the complete removal of P₂O₅ after acid washing (Fig. 7.20) would not be a result of the removal of amphibole, and would rather be a result of the removal of apatite. As well, the crystallization of amphibole would not cause the observed Ce anomalies in the samples, due to the low (< 1) partition coefficient for Ce in amphibole (Appendix I, Table XII). Based on these observations, it is unlikely that the removal of amphibole would cause

the observed trend in the REEs after acid washing, and the removal of apatite is a more likely culprit.

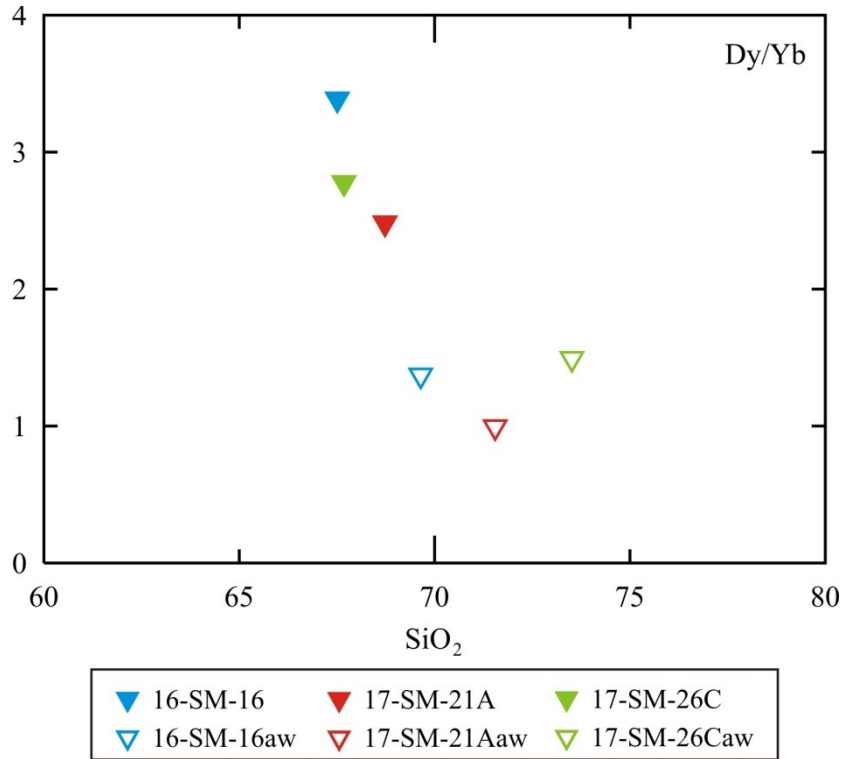


Figure 7.27: The fractionation of amphibole before and after the acid washing process. Dy/Yb is used to represent the formation of amphibole as amphibole preferentially partitions Dy into its structure, but takes in much less Yb. As the Dy/Yb decreased after acid washing, the SiO₂ content increased. An increase in the SiO₂ content can be explained by the low amount of SiO₂ in amphibole (~50%).

REE enriched clays

Another weathering phase which could be causing the Ce anomalies is REE enriched clays. Fresh and weathered dolerites from Karoo were analysed by Marsh (1991) and were observed to have both negative and positive Ce anomalies in all weathered samples. All REEs and Y were found to be enriched in weathered rinds in the samples, and negative Ce anomalies were also found in these REE enriched samples. The geochemical trends in the weathered dolerites were found to reflect the production of clays, particularly kaolinite, from the alteration of silicate minerals through the leaching of groundwater. Leached REEs and Y from the weathering product were taken up by the rocks that were subsequently altered by the REE enriched fluids. This caused an enrichment of REEs and Y in the altered rocks; more specifically an enrichment of LREEs relative to HREEs, and a negative Ce anomaly. In oxidizing environments, Ce^{3+} can be oxidized to Ce^{4+} and remain stable as CeO_2 . Due to this immobility of Ce, the REEs in the weathered sample would show a negative Ce anomaly due to the enrichment of all of the other REEs. The positive Ce anomaly observed in the weathering product would be caused by the immobility of the Ce in the rock from which the REEs and Y are being leached. This positive Ce anomaly and REE depletion has also been observed in felsic rocks (Boulangé et al., 1990; Braun et al., 1990).

The uptake of these REEs and Y into weathering rinds or zones in the tuff of Clipper Gap samples could account for the observed geochemical trends in the REEs. For example, the higher REE enrichment in the porphyritic pumice with large negative Ce anomalies

compared to the non-anomalous tuff of Clipper Gap. This suggests that mobility of the other REEs is the culprit behind the Ce anomalies, rather than a depletion or enrichment of Ce. The negative Ce anomalies present in these samples could therefore be caused by the interaction of the rock with groundwater containing REEs and Y from another source, causing enrichment in those elements but not in Ce. The overall depletion in all REEs after acid washing could therefore be caused by the removal of an REE bearing weathering phase from the samples, and not a Ce bearing phase. More evidence for this also exists in the observed change in the Eu anomaly after acid washing. The large negative Eu anomaly observed in most samples appears to become smaller after acid washing, however, the actual abundance of Eu stays relatively the same while the rest of the REEs are depleted. This is likely causing the Eu anomaly to appear smaller, however, the actual amount of Eu in the sample remains relatively constant. Since Eu is incorporated into silicate minerals, such as plagioclase and potassium feldspar, they are less likely to be removed by acid washing. This heavy depletion in REEs may also account for why sample 17-SM-21A appears to gain a positive Eu anomaly after acid washing. Ba and Sr also show very large negative anomalies in these rocks, and while these phases are incorporated into feldspars, their depletion could also be due to weathering as is seen in the Karoo samples (Marsh, 1991). Further evidence for this mechanism can be observed in the line diagram depicting the change in concentration of trace elements after acid washing as the removal of Y out of most of the samples by acid washing suggests that it could be part of a secondary phase removed by acid washing.

Formation of the enriched anomalous REEs by groundwater is also supported by the isotopic data. As observed in the isotope diagrams before and after acid washing, the anomalous REE samples experienced changes in initial values for $^{87}\text{Sr}/^{86}\text{Sr}$, ϵNd , $^{206}\text{Pb}/^{204}\text{Pb}$, and $^{208}\text{Pb}/^{204}\text{Pb}$. In particular, all acid-washed samples experienced decreases in their $^{87}\text{Sr}/^{86}\text{Sr}$ ratios, and while the samples did not all decrease by the same amount, they did decrease to relatively similar initial ratios as the “fresh” Underdown Caldera complex ignimbrites. Since the samples have such a small concentration of Sr, it is possible that a fluid rich in Sr could have easily altered the Sr isotopic ratios of the samples after deposition. Probable addition of Nd from other rocks via groundwater likely also decreased the $^{143}\text{Nd}/^{144}\text{Nd}$ ratios in the anomalous REE samples.

Based on observations from field work, the anomalous REE samples were commonly found in upper and lower sections of the sampled units. For example, at the Moore’s Canyon Road outcrop, the anomalous REE samples were located at the very top of the exposure, while samples collected from the unwelded base and middle cooling units were not found to contain any REE enrichment or Ce anomalies. Similarly, samples collected from Butler Ranch in Monitor Valley which show negative Ce anomalies were collected from the base of the exposure, beneath a vitrophyre and columnar jointed section. Finally, anomalous REE samples collected in the 2016 field season were found at the top of an outcrop as well as in a subcrop located beneath the main outcrop. Sample 16-SM-14, which exhibits a positive Ce anomaly, was collected from the unit directly

below sample 16-SM-15A (a sample of porphyritic pumice with a large negative Ce anomaly). The location of these samples on the outer margins of the section could cause them to be more susceptible to weathering by groundwater than the inner rocks. Field notes from these locations state that the rocks and porphyritic pumice from these units show alteration and appear to be vapour phase altered. Under petrographic observation, all of the porphyritic pumice samples appeared highly altered, especially in the matrices.

Based on the evidence of REE enrichment, and the presence of both positive and negative Ce anomalies in these Clipper Gap samples, we postulate that the Ce anomalies in the tuff of Clipper Gap may be caused by the presence of REE enriched clays. These clays were not observed during petrographic analysis; however the fine grained, altered matrix of these samples may have made their identification in regular microscopy impossible. The clays may exist as rinds around other grains, and could contain phases like secondary apatite. Analysis by scanning electron microscope and electron microprobe would be necessary to determine their presence in the samples.

7.3 Other potentially related exposures

While section 7.1 focused on the characteristics of the intracaldera tuffs and the tuff of Clipper Gap, this section investigates some of the slightly older ignimbrites sampled outside of the Underdown Caldera, as well as new potential outflow units to the west of the caldera, to determine whether these units have any relation to the Underdown Caldera magmatic event.

7.3.1 The tuff of Gabbs Valley

Henry and John (2013) question a previously interpreted caldera at Fissure Ridge which was proposed to be a source for the tuffs of Gabbs Valley (originally proposed by Ekren and Byers, 1976 and 1986). This fissure is now interpreted to be a canyon which was eroded into two older tuffs of Gabbs Valley, TgV1 and TgV2. In this situation, TgV2 and the uppermost unit, TgV3, would likely have been outflow tuffs deposited into a paleovalley, rather than ignimbrite deposits formed in a caldera as originally proposed, based on the lack of lithic fragments and megabreccia deposits commonly seen in intracaldera tuffs (Henry and John, 2013, and references therein). It is proposed that the eroded valley has been filled with the youngest tuff unit, TgV3. Both TgV2 and TgV3 were sampled as potential outflow tuffs from the Underdown Caldera.

While these units are currently identified as the tuff of Gabbs Valley (TgV), a widespread, sparsely porphyritic ash-flow tuff in the Western Nevada Volcanic Field (Henry and John, 2013; John, 1974), TgV2 is much more porphyritic than the tuff of

Gabbs Valley. In the field TgV2 was observed to have 20-25% phenocrysts in the poorly welded base and up to 35% phenocrysts in the densely welded upper portion, both of which are also more porphyritic than the Underdown Tuff and the tuff of Clipper Gap. Samples were collected from the poorly welded base (17-SM-28), the moderately welded middle (17-SM-29), and densely welded top (17-SM-30) of TgV2. Above the vitrophyre that separates TgV2 and TgV3, TgV3 was observed to have far fewer phenocrysts than TgV2 and dark porphyritic pumice were observed in a moderately welded matrix. The porphyritic pumice was sampled for geochemical analysis (17-SM-31). Based on the field observations, it is more likely that TgV3 is an Underdown-Clipper Gap equivalent than is TgV2. TgV2 has been determined to be slightly too old to be an Underdown Caldera outflow tuff (25.109 ± 0.080 Ma, C. Henry, pers. comm., 2018), but is similar in age to the tuff of Arc Dome (25.19 ± 0.04 Ma, C. Henry, pers. comm., 2018). However, the age of TgV3 (24.875 ± 0.048 Ma, C. Henry, pers. comm., 2018) suggests that it could be a possible Underdown Caldera outflow tuff. Therefore TgV2 will be compared to the tuff of Arc Dome, and TgV3 will be compared to the Underdown Tuff.

In chondrite normalized REE and primitive mantle normalized trace element diagrams, samples of TgV2 show the same patterns as the tuff of Arc Dome (Fig. 7.28). Primitive mantle normalized trace element patterns for the tuff of Arc Dome have large variations in negative Ba, Sr, and Eu anomalies which are also observed in the TgV2 samples. In particular, sample 17-SM-30 from the welded upper section of TgV2 shows the same

patterns as tuff of Arc Dome samples 16-SM-09 and 17-SM-14 on both the chondrite normalized REE and primitive mantle normalized trace element diagrams (Fig. 7.29).

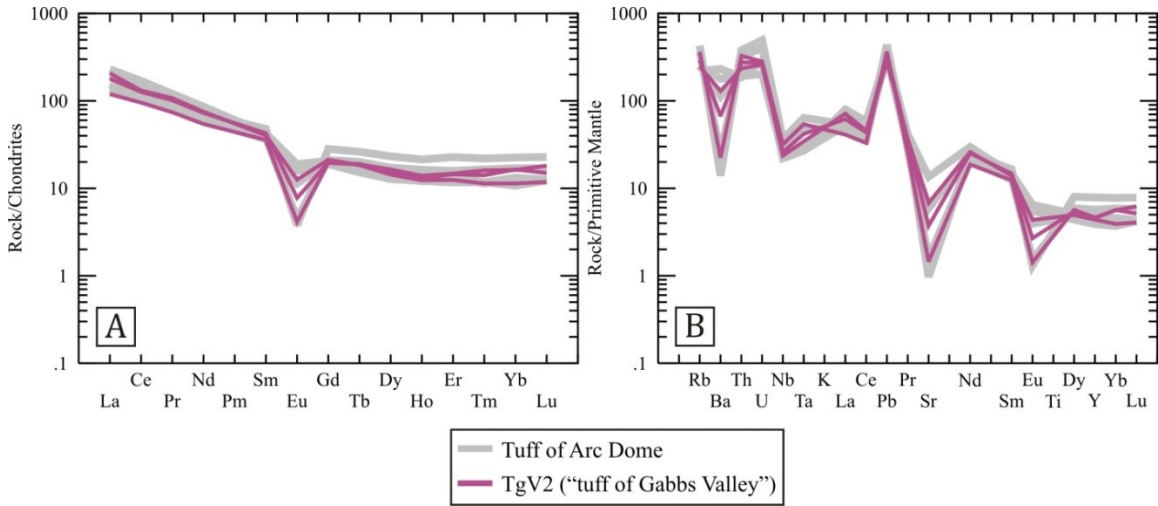


Figure 7.28: (A) Chondrite normalized REE and (B) primitive mantle normalized trace element diagrams comparing TgV2 ("tuff of Gabbs Valley") and the tuff of Arc Dome. In both diagrams, TgV2 appears to be nearly identical to the tuff of Arc Dome, showing the same enrichment in LREEs and flattening to HREEs, and identical ranges of Ba, Sr, and Eu anomalies (normalizing data from Sun and McDonough, 1989).

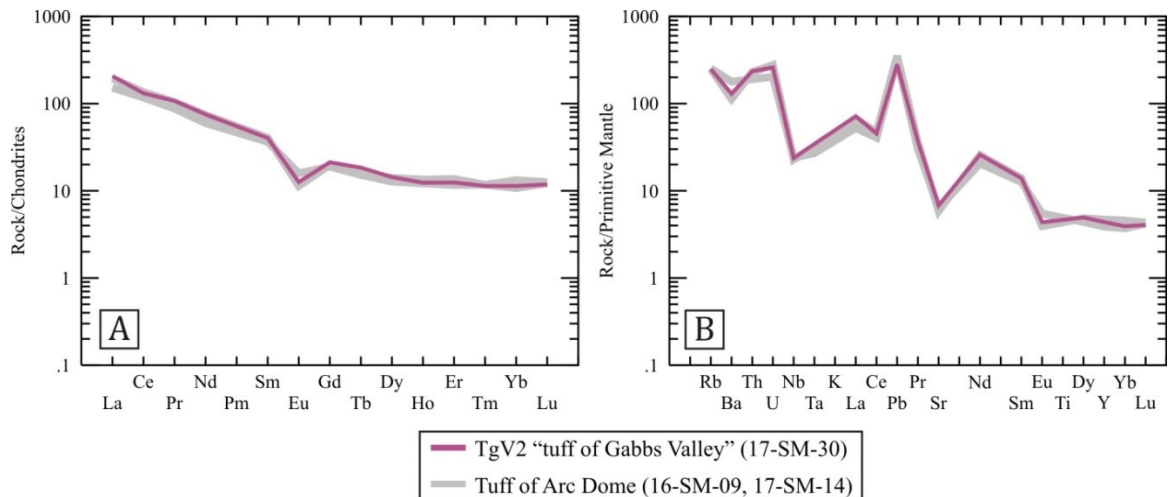


Figure 7.29: (A) Chondrite normalized REE and (B) primitive mantle normalized trace element diagrams comparing all samples from TgV2 (“tuff of Gabbs Valley”) and two samples (17-SM-14, 16-SM-09) from the tuff of Arc Dome. The two tuff of Arc Dome samples plot nearly identical to the sample from TgV2 (normalizing data from Sun and McDonough, 1989).

TgV3 porphyritic pumice was compared to the porphyritic pumice from the Underdown Tuff (Fig. 7.30). Despite both being porphyritic pumice samples, TgV3 porphyritic pumice has a much more depleted HREE signature on a chondrite normalized REE diagram and lacks the characteristic negative Ba and Eu anomalies observed in most of the Underdown porphyritic pumice on the primitive mantle normalized trace element diagram. Chondrite normalized REE and primitive mantle normalized trace element patterns of TgV3 show more similarity to a whole rock sample from the Bonita Canyon Formation (16-SM-26) (Fig. 7.31). These samples were plotted with the lone sample of porphyritic pumice (17-SM-17C) from the Underdown Tuff which also shows no negative Eu anomaly. On the chondrite normalized REE diagram, TgV3 appears to be slightly more enriched in LREEs, and show a slightly steeper pattern to the HREEs than the

Bonita Canyon Formation and the Underdown porphyritic pumice. The Bonita Canyon Formation shows the most similarity in HREE depletion to TgV3. TgV3 also appears more similar to the Bonita Canyon Formation in the primitive mantle normalized trace element diagram. Both TgV3 and the Bonita Canyon Formation samples lack the negative Ba anomaly that is observed in the Underdown porphyritic pumice. TgV3 shows slightly stronger depletion in Nb and Ta, and higher enrichment in La than both the Underdown Tuff and Bonita Canyon Formation.

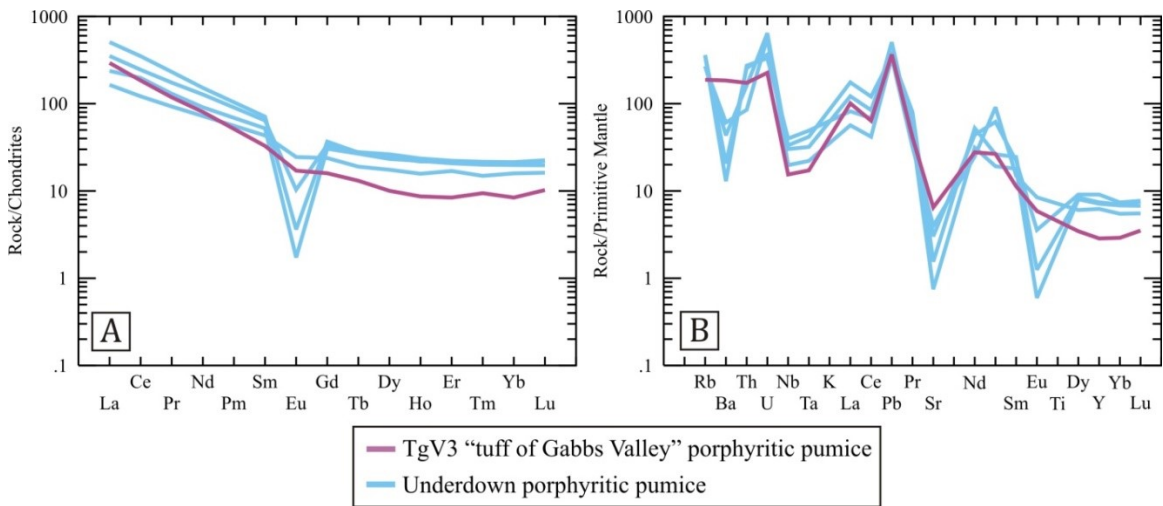


Figure 7.30: (A) Chondrite normalized REE and (B) primitive mantle normalized trace element diagrams comparing TgV3 ("tuff of Gabbs Valley" porphyritic pumice) to the Underdown porphyritic pumice samples. On panel (A) TgV3 shows a steeper pattern from the LREEs to the HREEs than the Underdown porphyritic pumice, as well as no negative Eu anomaly. TgV3 also lacks a negative Ba anomaly which is observed in all Underdown porphyritic pumice samples (B) (normalizing data from Sun and McDonough, 1989).

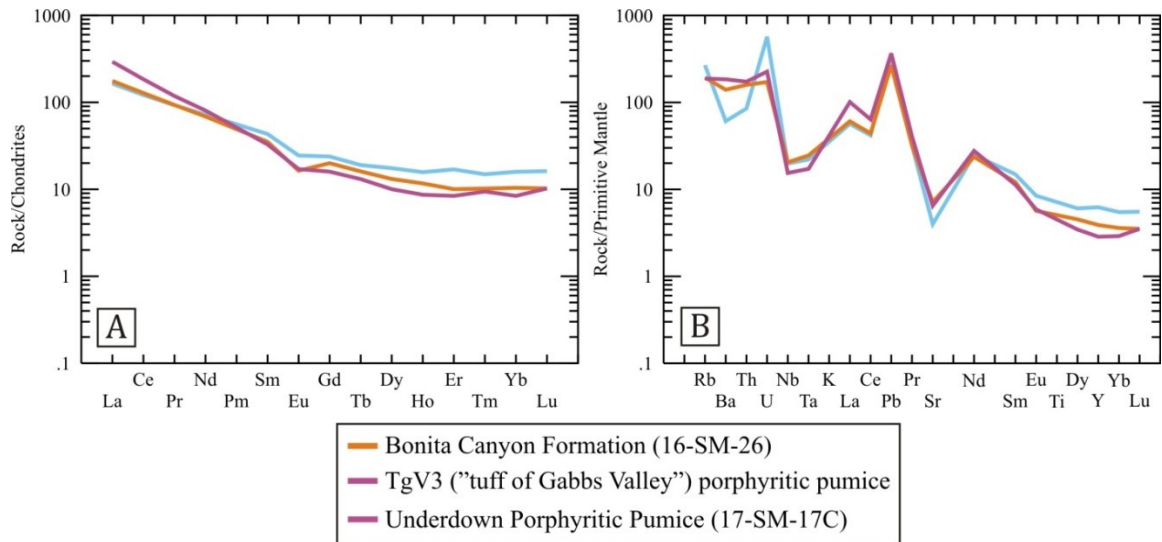


Figure 7.31: Chondrite normalized rare earth element plot (A) and primitive mantle normalized trace element plot (B) comparing TgV3 with the Bonita Canyon Formation and the Underdown Tuff (porphyritic pumice). While the chondrite normalized pattern of TgV3 appears similar to both units on panel (A), TgV3 shows the most similarity to the Bonita Canyon Formation whole rock when normalized to primitive mantle. Like the Bonita Canyon Formation sample, TgV3 is lacking a negative Ba anomaly which is observed in the Underdown porphyritic pumice sample (B) (normalizing data from Sun and McDonough, 1989).

Isotopic values for TgV2 and TgV3 are fairly similar in the Sr and Pb isotopic systems, as observed in the isotope result diagrams in Section 6.0 (Fig. 6.21-6.29). However, differences exist between them in their ϵ_{Nd} values which give clues as to their identities (Fig. 7.32). TgV2 appears to be most similar to the tuff of Arc Dome, while TgV3 shows the most similarities to the Bonita Canyon Formation. In the Sr and Pb isotopic systems, TgV2 and TgV3 typically plot in a cluster with the tuff of Arc Dome. When comparing initial ϵ_{Nd} to $^{87}Sr/^{86}Sr$ and ϵ_{Nd} to Nd concentration, TgV2 and the tuff of Arc Dome appear isotopically identical.

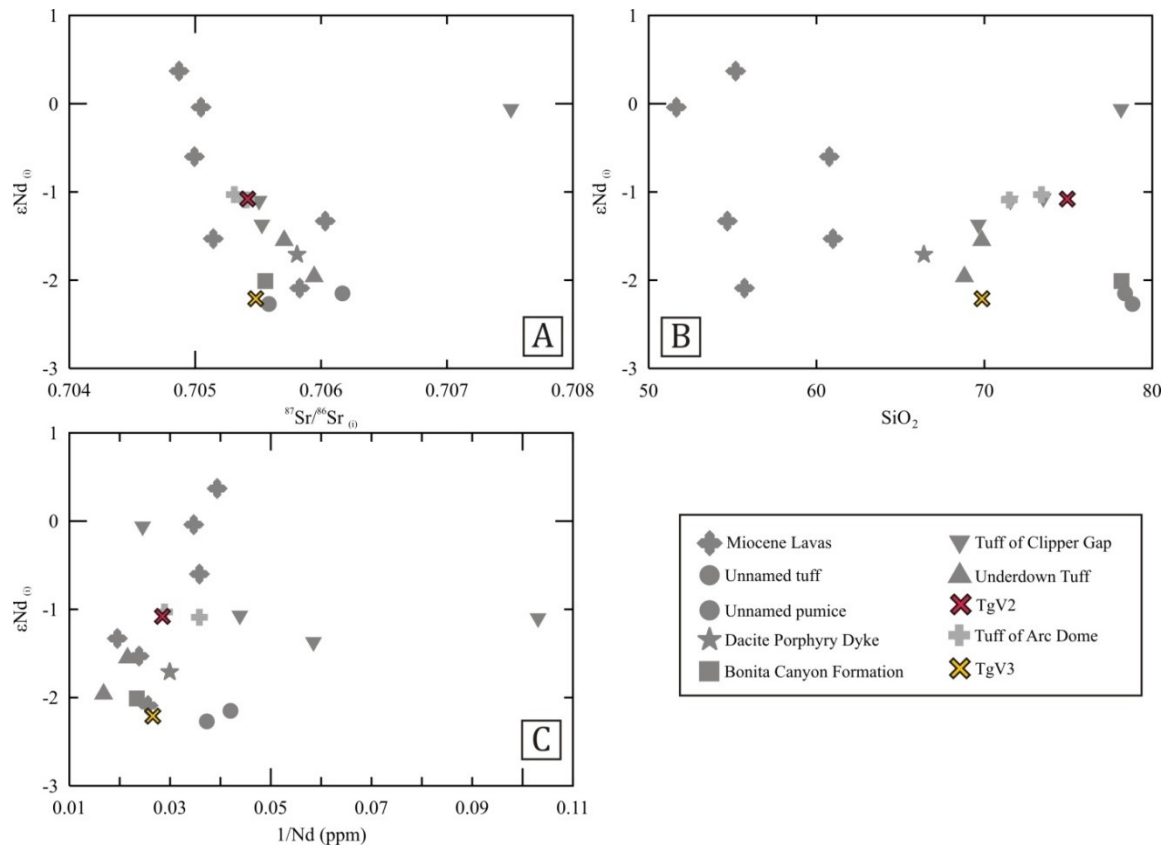


Figure 7.32: Nd isotopic diagrams showing the difference in initial ϵNd values between TgV2 and TgV3. Panel (A) shows the comparison between initial ϵNd values and $^{87}\text{Sr}/^{86}\text{Sr}$ ratios, and the similarities between TgV2 and the tuff of Arc Dome, while TgV3 appears more similar to the Bonita Canyon Formation and the Unnamed Tuff. Panel (B) shows the comparison between initial ϵNd values and SiO_2 content. Again, TgV2 is more similar to the tuff of Arc Dome while TgV3 is less evolved and appears similar to the Underdown Tuff. Panel (C) shows the comparison between initial ϵNd values and Nd concentration. As observed in panels (A) and (C), TgV2 overlaps the tuff of Arc Dome while TgV3 shows the most similarity to the Bonita Canyon Formation.

In summary, based on its crystal-rich texture, age and geochemistry, TgV2 from Fissure Ridge is interpreted to be equivalent to the tuff of Arc Dome. Based on field observations, TgV3 shows similarity to the Underdown Tuff and tuff of Clipper Gap. However, geochemically, TgV3 shows the most similarity to the Bonita Canyon Formation. These observations and the age of the unit suggest that TgV3 may represent a phase of outflow tuff correlative to the Bonita Canyon Formation. Both TgV2 and TgV3 are not correlative to be the tuff of Gabbs Valley as they were previously interpreted.

7.3.2 The tuff of Arc Dome

The megabreccia block and tuff of Arc Dome have been dated at 25.19 ± 0.04 Ma (C. Henry, pers. comm., 2018) and 25.18 ± 0.06 Ma (Henry and John, 2013), respectively. Therefore the sampled megabreccia block from the Underdown Caldera complex is similar in age to the tuff of Arc Dome. Chondrite normalized and primitive mantle normalized spider patterns show that the megabreccia block has patterns similar to those of the tuff of Arc Dome (Fig. 7.33). The megabreccia block sample was analyzed isotopically along with one tuff of Arc Dome whole rock sample (16-SM-09 and 17-SM-14, respectively). As observed in the isotopic results, both the samples have similar isotopic ratios in all three isotopic systems (Fig. 6.21-6.29). The isotopic similarities between the samples support the suggestion that the megabreccia block is a large piece of the tuff of Arc Dome based on the date by C. Henry (pers. comm., 2018). Large blocks and spires of the tuff of Arc Dome found within the caldera may represent pieces of caldera wall rock that fell inwards during caldera collapse.

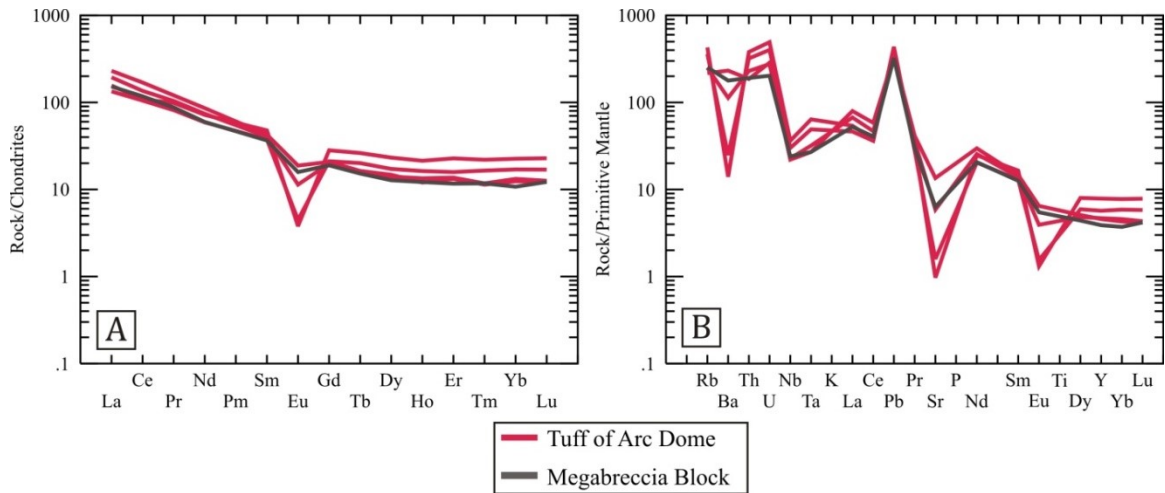


Figure 7.33: Chondrite normalized rare earth element diagram (A) and primitive mantle normalized trace element diagram (B) showing the comparison between the Tuff of Arc Dome and the megabreccia block sampled from the Underdown Caldera. The megabreccia block shows the same trace element arc signature as the other samples of the tuff of Arc Dome collected from outside of the caldera (normalizing data from Sun and McDonough, 1989).

7.3.3 The tuff of Brunton Pass

The tuff of Brunton Pass collected from the margins of the Underdown Caldera complex has been dated at 24.892 ± 0.053 Ma (C. Henry, pers. comm., 2018), while Henry and John (2013) dated another sample of the tuff of Brunton Pass at 25.12 ± 0.06 Ma. The two samples collected from the tuff of Brunton Pass included a welded (17-SM-13A) and an unwelded (17-SM-13B) whole rock. As observed in the major and trace element bivariate diagrams (Fig. 6.10, 6.13) the tuff of Brunton Pass plots within the same fractionation trends as the other Oligocene tuffs, but appears to be relatively homogeneous in composition (however, the few number of samples may be responsible

for this apparent homogeneity). In chondrite normalized REE and primitive mantle normalized trace element diagrams, the tuff of Brunton Pass appears to have patterns similar to the Underdown Tuff (Fig. 7.34). However, the welded sample shows a small negative Ce anomaly in the chondrite normalized REE plot, similar to what has been observed in the anomalous REE-enriched samples of the tuff of Clipper Gap (however the sample with a Ce anomaly does not have enriched REEs compared to the sample without a Ce anomaly). The LREE enrichment in the welded tuff of Brunton Pass is similar to the LREE enrichment in the anomalous REE-enriched whole rock tuff of Clipper Gap samples, but is less than the LREE enrichment in the anomalous REE tuff of Clipper Gap porphyritic pumice (Fig. 7.35). On a primitive mantle normalized Th/La vs. SiO₂ diagram, the tuff of Brunton Pass samples plot within the increasing correlation showing possible crustal addition formed by the Miocene lavas and the Oligocene tuffs, suggesting similar mixing endmembers for these units (Fig. 7.36).

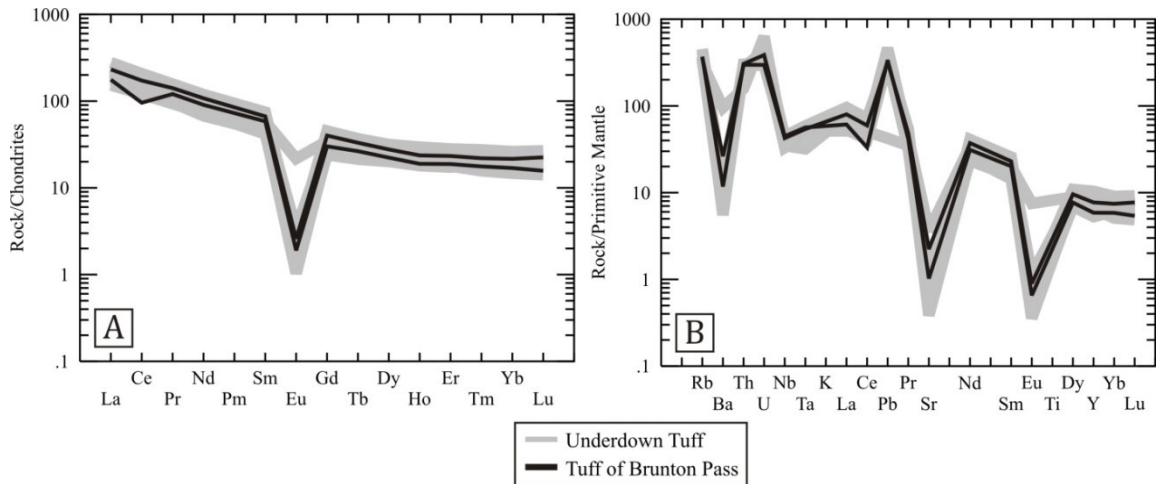


Figure 7.34: Chondrite normalized REE (A) and primitive mantle normalized trace element (B) diagrams showing similar patterns in both the Underdown Tuff and the tuff of Brunton Pass. The welded whole rock sample from the tuff of Brunton Pass shows a small negative Ce anomaly, however, there doesn't appear to be the same enrichment in LREEs compared to the non-anomalous whole rock sample that is present in the anomalous REE tuff of Clipper Gap samples (normalizing data from Sun and McDonough, 1989).

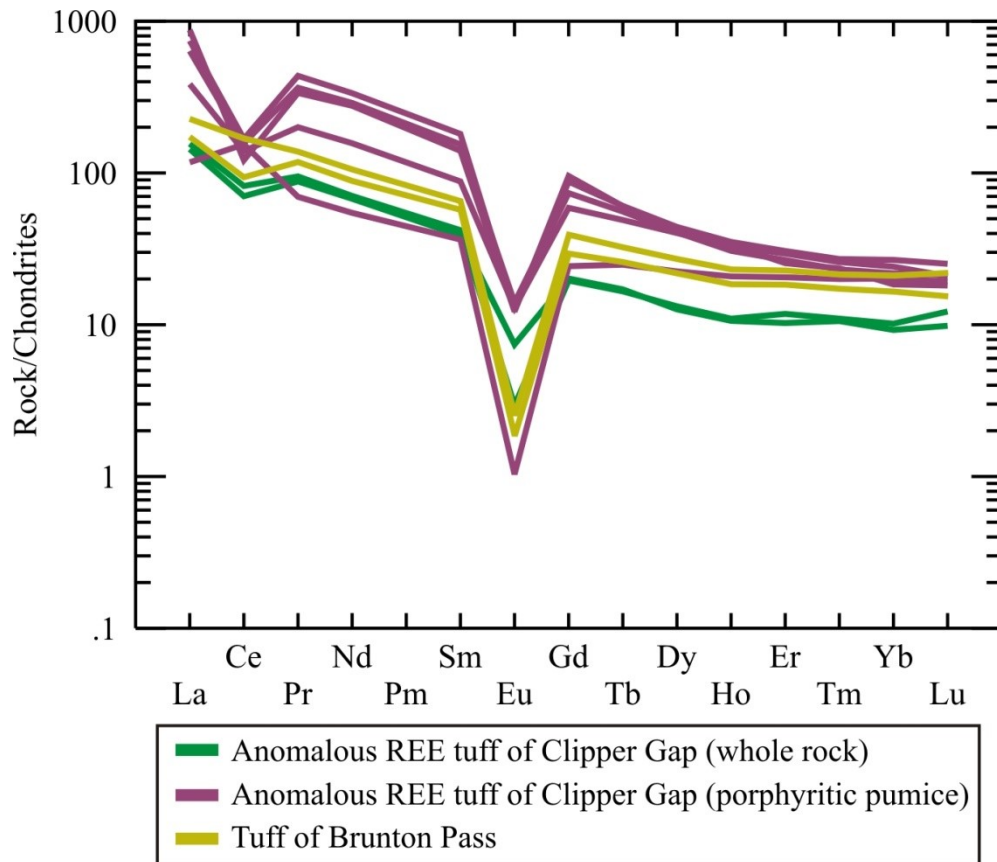


Figure 7.35: Chondrite normalized REE diagram showing the comparison between the anomalous REE Clipper Gap whole rock and porphyritic pumice samples to the tuff of Brunton Pass. The welded tuff of Brunton Pass sample with a small negative Ce anomaly shows less LREE enrichment than the anomalous REE Clipper Gap porphyritic pumice, but slightly more LREE enrichment than in the anomalous REE Clipper Gap whole rock samples (normalizing data from Sun and McDonough, 1989).

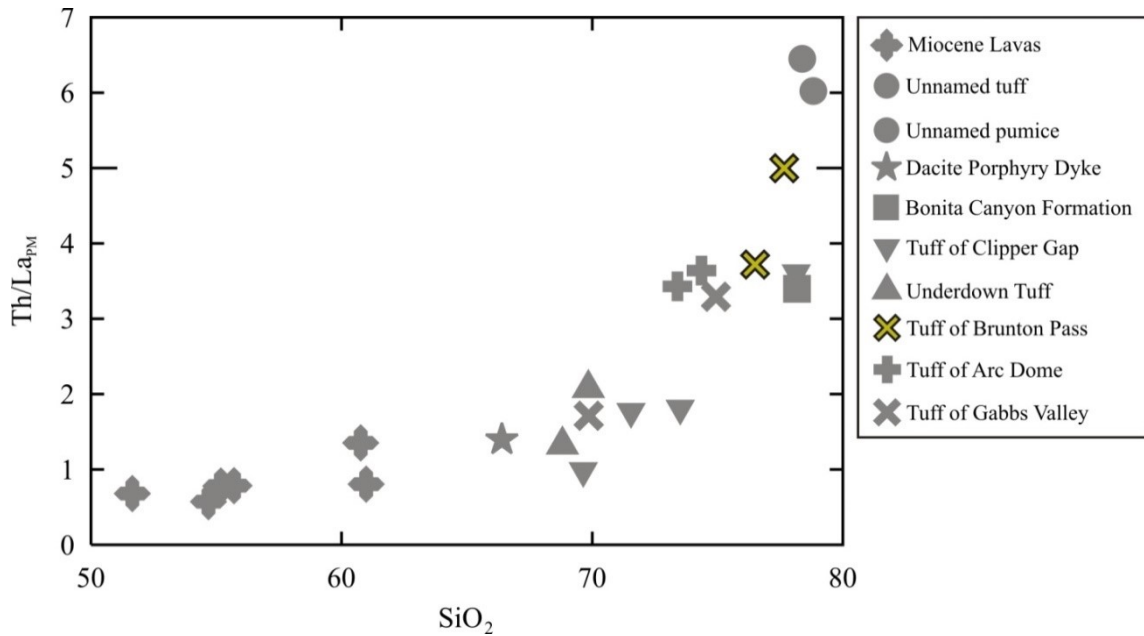


Figure 7.36: Primitive mantle normalized Th/La vs. SiO₂ content indicating crustal addition into the Oligocene tuffs and Miocene lavas. The tuff of Brunton Pass samples plot along this curve, suggesting they may be derived from the same sources as the Oligocene tuffs and the Miocene lavas (primitive mantle normalizing values from Sun and McDonough, 1989).

The age of the tuff of Brunton Pass samples collected from the margins of the Underdown Caldera, in addition to its sparsely porphyritic texture, anomalous REEs observed in the welded sample, and similarity of the Th/La ratios to the other evolved (high-SiO₂) Oligocene tuffs suggests that this unit may be from the tuff of Clipper Gap, as opposed to the tuff of Brunton Pass as it is currently identified.

7.3.4 The Terrill Mountains tuffs

While the current mapped exposures of the tuff of Clipper Gap are primarily to the east of the caldera (Best et al., 2013), a series of ignimbrites of similar age have recently been found to the west of the caldera in the Terrill Mountains (Carlson, 2018) and were sampled for comparison. This unit was originally identified as the tuff of Gabbs Valley, however it has an age of 24.95 ± 0.02 Ma, which is younger than the tuff of Gabbs Valley (Carlson, 2018).

As observed in Figures 6.10 and 6.13, the Terrill Mountains tuffs plot as a cluster at the most evolved (highest SiO_2) end of the fractionation trends of the Oligocene tuffs on major element and trace element bivariate diagrams. However, as has already been discussed, most of the ignimbrites in the WNVF plot along these same major element fractionation trends, therefore other comparisons must be used to determine their relationship to the Underdown Tuff and tuff of Clipper Gap. Chondrite normalized REE and primitive mantle normalized trace element diagrams show how the Terrill Mountains tuffs have normalized patterns identical to the Underdown Tuff whole rock samples (Fig. 7.37). In a Th/La (normalized to primitive mantle) versus SiO_2 diagram, the Terrill Mountains tuffs plot along the correlation formed by the Miocene lavas and Oligocene tuffs (Fig. 7.38). In this plot, the Terrill Mountains tuffs cluster with the tuff of Arc Dome, TgV2, Bonita Canyon Formation and tuff of Clipper Gap samples. This suggests that the Terrill Mountains tuffs (24.95 ± 0.02 Ma, Carlson, 2018) may be

related to the Underdown Caldera ignimbrites with which they cluster, and that they may originate from the same sources as the Miocene lavas and the Oligocene tuffs.

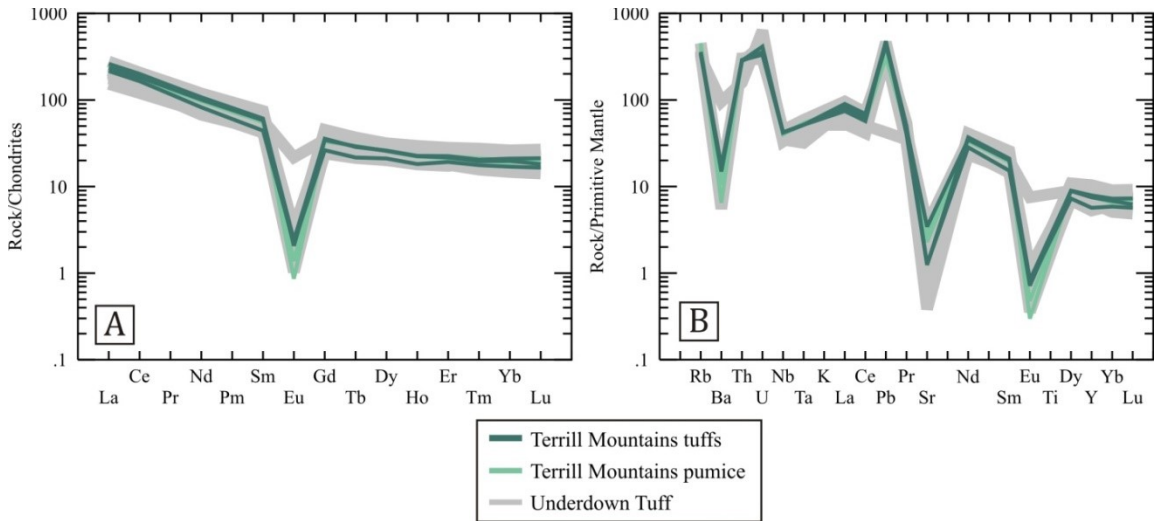


Figure 7.37: (A) Chondrite normalized REE and (B) primitive normalized trace element diagrams showing the comparison between the Underdown Tuff (whole rock samples), the Terrill Mountains tuffs and the Terrill Mountains pumice. The Terrill Mountains tuffs and pumice show normalized patterns nearly identical to the Underdown Tuff in both diagrams (normalizing data from Sun and McDonough, 1989).

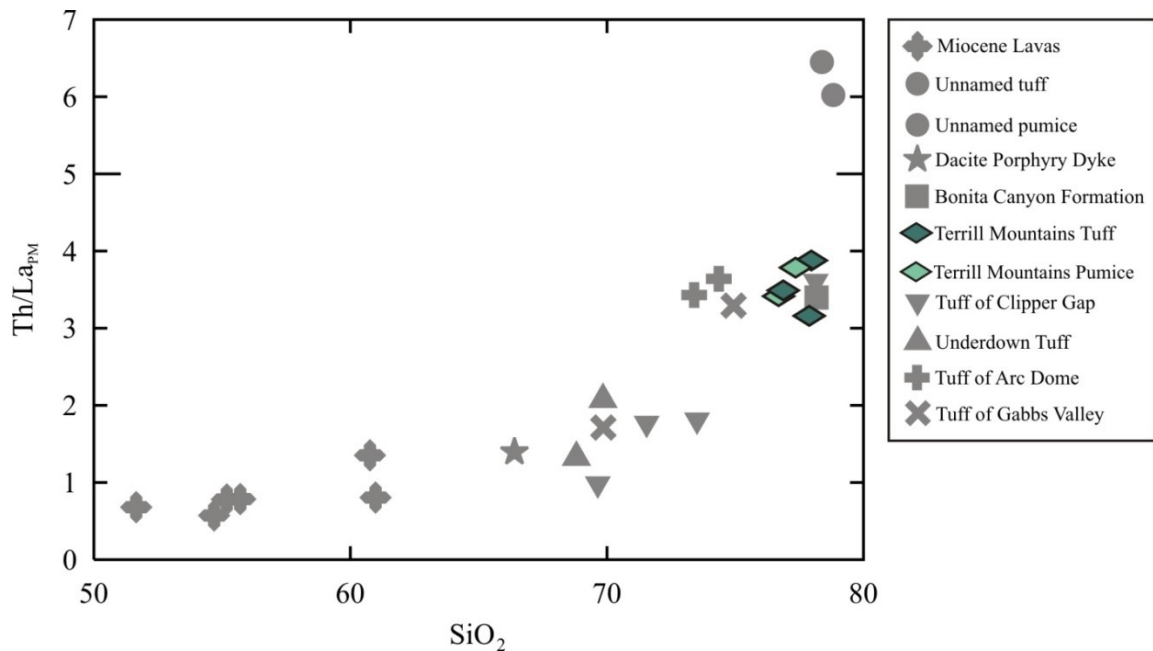


Figure 7.38: Primitive mantle normalized Th/La vs. SiO₂ content indicating crustal addition into the Oligocene tuffs and Miocene lavas. The Terrill Mountains tuffs plot along this curve, suggesting they may be mixtures of the same sources for the Oligocene tuffs (primitive mantle normalizing values from Sun and McDonough, 1989).

As shown in Figure 7.1, the Sr isotopic data for the Terrill Mountains tuffs are suspect. Therefore, Nd and Pb isotopes were used to compare the Terrill Mountains tuffs with the ignimbrites from the Underdown Caldera (data for the tuff of Clipper Gap is from the acid-washed samples). On an initial ϵNd versus $^{206}\text{Pb}/^{204}\text{Pb}$ diagram, the Terrill Mountains tuffs show the most isotopic similarity to the Unnamed Tuff, Bonita Canyon Formation, Underdown Tuff and TgV3 (now assumed to be a Bonita Canyon Formation outflow tuff), while the acid-washed tuff of Clipper Gap samples plot at higher ϵNd values (Fig. 7.39A). On a $^{208}\text{Pb}/^{204}\text{Pb}$ versus $^{206}\text{Pb}/^{204}\text{Pb}$ diagram, the Terrill Mountains tuffs show the most similarity to the same units as the previous comparison (Unnamed

tuff, Bonita Canyon Formation, Underdown Tuff) (Fig. 7.39B). However, the whole rock sample from the Terrill Mountains tuffs is more similar to TgV2 and the tuff of Arc Dome samples. Once again, the Terrill Mountains tuffs plot away from the acid-washed tuff of Clipper Gap samples.

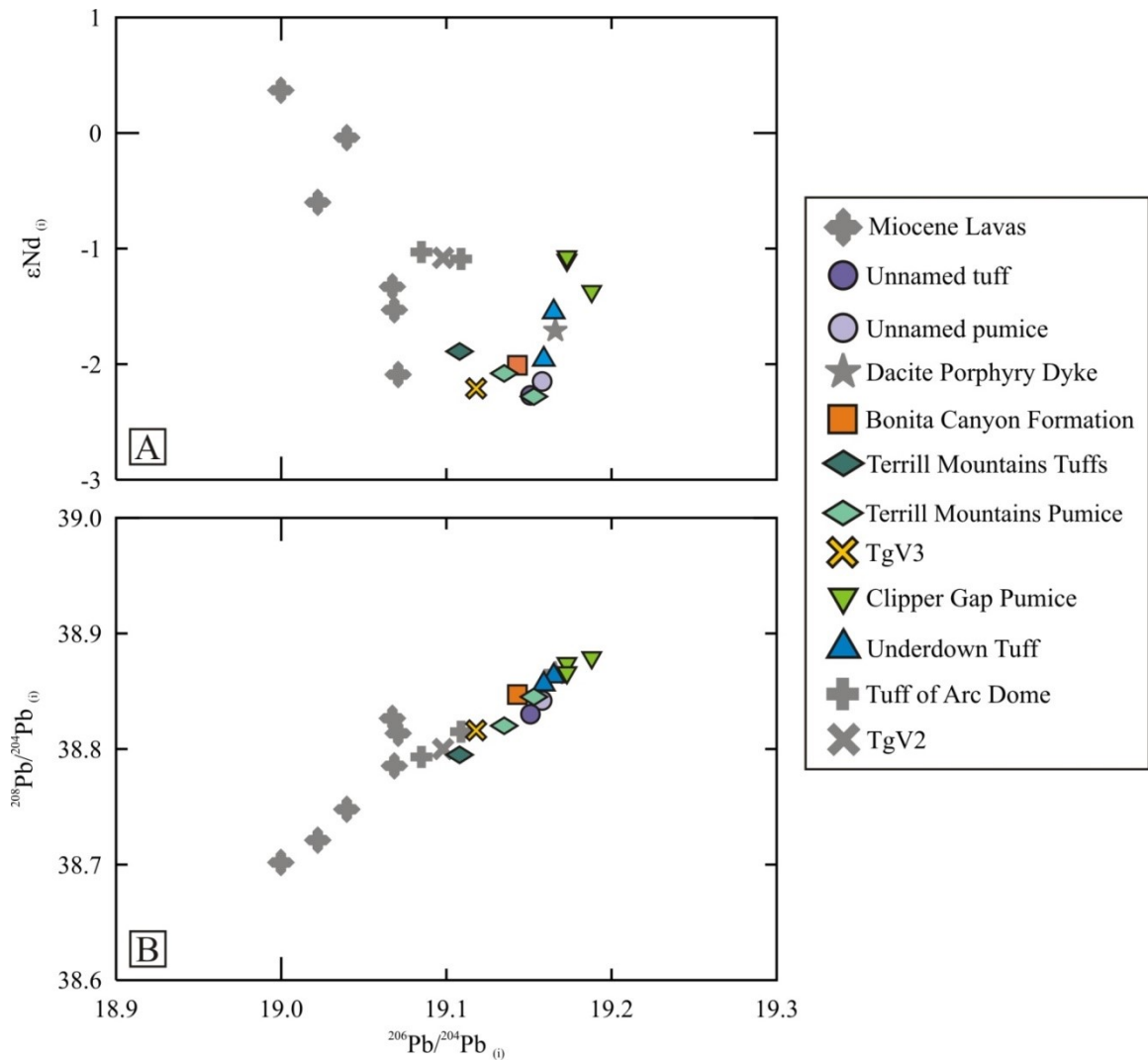


Figure 7.39: (A) Initial ϵNd versus $^{206}\text{Pb}/^{204}\text{Pb}$ and (B) initial $^{208}\text{Pb}/^{204}\text{Pb}$ versus $^{206}\text{Pb}/^{204}\text{Pb}$ showing the comparison between the Terrill Mountains tuffs and the other Oligocene tuffs from the Underdown Caldera complex. The Nd and Pb isotopic data of the Terrill Mountains tuffs show similarity to the Unnamed tuff, Bonita Canyon Formation, and TgV3, as well as the Underdown tuff in the Pb isotopic comparison. The samples show fewer isotopic similarities to the acid-wash tuff of Clipper Gap samples than the other ignimbrites.

In summary, based on the age and geochemical characteristics of the Terrill Mountains tuffs, the ignimbrites are postulated to be outflow tuffs from the Underdown Caldera complex, and the position of the Terrill Mountains tuffs along the Th/La crustal addition curve suggests a similar origin as the other Oligocene tuffs. The Terrill Mountains tuffs isotopic data suggest that these units are most similar to the Bonita Canyon Formation. While the Unnamed tuff shows isotopic similarities to the Terrill Mountains tuffs (24.95 ± 0.02 Ma, Carlson, 2018) on the isotopic diagrams, the age of the Unnamed tuff (24.755 ± 0.037 Ma, C. Henry, pers. comm., 2018), rules out that these two units are correlative. The identification of these units suggests that there are potentially more exposures of Underdown Caldera outflow tuff which exists to the west of the caldera complex, expanding the current range, and that the Bonita Canyon Formation may have a correlative tuff outside of the Underdown Caldera Complex.

7.3.5 Young Sierra Nevada tuffs

Igimbrites from the Sierra Nevada Mountains in California of similar age to the Underdown Caldera event are postulated to represent more outflow tuff from the Underdown Caldera, and will be referred to as the Young Sierra Nevada tuffs. The Young Sierra Nevada tuffs were found overlying the Nine Hill Tuff and have been dated at 24.888 ± 0.015 Ma (C. Henry, pers. comm., 2018) which is similar to the Underdown Tuff. The Young Sierra Nevada tuffs have been compared to the Underdown Tuff to investigate their possible relationship. Major and trace element geochemistry was provided by C. Henry (personal communication, 2018).

Major Element Geochemistry

Major element data of the Young Sierra Nevada tuffs are listed in Appendix I, Table IV. The Young Sierra Nevada tuffs are felsic in composition and plot within the rhyolite field in a TAS diagram (Le Maitre et al., 1989) within a cluster of Underdown Tuff samples (Fig. 7.40). On major element bivariate diagrams, the Young Sierra Nevada tuffs plot as a cluster with the cluster of Underdown Tuff whole rock samples for all major element oxides (Fig. 7.41).

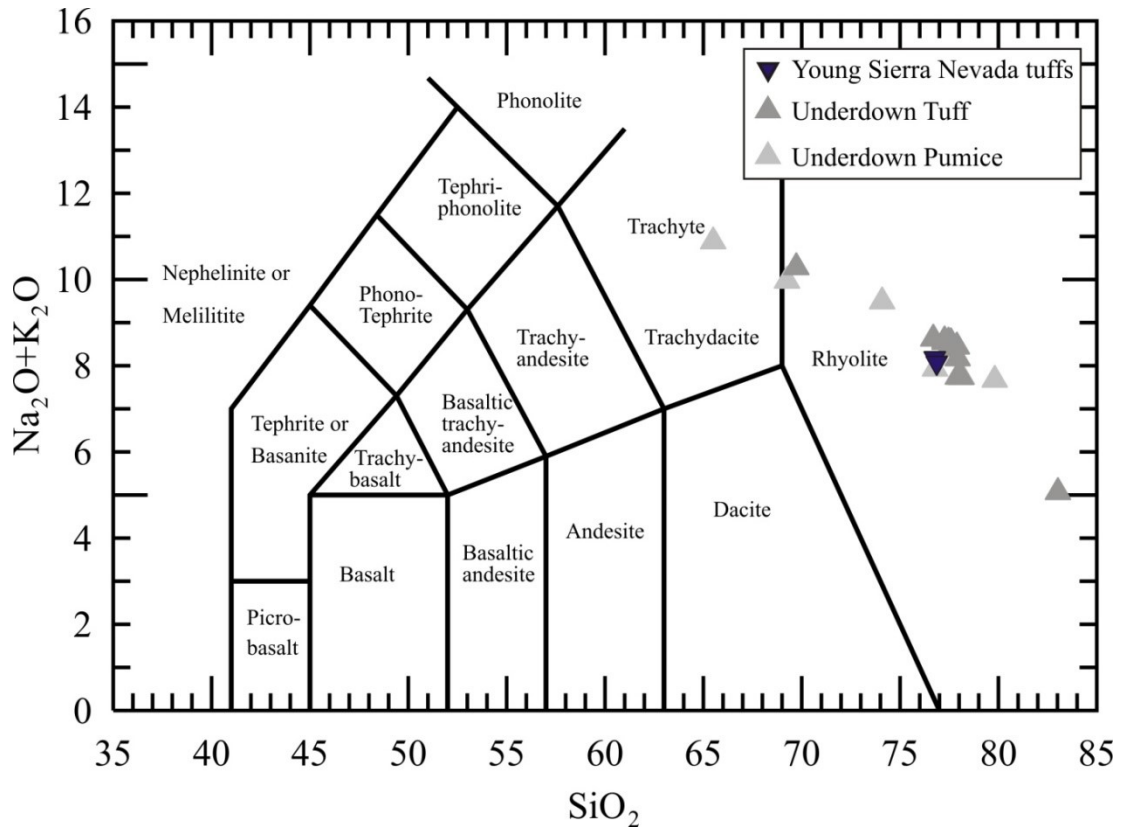


Figure 7.40: Total alkalis-silicate diagram (Le Maitre et al., 1989) comparing the Young Sierra Nevada tuffs to the Underdown Tuff. The Young Sierra Nevada tuffs are felsic in composition and plot in the rhyolite field with a cluster of the Underdown Tuff whole rock samples.

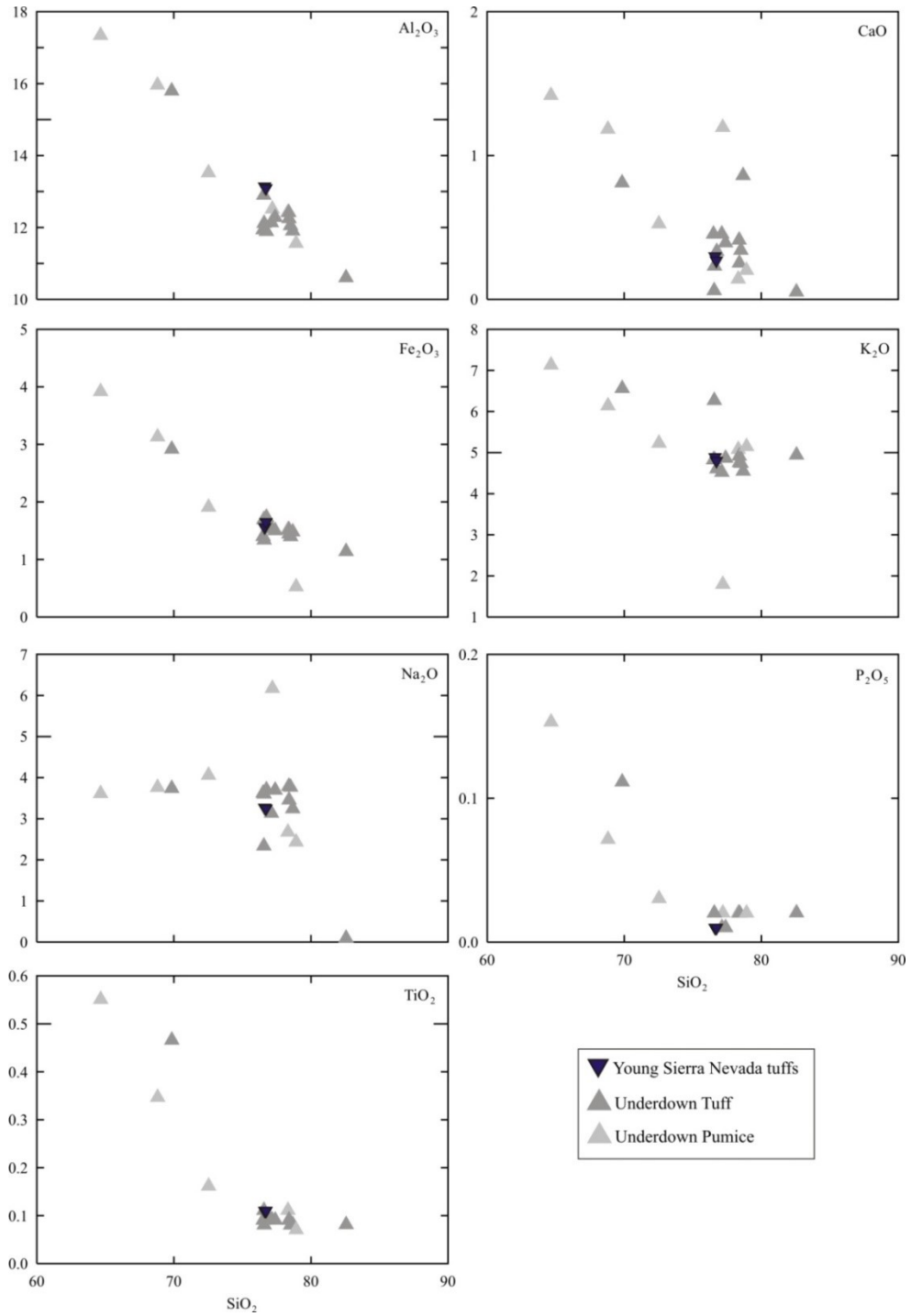


Figure 7.41: Major element variation diagrams comparing the Young Sierra Nevada tuffs with the Underdown Tuff. The Young Sierra Nevada tuffs show similar major element oxide abundances as clusters of the Underdown Tuff whole rocks in all major element oxides.

Trace Element Geochemistry

Trace element data for the Young Sierra Nevada tuffs are listed in Appendix I, Table VI. Similar to the major element bivariate diagrams, the Young Sierra Nevada tuffs show similar trace element concentrations as whole rock samples from the Underdown Tuff. In all trace element versus SiO_2 comparisons the Young Sierra Nevada tuffs plot as a cluster with the Underdown Tuff whole rock samples (Fig. 7.42).

In a chondrite normalized rare earth element diagram, the Young Sierra Nevada tuffs shows the same enrichment in LREEs and flattening pattern to the HREEs as the Underdown Tuff whole rock samples (Fig. 7.43). The negative Eu anomaly observed in the Young Sierra Nevada tuffs is also identical to the negative Eu anomaly observed in the Underdown Tuff. Similarly, in a primitive mantle trace element diagram, the Young Sierra Nevada tuffs show a pattern nearly identical to the Underdown Tuff whole rock samples (Fig 7.43). The same negative anomalies are observed in Ba, Sr, and Eu, as well as the same positive Pb anomaly. In addition, the Young Sierra Nevada tuffs lack a negative Nb-Ta anomaly which is also mostly absent from the Underdown Tuff.

The Young Sierra Nevada tuffs were also plotted with the Oligocene tuffs and Miocene lavas on a Th/La (normalized to primitive mantle) versus SiO_2 diagram (Fig. 7.44). The Young Sierra Nevada tuffs plot within the correlation formed by the Miocene lavas and Oligocene tuffs, suggesting that they have a similar input of crustal addition into their melt as ignimbrites from the Underdown Caldera complex, and may originate from the same sources as the Miocene lavas and the Underdown Caldera ignimbrites.

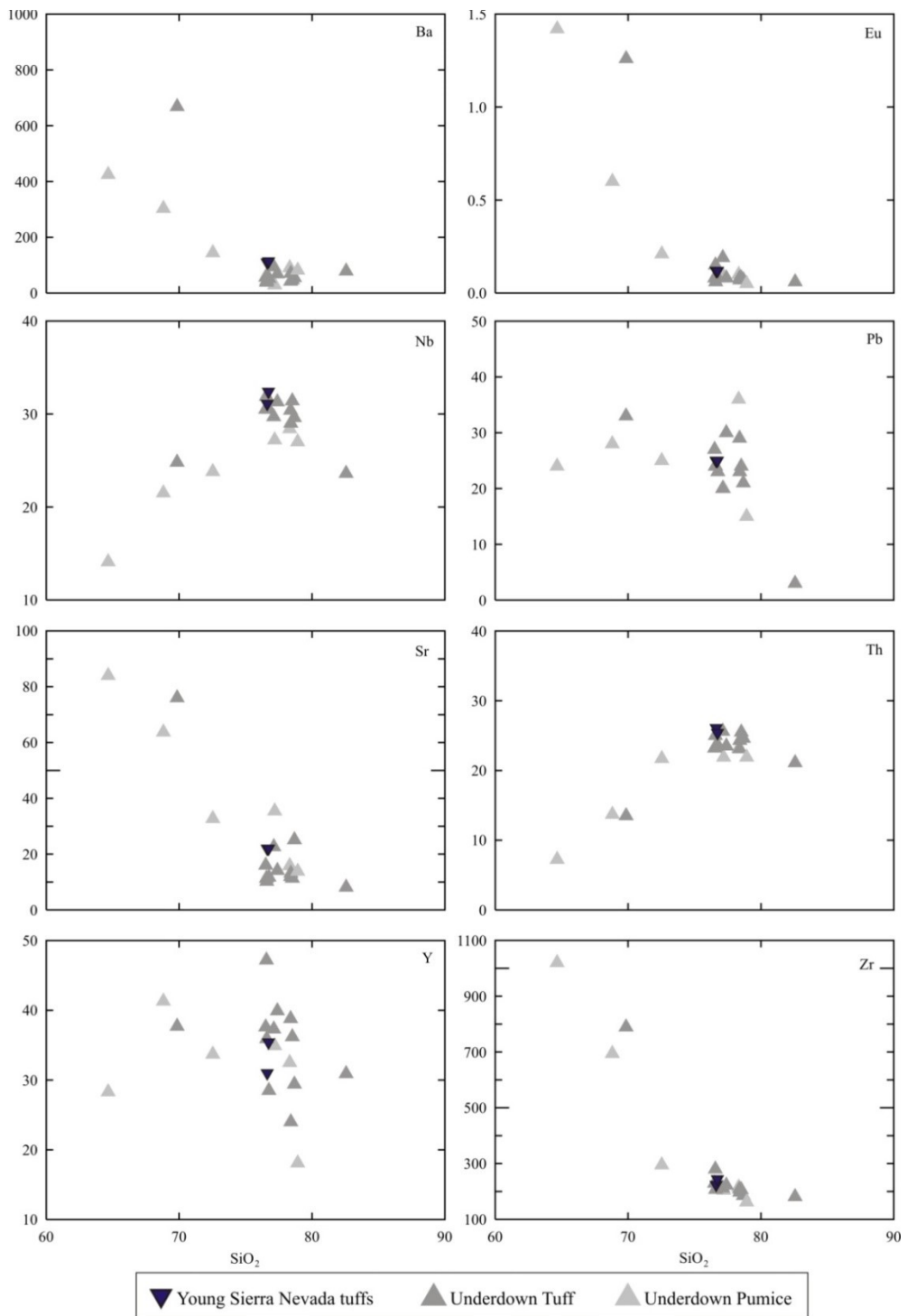


Figure 7.42: Trace element bivariate diagrams comparing the Young Sierra Nevada tuffs to the Underdown Tuff. The Young Sierra Nevada tuffs plot as a cluster with the Underdown Tuff whole rock samples in all trace element comparisons except for Y which appears scattered in both units.

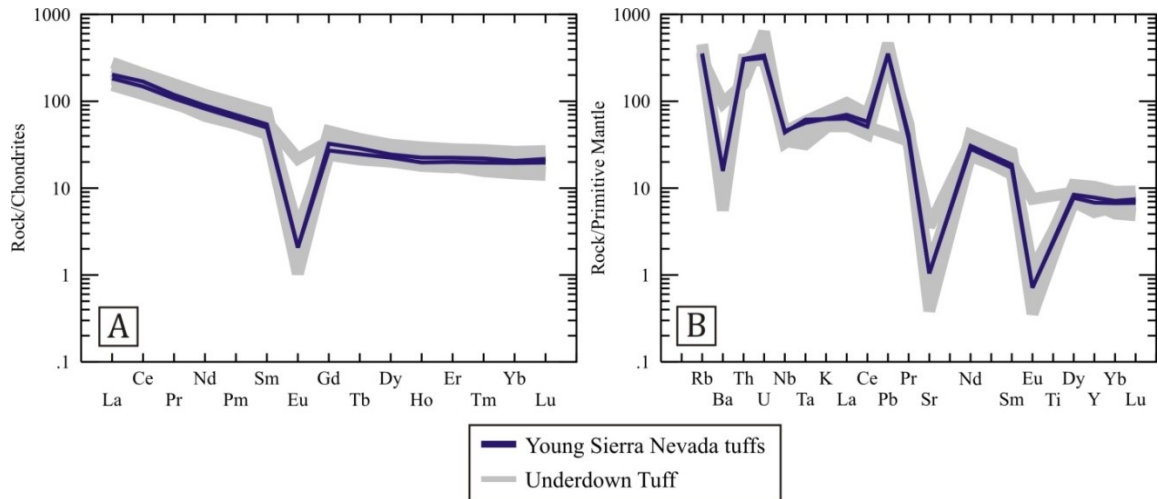


Figure 7.43: (A) Chondrite normalized REE and (B) primitive mantle normalized trace element diagrams comparing the Young Sierra Nevada tuffs with the Underdown Tuff. In panel (A) the Young Sierra Nevada tuffs show the same enrichment in LREEs and flattening pattern to the HREEs as the Underdown Tuff, as well as a similar negative Eu anomaly. In panel (B) the Young Sierra Nevada tuffs shows the same sized negative anomalies in Ba, Sr, and Eu, and the same sized positive Pb anomaly. The unit also lacks a negative Nb-Ta anomaly which is also observed in the Underdown Tuff (normalizing data from Sun and McDonough, 1989).

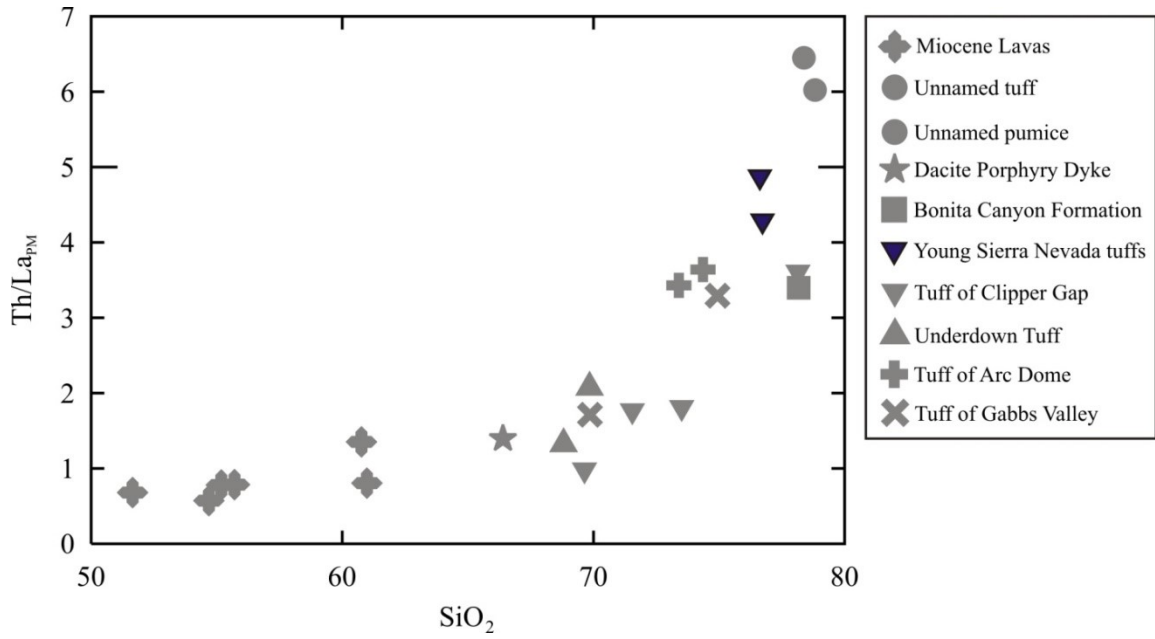


Figure 7.44: Primitive mantle normalized Th/La vs. SiO₂ content indicating crustal addition into the Oligocene tuffs and Miocene lavas. The Young Sierra Nevada tuffs plot along this curve, suggesting they may be derived from the same sources as the Oligocene tuffs and the Miocene lavas (primitive mantle normalizing values from Sun and McDonough, 1989).

On the crustal addition diagram (Fig. 7.44), the Young Sierra Nevada tuffs appear to show more similarity to the Bonita Canyon Formation than the Underdown Tuff. To further investigate this comparison, the Young Sierra Nevada tuffs and Bonita Canyon Formation were plotted on chondrite normalized REE and primitive mantle normalized trace element diagrams (Fig. 7.45). On these plots, the Young Sierra Nevada tuffs appear similar to the Bonita Canyon Formation (especially the most chemically evolved Bonita Canyon Formation samples), however do not show the identical normalized patterns which were observed when compared to the Underdown Tuff (Fig. 7.43).

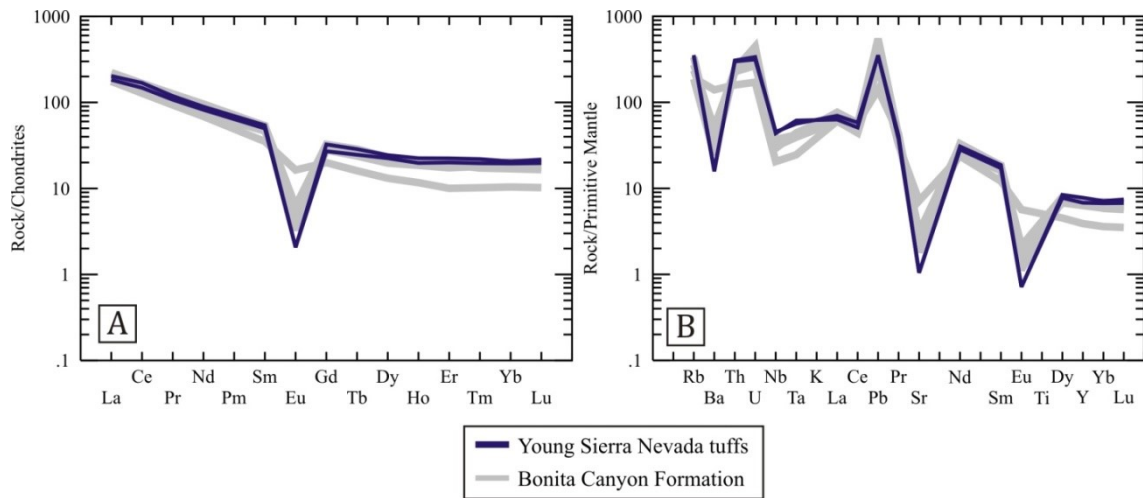


Figure 7.45: (A) Chondrite normalized REE and (B) primitive mantle normalized trace element diagrams showing the comparison between the Young Sierra Nevada tuffs and the Bonita Canyon Formation. While the normalized patterns are similar in both units, they are not identical as was observed when the Young Sierra Nevada tuffs were compared to the Underdown Tuff. The Young Sierra Nevada tuffs appear to have higher enrichments of Th, Nb and Ta than the Bonita Canyon Formation, as well as slightly larger negative Sr and Eu anomalies (normalizing data from Sun and McDonough, 1989).

As the Young Sierra Nevada tuffs appear, with the available major and trace element data, to be nearly indistinguishable from the Underdown Tuff, it is possible that they may represent an exposure of outflow tuff in California, far to the west of the Underdown Caldera complex. However, the diagram of crustal addition suggests a higher crustal component in the Young Sierra Nevada Tuffs than in the Underdown Tuff, which is more similar to the Bonita Canyon Formation. Comparison using isotopic data would be imperative to fully determine the identity of the Young Sierra Nevada tuffs.

Paleovalleys would have played an integral role in the distribution of outflow tuff from the Underdown Caldera, depositing the Terrill Mountains tuffs, the Young Sierra Nevada tuffs, and likely other unidentified exposures of outflow tuff in western Nevada and the Sierra Nevada Mountains. At the time of the Underdown Caldera magmatic event, the Sierra Nevada Mountains were not the topographic barrier they are today, as the region had not yet been affected by Great Basin extension. Henry and John (2013) illustrate the location and flow direction of paleovalleys in the Western Great Basin, however all identified western outflow tuffs on this map are related to the Nine Hill Tuff and tuff of Campbell Creek (Fig. 7.46). However, this isn't to say that there are no western outflow tuffs from the Underdown Caldera complex, as indicated by the Terrill Mountains tuffs and the Young Sierra Nevada tuffs. Based on the presented geochemical data, it is possible that these two western outflow units could be related; however, additional data for each unit, as well as isotopic data for the Young Sierra Nevada tuffs, would enable a more complete comparative study.

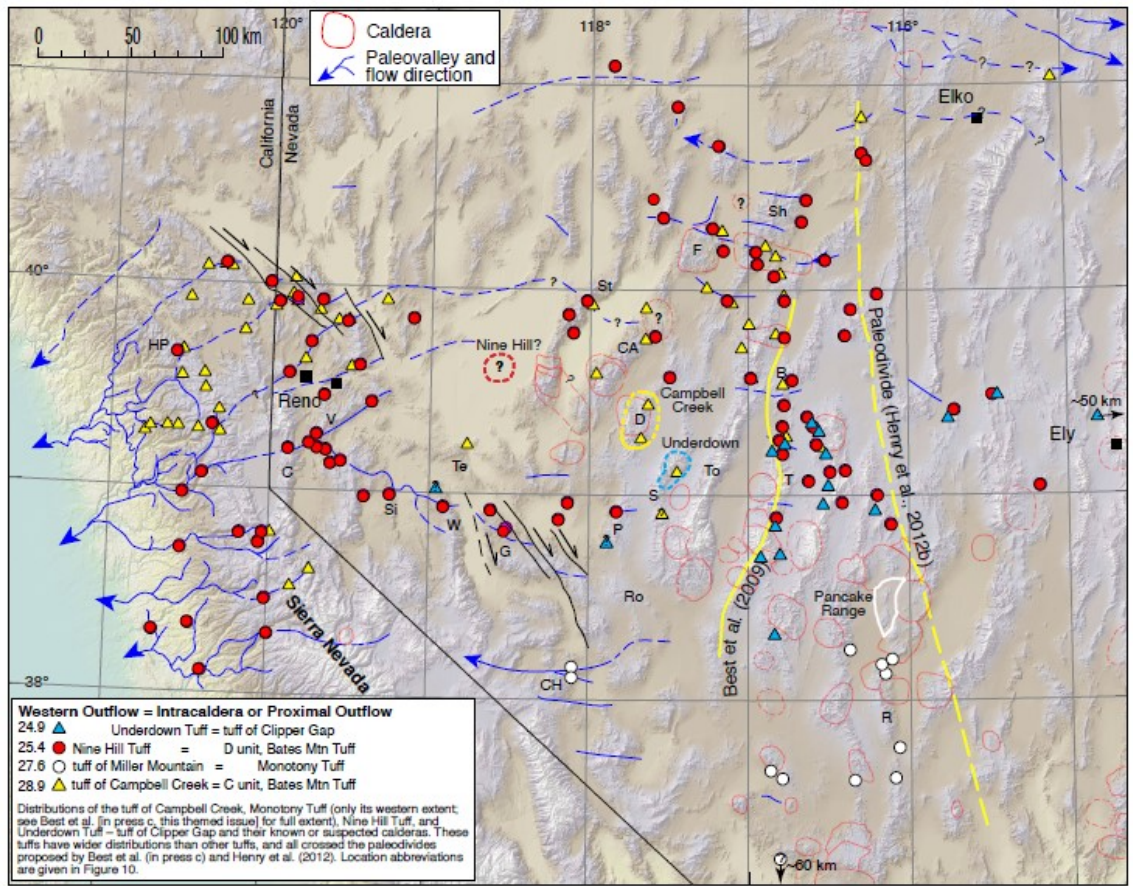


Figure 7.46: Map of the Western Great Basin, showing the location of the Underdown Tuff (light blue dashed circle) and the placement and flow direction of paleovalleys. The high concentration of paleovalleys travelling across the Nevadaplano and through what is now the Sierra Nevada Mountains would have funneled outflow tuffs from the Underdown Caldera to the west of the paleodivide (from Henry and John, 2013).

7.4 The Origin of Porphyritic Pumice in the Underdown Tuff

Porphyritic pumice was present in two ignimbrite units in the Underdown caldera complex; the Underdown Tuff and the tuff of Clipper Gap. This crystal rich pumice is a stark contrast to the white, aphyric pumice which is found in the vast majority of Underdown Tuff and tuff of Clipper Gap exposures. The question of where these two pumice types originate from is the focus of this section. All samples of porphyritic pumice from the tuff of Clipper Gap contain anomalous REE abundances and therefore only the porphyritic pumice from the Underdown Tuff will be discussed.

7.4.1 Field Observations and Petrography

In the field, the porphyritic pumice had a characteristic dark purple colour and was observed to contain phenocrysts of two feldspars and quartz. The pumice ranged in shape from very small and flattened to very large (Fig. 7.47). In general, the porphyritic pumice appeared highly altered under petrographic observation. This included alteration in the glassy matrix and alteration of the phenocrysts. The porphyritic pumice samples were determined to contain plagioclase + sanidine + quartz \pm trace amounts of biotite and hornblende.



Figure 7.47: Field photograph of a porphyritic pumice from the Underdown Tuff. Porphyritic pumices observed in the field in the Underdown Tuff and the tuff of Clipper Gap are purple and contain quartz and feldspar phenocrysts. The hammer head is 18 cm long.

7.4.2 Major Element Geochemistry

The porphyritic pumice of the Underdown Tuff plots in a trend from rhyolite to trachyte on a TAS diagram (Fig. 7.48, Le Maitre, 1989). The Underdown Tuff whole rock samples generally plot as a cluster between 75-80 weight percent in the rhyolite field with one outlying high silica rhyolite sample. The outlying sample is interpreted to have undergone post-deposition silicification, and will be removed from the remainder of the discussion. Two porphyritic pumice samples plot with the cluster of whole rock data in the rhyolite field. Major element oxide concentrations in the porphyritic pumice samples show more compositional variation than in the Underdown Tuff whole rock samples (Fig. 7.49). Generally, the porphyritic pumice have a lower SiO₂ content than whole rock samples however, two porphyritic pumice samples plot in a cluster with whole rock and the white pumice.

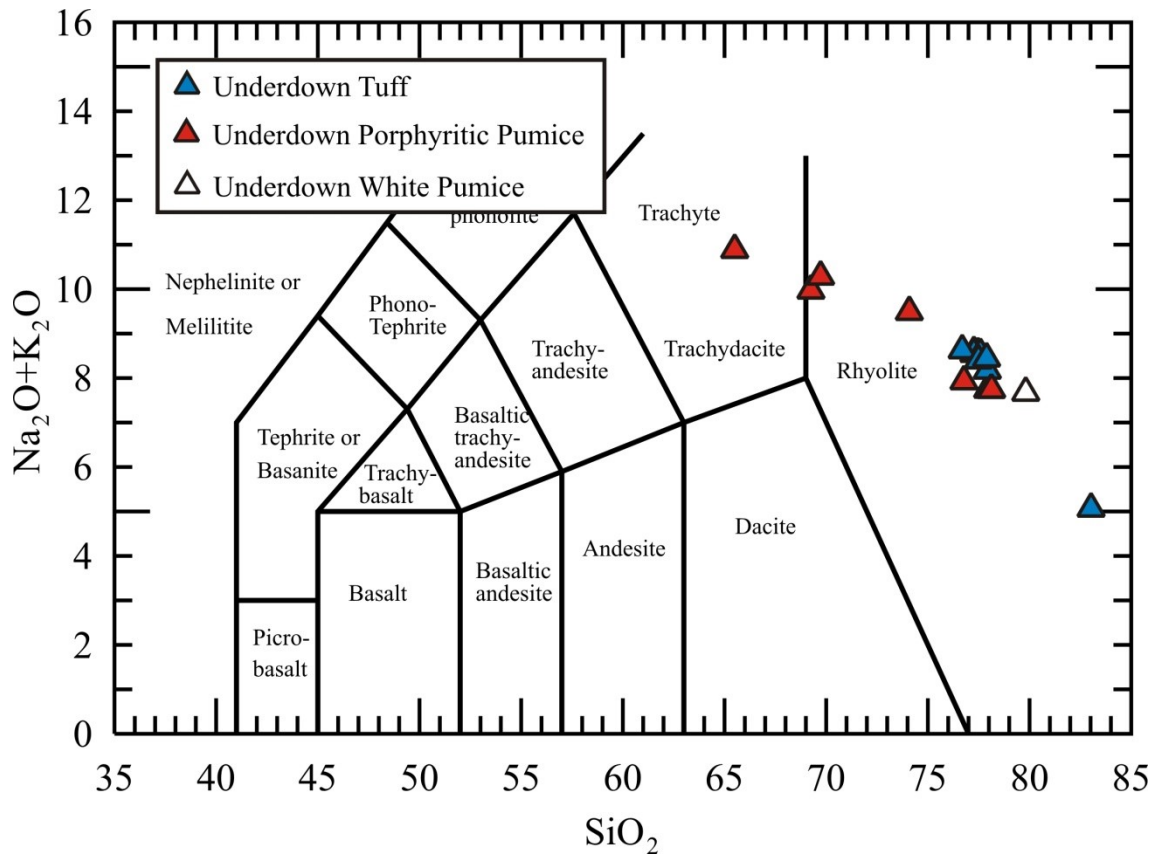


Figure 7.48: Total alkalis-silica diagram (Le Maitre et al., 1989) of the Underdown Tuff, porphyritic pumice and white pumice. The porphyritic pumice plots in a trend from rhyolite into the trachyte field while the Underdown whole rock samples plot as a cluster in the rhyolite field with one outlying high silica rhyolite sample. The white pumice is rhyolitic in composition. The high-silica rhyolite outlier (~83% SiO_2) is interpreted to have undergone post-deposition silicification.

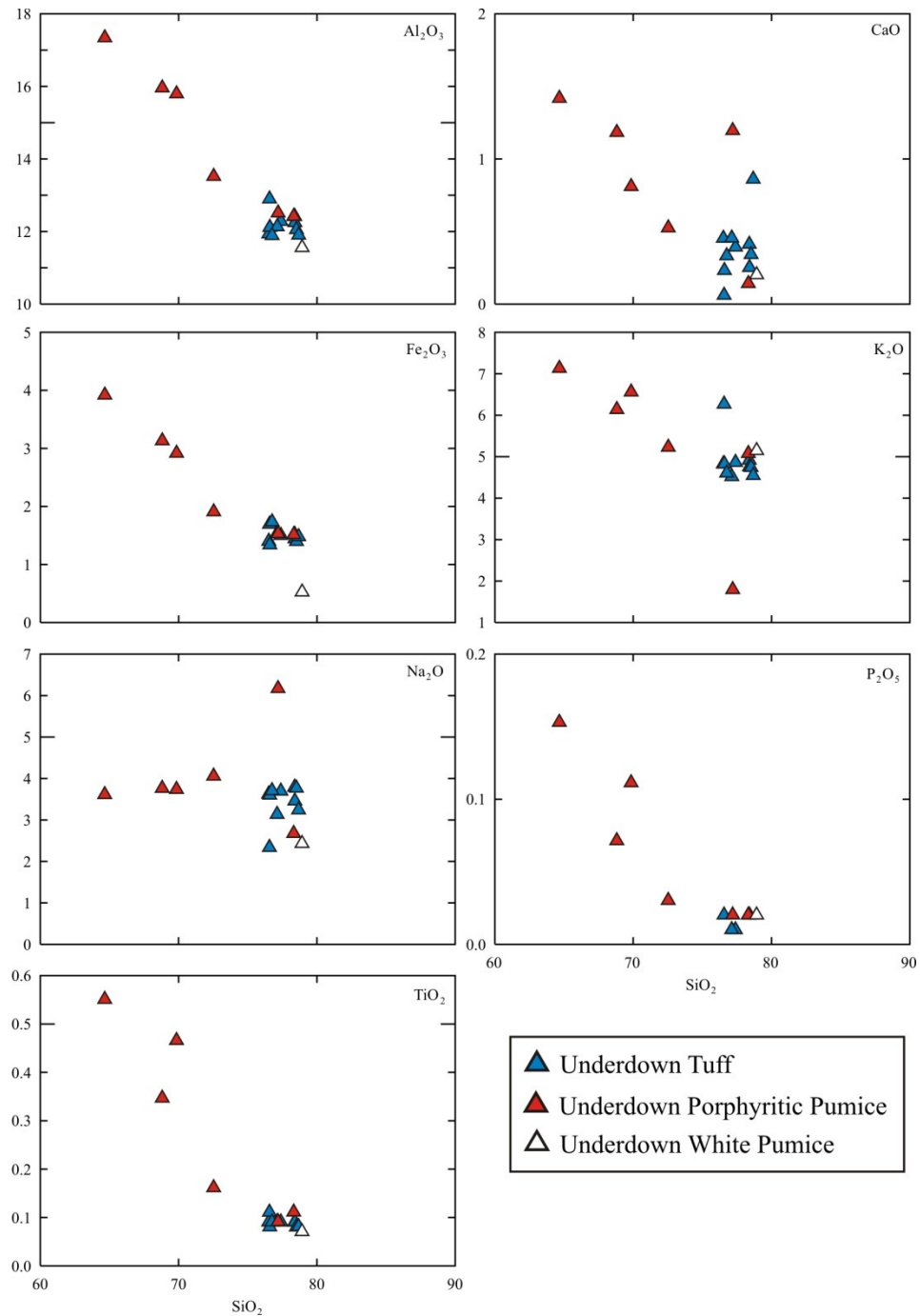


Figure 7.49: Major element oxide versus SiO₂ content diagrams for the Underdown Tuff. Porphyritic pumice is generally more primitive than the whole rock and white pumice of the Underdown Tuff, with two exceptions. The porphyritic pumice show more compositional variation between the samples than the whole rock samples which generally cluster between 75-80 weight percent.

7.4.3 Trace Element Geochemistry

Barium, Eu, Sr, and Zr behave as compatible elements in the Underdown porphyritic pumice while Nb and Th behave as incompatible elements. Pb and Y show scattered abundances in the porphyritic pumice data. The Underdown Tuff whole rock samples plot as a cluster in all trace elements except for Pb and Y where the samples show more scatter (Fig. 7.50).

A chondrite normalized rare earth element diagram (Fig. 7.51A) comparing average whole rock, average porphyritic pumice and white pumice from the Underdown Tuff shows that whole rock, white pumice, and porphyritic pumice are enriched in LREEs relative to the HREEs, while the porphyritic pumice appears to be slightly more enriched in the LREEs compared to the whole rock samples. The whole rock and white pumice samples have similar large negative Eu anomalies that are larger than those in the porphyritic pumices. The average porphyritic pumice and whole rock samples show a flattened pattern in the HREEs, while the white pumice shows a more depleted pattern in the HREEs. On a primitive mantle normalized trace element diagram (Fig. 7.51B) the whole rock and white pumice samples show similar patterns except in the HREEs. The average porphyritic pumice shows smaller negative anomalies in Ba, Sr, and Eu than are observed in the whole rock and white pumice. The porphyritic pumices also include a lower Th and higher U enrichment than the whole rock and white pumice, and have a more pronounced Nb-Ta anomaly.

The most evolved and least evolved porphyritic pumice samples were plotted on chondrite normalized REE and primitive mantle normalized trace element diagrams with the average whole rock samples and white pumice sample to illustrate the variation in trace element abundance across the porphyritic pumices (Fig. 7.52). In both diagrams, the most evolved porphyritic pumice (16-SM-29A) shows a similar pattern of LREE enrichment and HREE flattening as the average whole rock. However, the least evolved porphyritic pumice (17-SM-17C) shows a much smaller Eu anomaly on the chondrite normalized REE plot. When normalized to primitive mantle, the least evolved porphyritic pumice shows differences in the Ba, Sr, and Eu anomalies (all are smaller negative anomalies), lower enrichment in Th, higher enrichment in U, and a more negative Nb-Ta anomaly.

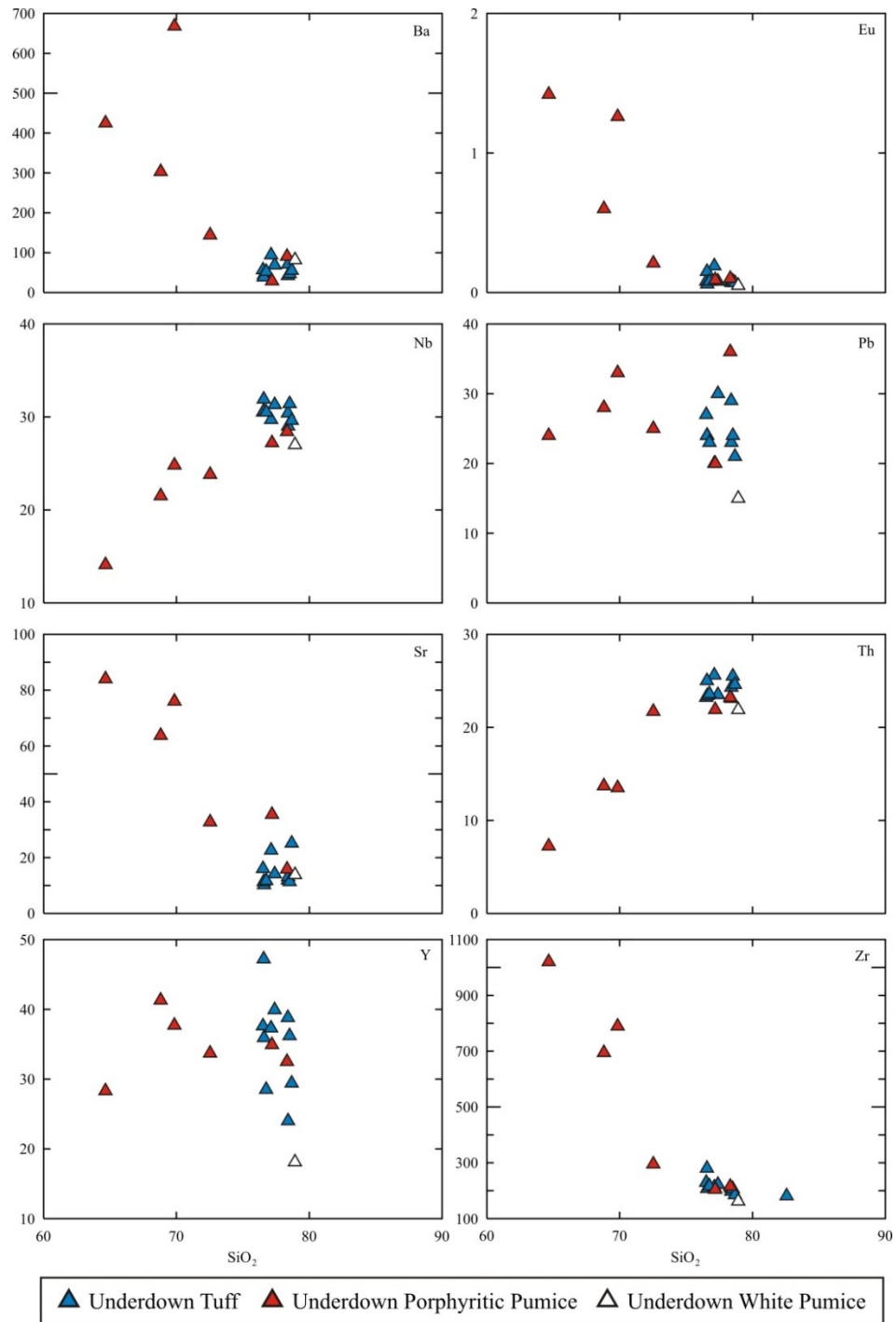


Figure 7.50: Trace element bivariate diagrams showing the compatibility of trace elements in the Underdown Tuff whole rock, porphyritic pumice and white pumice. Similar to the major element oxides, the porphyritic pumice show more compositional variation than the whole rock samples.

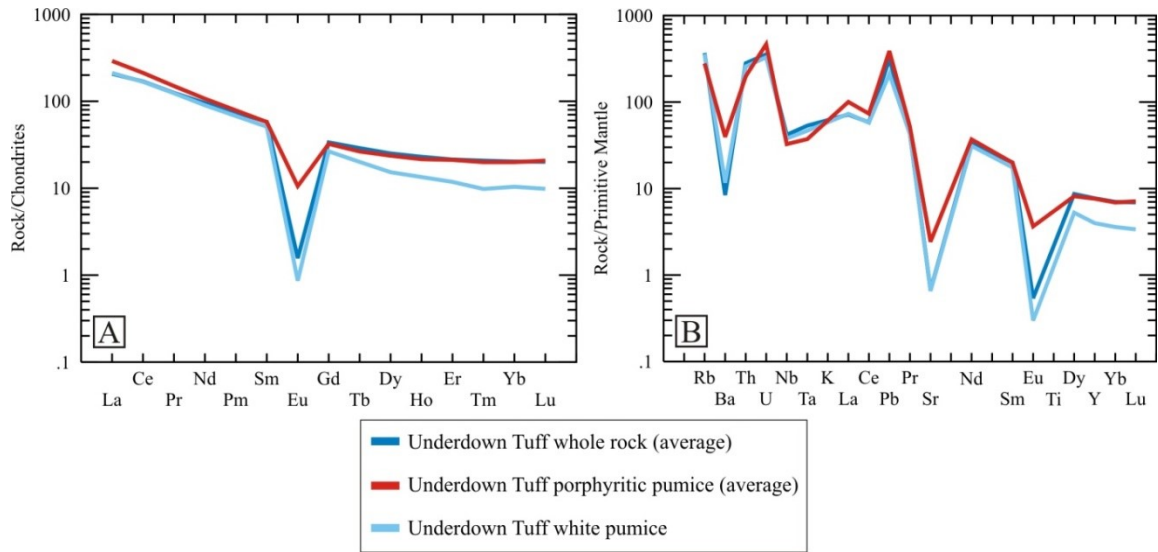


Figure 7.51: (A) Chondrite normalized rare earth element plot and (B) primitive mantle normalized trace element plot of the average Underdown Tuff whole rock, average porphyritic pumice, and white pumice samples (normalizing data from Sun and McDonough, 1989).

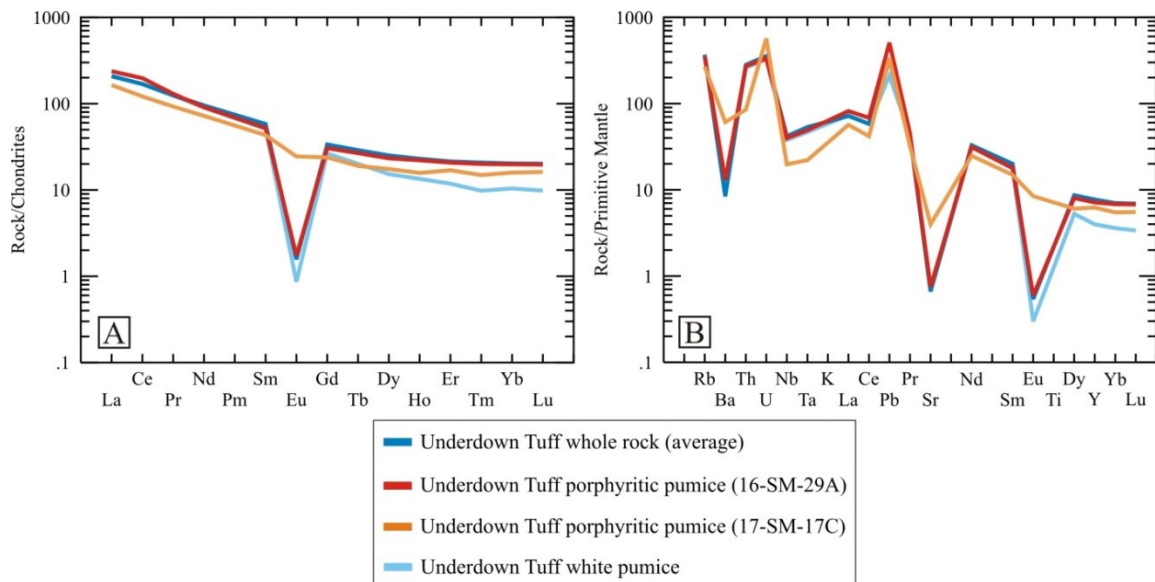


Figure 7.52: (A) Chondrite normalized rare earth element plot and (B) primitive mantle normalized trace element plot of the average Underdown Tuff whole rock sample, most evolved porphyritic pumice sample (16-SM-29A), least evolved porphyritic pumice sample (17-SM-17C), and white pumice sample (16-SM-29B) (normalizing data from Sun and McDonough, 1989).

7.4.4 Source of the Porphyritic Pumice

Despite some differences in geochemistry between the porphyritic pumice and whole rock samples of the Underdown Tuff, the porphyritic pumice likely originates from a similar source as the Underdown Tuff. The more primitive geochemistry of many of the porphyritic pumice samples is likely a result of weathering which has removed SiO_2 and increased the alkali content in the pumice, causing the samples to plot in a trend from the rhyolite to trachyte fields. A similar trend is observed in the tuff of Clipper Gap porphyritic pumice samples, and in the pumice of the Fish Creek Mountains tuff (Varve, 2013). Two porphyritic pumice samples plot with the group of whole rock Underdown

data on the TAS diagram and in the major and trace element bivariate diagrams. These two samples are interpreted to not be weathered. If the porphyritic pumice were from a more primitive source than the whole rock and white pumice, they would likely all plot at a more primitive SiO_2 content in the subalkaline field, rather than in a trend towards alkaline rocks. On the normalized REE and trace element plots, the average porphyritic pumice appears to have differences in anomaly size compared to the average whole rock and white pumice samples. This is likely a result of the variation in trace element concentration between the samples, as made evident by the trace element bivariate plots and the normalized REE and trace element diagrams. The most evolved (highest SiO_2) porphyritic pumice sample used for this comparison (16-SM-29A) was collected from the same unit as the white pumice sample. The sample plots with the group of whole rock samples on the TAS, major element bivariate plots, and trace element bivariate plots, and is interpreted to be less weathered than other porphyritic pumice samples. The least evolved, lowest SiO_2 porphyritic pumice sample was collected from float at the base of a large Underdown Tuff outcrop in Barrett Canyon. This sample plots in the trachyte field of the TAS diagram and has the lowest SiO_2 content of all the porphyritic pumice samples. This comparison shows that the porphyritic pumice which is potentially fresh appears to be from the same source as the whole rock sample, and the least evolved porphyritic pumice sample has a trace element signature which is likely a result of weathering that has removed certain trace element containing phases from the rock. Based on the geochemical data, the porphyritic pumice in the Underdown Tuff is interpreted to be from a similar source as the whole rock and white

pumice samples, and observed differences in geochemistry are a result of weathering. In addition to the geochemical data, the shape of the porphyritic pumice suggests that they are not fragments of rock broken off of another source and incorporated into the magma, for example from wall rock in a magma chamber.

Since the porphyritic pumice is much more crystal rich than the whole rock of the Underdown Tuff and the aphyric white pumice (which is interpreted to represent the pure magma which formed the ignimbrite), the porphyritic pumice must originate from a more crystal rich liquid than the melt forming the bulk of the ignimbrite. It is possible that the magma reservoir from which the Underdown Tuff originates tapped a more crystalline liquid source, such as a magma mush, and blobs of crystal rich material were incorporated into the melt. A magma mush zone consists mainly of crystals surrounded by an interconnected network of melt which may make up as little as one percent of the material in the magma mush (Bachmann and Bergantz, 2008; Winter, 2001). The erupted blobs of crystal mush may represent the purple porphyritic pumice observed in the Underdown Tuff. It is assumed that the same processes are responsible for the formation of the porphyritic pumice in the tuff of Clipper Gap. However, the presence of purple porphyritic pumice is not restricted to the Underdown Tuff and tuff of Clipper Gap. Similar porphyritic pumice was observed in the tuff of Campbell Creek, a 28.9 Ma ash flow tuff in the WNVF (Henry and John, 2013) (Fig. 7.53). The presence of the large, porphyritic pumice in a tuff unit unrelated to the Underdown event suggests that their presence may be more common in Great Basin ignimbrites than previously thought.

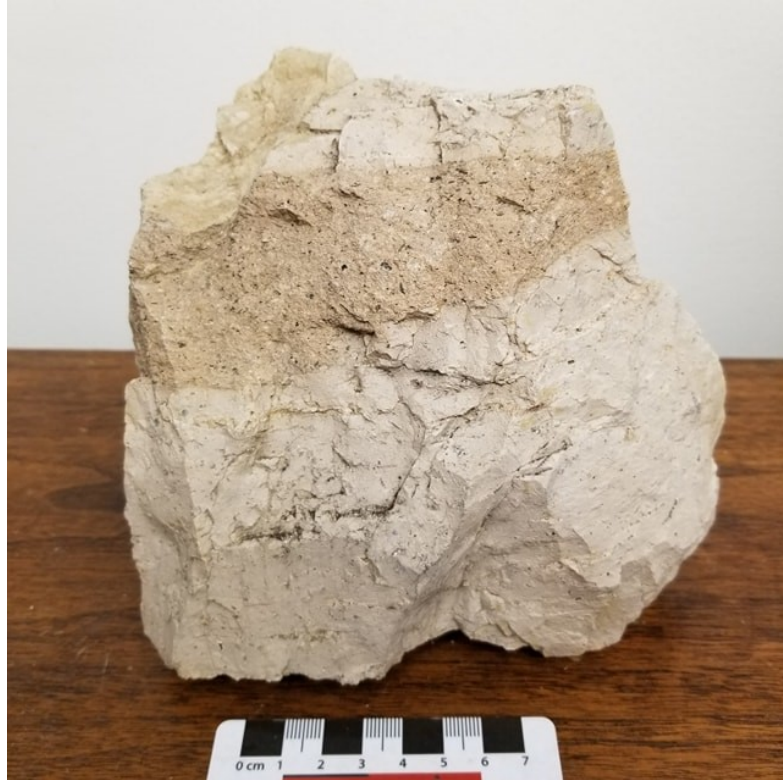


Figure 7.53: Porphyritic pumice in the Tuff of Campbell Creek. The observation of porphyritic pumice in a crystal poor ash flow tuff outside of the Underdown Caldera suggests that the presence of porphyritic pumice in Great Basin ignimbrites may be more common than previously thought.

8.0 Conclusions

8.1 The Underdown Caldera Complex

The Oligocene tuffs of the Underdown Caldera complex are “Great Basin” style ignimbrites. Isotopic data supports a common primary magma source as the Miocene lavas located on the margin of the caldera; potentially a mixture of the sub-continental lithospheric mantle and local crustal source. The rocks of the Underdown Caldera complex have undergone post-deposition alteration by groundwater which has altered some initial Sr isotopic ratios. Measured negative Ce anomalies in several ignimbrite samples are the result of enrichment of rare earth elements produced by groundwater alteration which appears to have more strongly affected porphyritic pumice of the tuff of Clipper Gap than in other units. Porphyritic pumice may originate from a crystal mush beneath the caldera, and may be more common in the Western Nevada Volcanic Field than previously thought. The Bonita Canyon Formation appears to be a distinct ignimbrite unit overlying the Underdown Tuff, and the Unnamed tuff is likely not an exposure of the Tuff of Toiyabe as it is currently mapped. The Unnamed tuff is more likely a younger ignimbrite unit of the Underdown Caldera complex which may represent a later stage of caldera forming volcanism. Spires of the older tuff of Arc Dome and Pablo Formation found within the Underdown caldera margins are postulated to represent pieces of wall rock of the Underdown Caldera which fell inwards during caldera collapse. Outflow tuff from the Underdown Caldera complex is not restricted to the east of the caldera, however outflow to the west and the south may

not necessarily be correlative to just the Underdown Tuff. Two ignimbrites exposed in Gabbs Valley (TgV2 and TgV3) are more likely the tuff of Arc Dome and Bonita Canyon outflow tuff, as opposed to the tuff of Gabbs Valley. The similarities between the Bonita Canyon Formation and newly identified outflow tuffs suggest there may be more than one outflow unit from the Underdown Caldera complex.

8.2 Future Work

In the future, any new samples collected from the Underdown Caldera ignimbrites should be acid-washed before isotopic analysis, as multiple samples in this study were affected by alteration. Blocks mapped as Pablo Formation on the Bonham map (1970) should be re-mapped as their correct units. An extension of mapping to the north and south of the range of Bonham's map could also provide more information about the extent of the Underdown Caldera. New Sr isotopic data for the Terrill Mountains tuffs would allow for a more confident comparison of the potential outflow unit to the Underdown Caldera ignimbrites. As well, scanning electron microscope (SEM) analysis of the anomalous REE samples could identify the presence of REE enriched clays that are postulated to be responsible for apparent Ce anomalies. Finally, isotopic data from the Young Sierra Nevada tuffs would allow for a more complete comparison of this unit to the Underdown Tuff or Bonita Canyon Formation.

References

- Aitcheson, S.J., Harmon, R.S., Moorbath, S., Schneider, A., Soler, P., Soria-Escalante, E., Steele, G., Swainbank, I. and Wörner, G., 1995, Pb isotopes define basement domains of the Altiplano, central Andes. *Geology*, v. 23(6), p. 555-558.
- Allègre, C.J., 2008, *Isotope geology* (p. 512). Cambridge: Cambridge University Press.
- Annen, C., Sparks, R.S.J., 2002, Effects of repetitive emplacement of basaltic intrusions on thermal evolution and melt generation in the crust: *Earth and Planetary Science Letters*, v. 203, p. 927-955
- Annen, C., Blundy, J.D., Sparks, R.S.J., 2006, The Genesis of Calcalkaline Intermediate and Silicic Magmas in Deep Crustal Hot Zones: *Journal of Petrology* v. 47, p. 505-539.
- Annen, C., Blundy, J.D., Sparks R.S.J., 2008, The sources of granitic melt in Deep Hot Zones: *Transactions of the Royal Society of Edinburgh: Earth Sciences*, v. 97(4), p. 297-309.
- Armstrong, L.R., Ward, P., 1991, Evolving geographic patterns of Cenozoic magmatism in the North American Cordillera: The temporal and spatial association of magmatism and metamorphic core complexes: *Journal of Geophysical Research: Solid Earth*, v. 96(B8), p. 13201-13224.
- Atwater, T, 1970, Implications of plate tectonics for the Cenozoic tectonic evolution of western North America: *Geological Society of America Bulletin*, v. 81(12), p. 3513-3536.
- Bachmann, O., Bergantz, G.W., 2008, Rhyolites and their source mushes across tectonic settings: *Journal of Petrology*, v. 49, n. 12, p. 2277-2285, doi: 10.1093/petrology/egn068.
- Best, M.G., Armstrong, R.L., Graustein, W.C., Embree, G.F., and Ahlborn, F.C., 1974, Mica granites of the Kern Mountains pluton, eastern White Pine County, Nevada: Remobilized basement of the Cordilleran miogeosyncline: *Geological Society of America Bulletin*, v. 85, p. 1277–1286, doi: 10.1130/0016-7606(1974)85
- Best, M.G., Gromme, S., Deino, A.L., Christiansen, E.H., Hart, G.L., Tingey, D.G., 2013, The 36-18 Ma Central Nevada ignimbrite field and calderas, Great Basin, USA: Multicyclic super-eruptions: *Geosphere*, v. 9, p. 1562-1636, doi: 10.1130/GES00945.1.

- Best, M.G., Christiansen, E.H., de Silva, S., Lipman, P.W., 2016, Slab-rollback ignimbrite flareups in the southern Great Basin and other Cenozoic American arcs: A distinct style of arc volcanism: *Geosphere*, v. 12(4), p. 1097-1135, doi: 10.1130/GES01285.1.
- Bohnam, H.F., 1970, Geologic map and sections of a part of the Shoshone Mountains, Lander and Nye counties, Nevada. Nevada Bureau of Mines.
- Boulangé, B., Muller J.P., Sigolo, J.B., 1990, Behaviour of the rare earth elements in a lateritic bauxite from syenite (Brasil): Geochemistry of the Earth's surface of mineral formation, *Spec. Issue Chem. Geol.*, v. 84, p. 350-351.
- Braun, J.J., Pagel, M., Muller, J.P., Bilong, P., Michard, A., Guillet, B., 1990, Cerium anomalies in lateritic profiles: *Geochimica et Cosmochimica Acta*, v. 54, p. 781-796.
- Cadek, O., Fleitout, L., 2003, Effect of lateral viscosity variation in the top 300 km on the geoid and dynamic topography: *Geophysical Journal International*, v. 152(3), p. 566-580.
- Camp, V.E., Pierce, K.L. and Morgan, L.A., 2015, Yellowstone plume trigger for Basin and Range extension, and coeval emplacement of the Nevada-Columbia Basin magmatic belt. *Geosphere* 11, doi: 10.1130/GES01051.1.
- Carlson, C.W., 2018, Geological Map of the Terrill Mountains Quadrangle, Churchill and Mineral Counties, Nevada: Nevada Bureau of Mines and Geology Map 187.
- Chamberlin, R.M., 1983, Cenozoic domino-style crustal extension in the Lemitar Mountains, New Mexico: A summary. In *Guidebook, 34th Field Conference, Socorro Region II* (V. 34, p. 111-118). New Mexico Geological Society Socorro, New Mexico.
- Christiansen, E.H., 2005, Contrasting processes in silicic magma chambers: evidence from very large volume ignimbrites: *Geology*, v.142, n.6, p. 669-681, doi: 10.1017/S0016756805001445.
- Clemens, J.D. and Stevens, G., 2012, What controls chemical variation in granitic magmas?: *Lithos*, 134, p. 317-329.
- Colgan, J.P., and Henry, C.D., 2009, Rapid middle Miocene collapse of the Sevier orogenic plateau in north-central Nevada: *International Geology Review*, v. 51, p. 920-961.
- Colgan, J.P., Watts, K.W., Henry, C., and John, D., 2013, Characterizing geographic variability in magma composition and eruptive style during voluminous mid-Tertiary magmatism in the northern Great Basin using zircon U-Pb geochronology and

phenocryst O isotopic data: Washington, D.C., American Geophysical Union, Fall Meeting, abstract V33E-2831.

Coney, P.J., 1978, Mesozoic–Cenozoic Cordilleran plate tectonics, in Smith, R.B., and Eaton, G.P., eds., *Cenozoic Tectonics and Regional Geophysics of the Western Cordillera*: Geological Society of America Memoir 152, p. 33–50.

Cousens, B.L., Spera, F.J., Dobson, P.F., 1993, Post-eruptive alteration of silicic ignimbrites and lavas, Gran Canaria, Canary Islands: Strontium, neodymium, lead, and oxygen isotopic evidence: *Geochimica et Cosmochimica Acta*, v. 57, p. 631-640.

Cousens, B.L., Prytulak, J., Henry, C.D., Alcazar, A. and Brownrigg, T., 2008, The geology, geochronology and geochemistry of the Miocene-Pliocene Ancestral Cascades Arc, northern Sierra Nevada, California/Nevada: The roles of the upper mantle, subducting slab, and the Sierra Nevada lithosphere: *Geosphere*, v. 4(5): 829-853.

Cousens, B.L., Henry, C.D., and Gupta, V., 2012, Distinct mantle sources for Pliocene Quaternary volcanism beneath the modern Sierra Nevada and adjacent Great Basin, northern California and western Nevada, USA. *Geosphere*, v. 8, p. 562-580.

Cousens, B.L., Henry, C.D., Stevens, C., Varve, S., John, D.A., Wetmore, S., 2019, Igneous rocks in the Fish Creek Mountains and environs, Battle Mountains area, north-central Nevada: A microcosm of Cenozoic igneous activity in the northern Great Basin, Basin and Range Province, USA: *Earth-Science Reviews*, v. 192, p. 403-444, doi: 10.1016/j.earscirev.2019.03.013

Davidson, J., 1985, Mechanisms of contamination in Lesser Antilles island arc magmas from radiogenic and oxygen isotope relationships: *Earth and Planetary Science Letters*, v. 72, p. 163-174.

Decelles, P.G., 2004, Late Jurassic to Eocene evolution of the Cordilleran thrust belt and foreland basin system, western USA: *American Journal of Science*, v. 304, p. 105-168.

DePaolo, D.J., 1981, Trace element and isotopic effects of combined wallrock assimilation and fractional crystallization. *Earth and Planetary science letters*, v. 53(2), p. 189-202.

de Silva, S., 2008, Arc magmatism, calderas, and supervolcanoes: *Geology*, v. 36, p. 671–672.

Dickin, A.P., 2005, *Radiogenic isotope geology* (p. 492). Cambridge University Press.

- Dickinson, W.R., 2006, Geotectonic evolution of the Great Basin: *Geosphere*, v. 2, p. 353-368.
- Engebretson, D.C., Cox, A., Gordon, R.G, 1985, Relative motions between oceanic and continental plates in the Pacific basin: *Geological Society of America Special Papers*, 206, p. 1-60.
- Farmer, G.L., DePaolo, D.J., 1983, Origin of Mesozoic and Tertiary granite in the western United States and implications for Pre-Mesozoic crustal structure: 1. Nd and Sr isotopic studies in the geocline of the Northern Great Basin: *Journal of Geophysical Research*, v. 88(B4), p. 3379-3401, doi: 10.1029/JB088iB04p03379.
- Geist D. Richards M., 1993, Origin of the Columbia Plateau and Snake River Plain: Deflection of the Yellowstone plume: *Geology*, v. 21, p. 789–792.
- Hart, S.R., 1984, A large-scale isotope anomaly in the Southern Hemisphere mantle. *Nature*, v. 309(5971), p. 753-757.
- Henry, C.D., John, D.A., 2013, Magmatism, ash-flow tuff and calderas of the ignimbrite flareup in the western Nevada volcanic field, Great Basin, USA: *Geosphere* v. 9(3), p. 951-1008.
- Hildreth, W., 1981, Gradients in silicic magma chambers: Implications for lithospheric magmatism: *Journal of Geophysical Research*, v. 86, p. 10,153-10,192.
- Hildreth, W., and Moorbath, S., 1988, Crustal contributions to arc magmatism in the Andes of central Chile: *Contributions to Mineralogy and Petrology*, v. 98, p. 455-489.
- Humphreys, E., 2009, Relation of flat subduction to magmatism and deformation in the western United States: *Geological Society of America Memoirs*, v. 204, p. 85-98.
- Hutton, J., 1794, II. Observations on Granite: *Transaction of the Royal Society of Edinburg*, v. 3 (02), p. 77-85.
- Jarrard, R.D., 1986, Relations among subduction parameters: *Reviews of Geophysics*, v. 24(2), p. 217-284.
- John, D. A., 1974, Stratigraphy, regional distribution, and reconnaissance geochemistry of Oligocene and Miocene volcanic rocks in the Paradise Range and northern Pactolus hills, Nye County, Nevada: *U.S. Geological Survey Bulletin*, v. 67, doi: 10.3133/b1974.

John, D.A., Wallace, A.R., Ponce, D.A., Fleck, R.B. and Conrad, J.E., 2000, New perspectives on the geology and origin of the northern Nevada Rift. In: J.K. Cluer, J.G. Price, E.M. Struhsacker, R.F. Hardyman and C.L. Morris (Editors), *Geology and Ore Deposits 2000: The Great Basin and Beyond*, Symposium Proceedings. Geological Society of Nevada, pp. 127-154.

Le Maitre, R.W.B., Dudek, P., Keller, A., Lameyre, J., Le Bas, J., Sabine, M.J., Schmid, P.A., Sorensen, R., Streckeisen, H., Woolley, A. and Zanettin, A.R., 1989, A classification of igneous rocks and glossary of terms: Recommendations of the International Union of Geological Sciences, Subcommission on the Systematics of Igneous Rocks (No. 552.3 CLA). International Union of Geological Sciences.

Lee, D.E., Christiansen, E.H., 1983, The granite problem as exposed in the southern Snake Range, Nevada: *Contributions to Mineralogy and Petrology*, v. 83(1-2), p. 99-116, doi: 10.1007/BF00373083.

Lipman, P.W., Prostka, H.J., and Christiansen, R.L., 1972, Cenozoic volcanism and plate tectonic evolution of western United States, Part 1: Early and middle Cenozoic: *Philosophical Transactions of the Royal Society of London, Series A*, v. 271, p. 217–248, doi:10.1098/rsta.1972.0008.

Lipman, P.W., Prostka, P.J., and Christiansen, R.L., 1992, A discussion on volcanism and the structure of the Earth-Cenozoic volcanism and plate tectonic evolution of the western United States. 1. Early and middle Cenozoic, *Philosophical Transactions of the Royal Society A*, v. 271(1213), doi: 10.1098/rsta1972.0008.

Mahood, G. A. and Hildreth, W., 1983, Large partition coefficients for trace elements in high-silica rhyolites. *Geochemica et Cosmochimica Acta*, v. 47, p. 11-30.

Marsh, J.S., 1991, REE fractionation and Ce anomalies in weathered Karoo dolerite: *Chemical Geology*, v. 90, p. 189-194

McKee, E.H., 1971, Tertiary igneous chronology of the Great Basin of the western United States—Implications for tectonic models: *Geological Society of America Bulletin*, v. 82, p. 3497–3502.

Noble, D.C., 1972, Some observations on the Cenozoic volcano-tectonic evolution of the Great Basin, western United States: *Earth and Planetary Science Letters*, v. 17, p. 142-150, doi: 10.1016/0012-821X(72)90269-5.

- O'Driscoll, L.J., Humphreys, E.D., Saucier, F., 2009, Subduction adjacent to deep continental roots: Enhanced negative pressure in the mantle wedge, mountain building and continental motion: *Earth and Planetary Science Letters*, v. 280(1), p. 61-70.
- Parsons, T., McCarthy, J., Kohlery, W.M., Ammon, C.J., Benz, H.M., Hole J.A., Criley, E.E., 1996, Crustal structure of the Colorado Plateau, Arizona: Application of new long-offset seismic data analysis techniques: *Journal of Geophysical Research: Solid Earth*, v. 101(B5), p. 11,173-11,194.
- Perry, F.V., DePaolo, D.J. and Baldrige, W.S., 1993, Neodymium isotopic evidence for decreasing crustal contributions to Cenozoic ignimbrites of the western United States: Implications for the thermal evolution of the Cordilleran crust: *Geological Society of America Bulletin*, v. 105(7), p. 872-882.
- Proffett, J.M., Jr., 1977, Cenozoic geology of the Yerington district, Nevada, and implications for the nature and origin of Basin and Range faulting: *Geological Society of America Bulletin*, v. 88, p. 247-266.
- Putirka, K. and Busby, C.J., 2007, The tectonic significance of high-K₂O volcanism in the Sierra Nevada, California. *Geology*, v. 35(10), p. 923-926.
- Rollinson, H.R., 1993, *Using geochemical data: evaluation, presentation, interpretation* (p. 352): Essex: Pearson Education Limited.
- Rudnick, R.L., Fountain, D.M., 1995, Nature and composition of the continental crust: A lower crustal perspective: *Reviews of Geophysics*, v. 33, p. 267-309. doi: 10.1029/95RG01302
- Siebel, W., Schnurr, W.B., Hahne, K., Kraemer, B., Trumbull, R.B., van den Bogaard, P. and Emmermann, R., 2001, Geochemistry and isotope systematics of small-to medium-volume Neogene-Quaternary ignimbrites in the southern central Andes: evidence for derivation from andesitic magma sources. *Chemical Geology*, v. 171(3), p. 213-237.
- Smith, R.L., 1979, *Ash-flow magmatism*: Geological Society of America Special Paper 180, p. 5-27.
- Solano, J.M.S., Jackson, M.D., Sparks, R.S.J., Blundy, J.D. and Annen, C., 2012, Melt segregation in deep crustal hot zones: a mechanism for chemical differentiation, crustal assimilation and the formation of evolved magmas. *Journal of Petrology*, v. 53(10), p. 1999-2026.

Sparks, R.S.J., Self, S., Walker, G.P.L., 1973, Products of ignimbrite eruptions: *Geology*, v. 1, p. 115-118.

Stepner, D., 2017, Source and Magma Evolution of the tuff of Elevenmile Canyon, Stillwater Range, Clan Alpine and northern Desatoya Mountains, western Nevada (Masters of Science thesis). University of Ottawa, Ottawa, Ontario.

Sun, S.S. and McDonough, W.S., 1989, Chemical and isotopic systematics of oceanic basalts: implications for mantle composition and processes. *Geological Society, London, Special Publications*, v. 42(1), p. 313-345.

Tennant, E., 2018, Geochemistry and origin of mafic to intermediate lava flows in the Shoshone Mountains, Nevada, USA (Bachelor of Science Thesis). Carleton University, Ottawa, Ontario.

Timmermans, A.C., 2015, A Geochemical Study of Cenozoic Magmatism Along an East-West Transect from Central Great Basin, Nevada to the Ancestral Cascade Arc, California – A Compositional Journey Over Space and Time (Doctoral Dissertation). Carleton University, Ottawa, Ontario.

Varve, S., 2013, Stratigraphy, Geochemistry, and Origin of the Fish Creek Mountains Tuff, Battle Mountain Area, North-Central Nevada, U.S.A (Master of Science Thesis). Carleton University, Ottawa, Ontario.

van Hunen, J., Van Den BERG, A.P., Vlaar, N.J., 2002, On the role of subducting oceanic plateaus in the development of shallow flat subduction: *Tectonophysics*, v. 352(3), p. 317-333.

Watts, K.E., John, D.A., Colgan, J.P., Henry, C.D., Bindeman, I.N., Schmitt, A.K., 2016, Probing the volcanic-plutonic connection and the genesis of crystal-rich rhyolite in a deeply dissected supervolcano in the Nevada Great Basin: Source of the Late Eocene Caetano Tuff: *Journal of Petrology*, v. 57(18), p. 1599-1644, doi: 10.1093/petrology/egw051.

Winter, J.D., 2001, *An Introduction to igneous and metamorphic petrology* (p. 697): New York: Prentice Hall.

Appendix I: Supporting Tables

Table I: $^{40}\text{Ar}/^{39}\text{Ar}$ Ages provided by C. Henry

Sample No.	Unit Name	$^{40}\text{Ar}/^{39}\text{Ar}$ Age	2σ
16-SM-32	Underdown Tuff	24.897	0.041
17-SM-26	Underdown Tuff	24.905	0.072
17-SM-21	Underdown Tuff	24.902	0.060
16-SM-21	Bonita Canyon Formation	24.999	0.043
H09-85	tuff of Clipper Gap	24.87	0.10
16-SM-16	tuff Clipper Gap	24.981	0.036
H17-46	tuff Clipper Gap	24.917	0.048
H01-136	Unnamed Tuff	24.72	0.05
16-SM-06	Unnamed Tuff	24.755	0.037
17-SM-20	Tuff of Arc Dome Vitrophyre	24.688	0.055
16-SM-09	Megabreccia block	25.19	0.04
17-SM-13	tuff of Brunton Pass	24.892	0.053
H00-97	tuff of Brunton Pass	25.12	0.06
16-SM-33	Dacite dyke	24.949	0.046
16-SM-53	Rhyolite Intrusive	24.774	0.051
H12-33	Tgv1	25.094	0.009
H12-34	Tgv1 below H12-33	25.094	0.007
H13-82	Tgv1 below H12-34	25.100	0.012
17-SM-29	Tgv2	25.109	0.080
H17-50	Tgv3	24.875	0.048
H12-32	Tgv3 vitrophyre	24.898	0.009
H18-SN6	Young Sierra Nevada tuff	24.888	0.015

Table II: Sample Locations

Sample No.	Unit	N	W	Zone	E	N	Elevation (ft)
NAD 27							
16-SM-01	Bonita Canyon Formation	39.1642	117.4012	11S	465340	4334870	7201
16-SM-02	Bonita Canyon Formation	39.1649	117.4022	11S	465249	4334948	7347
16-SM-03	Bonita Canyon Formation	39.1642	117.4014	11S	465325	4334864	7216
16-SM-04	Underdown Tuff	39.1548	117.4337	11S	462530	4338831	7900
16-SM-05	Bonita Canyon Formation	39.2358	117.3560	11S	469278	4342800	6467
16-SM-06A	Unnamed Tuff	39.0757	117.5444	11S	452906	4325110	8813
16-SM-06B	Unnamed Tuff	39.0757	117.5444	11S	452906	4325110	8813
16-SM-06C	Unnamed Tuff	39.0757	117.5444	11S	452906	4325110	8813
16-SM-06D	Unnamed Tuff	39.0757	117.5444	11S	452906	4325110	8813
16-SM-06E	Unnamed Tuff	39.0757	117.5444	11S	452906	4325110	8813
16-SM-06F	Unnamed Tuff	39.0757	117.5444	11S	452906	4325110	8813
16-SM-07	Bonita Canyon Formation	39.0729	117.5422	11S	453096	4324795	8282
16-SM-08	Bonita Canyon Formation	39.0832	117.5418	11S	453139	4325937	8017
16-SM-09	Tuff of Arc Dome	39.0822	117.5419	11S	453132	4325825	7955
16-SM-10	Qtz-feld porphyritic tuff	39.2198	116.8544	11S	512567	4340971	6513
16-SM-11	Tuff of Campbell Creek	39.2203	116.8528	11S	512711	4341024	6606
16-SM-12	Nine Hill Tuff	39.2211	116.8512	11S	512850	4341114	6826
16-SM-12B	Nine Hill Tuff	39.2211	116.8512	11S	512850	4341114	6826
16-SM-13A	Tuff of Clipper Gap	39.2216	116.8499	11S	512956	4341171	7009
16-SM-13B	Tuff of Clipper Gap	39.2216	116.8499	11S	512956	4341171	7009
16-SM-13C	Tuff of Clipper Gap	39.2216	116.8499	11S	512956	4341171	7009
16-SM-14	Tuff of Clipper Gap	39.2212	116.8495	11S	512995	4341130	7018
16-SM-15A	Tuff of Clipper Gap	39.2218	116.8495	11S	512988	4341191	7068
16-SM-15B	Tuff of Clipper Gap	39.2218	116.8495	11S	512988	4341191	7068
16-SM-16	Tuff of Clipper Gap	39.2225	116.8500	11S	512948	4341274	7036
16-SM-17	Tuff of Clipper Gap	39.2231	116.8502	11S	512933	4341335	7067
16-SM-18	Tuff of Clipper Gap	39.2207	116.8569	11S	512353	4341070	6414
16-SM-19	Pablo Formation	39.1049	117.5413	11S	453196	4328349	8627
16-SM-20A	Pablo Formation	39.1090	117.5460	11S	452790	4328807	9252
16-SM-20B	Pablo Formation	39.1090	117.5460	11S	452790	4328807	9252
16-SM-20C	Pablo Formation	39.1090	117.5460	11S	452790	4328807	9252
16-SM-21A	Bonita Canyon Formation	39.1109	117.5362	11S	453643	4329016	9156
16-SM-21B	Bonita Canyon Formation	39.1109	117.5362	11S	453643	4329016	9156
16-SM-21C	Bonita Canyon Formation	39.1109	117.5362	11S	453643	4329016	9156
16-SM-22	Bonita Canyon Formation	39.1101	117.5334	11S	453883	4328917	9060
16-SM-23	Bonita Canyon Formation	39.1067	117.5289	11S	454270	43285437	8948

Table II: Sample Locations Cont.

Sample No.	Unit	N	W	Zone	E	N	Elevation (ft)
NAD 27							
16-SM-24	Bonita Canyon Formation	39.1045	117.4247	11S	454628	4328294	8805
16-SM-25	Bonita Canyon Formation	39.1143	117.5199	11S	455049	4329377	8766
16-SM-26	Bonita Canyon Formation	39.0967	117.5274	11S	454390	4327430	7925
16-SM-27	Bonita Canyon Formation	39.0974	117.5242	11S	454671	4327503	7892
16-SM-28	Underdown Tuff	39.0927	117.4638	11S	459893	4326962	6984
16-SM-29A	Underdown Tuff	39.0936	117.4644	11S	459839	4327057	7056
16-SM-29B	Underdown Tuff	39.0936	117.4644	11S	459839	4327057	7056
16-SM-30	Bonita Canyon Formation	39.1067	117.4707	11S	459299	4328514	7227
16-SM-31	Underdown Tuff	39.1056	117.4707	11S	459304	4328392	7277
16-SM-32A	Underdown Tuff	39.0965	117.4935	11S	457321	4327391	7292
16-SM-32B	Underdown Tuff	39.0965	117.4935	11S	457321	4327391	7292
16-SM-32C	Underdown Tuff	39.0965	117.4935	11S	457321	4327391	7292
16-SM-32D	Underdown Tuff	39.0965	117.4935	11S	457321	4327391	7292
16-SM-33A	Dacite Porphyry Dyke	39.1785	117.3743	11S	467669	4336444	6614
16-SM-33B	Dacite Porphyry Dyke	39.1785	117.3743	11S	467669	4336444	6614
16-SM-34	Underdown Tuff	39.0230	117.5252	11S	454539	4319249	7616
16-SM-35	Underdown Tuff	39.0238	117.5257	11S	454491	4319345	7775
16-SM-36	Underdown Tuff	39.0235	117.5251	11S	454543	4319304	7708
16-SM-37	Bonita Canyon Formation	39.2011	117.5165	11S	455404	4339010	6925
16-SM-38A	Unnamed tuff	39.2010	117.5170	11S	455360	4339000	7053
16-SM-38B	Unnamed tuff	39.2010	117.5170	11S	455360	4339000	7053
16-SM-39	Unnamed tuff	39.1998	117.5178	11S	455286	4338866	7187
16-SM-40	Unnamed pumice	39.2001	117.5164	11S	455407	4338900	6978
16-SM-41	Unnamed tuff	39.1688	117.5506	11S	452436	4335393	6901
16-SM-42	Unnamed tuff	39.1575	117.5441	11S	452987	4334182	7086
16-SM-43	Unnamed tuff	39.1336	117.5659	11S	451087	4331544	7287
16-SM-44	Pablo Formation	39.1285	117.5629	11S	451348	4330975	7559
16-SM-45	Underdown Tuff	39.1582	117.3871	11S	466553	4334190	6747
16-SM-46	Underdown Tuff	39.1589	117.3872	11S	466548	4334275	6931
16-SM-47	Underdown Tuff	39.1590	117.3873	11S	466541	4334284	6938
16-SM-48	Underdown Tuff	39.1597	117.3876	11S	466512	4334367	7023
16-SM-49	Underdown Tuff	39.1604	117.3878	11S	466497	4334440	7060
16-SM-50	Underdown Tuff	39.1610	117.3882	11S	466461	4334501	7105
16-SM-51	Underdown Tuff	39.1618	117.3887	11S	466417	4334595	7163
16-SM-52	Rhyolite Intrusions	39.0156	117.5889	11S	449013	4318469	7473
16-SM-53	Rhyolite Intrusions	39.0158	117.5882	11S	449074	4318484	7568
16-SM-54	Bonita Canyon Formation	39.0151	117.5900	11S	448923	4318410	7477
16-SM-55	Unnamed Tuff	39.0236	117.5881	11S	449094	4319355	7626
16-SM-56	Rhyolite Intrusions	39.0214	117.5840	11S	449444	4319102	7893

Table II: Sample Locations Cont.

Sample No.	Unit	N	W	Zone	E	N	Elevation (ft)
NAD 83							
17-SM-01	Terrill Mountains tuffs	39.0298	-118.6917	11S	353570	4321441	4798
17-SM-02	Terrill Mountains tuffs	39.0290	-118.6916	11S	353578	4321353	4703
17-SM-03A	Terrill Mountains tuffs	39.0290	-119.6916	11S	353578	4321353	4703
17-SM-03B	Terrill Mountains tuffs	39.0290	-119.6916	11S	353578	4321353	4703
17-SM-03C	Terrill Mountains tuffs	39.0290	-119.6916	11S	353578	4321353	4703
17-SM-04	Underdown Tuff	39.3735	-115.7458				
17-SM-05	Nine Hill Tuff	39.3748	-115.7511				
17-SM-06	Tuff of Clipper Gap	39.4888	-115.4297				
17-SM-07	Tuff of Clipper Gap	39.4888	-115.4298				
17-SM-08	Tuff of Clipper Gap	39.4889	-115.4299				
17-SM-09	Tuff of Clipper Gap	39.4892	-115.4300				
17-SM-10	Tuff of Clipper Gap	39.4897	-115.4297				
17-SM-11	Tuff of Clipper Gap	39.4898	-115.4298				
17-SM-12	Tuff of Clipper Gap	39.4912	-115.4299				
17-SM-13A	Tuff of Brunton Pass	38.8752	-117.7375	11S	436027	4303189	6560
17-SM-13B	Tuff of Brunton Pass	38.8752	-117.7375	11S	436027	4303189	6560
17-SM-14	Tuff of Arc Dome	38.8767	-117.7382	11S	435966	4303356	6490
17-SM-15A	Tuff of Arc Dome	38.8968	-117.7832	11S	432084	4305620	6907
17-SM-15B	Tuff of Arc Dome	38.8968	-117.7832	11S	432084	4305620	6907
17-SM-16A	Gabbs Valley Tuff	38.8989	-117.7900	11S	431498	4305856	7015
17-SM-16B	Gabbs Valley Tuff	38.8989	-117.7900	11S	431498	4305856	7015
17-SM-17A	Underdown Tuff	39.1610	-117.3902	11S	466288	4334717	7049
17-SM-17B	Underdown Tuff	39.1610	-117.3902	11S	466288	4334717	7049
17-SM-17C	Underdown Tuff	39.1610	-117.3902	11S	466288	4334717	7049
17-SM-18	Pablo Formation	39.1097	-117.5047	11S	456369	4329070	7572
17-SM-19	Bonita Canyon Formation	39.1113	-117.5100	11S	455906	4329253	7861
17-SM-20	Tuff of Arc Dome	39.1589	-117.3256	11S	471873	4334460	6535
17-SM-21A	Clipper Gap Tuff	39.0547	-116.5085	11S	542529	4322963	7756
17-SM-21B	Clipper Gap Tuff	39.0547	-116.5085	11S	542529	4322963	7756
17-SM-22	Clipper Gap Tuff	39.0545	-116.5084	11S	542536	4322941	7714
17-SM-23	Clipper Gap Tuff	38.8550	-116.8353	11S	514293	4300699	7242
17-SM-24	Clipper Gap Tuff	38.8557	-116.8352	11S	514297	4300779	7369
17-SM-25	Clipper Gap Tuff	38.8565	-116.8359	11S	514238	4300864	7530
17-SM-26A	Clipper Gap Tuff	38.8568	-116.8359	11S	514238	4300900	7587
17-SM-26B	Clipper Gap Tuff	38.8568	-116.8359	11S	514238	4300900	7587
17-SM-26C	Clipper Gap Tuff	38.8568	-116.8359	11S	514238	4300900	7587
17-SM-27	Clipper Gap Tuff	38.8549	-116.8355	11S	514273	4300693	7193
17-SM-28	Gabbs Valley Tuff	38.8941	-118.1865	11S	397108	4305696	4550

Table II: Sample Locations Cont.

Sample No.	Unit	N	W	Zone	E	N	Elevation (ft)
NAD 83							
17-SM-29	Gabbs Valley Tuff	38.8922	-118.1832	11S	397324	4305473	4522
17-SM-30	Gabbs Valley Tuff	38.8924	-118.1834	11S	397370	4305502	4642
17-SM-31	Gabbs Valley Tuff	38.8929	-118.1832	11S	397390	4305550	4642
H18-SN6	Young Sierra Nevada tuff	39.1028	-120.4192				
H18-SN15	Young Sierra Nevada tuff	39.0660	-120.4596				

Table III: Thin Section Descriptions

Sample Number Unit Lithology % Phenocrysts	16-SM-01 Bonita Canyon Whole Rock 8%	16-SM-02 Bonita Canyon Pumice 16%	16-SM-03 Bonita Canyon Vitrophyre 10%	16-SM-04 Underdown Tuff Whole rock 8%
Plagioclase	2%, up to 1.0 mm, phenocrysts with polysynthetic twinning, some are altered and are sieve textured, some are fresh	5%, ~1.5 mm, fractured, unaltered phenocrysts with polysynthetic twinning	2%, up to 1.0 mm, fractured, unaltered phenocrysts with polysynthetic twinning, some show chemical zoning	None identifiable
Quartz	4%, up to 1.5 mm, quartz eyes with embayments, fractured unevenly	5%, 1.5-2.0 mm, quartz eyes with embayments, fractured unevenly	6%, up to 2.5 mm, quartz eyes with embayments, unevenly fractured and opaque inclusions	2%, 2.0 mm, fractured, quartz eyes with embayments
Sanidine	1%, <1.0 mm, phenocrysts with Carlsbad twinning, unaltered	5%, ~1.5 mm, fractured, unaltered phenocrysts	1%, very small phenocryst with Carlsbad twinning	6%, 1.0 mm, crystals are relatively fresh, show carlsbad twinning, and have uneven fractures
Biotite	1%, 0.25 mm, unaltered, phenocrysts in matrix and lithic fragment	1%, 0.25-0.5 mm long, unaltered, bent phenocrysts	1%, <0.25 mm, unaltered phenocryst	None identifiable
Amphibole	None identifiable	None identifiable	Trace, 0.5 mm, hexagonal crystal with fracturing	Trace, altered by chlorite
Accessory Phases	1%, opaque minerals, <0.1 mm Trace, microcrystalline Ti-oxides throughout matrix Trace, monazite	1%, opaque minerals throughout matrix 1%, rutile, microcrystalline grains in matrix Trace, monazite	Trace, opaque minerals Trace, Fe-Ti oxides	Opaque minerals are very small and are found throughout matrix
Lithics	10%, altered, most contain quartz and feldspar, one is dark red with abundant plagioclase laths, up to 2.0 mm	2%, fully altered clast with large altered feldspar inside, up to 2.0 mm	5%, most composed of quartz and plagioclase feldspar, some altered, one porphyritic, one microcrystalline, up to 2.0 mm	1%, very altered, composition looks similar to the groundmass, up to 2.0 mm
Textures	Matrix of highly altered glass shards with veins of silicification	Matrix has glass bubble shards, is phenocryst rich	Matrix is welded, fresh, light brown glass, glass shards throughout matrix Fiamme are entirely glass and are lighter than matrix	Matrix is composed of brown, welded glass which shows banding that wraps around phenocrysts, no pumice.
Alteration	Possible chlorite alteration in matrix	Matrix is altered heavily by chlorite	None identifiable	Large areas of quartz silicification (10%), chlorite alteration in matrix (1%)

Sample Number Unit Lithology % Phenocrysts	16-SM-05 Bonita Canyon Whole Rock 13%	16-SM-06 Unnamed Tuff Whole Rock 31%	16-SM-07 Bonita Canyon Whole Rock 6%	16-SM-08 Bonita Canyon Whole Rock 7%
Plagioclase	5%, ~0.5 mm, phenocrysts with polysynthetic twinning, fractured and chemically zoned 1%, ~1.5 mm, xenocryst, heavily sieved	10%, up to 1.5 mm, phenocrysts with polysynthetic twinning, fractured and unaltered	1%, <1.0 mm, very altered phenocryst with polysynthetic twinning	1%, ~0.25 mm, unaltered phenocrysts with polysynthetic twinning
Quartz	5%, up to 1.5 mm, phenocrysts with rounded corners and embayments, fractured	10%, up to 3.0 mm, phenocrysts with rounded corners and embayments, very fractured	5%, up to 1.5 mm, phenocrysts with rounded edges and embayments, unevenly fractured	5%, up to 0.5 mm, phenocrysts
Sanidine	2%, ~0.5 mm, phenocrysts with Carlsbad twinning, highly fractured	10%, up to 4.0 mm, unaltered phenocrysts with Carlsbad twinning	None identifiable	None identifiable
Biotite	1%, up to 0.5 mm long, thin, unaltered, bent phenocrysts	1%, 0.5 mm, relatively fresh phenocrysts with opaque rims	None identifiable	1%, up to 1.0 mm long, phenocryst altered slightly by chlorite
Amphibole	None identifiable	Trace, <0.1 mm, unaltered phenocryst	None identifiable	None identifiable
Accessory Phases	Trace, rutile, disseminated grains in matrix	1%, opaque minerals, most ≤0.1 mm, up to 0.2 mm Trace, Fe-Ti oxides, ~0.25 mm Trace, monazite	Trace, rutile, disseminated red to opaque oxides	Trace, monazite
Lithics	5%, mostly quartz and feldspar, up to 2.0 mm	5%, one up to 3mm, microcrystalline and patchy, most are ~1.0 mm with small plagioclase laths	None identifiable	1%, up to 1.5 mm, composed mostly of quartz
Textures	Matrix is green, altered glass	Matrix is orange-brown glass and welded, pumice is light brown and either aphyric or phyric with large phenocrysts, phenocrysts are highly fractured, phenocrysts in pumice have radiating cracks going into glassy pumice	Matrix is altered, microcrystalline, and silicified Pumice likely completely replaced by patchy alteration	Matrix is altered, unwelded, and vesicular
Alteration	3%, wispy sericite alteration in matrix	Some phenocrysts have light yellow rims of alteration	2% veiny yellow alteration in matrix	2% calcite alteration in matrix

Sample Number Unit Lithology % Phenocrysts	16-SM-09 Tuff of Arc Dome Mega Breccia Block ~17%	16-SM-10 Tuff of Clipper Gap Whole Rock 14%	16-SM-11 Tuff of Campbell Creek Whole rock ~4%	16-SM-13C Tuff of Clipper Gap Whole rock ~6%
Plagioclase	10%, up to 1.5 mm, altered phenocrysts with polysynthetic twinning, partially resorbed	7%, up to 2.0 mm, unaltered, fractured phenocrysts with polysynthetic twinning, some show chemical zoning	2%, up to 2.0 mm, fractured phenocrysts with polysynthetic twinning, some are resorbed or plucked	1%, 0.1-1.0 mm, unaltered phenocrysts with polysynthetic twinning
Quartz	10%, up to 2.5 mm, phenocrysts with rounded corners and embayments	10%, microcrystalline quartz in matrix	None identifiable	2%, 1.75-2.0 mm, fractured phenocrysts with rounded corners and embayments
Sanidine	~5%, up to 1.0 mm, altered phenocrysts with Carlsbad twinning, partially resorbed	7%, up to 2.0 mm, unaltered, fractured phenocrysts with Carlsbad twinning, one crystal has been completely sieved	2%, up to 2.0 mm, fractured phenocrysts with Carlsbad twinning	3%, 1.0-2.0 mm, fractured, unaltered phenocrysts, some with Carlsbad twinning
Biotite	2%, up to 1.0 mm, phenocrysts with opaque rims	Trace, up to 0.75 mm, altered phenocryst	Trace, up to 0.5 mm, crystals have opaque rims	Trace-1%, 0.1-0.25 mm, phenocrysts, some slightly bent
Amphibole	None identifiable	None identifiable	None identifiable	None identifiable
Accessory Phases	2%, opaque minerals, up to 0.4 mm	1%, opaque minerals, ≤0.2 mm Trace, Fe-Ti oxides, <0.1 mm, disseminated grains in matrix, larger >0.1 mm around plucked out minerals	Trace-1%, opaque minerals, up to 0.5 mm Trace-1%, pyroxene, up to 0.75 mm	3-4%, opaque minerals, up to 0.2 mm, some rim phenocrysts, Trace, Fe-Ti oxides, 0.1-1.0 mm, Trace, pyroxene?, ~1.0 mm, pink, slightly fractured, unaltered
Lithics	1%, up to 3.5 mm, microcrystalline	None identifiable	1%, 2.0 mm, brown, very altered, possibly looks spherulitic under alteration	None identifiable
Textures	Matrix is brown and spherulitic, with some microcrystalline quartz (~5%)	Matrix is glassy, has some microcrystalline quartz, unwelded, some areas of spherulites	Matrix is highly welded, colourless, composed of glass shards, some glass shards are light brown White and banded fiamme are both mostly aphyric, one large sanidine crystal on edge that may be in matrix	Matrix is composed of glass shards
Alteration	Brown alteration in matrix	None identifiable	None identifiable	Slight alteration in matrix

Sample Number Unit Lithology % Phenocrysts	16-SM-14 Tuff of Clipper Gap Pumice ~10%	16-SM-15A Tuff of Clipper Gap Porphyritic pumice 13%	16-SM-15B Tuff of Clipper Gap Whole rock 13%	16-SM-16 Tuff of Clipper Gap Porphyritic Pumice 25%	16-SM-17 Tuff of Clipper Gap Porphyritic pumice 13%
Plagioclase	Trace, ≤ 0.2 mm, unaltered phenocrysts with polysynthetic twinning,	3%, 1.0-2.5 mm, phenocrysts with polysynthetic twinning, alteration on rims, and sieve texture	None identifiable	10%, 1.0-2.5 mm, partially altered phenocrysts with polysynthetic twinning, some chemical zoning	3%, up to 2.5 mm, phenocrysts with polysynthetic twinning, alteration on rims, and sieve texture
Quartz	2%, 1.25 - 2.0 mm, unevenly fractured phenocrysts with rounded corners and embayments,	None identifiable	10% microcrystalline quartz in matrix	None identifiable	None identifiable
Sanidine	5%, 1.0 - 2.5 mm, fractured, unaltered phenocrysts, some show Carlsbad twinning	10%, up to 3.0 mm, altered, rectangular crystals	3%, up to 1.5 mm, unaltered, fractured phenocrysts	15%, 1.0-4.5 mm, fractured, partially altered phenocrysts, some show simple twinning	10%, up to 3.0 mm, altered, rectangular crystals
Biotite	Trace, 0.1 - 0.25 mm, generally thin, unaltered	None identifiable	Trace, ~0.75 mm, altered, dark red to opaque on edges and partially resorbed	None identifiable	None identifiable
Amphibole	None identifiable	None identifiable	None identifiable	None identifiable	None identifiable
Accessory Phases	Trace, opaque minerals, ~0.1mm, blocky, Trace, Fe-Ti oxides, ≤ 0.25mm, blocky, 2%, pyroxene?, 0.5-1.75 mm, unaltered, 2 nd order interference	2%, Fe-Ti oxides, clustered, 0.5-1 mm 1%, opaque minerals, 0.25-0.5 mm Trace, monazite	Trace, opaque minerals, ≤0.1 mm Trace, monazite	2%, Fe-Ti oxides, ~1.0 mm, blocky clusters, 1%, opaque minerals, ≤0.25 mm, blocky Trace, monazite	2%, Fe-Ti oxides, clustered, 0.5-1 mm 1%, opaque minerals, 0.25-0.5 mm Trace, monazite
Lithics	None identifiable	None identifiable	None identifiable	None identifiable	None identifiable
Textures	Matrix is altered and spherulitic, one area of matrix is orange and more glassy	Matrix is reddish, opaque, altered glass, very porphyritic	Matrix is altered glass, part of matrix is microcrystalline quartz, little evidence of welding	Matrix is brown, altered, patchy glass	Matrix is reddish, opaque, altered glass, very porphyritic
Alteration	Some matrix alteration	Alteration in matrix	Alteration in matrix	Alteration in matrix	Alteration in matrix

Sample Number Unit Lithology % Phenocrysts	16-SM-18 Tuff of Clipper Gap Whole rock 17%	16-SM-19 Pablo Formation Whole Rock -	16-SM-20B Pablo Formation Whole Rock -	16-SM-21A Bonita Canyon Whole Rock 10%
Plagioclase	7%, up to 2.5 mm, phenocrysts with polysynthetic twinning, slightly altered and fractured, some show chemical zoning and sieve texture	60%, 0.1-2.5 mm, phenocrysts and matrix material with polysynthetic and simple twinning, altered by sericite	40%, 0.1-1.5 mm, large crystals are heavily altered by sericite, small crystals are fresh	2%, up to 0.5 mm, unaltered, fractured, phenocrysts
Quartz	None identifiable	5%, up to 0.5 mm, secondary, mostly microcrystalline in veins, one large crystal is being eaten away at edges	None identifiable	4%, up to 2.0 mm, phenocrysts with rounded corners and embayments Smaller grains are in silicified areas of matrix
Sanidine	7%, up to 4.0 mm, unaltered, fractured phenocrysts, some with Carlsbad twinning	None identifiable	None identifiable	2%, up to 2.0 mm, unaltered, fractured, phenocrysts
Biotite	1%, up to 2.0 mm, altered phenocrysts, opaque dehydration rim around edges of crystals	Trace, up to 0.5 mm, altered, bent phenocrysts	None identifiable	2%, up to 0.5 mm, unaltered, bent, phenocrysts
Amphibole	2%, up to 2 mm, altered by chlorite, opaque dehydration rim around edges of crystals	~32%, up to 1.5 mm, elongate and hexagonal crystals altered by chlorite, some opaque inclusions and simple twinning	30%, up to ~3.0 mm, elongate and hexagonal crystals altered by chlorite, some opaque inclusions and simple twinning	None identifiable
Accessory Phases	1%, Fe-Ti oxides, <0.1 mm, red to opaque Trace, opaque minerals <0.1 mm	3%, opaque minerals, up to 0.5 mm	1%, pyrite, ~1.75 mm Trace, Fe-Ti oxides, up to ~0.1 mm	Trace, monazite Trace, opaque minerals, disseminated in matrix Trace, Fe-Ti oxides in matrix, <0.1 mm
Lithics	None identifiable	None identifiable	None identifiable	5%, lithics with different compositions from different sources; red opaque with quartz, spherulitic lithics, completely altered lithics, microcrystalline quartz, up to 2.5 mm
Textures	Welded, altered, glassy matrix, glass shards, banding of matrix around phenocrysts	Matrix is split in two halves, one more altered and one with microcrystalline matrix	Matrix is ~20% microcrystalline material (too small to be identified)	Matrix is fresh, glassy, with glass shards, pumice is not flattened
Alteration	Sericite alteration in matrix	Chlorite and sericite	5%, calcite alteration in matrix, crystals up to ~1.75 mm Sericite alteration of plagioclase	Wispy yellow alteration in matrix

Sample Number Unit Lithology % Phenocrysts	16-SM-21B Bonita Canyon White Pumice 11%	16-SM-21C Bonita Canyon Whole Rock 17%	16-SM-22-1 Bonita Canyon Whole Rock 16%	16-SM-23 Bonita Canyon Whole Rock 16%
Plagioclase	4%, ~1.5 mm, rectangular phenocrysts with polysynthetic twinning, unaltered, some show chemical zoning	5%, ≤ 0.5 mm, phenocrysts with polysynthetic twinning, unaltered and unevenly fractured	3%, up to 0.75 mm, phenocrysts with polysynthetic twinning, fractured and chemically zoned 2% feldspar xenocrysts, 0.25-0.5mm, with only rim of crystals remaining	3%, up to 0.75 mm, phenocrysts with polysynthetic twinning, fractured and chemically zoned 2% feldspar xenocrysts, 0.25-0.5mm, with only rim of crystals remaining
Quartz	3%, up to 2.0 mm, phenocrysts with rounded edges and embayments, unevenly fractured	10%, 0.5-1.5 mm, phenocrysts with some rounded edges, unfractured	3%, up to 2.0 mm, phenocrysts with rounded corners, very fractured	3%, up to 2.0 mm, phenocrysts with rounded corners, very fractured
Sanidine	2%, up to 1.5 mm, unaltered phenocrysts with no visible twinning	10%, 0.5-1.5 mm, rectangular phenocrysts with fractures, one crystal is zoned	3%, up to 1.5 mm, rectangular phenocrysts, fractured	3%, up to 1.5 mm, rectangular phenocrysts, fractured
Biotite	2%, up to 0.5mm, bent, unaltered phenocrysts	2%, most 0.5-0.1 mm, largest up to 1-1.5mm long, unaltered, bent phenocrysts	5%, <0.5 mm, unaltered, bent phenocrysts with red opaque inclusions One phenocryst up to 2.5mm being resorbed in the middle	5%, <0.5 mm, unaltered, bent phenocrysts with red opaque inclusions One phenocryst up to 2.5mm being resorbed in the middle
Amphibole	Trace, possible	None identifiable	None identifiable	None identifiable
Accessory Phases	Trace, opaque minerals microcrystalline in matrix, <0.1 mm Trace, Fe-Ti oxides, microcrystalline in matrix, <0.1 mm	Trace, opaque minerals, <0.1 mm in matrix Trace, Fe-Ti oxides, <0.1 mm in matrix	Trace, Fe-Ti oxides, <0.1 mm, square Trace, opaque minerals, <0.1 mm, disseminated in matrix and inclusions Trace, monazite	Trace, Fe-Ti oxides, <0.1 mm, square Trace, opaque minerals, <0.1 mm, disseminated in matrix and inclusions Trace, monazite
Lithics	None identifiable	3%, 1.0-1.5 mm, mostly microcrystalline clasts that look similar in composition, two altered completely	2%, 2.0 mm, red opaque, microcrystalline	2%, 2.0 mm, red opaque, microcrystalline
Textures	Matrix made up of glass shards	Matrix is fresh glass, pumice is not flattened, ~5% vesicles	Matrix is glassy and relatively fresh, unwelded-poorly welded	Matrix is glassy and relatively fresh, unwelded-poorly welded
Alteration	Chlorite alteration in matrix?	None identifiable	Slightly altered aphyric pumice	Slightly altered aphyric pumice

Sample Number Unit Lithology % Phenocrysts	16-SM-24 Bonita Canyon Whole Rock 14%	16-SM-26 Tuff of Arc Dome Mega Breccia Block 23%	16-SM-27 Bonita Canyon Whole rock 5%	16-SM-30 Bonita Canyon Whole Rock 11%
Plagioclase	3%, up to 0.5 mm, phenocrysts with polysynthetic twinning, sieve texture, slightly altered and fractured	10%, up to 5.0 mm, phenocrysts with polysynthetic twinning, some inclusions, altered by sericite and calcite	None identifiable	1%, 0.25 mm, unaltered phenocryst with polysynthetic twinning
Quartz	6%, up to 2.0 mm, phenocrysts with rounded corners and embayments, highly fractured	7%, up to 2.0 mm, rounded phenocrysts with embayments, highly to slightly fractured	5%, 2.5 mm, phenocrysts with rounded corners and embayments 90%, microcrystalline qtz in matrix	5%, up to 1.5 mm, phenocrysts with rounded corners and embayments 50%, ~0.1 mm, crystals in silicified veins
Sanidine	2%, 0.5 mm, phenocryst with Carlsbad twinning, with sieve texture and alteration	5%, up to 4.0 mm, phenocrysts with Carlsbad twinning, heavily altered	None identifiable	5%, 0.5 mm, phenocrysts altered and sieved
Biotite	3%, 0.1-0.5 mm, largest up to 1mm, bent phenocrysts	1%, up to 1.5 mm, altered phenocrysts with opaque rims, some completely replaced	None identifiable	None identifiable
Amphibole	Trace, 1mm, completely replaced by chlorite	Trace, ~0.2mm, very altered, opaque rim	None identifiable	None identifiable
Accessory Phases	Trace, opaque minerals, 0.1 mm in matrix Trace, Fe-Ti oxides, <0.1 mm inclusions	2%, opaque minerals, most ≤0.1 mm, largest up to 1.0 mm	3%, calcite, up to 1.5 mm crystals filling voids where feldspars are altered out, some found in matrix Trace, opaque minerals, <0.1 mm, disseminated throughout matrix	Trace, opaque minerals, <0.1 mm Trace, monazite, <0.1 mm
Lithics	10%, 3.0 mm, most composed of altered quartz and feldspar, spherulites, one is microcrystalline qtz and rich in Ti-oxides	None identifiable	None identifiable	5%, 2.5 mm, composed of microcrystalline quartz
Textures	Relatively unaltered, unwelded matrix, 5% vesicles	Matrix is altered, contains microcrystalline quartz and is slightly spherulitic	Matrix is completely silicified, composed of microcrystalline quartz, spherulites throughout matrix	Matrix is heavily silicified
Alteration	Slightly altered aphyric pumice	8%, calcite alteration on feldspars and in matrix	Calcite alteration and silicification	1% green, chlorite alteration in matrix

Sample Number Unit Lithology % Phenocrysts	16-SM-31 Underdown Tuff Whole Rock ~20%	16-SM-32A Underdown Tuff Porphyritic pumice ~10%	16-SM-32B Underdown Tuff Whole Rock 12%	16-SM-32C Underdown Tuff Whole Rock ~10%
Plagioclase	10%, 2.0-3.0 mm, phenocrysts show sieve texture and are very altered	10%, 2.0 mm, phenocrysts showing polysynthetic twinning are highly altered by sericite and some calcite, with some small inclusions	3%, up to 1.5 mm, phenocrysts almost completely replaced by calcite	5%, up to 2.5 mm, altered feldspar phenocrysts, calcite and sericite alteration, some small crystals with polysynthetic twins on edges of voids where quartz and calcite are found
Quartz	10%, up to 2.0 mm, quartz eyes with embayments, are fractured	5%, 0.5 mm, small grains in matrix, a result of silicification	5%, up to 2.0 mm, quartz eye phenocrysts with embayments, yellow-red inclusions 40%, microcrystalline silicification	5%, up to 1.0 mm, fractured quartz eyes
Sanidine	1%, up to 1.0 mm, phenocrysts showing carlsbad twinning	10%, up to 1.5 mm, phenocrysts showing recrystallization around the edges of the crystal	3%, up to 1.5 mm, phenocrysts with Carlsbad twinning have sericite alteration on the edges	1%, up to 1.5 mm, relatively fresh phenocrysts
Biotite	None identifiable	2%, 0.1 mm, altered by chlorite	1%, up to 0.1 mm, completely replaced by chlorite	None identifiable
Amphibole	None identifiable	2%, 0.1 mm, altered by chlorite	Trace, completely replaced by chlorite, up to 0.1 mm	None identifiable
Accessory Phases	1% opaque minerals in matrix, trace Fe-Ti oxides, <0.1 mm	1% calcite alteration, 1% very small opaques throughout matrix and as inclusions in feldspar phenocrysts, <0.1 mm	1%, up to 0.1mm, opaque minerals in matrix and as inclusions in phenocrysts Trace, monazite, <0.1 mm	Calcite crystals between 1.5-2.0 mm fill voids in matrix
Lithics	None identifiable	None identifiable	None identifiable	None identifiable
Textures	Matrix has grey glassy areas and microcrystalline quartz, banding of matrix wraps around phenocrysts, spherulitic areas	Matrix is made of brown altered glass, phenocryst rich	Matrix has grey glassy areas and microcrystalline quartz, banding of matrix wraps around phenocrysts, spherulitic areas	Matrix is spherulitic
Alteration	Calcite alteration on feldspar phenocrysts	Calcite and chlorite alteration	Calcite alteration on feldspars	Chlorite alteration in matrix

Sample Number Unit Lithology % Phenocrysts	16-SM-32D Underdown Tuff Whole Rock 7%	16-SM-33A Dacite Dyke Whole rock 26%	16-SM-33B Dacite Dyke Whole rock 14%	16-SM-34 Underdown Tuff Whole Rock 28%
Plagioclase	3%, up to 2.5 mm, phenocrysts altered heavily by sericite and have sieve texture	25%, up to 5.0 mm, phenocrysts with polysynthetic twinning, sericite alteration, some chemical zoning ~65%, ≤0.1 mm, fine grained in matrix	14%, up to 2.25 mm, phenocrysts with polysynthetic twinning heavily altered by sericite, opaque inclusions 70%, 0.1-0.5 mm, small plag laths in matrix	10%, up to 2.5 mm, feldspar, heavily altered and sieved, heavily resorbed
Quartz	2%, between 1.0-2.0 mm, quartz eye phenocrysts with embayments with some small opaque inclusions 20%, ~0.5 mm, crystals filling voids	None identifiable	None identifiable	12%, between 2.5-3.0 mm, largest phenocryst up to 5mm, quartz eyes with embayments are fractured irregularly, with resorbed edges
Sanidine	2%, between 1.0-0.5 mm, phenocrysts with Carlsbad twinning altered by sericite	None identifiable	None identifiable	50%, microcrystalline in matrix 3%, up to 1.5 mm, phenocrysts with Carlsbad twinning have sericite alteration on the edges
Biotite	None identifiable	1%, up to 1.75 mm, filling voids, last to crystallize or secondary, unaltered	Trace, ~0.5mm, filling voids, last to crystallize or secondary, unaltered	None identifiable
Amphibole	None identifiable	None identifiable	None identifiable	None identifiable
Accessory Phases	3%, calcite up to 1.0 mm, filling voids in matrix 1%, opaque minerals, most <0.1 mm, up to 1.0 mm throughout matrix Trace, monazite	3%, opaque minerals, most <0.1 mm in matrix, largest up to 0.5mm	3%, opaque minerals, up to 0.2 mm, some elongate opaque needles <0.1 mm Trace-1%, Fe-Ti oxides, <<0.1 mm Trace, monazite	2%, opaque minerals, <0.1- 1.0 mm, throughout matrix and in groupings Trace, Fe-Ti oxides are inclusions in quartz, < 0.1 mm Trace, monazite
Lithics	None identifiable	None identifiable	None identifiable	None identifiable
Textures	Matrix is completely spherulitic with areas of quartz silicification and calcite	Matrix is fine grained plagioclase, altered	Matrix is microcrystalline plag, all phenocrysts are altered, some completely replaced	Matrix is silicified, microcrystalline, and altered
Alteration	Sericite alteration on feldspars, and secondary calcite in matrix	5%, sericite, up to 0.5-1.0 mm, fully replacing another mineral, radial looking in XPL, 2%, calcite, up to 0.5 mm, fully replacing another mineral or filling a void	10%, calcite, alteration on feldspars and in matrix, 1%, chlorite alteration, green, spherulite looking	3%, sericite alteration in matrix

Sample Number	16-SM-35	16-SM-36	16-SM-37	16-SM-38A
Unit	Underdown Tuff	Underdown Tuff	Bonita Canyon	Unnamed Tuff
Lithology	Whole Rock	Whole Rock	Whole Rock	Whole Rock
% Phenocrysts	11%	11%	4%	~30%
Plagioclase	5%, ~1.5 mm, feldspar phenocrysts, heavily altered by sericite, some completely replaced	5%, ~1.5 mm, feldspar phenocrysts, heavily altered by sericite, some completely replaced	1%, 0.5 mm, fractured phenocrysts with polysynthetic twinning	10%, up to 1.5 mm, unaltered phenocrysts with polysynthetic twinning, slightly fractured
Quartz	5%, ~2.0 mm, phenocrysts with rounded edges and embayments, weakly to very fractured	5%, ~2.0 mm, phenocrysts with rounded edges and embayments, weakly to very fractured	3%, up to 0.5 mm, unfractured phenocrysts	10%, up to 2.5 mm, phenocrysts with rounded corners, fractured
Sanidine	2%, between 1.0-0.5 mm, phenocrysts with Carlsbad twinning altered by sericite	2%, between 1.0-0.5 mm, phenocrysts with Carlsbad twinning altered by sericite	Trace, up to 1.0 mm, fragment of phenocryst, fractured	10%, up to 2.5 mm, fractured, unaltered phenocrysts with Carlsbad twinning
Biotite	Trace, altered	Trace, altered	1%, 0.5-0.75 mm thin, bent phenocrysts	Trace, up to 0.75 mm, phenocrysts with opaque rims, altered by chlorite
Amphibole	1%, up to 1.5 mm long, fully replaced by chlorite	1%, up to 1.5mm long, fully replaced by chlorite	None identifiable	Trace, up to 1.0 mm, phenocrysts with opaque rim, altered by chlorite
Accessory Phases	1%, opaque minerals, smallest found in silicified matrix, larger crystals in altered and silicified areas	1%, opaque minerals, smallest found in silicified matrix, larger crystals in altered and silicified areas	Trace, monazite	1%, opaque minerals, up to 0.2 mm
	Trace, monazite, <0.1 mm	Trace, monazite, <0.1 mm		Trace, Fe-Ti oxides, ~0.2 mm
	Trace, rutile <0.1 mm	Trace, rutile, <0.1 mm		
Lithics	None Identifiable	None Identifiable	2%, 2.0 mm, composed of microcrystalline quartz	None identifiable
Textures	Matrix is grey and altered, has large areas of patchy, altered material, possibly altered pumice	Matrix is grey and altered, has large areas of patchy, altered material, possibly altered pumice	Matrix is unwelded, 5% vesicles	Matrix is glassy and welded, pumice is recrystallized and microcrystalline
Alteration	3% sericite alteration in altered areas of matrix	3% sericite alteration in altered areas of matrix	Wispy yellow alteration in matrix	Chlorite alteration on hornblende and biotite
	2% chlorite alteration in altered areas of matrix	2% chlorite alteration in altered areas of matrix		

Sample Number	16-SM-39	16-SM-40	16-SM-41
Unit	Unnamed Tuff	Unnamed Tuff	Unnamed Tuff
Lithology	Whole Rock	Whole Rock	Whole Rock
% Phenocrysts	27%	30%	~30%
Plagioclase	8%, up to 1.5 mm, unaltered, fractured phenocrysts with polysynthetic twinning	10%, up to 1.5 mm, unaltered phenocrysts with polysynthetic twinning and slight uneven fracturing	8%, up to 1.5 mm, unaltered, fractured, phenocrysts with polysynthetic twinning
Quartz	7%, up to 2.5 mm, highly fractured phenocrysts with rounded corners	10%, up to 3.0 mm, unevenly fractured phenocrysts with rounded corners	8%, up to 2.5 mm, unevenly fractured phenocrysts with rounded corners
Sanidine	40%, microcrystalline quartz in matrix	50%, microcrystalline quartz in matrix	30%, microcrystalline quartz in pumice
Biotite	12%, up to 3.0 mm, unaltered, fractured phenocrysts with Carlsbad twinning	10%, up to 3.0 mm, highly fractured, unaltered, phenocrysts with Carlsbad twinning	10%, up to 2.5 mm, unaltered, fractured phenocrysts with Carlsbad twinning
Amphibole	Trace, up to 0.5 mm, thin phenocrysts	Trace, ≤0.1 mm, opaque rim on phenocrysts	1%, up to 1.0 mm, bent, phenocrysts with opaque spots and possible alteration
Accessory Phases	Trace, up to 1.0 mm, phenocrysts with a slightly altered rim	None identifiable	2%, up to 2.5 mm, relatively fresh phenocrysts with slightly altered edges and opaque inclusions concentrated on edges
Lithics	1%, opaque minerals, ≤0.25 mm	1%, opaque minerals, ≤0.25 mm	1%, opaque minerals, ≤0.25 mm
Textures	Trace, monazite, <0.1 mm	Trace, Fe-Ti oxides, most ≤0.1 mm, largest up to 0.5 mm	Trace, monazite, <0.1 mm
Alteration	2%, 2.0 mm, composed of microcrystalline qtz or feldspar, altered by sericite	1%, monazite, <<0.1 mm, inclusions in opaque material in cracks of feldspars and in groupings around voids	None identifiable
	Matrix is brown and glassy, relatively unaltered, pumice silicified to microcrystalline quartz	None identifiable	None identifiable
	Possible chlorite alteration on hornblende	Matrix composed of microcrystalline quartz, brownish matrix has some banding around phenocrysts	Matrix is glassy, pumice has been silicified and is microcrystalline quartz
		None identifiable	Possible chlorite alteration on hornblende and biotite

Sample Number Unit Lithology % Phenocrysts	16-SM-42 Unnamed Tuff Whole Rock ~26%	16-SM-43 Unnamed Tuff Whole Rock 30%	16-SM-44 Pablo Formation Whole Rock -	16-SM-45 Underdown Tuff Whole Rock 13%
Plagioclase	8%, up to 1.5 mm, unaltered phenocrysts with polysynthetic twinning	7%, up to 1.5 mm, unaltered phenocrysts with polysynthetic twinning	60%, 0.1-2.5 mm, phenocrysts with polysynthetic twinning, very altered by calcite and sericite, some show chemical zoning	2%, up to 2.5 mm, phenocrysts with polysynthetic twinning, altered and sieve textured
Quartz	5%, up to 1.5 mm, pieces of phenocrysts with rounded corners 30%, microcrystalline quartz in matrix	5%, up to 2.0 mm, unevenly fractured phenocrysts with rounded corners 40%, microcrystalline quartz in pumice	None identifiable	5%, up to 2.5 mm, rounded edged phenocrysts with embayments, unevenly fractured, with inclusions of rutile 70%, microcrystalline quartz, in matrix, larger crystals in veins 6%, up to 1.5 mm, phenocrysts with Carlsbad twins, slightly altered and sieve textured
Sanidine	12%, up to 2.0 mm, unaltered, fractured phenocrysts, some with Carlsbad twinning	15%, up to 2.5 mm, unaltered, unevenly fractured phenocrysts with Carlsbad twinning	None identifiable	6%, up to 1.5 mm, phenocrysts with Carlsbad twins, slightly altered and sieve textured
Biotite	Trace, up to 0.5 mm, slightly altered, and bent phenocrysts	1%, up to 1.75 mm, bent, unaltered phenocrysts	None identifiable	None identifiable
Amphibole	1%, up to 1.5 mm, phenocrysts with altered rims and opaque inclusions in rims	2%, up to 1.0 mm, phenocrysts with alteration on rim	15%, up to 1.75 mm, elongate and hexagonal crystals with some opaque inclusions 15%, pyroxene, <0.1-1.75 mm, phenocrysts and groundmass with some chemical zoning and simple twinning	Trace, ~0.5 mm, fully replaced
Accessory Phases	Trace, opaque minerals, ≤0.25 mm Trace, monazite, <0.1 mm	1%, opaque minerals, up to 1.0 mm	5%, opaque minerals, some are blocky (<0.1 mm), some fill voids (up to ~3.0 mm) Trace, Fe-Ti oxides, <0.1 mm	3%, rutile, reddish alteration on feldspar and found throughout matrix, <0.1 mm 1%, very small opaque minerals, throughout matrix, <<0.1 mm
Lithics	None identifiable	None identifiable	None identifiable	None identifiable
Textures	Matrix is brown and glassy, pumice has been recrystallized to microcrystalline pumice	Matrix is brown and glassy, pumice has been silicified with microcrystalline quartz	Matrix is microcrystalline	Matrix is microcrystalline quartz, primary banding of matrix is preserved and wrapped around matrix
Alteration	Possible chlorite alteration on rims of hornblende	Possible chlorite alteration on hornblende	5%, calcite alteration on plagioclase and pyroxene (?), up to ~1.5 mm	

Sample Number Unit Lithology % Phenocrysts	16-SM-46 Underdown Tuff Whole Rock 9%	16-SM-47 Underdown Tuff Whole Rock 13%	16-SM-48 Underdown Tuff Whole Rock 10%	16-SM-49 Underdown Tuff Whole Rock 13%	16-SM-50-1 Underdown Tuff Porphyritic pumice 20%
Plagioclase	1%, up to 1.0 mm, phenocryst completely altered by sericite shows some polysynthetic twinning	2%, up to 2.5 mm, phenocrysts with polysynthetic twinning, altered and sieve textured	Trace	2%, up to 2.5 mm, phenocrysts with polysynthetic twinning, altered and sieve textured	10%, up to 2.0 mm, phenocrysts altered heavily by sericite and calcite, show polysynthetic twinning
Quartz	3%, up to 1.0 mm, quartz eye phenocrysts with embayments	5%, up to 2.5 mm, rounded edged phenocrysts with embayments, unevenly fractured, with inclusions of rutile	3%, up to 2.5 mm, quartz eye phenocrysts with embayments 15%, quartz silicification in veins	5%, up to 2.5 mm, rounded edged phenocrysts with embayments, unevenly fractured, with inclusions of rutile	10%, up to 0.5 mm, small grains in silicified veins
Sanidine	5%, up to 3.5 mm, fractured phenocrysts with sieve texture	6%, up to 1.5 mm, phenocrysts with Carlsbad twins, slightly altered and sieve textured	7%, up to 1.5 mm, phenocrysts are fractured and show Carlsbad twinning	6%, up to 1.5 mm, phenocrysts with Carlsbad twins, slightly altered and sieve textured	10%, up to 1.5 mm, phenocrysts altered by yellow alteration
Biotite	None identifiable	None identifiable	None identifiable	None identifiable	None identifiable
Amphibole	None identifiable	Trace, ~0.5 mm, fully replaced	None identifiable	Trace, ~0.5 mm, fully replaced	None identifiable
Accessory Phases	1%, small opaque minerals in matrix, some larger are square and round <0.1 mm Trace, microcrystalline Ti-oxides, <<0.1 mm	3%, rutile, reddish alteration on feldspar and found throughout matrix <0.1 mm 1%, very small opaque minerals, throughout matrix, <<0.1 mm	Trace, opaques throughout matrix, <0.1 mm Trace, Fe-Ti oxides throughout matrix, <0.1 mm	3%, rutile, reddish alteration on feldspar and found throughout matrix, <0.1 mm 1%, very small opaque minerals, throughout matrix, <<0.1 mm	2% opaque minerals are included in feldspars and larger grains in groundmass, up to 0.1 mm, trace monazite, <0.1 mm
Lithics	None identifiable	None identifiable	1%, heavily altered	None identifiable	None identifiable
Textures	Matrix is microcrystalline, possibly quartz, little to no glass, some relict banding visible that slightly wraps phenocrysts	Matrix is microcrystalline quartz, primary banding of matrix is preserved and wrapped around matrix	Matrix is glassy, has silicified veins, and banding that wraps around phenocrysts	Matrix is microcrystalline quartz, primary banding of matrix is preserved and wrapped around matrix	Matrix is brown altered glass
Alteration	~1% chlorite alteration in matrix	None identifiable	Chlorite alteration in matrix	None identifiable	1% calcite alteration

Sample Number	16-SM-50-2	16-SM-51	16-SM-52	16-SM-53
Unit	Underdown Tuff	Underdown Tuff	Rhyolite Intrusive	Rhyolite Intrusive
Lithology	Whole Rock	Whole Rock	Whole rock	Whole rock
% Phenocrysts	15%	8%	-	-
Plagioclase	2%, up to 2.0 mm, fractured, unaltered phenocrysts	None identifiable	10%, up to 3.0 mm, phenocrysts with polysynthetic twinning, some altered and resorbed	5%, up to 1.75 mm, fractured phenocrysts with polysynthetic twinning
Quartz	3%, up to 2.0 mm, fractured, unaltered phenocrysts 5%, up to 0.5 mm, small grains of quartz in silicified veins 8%, up to 1.5 mm, fractured, mildly altered phenocrysts show Carlsbad twinning and small opaque inclusions	3%, up to 1.5 mm, fractured, quartz eye phenocrysts with embayments	15%, up to 1.5 mm, fractured phenocrysts with rounded corners and embayments	8%, up to 2.5 mm, fractured phenocrysts with rounded corners and embayments 35%, ≤0.5 mm, in matrix
Sanidine		5%, up to 1.5 mm, altered and fractured phenocrysts	15%, up to 1.75 mm, fractured phenocrysts with Carlsbad twinning	8%, up to 2.5 mm, fractured phenocrysts, some with Carlsbad twinning
Biotite	1%, up to 0.5 mm, altered by chlorite	Trace, 0.1 mm, appears relatively fresh	5%, up to 2.0 mm, generally fresh phenocrysts, some bent, some replaced by opaque minerals	Trace, 1.0 mm, almost completely replaced by opaque minerals
Amphibole	1%, up to 0.5 mm, altered by chlorite	Trace, 0.1 mm, fully replaced by chlorite	None identifiable	None identifiable
Accessory Phases	Trace small Fe-Ti oxides are bright red and disseminated throughout groundmass, <0.1 mm, Trace opaque minerals, <0.1 mm, found throughout groundmass	1%, small square grains, possibly magnetite, <0.1 mm	Trace, opaque minerals, up to 0.25 mm Trace, Fe-Ti oxides, up to 0.5 mm Trace, monazite, in matrix and inclusion in biotite	1%, opaque minerals, most <<0.1 mm, largest up to 0.25 mm Trace, Fe-Ti oxides, most <<0.1 mm, largest up to 0.5 mm Trace, monazite, <0.1 mm
Lithics	None identifiable	None identifiable	None identifiable	None identifiable
Textures	Matrix is brown altered glass that shows banding which wraps around phenocrysts. Phenocryst poor	Matrix is glassy, and has banding and wraps around phenocrysts	Microcrystalline quartz in matrix	Microcrystalline quartz in matrix
Alteration	Some chlorite alteration in the matrix	Chlorite alteration of amphibole, matrix alteration	None identifiable	None identifiable

Sample Number Unit Lithology % Phenocrysts	16-SM-54 Bonita Canyon Whole Rock 6%	16-SM-55 Unnamed Tuff Whole Rock ~12%	16-SM-56 Rhyolite Intrusive Whole rock ~17%	17-SM-01 Terrill Mountains Tuff Whole Rock ~5%
Plagioclase	Trace, 0.1-0.5 mm, phenocrysts with polysynthetic twinning	2%, up to 1.0 mm, phenocrysts with polysynthetic twinning	3%, up to 1.5 mm, phenocrysts with polysynthetic twinning, some resorption	Trace, ~0.25 mm, fractured phenocryst with polysynthetic twinning and some opaque inclusions
Quartz	5%, ~0.25 mm, phenocrysts with rounded corners and embayments	8%, up to 1.5 mm, slightly unevenly fractured phenocrysts with rounded corners and embayments ~70% microcrystalline quartz in matrix	8%, up to 2.25 mm, fractured phenocrysts with rounded corners and embayments ~35%, ≤0.25mm, in matrix	3%, up to 1.5 mm, highly fractured phenocrysts with rounded corners and embayments
Sanidine	None identifiable	2%, up to 2.0 mm, unaltered phenocrysts some with Carlsbad twinning	5%, up to 1.75 mm, fractured phenocrysts with some Carlsbad twinning	1%, ~1.5 mm, fractured phenocrysts, some with Carlsbad twinning
Biotite	1%, up to 0.5 mm long, thin, unaltered phenocrysts	Trace, up to 0.2 mm, altered phenocrysts with opaque rim	Trace-1%, up to 0.75 mm, almost completely replaced by opaque minerals	None identifiable
Amphibole	None identifiable	None identifiable	None identifiable	None identifiable
Accessory Phases	Trace, opaque minerals, most <0.1 mm, largest up to 0.25 mm Trace Ti-oxides <0.1 mm	Trace, opaque minerals, most <0.1 mm, largest up to 0.25 mm 1%, Fe-Ti oxides, up to 0.2 mm completely replaced biotite or amphibole up to 2.0 mm long	Trace, opaque minerals, most <0.1 mm in matrix, blocky grains up to 0.2 mm Trace, Fe-Ti oxides, most <0.1 mm, one cluster up to 0.5 mm	Trace, opaque minerals, <<0.1 mm Trace, Fe-Ti oxides, <<0.1 mm
Lithics	1%, 1.0 mm, composed of microcrystalline quartz Matrix is unwelded-poorly welded, 5% vesicles, all phenocrysts are small fractures of crystal	None identifiable	None identifiable	Trace-1%, up to 1.0 mm, microcrystalline and altered
Textures		Matrix is patchy, altered slightly, and microcrystalline quartz	Matrix appears patchy, possibly spherulitic, some microcrystalline quartz in matrix	Matrix is altered, brown and microcrystalline, pumice is spherulitic
Alteration	None identifiable	None identifiable	None identifiable	Alteration of matrix

Sample Number	17-SM-02	17-SM-03C	17-SM-05	17-SM-06
Unit	Terrill Mountains Tuff	Terrill Mountains Tuff	Nine Hill Tuff	Tuff of Clipper Gap
Lithology	Vitrophyre	Whole rock	Whole rock	Whole rock
% Phenocrysts	~5%	~5%	~5%	~4%
Plagioclase	Trace-1%, up to 1.0 mm, fractured phenocrysts with polysynthetic twinning	Trace-1%, up to 0.75 mm, unaltered, fractured phenocrysts with polysynthetic twinning	1%, ~1.0 mm, unevenly fractured and unaltered phenocrysts with polysynthetic twinning	Trace, <0.5 mm, fractured phenocrysts with polysynthetic twinning
Quartz	2%, ~1.75 mm, fractured phenocrysts with rounded corners and embayments	1%, up to 1.5 mm, phenocrysts with rounded corners and embayments	None identifiable	None identifiable
Sanidine	2%, ~0.1 mm, highly fractured phenocrysts with Carlsbad twinning	2%, up to 1.0 mm, unaltered, fractured phenocrysts	2%, up to 1.5 mm, unaltered phenocrysts, some with chemical zoning	3%, up to 2.0 mm, unaltered, fractured phenocrysts
Biotite	Trace, up to 0.25 mm, unaltered, bent phenocrysts	Trace, up to 0.5 mm, almost completely opaque	Trace-1%, up to 1.25 mm, almost opaque	1%, up to 0.2 mm, phenocrysts altered by chlorite
Amphibole	None identifiable	None identifiable	Trace, ~0.2 mm	None identifiable
Accessory Phases	Trace, possible pyroxene, up to 1.0 mm Trace, opaque minerals, <<0.1 mm	Trace, opaque minerals, <0.1 mm	Trace-1%, opaque minerals, ≤0.2 mm, crystals are singular and blocky or in clusters Trace, pyroxene, up to 0.5 mm, red alteration on edges Trace, Fe-Ti oxides, <0.1 mm	1%, opaque minerals, <0.1 mm, one hexagonal crystal is ~0.5 mm 1%, Fe-Ti oxides, disseminated grains throughout matrix, <<0.1 mm
Lithics	5%, 2.5 mm, green, small opaques 6.5 mm, phenocryst rich with bt, qtz, and san (might be pumice) Matrix is fresh, welded, and composed of glass shards	None identifiable	1%, ~1.75 mm, composed of red opaque material and plagioclase laths	2%, 1.5-2.0 mm, brown opaque with plagioclase laths and opaques, multiple of the same composition
Textures	White fiamme is generally aphyric, some fiamme look banded	Matrix is welded, and composed of fresh brown glass shards Fiamme is banded or white and both phyric and aphyric	Matrix is altered glass, composed of yellow glass shards, wispy areas are likely pumice	Matrix is welded and glassy, contains ~5% pumice, and glass shards, pumice is phyric and either white or banded
Alteration	None identifiable	None identifiable	Matrix alteration	Chlorite alteration of biotite

Sample Number	17-SM-07	17-SM-10	17-SM-11	17-SM-12
Unit	Tuff of Clipper Gap	Tuff of Clipper Gap	Tuff of Clipper Gap	Tuff of Clipper Gap
Lithology	Whole rock	Whole rock	Whole Rock	Whole Rock
% Phenocrysts	~4%	~5%	~10%	~5%
Plagioclase	Trace, <0.5 mm, fractured phenocrysts with polysynthetic twinning	1%, up to 1.5 mm, phenocrysts with polysynthetic twinning	3%, up to 1.5 mm, 2.5 mm in fiamme, phenocrysts with polysynthetic twinning, unaltered with some opaque inclusions	1%, up to 0.5 mm, slightly altered phenocrysts with polysynthetic twinning
Quartz	None identifiable	Trace, up to 1.5 mm, highly fractured phenocryst with rounded corners and embayments	3%, up to 1.5 mm, phenocrysts with rounded corners and embayments, fractured	1%, up to 1.5 mm, phenocrysts with rounded corners and embayments, fractured
Sanidine	3%, up to 2.0 mm, unaltered, fractured phenocrysts	3%, up to 2.0 mm, fractured phenocrysts	2%, 1.5 mm, fractured, unaltered phenocrysts	2%, up to 1.0 mm, fractured, unaltered
Biotite	1%, up to 0.2 mm, phenocrysts altered by chlorite	Trace, up to 0.2 mm, altered by chlorite	Trace, up to 0.5 mm in fiamme, up to 0.25 mm in matrix, altered phenocrysts	Trace, up to 0.5 mm, altered red
Amphibole	None identifiable	None identifiable	1%, up to 1.0 mm, altered and replaced, in fiamme	Trace, up to 1.75 mm, phenocryst with thick dehydration rim
Accessory Phases	1%, opaque minerals, <0.1 mm, one hexagonal crystal is ~0.5 mm 1%, Fe-Ti oxides, disseminated grains throughout matrix, <<0.1 mm	Trace, opaque minerals, <0.1 mm	Trace, opaque minerals, <0.1 mm, in fiamme and matrix Trace, Fe-Ti oxides, <0.1 mm Trace, monazite	Trace, opaque minerals, <0.1 mm Trace, Fe-Ti oxides, <0.1 mm Trace, monazite
Lithics	2%, 1.5-2.0 mm, brown opaque with plagioclase laths and opaques, multiple of the same composition	1%, composed of red opaque material, 1.0 mm	None identifiable	None identifiable
Textures	Matrix is welded and glassy, contains ~5% pumice, and glass shards, pumice is phyrical and either white or banded	Matrix is glassy and spherulitic, appears welded	Matrix is brown, welded and glassy, voids or pockets of glass are recrystallized on the edges, dark brown opaque areas of matrix	Matrix is altered and composed of glass shards
Alteration	Chlorite alteration of biotite	Chlorite alteration of biotite	10%, calcite or sericite alteration in matrix	10%, calcite or sericite alteration in matrix

Sample Number Unit Lithology % Phenocrysts	17-SM-13A Tuff of Brunton Pass Whole rock ~6%	17-SM-13B Tuff of Brunton Pass Whole rock ~3%	17-SM-14 Tuff of Arc Dome Whole Rock 21%	17-SM-15A Tuff of Arc Dome Pumice 11%
Plagioclase	Trace, up to 0.75 mm, slightly fractured phenocrysts with polysynthetic twinning	Trace, up to 0.5 mm, phenocrysts with polysynthetic twinning	7%, up to 1.5 mm, phenocrysts with polysynthetic twinning	5%, up to 1.5 mm, slightly fractured phenocrysts with polysynthetic twinning, some are weakly chemically zoned
Quartz	2%, up to 2.0 mm, phenocrysts with rounded corners and embayments, some have resorption in the middle	Trace, up to ~1.25 mm, unevenly fractured phenocrysts with rounded corners and embayments	2%, up to 1.0 mm, weakly fractured, unaltered phenocrysts	5%, up to 2.0 mm, fractured phenocrysts with rounded corners ~30% microcrystalline in matrix
Sanidine	3%, up to ~1.75 mm, fractured phenocrysts, some with Carlsbad twinning, some have resorption	2%, up to ~1.75 mm, fractured phenocrysts, some with Carlsbad twinning	10%, up to 2.5 mm, phenocrysts, some with Carlsbad twinning and uneven fractures, some are weakly chemically zoned	5%, 0.5-1.0 mm, phenocrysts with Carlsbad twinning
Biotite	Trace, ~0.25 mm, altered	Trace, up to 0.5 mm	2%, up to 0.75 mm, slightly bent phenocrysts	1%, up to 1.0 mm, bent phenocrysts, some partially opaque
Amphibole	None identifiable	None identifiable	2%, up to 2.0 mm, altered edges, some phenocrysts completely replaced	None identifiable
Accessory Phases	Trace, opaque minerals, up to 0.4 mm Trace, Fe-Ti oxides, most <0.1 mm, one up to 0.2 mm	1%, opaque minerals, most ≤0.1 mm, up to 0.5 mm Trace, Fe-Ti oxides, <0.1 mm	1%, opaque minerals, up to 0.2 mm Trace, monazite, <0.1 mm	Trace, opaque minerals, most ≤0.1 mm, largest up to 1.0 mm
Lithics	3%, up to ~3.0 mm, composed of microcrystalline quartz	1-2%, up to 0.5 mm, greenish, altered, composed of microcrystalline qtz	None identifiable	None identifiable
Textures	Matrix is welded, orange-brown, composed of spherulitic glass shards White and banded fiamme are spherulitic and aphyric	Matrix is glassy, altered and spherulitic, doesn't appear as welded as 17-SM-13B Matrix has air bubbles with glassy rims that haven't been compacted Possible pumice is all spherulitic	Matrix is brown, glassy, and wraps phenocrysts Pumice is spherulitic	Matrix is glassy, brown and slightly banded which wraps phenocrysts, partially microcrystalline quartz
Alteration	None identifiable	~5%, calcite or sericite alteration in matrix	None identifiable	None identifiable

Sample Number Unit Lithology % Phenocrysts	17-SM-15B Tuff of Arc Dome Whole rock 22%	17-SM-16A Gabbs Valley Tuff Whole rock ~1%	17-SM-16B Gabbs Valley Tuff Whole rock ~6%	17-SM-17A Underdown Tuff Porphyritic pumice 20%
Plagioclase	5%, up to 1.5 mm, phenocrysts with polysynthetic twinning	None identifiable	1%, ~0.3-2.0 mm, fractured phenocrysts with polysynthetic twinning	10%, 2.0 mm, phenocrysts altered heavily by sericite and calcite, show polysynthetic twinning
Quartz	8%, up to 2.5 mm, fractured phenocrysts with rounded corners, many are plucked or resorbed	1%, ~0.1-0.4 mm, possibly secondary, most are small phenocrysts	1%, up to 2.0 mm, fractured phenocrysts with rounded corners and embayments	10%, 0.5 mm, small grains in silicified veins
Sanidine	8%, up to 2.0 mm, phenocrysts, some have Carlsbad twins	None identifiable	2%, up to ~2.0 mm, fractured phenocrysts with Carlsbad twinning	10%, 2.0 mm, phenocrysts altered by yellow alteration
Biotite	1%, up to 1.75 mm, phenocrysts with reddish alteration on edges, some are completely opaque, some partially resorbed in the middle	Trace, ~1.75 mm, fresh, opaque inclusion, located in pumice	Trace-1%, up to ~0.4 mm, slightly bent phenocrysts with thin opaque rims	None identifiable
Amphibole	None identifiable	None identifiable	Trace, <0.1 mm, small green fragment	None identifiable
Accessory Phases	1%, opaque minerals, up to 0.25 mm Trace, monazite	Trace, opaque minerals, ≤0.1 mm	Trace, opaque minerals, 0.1-0.25 mm Trace, mystery blue fragments, ≤0.1 mm	2% opaque minerals are included in feldspars and larger grains in groundmass, trace monazite
Lithics	1%, microcrystalline, 1.0 mm	None identifiable	2%, ~1.75 mm, porphyritic with a microcrystalline matrix	None identifiable
Textures	Matrix is brown and glassy, pumice is spherulitic	Matrix is welded, composed of orange-brown glass shards White pumice is aphyric, completely spherulitic Dark pumice is phryic, with bt and qtz phenocrysts, and glass shards Banded pumice is spherulitic	Matrix is welded, brown, glassy, shows some glass shards and slight banding that wraps around phenocrysts Banded and white pumice are spherulitic and phryic	Matrix is brown altered glass
Alteration	None identifiable	None identifiable	None identifiable	1% calcite alteration

Sample Number Unit Lithology % Phenocrysts	17-SM-17B Underdown Tuff Whole Rock 10%	17-SM-17C Underdown Tuff Porphyritic pumice 20%	17-SM-18 Pablo Formation Whole Rock -	17-SM-19 Bonita Canyon Whole Rock ~10%
Plagioclase	3%, up to 2.5 mm, phenocrysts highly altered by calcite	10%, up to 2.0 mm, phenocrysts altered heavily by sericite and calcite, show polysynthetic twinning	68%, up to 1.75 mm, phenocrysts with polysynthetic twinning, altered by sericite, some show chemical zoning	3%, up to 2.5 mm, most ~1.5mm, phenocrysts, calcite alteration
Quartz	3%, up to 1.5 mm, quartz eye phenocrysts have embayments, and are slightly fractured 50%, microcrystalline quartz in silicified areas of matrix	10%, up to 2.0 mm, small grains in silicified veins	None identifiable	5%, up to 1.5 mm, fractured phenocrysts with rounded corners and embayments
Sanidine	3%, up to 2.5 mm, phenocrysts have Carlsbad twinning, and sieve texture	10%, up to 2.0 mm, phenocrysts altered by yellow alteration	None identifiable	2%, ~1.5 mm, highly altered, sieved, phenocrysts
Biotite	None identifiable	None identifiable	None identifiable	Trace, up to 2.0 mm long, thin, altered, phenocrysts
Amphibole	1%, up to 0.5 mm, completely replaced by opaque minerals	None identifiable	30%, up to 1.5 mm, unaltered phenocrysts	None identifiable
Accessory Phases	1%, opaque minerals are up to 0.5 mm and found throughout matrix	2% opaque minerals are included in feldspars and larger grains in groundmass, <0.1 mm trace monazite, <0.1 mm	2%, opaque minerals, blocky, most ~0.1 mm, one up to 0.25 mm	Trace, opaque minerals, <0.1 mm
Lithics	None identifiable	None identifiable	None identifiable	5%, size, composed mostly microcrystalline quartz, are patchy looking
Textures	Matrix is crystalline with some altered brown glass showing banding that wraps phenocrysts, some areas of silicification	Matrix is brown altered glass	Matrix is microcrystalline	Matrix is glassy, has some microcrystalline quartz
Alteration	1% chlorite alteration in matrix	1% calcite alteration	Sericite alteration on plagioclase	1% wispy yellow alteration (chlorite?)

Sample Number Unit Lithology % Phenocrysts	17-SM-20 Tuff of Arc Dome Whole Rock 27%	17-SM-21A Tuff of Clipper Gap Porphyritic pumice 18%	17-SM-21B Tuff of Clipper Gap Whole Rock ~6%	17-SM-22 Tuff of Clipper Gap Whole Rock ~16%
Plagioclase	10%, up to 2.5 mm, phenocrysts with polysynthetic twinning, some chemically zoned	4%, 1.0-1.5 mm, fractured phenocrysts with polysynthetic twinning, some show chemical zoning and resorption	1%, up to 1.5 mm, most <0.1mm, unaltered phenocrysts with polysynthetic twinning	5%, 1.0-1.25 mm, fractured phenocrysts with polysynthetic twinning, some resorption
Quartz	None identifiable	None identifiable	2%, up to 1.0 mm, phenocrysts with rounded corners and embayments	1%, ~2.0 mm, unevenly fractured phenocrysts with rounded corners and embayments
Sanidine	10%, up to 3.0 mm, fractured phenocrysts, some with Carlsbad twinning	12%, 1.0-2.5 mm, fractured phenocrysts, some show chemical zoning and resorption, some with Carlsbad twinning	3%, up to 2.5 mm, unaltered phenocrysts with Carlsbad twinning	5%, 1.0-1.5 mm, unaltered, fractured phenocrysts, some with Carlsbad twinning
Biotite	3%, up to 2.5 mm, unaltered phenocrysts, some slightly bent	None identifiable	Trace, ~0.25 mm, dark and almost and opaque	2-3%, 0.75-1.75 mm, unaltered phenocrysts
Amphibole	1%, up to 1.5 mm, unaltered phenocrysts	None identifiable	None identifiable	2%, ~1.0 mm, unaltered phenocrysts, elongate or hexagonal
Accessory Phases	3%, pyroxene, up to 2.0 mm, phenocrysts with some inclusions of opaque minerals and Fe-Ti oxides 1%, opaque minerals, 0.5-1.0 mm	1%, opaque minerals, ≤0.2 mm, Trace, monazite	Trace, opaque minerals, most <<0.1mm, one up to 0.1 mm	2%, opaque minerals, ≤0.2 mm
Lithics	None identifiable	None identifiable	None identifiable	5%, ~2.0 mm, patchy and microcrystalline, plagioclase rich
Textures	Matrix is fresh and glassy	Matrix is glassy and altered	Matrix is glassy, welded, with some glass shards, some areas of spherulites and microcrystalline quartz, relatively unaltered	Matrix is densely welded, composed of glass shards, large aphyric fiamme
Alteration	None identifiable	Alteration in matrix	None identifiable	None identifiable

Sample Number Unit Lithology % Phenocrysts	17-SM-24A Tuff of Clipper Gap Banded Pumice 3%	17-SM-25 Tuff of Clipper Gap Whole Rock 6%	17-SM-26A Tuff of Clipper Gap Whole rock 7%	17-SM-26B Tuff of Clipper Gap Porphyritic Pumice ~10%
Plagioclase	1%, up to 1.0 mm, phenocryst with polysynthetic twinning	1%, up to 0.2 mm, unaltered phenocrysts with polysynthetic twinning	1-2%, ~1.75 mm, unaltered, weakly fractured phenocrysts with polysynthetic twinning	None identifiable
Quartz	None identifiable	None identifiable	1%, 1.0-1.5 mm, weakly fractured phenocrysts with rounded corners and embayments	5%, up to 2.0 mm, phenocrysts with rounded corners, partially resorbed in the center
Sanidine	2%, up to 2.0 mm, fractured, unaltered phenocrysts	3%, up to 1.5 mm, unaltered phenocrysts	4%, 1.0-1.5 mm, unaltered, fractured phenocrysts, some with Carlsbad twinning	5%, up to 2.0 mm, slightly altered, fractured phenocrysts
Biotite	None identifiable	2%, up to 1.5 mm, dark, nearly opaque phenocrysts, some are bent	None identifiable	Trace, up to 0.5 mm, altered, nearly opaque phenocryst
Amphibole	None identifiable	None identifiable	Trace, ~0.5 mm, altered with a dark brown rim	Trace, up to 0.5 mm, phenocryst completely replaced by chlorite
Accessory Phases	Trace, opaque minerals, ≤0.1 mm Trace, Fe-Ti oxides, <<0.1 mm	1%, opaque minerals, ≤0.1 mm Trace, monazite, <0.1 mm	1%, opaque minerals, ~0.1 mm, some blocky, others look like fillers (but are thin), Trace-1%, Fe-Ti oxides, <0.1 mm Trace, monazite, <0.1 mm	Trace, opaque minerals, up to 0.2 mm Trace, Fe-Ti oxides, <0.1 mm
Lithics	None identifiable	5%, microcrystalline clasts, some with Ti-oxides, ranging from 0.5-5.5 mm	None identifiable	None identifiable
Textures	Matrix is glassy, banded and wraps around phenocrysts	Matrix is yellow, glassy and welded with yellow glass shards, pumice is yellow and banded 5% pumice that is spherulitic	Matrix is spherulitic, reddish-brown areas, some areas of matrix have smaller pieces of phenocrysts, some parts of matrix appear to wrap around phenocrysts	Matrix is altered, red and streaky, has spherulites and microcrystalline quartz
Alteration	None identifiable	Yellow alteration of matrix	Red alteration in matrix	Alteration in matrix

Sample Number	17-SM-26C	17-SM-27	17-SM-28	17-SM-29
Unit	Tuff of Clipper Gap	Tuff of Clipper Gap	Gabbs Valley Tuff	Gabbs Valley Tuff
Lithology	Porphyritic pumice?	Whole rock	Whole rock	Whole rock
% Phenocrysts	~15%	~10%	~13%	22%
Plagioclase	5%, up to 2.0 mm, phenocrysts with polysynthetic twinning, some are chemically zoned and altered	5%, ≤1.5 mm, phenocrysts with polysynthetic twinning, some are yellow in XPL, singular or clustered	2%, ≤0.5 mm, phenocrysts with polysynthetic twinning	5%, up to ~1.0 mm, fractured phenocrysts with polysynthetic twinning, some are resorbed in the centre
Quartz	None identifiable	Trace, ~1.25 mm, phenocrysts with rounded corners and embayments, very fractured	7%, up to ~2.0 mm, phenocrysts with rounded corners and embayments	10%, up to ~2.5 mm, highly fractured phenocrysts with rounded corners and embayments, uneven fractures are brown-reddish
Sanidine	10%, 1.25-2.0 mm, weakly fractured phenocrysts, some are altered and show Carlsbad twinning	5%, 1.5-2.0 mm, slightly fractured phenocrysts with Carlsbad twinning	3%, up to ~1.25 mm, slightly fractured phenocrysts with Carlsbad twinning	5%, up to ~1.75 mm, fractured phenocrysts with Carlsbad twinning
Biotite	None identifiable	Trace, ≤0.5 mm, very pleochroic, possibly slightly altered	1%, up to ~0.75 mm, bent phenocrysts with red edges, reddish-orange to opaque inclusions	2%, up to ~1.75 mm, bent phenocrysts
Amphibole	Trace, ~0.25 mm, altered	Trace, ~0.75 mm, possibly slightly altered	Trace, ~0.2 mm, very altered	None identifiable
Accessory Phases	1%, opaque minerals, ≤0.25 mm, blocky, Trace, monazite, Trace, Fe-Ti oxides, yellow, possibly replacing biotite based on the shape	1%, opaque minerals, ≤0.25 mm, blocky	Trace, opaque minerals, ≤0.2 mm Trace, Fe-Ti oxides, <<0.1 mm Trace, monazite Trace, mystery blue fragments, <<0.1 mm	Trace-1%, opaque minerals, up to 0.25 mm Trace, monazite, <0.1 mm
Lithics	None identifiable	3%, 1.0-1.5 mm, most microcrystalline with opaque minerals	1%, up to 1.25 mm, altered orange-yellow clast with a yellow rind	1%, microcrystalline, 1.0 mm
Textures	Matrix is red-orange and nearly opaque, most altered phenocrysts are in groupings or vein-like structures, no banding	Matrix is composed of unaltered glass shards, fiamme are banded and generally aphyric	Matrix is microcrystalline, possibly glassy, poorly welded Phyric pumice is spherulitic	Matrix is welded, composed of orange-brown glass shards, banding wraps around phenocrysts Some veiny areas of microcrystalline quartz, and microcrystalline areas of matrix
Alteration	Alteration in matrix	None identifiable	None identifiable	None identifiable

Sample Number	17-SM-30	17-SM-31
Unit	Gabbs Valley Tuff	Gabbs Valley Tuff
Lithology	Whole rock	Pumice
% Phenocrysts	15%	16%
Plagioclase	10%, up to ~3.0 mm, fractured phenocrysts with polysynthetic twinning, some show chemical zoning, some resorption in centres	7%, up to 1.5 mm, fractured phenocrysts with polysynthetic twinning, altered by calcite and sericite
Quartz	3%, up to ~1.2 5mm, rounded phenocrysts with embayments	None identifiable
Sanidine	10%, up to ~3.0 mm, fractured phenocrysts with Carlsbad twinning	7%, up to 2.5 mm, fractured phenocrysts with some resorption
Biotite	2%, up to ~2.25 mm, phenocrysts with opaque inclusions, some bent	2%, ~1.25-1.75 mm, most phenocrysts look fresh, some almost completely opaque, some are bent and wrap around other phenocrysts
Amphibole	None identifiable	None identifiable
Accessory Phases	1%, opaque minerals, up to 0.5 mm, most smaller Trace, Fe-Ti oxides, <<0.1 mm	1%, opaque minerals, up to ~0.5 mm Trace, Fe-Ti oxides, <0.1 mm
Lithics	None identifiable	None identifiable
Textures	Matrix is welded and composed of reddish-orange glass shards, matrix wraps around phenocrysts	Matrix is brown, glassy and spherulitic, banding in matrix wraps around phenocrysts, phenocrysts have glassy rims
Alteration	Possible alteration in matrix	None identifiable

Table IV: Major Element Oxide Abundances

Sample ID	Unit Name	Rock Type	SiO ₂	TiO ₂	Al ₂ O ₃	Fe ₂ O ₃	MnO
16-SM-02	Bonita Canyon Formation	pumice	66.46	0.15	18.77	2.17	0.043
16-SM-04	Underdown Tuff	tuff	78.41	0.09	12.25	1.44	0.040
16-SM-08	Bonita Canyon Formation	tuff	76.57	0.15	13.07	1.53	0.021
16-SM-09	Megabreccia block	tuff	71.49	0.35	14.23	2.46	0.031
16-SM-13A	Tuff of Clipper Gap	tuff	74.36	0.16	13.60	1.48	0.052
16-SM-13B	Tuff of Clipper Gap	tuff	74.51	0.10	12.54	1.36	0.041
16-SM-13C	Tuff of Clipper Gap	tuff	77.82	0.09	12.67	1.51	0.051
16-SM-14	Tuff of Clipper Gap	porphyritic pumice	78.10	0.08	12.36	1.41	0.020
16-SM-15A	Tuff of Clipper Gap	porphyritic pumice	66.57	0.40	16.08	3.44	0.051
16-SM-15A	Tuff of Clipper Gap	porphyritic pumice	68.03	0.40	16.47	3.62	0.051
16-SM-16	Tuff of Clipper Gap	porphyritic pumice	67.51	0.38	16.37	3.39	0.041
16-SM-20B	Pablo Formation	andesite	52.31	0.70	13.86	9.96	0.173
16-SM-20C	Pablo Formation	andesite	58.56	0.65	15.96	7.21	0.122
16-SM-21A	Bonita Canyon Formation	tuff	77.99	0.13	12.64	1.62	0.022
16-SM-21B	Bonita Canyon Formation	pumice	71.39	0.11	14.51	0.93	0.022
16-SM-22	Bonita Canyon Formation	tuff	77.26	0.18	12.51	1.75	0.052
16-SM-26	Bonita Canyon Formation	tuff	75.62	0.30	12.47	2.18	0.061
16-SM-29A	Underdown Tuff	porphyritic pumice	78.33	0.11	12.42	1.51	0.061
16-SM-29B	Underdown Tuff	white pumice	78.93	0.07	11.56	0.52	0.020
16-SM-30	Bonita Canyon Formation	tuff	79.62	0.15	11.98	1.62	0.041
16-SM-32A	Underdown Tuff	porphyritic pumice	72.54	0.16	13.52	1.91	0.050
16-SM-32B	Underdown Tuff	tuff	76.52	0.09	11.93	1.40	0.040
16-SM-32D	Underdown Tuff	banded pumice	77.19	0.09	12.51	1.53	0.142
16-SM-33A	Dacite Porphyry Dyke	dacite	66.40	0.55	16.96	4.09	0.102
16-SM-34	Underdown Tuff	tuff	76.57	0.11	12.90	1.69	0.020
16-SM-35	Underdown Tuff	tuff	82.57	0.08	10.60	1.14	0.010
16-SM-37	Bonita Canyon Formation	tuff	77.54	0.12	12.49	0.91	0.011
16-SM-38A	Unnamed tuff	tuff	79.45	0.07	11.95	1.08	0.020
16-SM-38B	Unnamed tuff	pumice	78.77	0.06	11.72	1.01	0.030
16-SM-40	Unnamed pumice	pumice	78.38	0.07	12.02	0.94	0.020
16-SM-42	Unnamed tuff	tuff	78.83	0.10	12.23	1.24	0.040
16-SM-44	Pablo Formation	andesite	53.84	0.83	15.40	9.92	0.163
16-SM-45	Underdown Tuff	tuff	76.76	0.09	11.89	1.73	0.071
16-SM-46	Underdown Tuff	tuff	78.52	0.08	12.05	1.40	0.020
16-SM-47	Underdown Tuff	tuff	78.39	0.09	12.41	1.52	0.040
16-SM-48	Underdown Tuff	tuff	77.40	0.09	12.28	1.50	0.040
16-SM-49	Underdown Tuff	tuff	76.59	0.08	12.11	1.34	0.030
16-SM-50	Underdown Tuff	tuff	69.85	0.47	15.79	2.92	0.051
16-SM-51	Underdown Tuff	tuff	78.68	0.08	11.90	1.48	0.041

Sample ID	MgO	CaO	Na ₂ O	K ₂ O	P ₂ O ₅	Cr ₂ O ₃	SrO	BaO	LOI	Total
16-SM-02	0.40	0.989	2.93	8.77	0.021	<0.01	0.011	0.032	6.41	101.16
16-SM-04	0.04	0.252	3.46	4.76	0.020	0.000	0.000	0.000	0.79	100.77
16-SM-08	0.16	1.091	2.28	4.40	0.041	0.000	0.000	0.000	2.9	99.47
16-SM-09	0.21	0.704	3.45	5.13	0.112	0.000	0.000	0.000	1.95	98.36
16-SM-13A	0.62	0.703	2.52	5.32	0.052	0.000	0.000	0.000	3.39	99.05
16-SM-13B	0.33	0.733	3.02	5.47	0.031	0.000	0.000	0.000	3.14	98.28
16-SM-13C	0.16	0.466	3.50	5.35	0.010	<0.01	<0.01	0.010	1.35	101.65
16-SM-14	0.07	0.343	3.76	5.04	<0.01	<0.01	<0.01	<0.01	0.92	101.2
16-SM-15A	0.21	1.045	4.44	6.49	0.183	0.000	0.000	0.000	1.46	98.98
16-SM-15A	0.22	1.088	4.41	6.61	0.153	<0.01	0.010	0.031	1.71	101.13
16-SM-16	0.22	0.996	4.50	6.56	0.061	<0.01	0.010	0.051	1.68	100.12
16-SM-20B	8.82	9.832	2.23	1.75	0.274	0.000	0.000	0.000	1.57	100.11
16-SM-20C	4.55	8.774	2.70	1.67	0.203	0.010	0.122	0.051	1.68	100.62
16-SM-21A	0.41	2.344	1.07	4.87	0.022	<0.01	<0.01	0.022	8.17	101.8
16-SM-21B	0.62	2.825	0.88	5.76	0.022	0.000	0.000	0.000	10.15	98.16
16-SM-22	0.23	0.405	3.45	4.44	0.052	<0.01	<0.01	0.031	3.86	100.51
16-SM-26	0.15	1.150	3.59	4.09	0.081	<0.01	0.020	0.112	1.77	99.85
16-SM-29A	0.05	0.141	2.67	5.08	0.020	0.000	0.000	0.000	0.94	100.41
16-SM-29B	0.04	0.202	2.43	5.15	0.020	0.000	0.000	0.000	0.92	98.96
16-SM-30	0.16	0.612	3.19	3.76	0.031	<0.01	<0.01	0.041	1.97	101.25
16-SM-32A	0.08	0.525	4.06	5.23	0.030	0.000	0.000	0.000	0.87	98.12
16-SM-32B	0.04	0.453	3.62	4.82	<0.01	<0.01	<0.01	0.010	0.68	98.94
16-SM-32D	0.04	1.195	6.17	1.79	0.020	0.000	0.000	0.000	1.31	100.71
16-SM-33A	0.63	2.799	4.10	5.98	0.153	<0.01	0.031	0.143	2.2	101.98
16-SM-34	0.04	0.060	2.34	6.27	0.020	0.000	0.000	0.000	0.75	100.02
16-SM-35	0.06	0.051	0.09	4.94	0.020	0.000	0.000	0.000	1.43	99.59
16-SM-37	0.17	1.908	2.03	4.78	0.022	<0.01	0.011	0.033	9.13	100.84
16-SM-38A	0.07	0.382	3.68	4.71	0.020	0.000	0.000	0.000	0.45	101.45
16-SM-38B	0.05	0.322	3.61	4.63	0.010	<0.01	<0.01	<0.01	0.6	100.21
16-SM-40	0.09	0.402	3.69	4.68	0.040	<0.01	<0.01	0.010	0.62	100.35
16-SM-42	0.10	0.443	3.57	4.78	<0.01	0.000	0.000	0.000	0.68	101.36
16-SM-44	6.62	9.656	3.03	1.98	0.224	0.031	0.082	0.061	2	101.86
16-SM-45	0.04	0.332	3.71	4.60	<0.01	<0.01	<0.01	0.010	0.73	99.24
16-SM-46	0.03	0.341	3.77	4.74	<0.01	0.000	0.000	0.000	0.41	100.95
16-SM-47	0.04	0.412	3.79	4.91	<0.01	<0.01	<0.01	<0.01	0.51	101.61
16-SM-48	0.05	0.393	3.69	4.86	0.010	<0.01	<0.01	0.010	0.65	100.33
16-SM-49	0.03	0.231	3.60	4.82	<0.01	<0.01	<0.01	<0.01	0.51	98.84
16-SM-50	0.17	0.810	3.74	6.56	0.111	0.000	0.000	0.000	1.24	100.57
16-SM-51	0.05	0.861	3.24	4.55	<0.01	0.000	0.000	0.000	1.27	100.9

Sample ID	Unit Name	Rock Type	SiO ₂	TiO ₂	Al ₂ O ₃	Fe ₂ O ₃	MnO
16-SM-53	Rhyolite Intrusions	rhyolite	77.71	0.05	11.63	1.21	0.020
16-SM-55	Unnamed Tuff	tuff	78.85	0.05	11.90	1.17	0.020
16-SM-56	Rhyolite Intrusions	rhyolite	79.04	0.05	12.35	0.89	0.020
17-SM-01	Terrill Mountains tuffs	tuff	77.97	0.11	12.74	1.77	0.020
17-SM-02	Terrill Mountains tuffs	tuff	77.89	0.11	12.84	1.48	0.031
17-SM-03 A	Terrill Mountains tuffs	white pumice	76.70	0.11	13.57	1.57	0.032
17-SM-03 B	Terrill Mountains tuffs	banded pumice	77.36	0.10	13.41	1.59	0.032
17-SM-03 C	Terrill Mountains tuffs	tuff	76.88	0.12	13.22	1.71	0.032
17-SM-06	Tuff of Clipper Gap	tuff	72.46	0.20	13.56	2.23	0.043
17-SM-07	Tuff of Clipper Gap	tuff	78.15	0.19	11.31	1.81	0.031
17-SM-08	Tuff of Clipper Gap	tuff	15.63	0.15	3.46	1.07	0.027
17-SM-09	Tuff of Clipper Gap	tuff	72.99	0.12	13.97	1.49	0.066
17-SM-10	Tuff of Clipper Gap	tuff	77.99	0.10	11.76	1.51	0.020
17-SM-11	Tuff of Clipper Gap	tuff	75.90	0.10	12.17	1.58	0.041
17-SM-12	Tuff of Clipper Gap	tuff	72.97	0.12	12.97	1.70	0.041
17-SM-13 A	Tuff of Brunton Pass	tuff	77.66	0.09	12.35	1.56	0.020
17-SM-13 B	Tuff of Brunton Pass	tuff	76.50	0.11	12.46	1.64	0.061
17-SM-14	Tuff of Arc Dome	tuff	73.41	0.21	13.36	1.84	0.040
17-SM-15 A	Tuff of Arc Dome	tuff	76.35	0.07	12.27	1.16	0.040
17-SM-15 B	Tuff of Arc Dome	tuff	76.90	0.09	11.88	1.21	0.030
17-SM-16 A	Tuff of Gabbs Valley	tuff	78.88	0.12	11.08	1.67	0.030
17-SM-16 B	Tuff of Gabbs Valley	tuff	73.79	0.16	13.37	1.73	0.040
17-SM-17 A	Underdown Tuff	porphyritic pumice	68.81	0.35	15.95	3.13	0.102
17-SM-17 B	Underdown Tuff	tuff	77.12	0.09	12.13	1.54	0.030
17-SM-17 C	Underdown Tuff	porphyritic pumice	64.66	0.55	17.34	3.92	0.082
17-SM-18	Pablo Formation	andesite	57.49	0.68	17.95	6.48	0.113
17-SM-19	Bonita Canyon Formation	tuff	78.17	0.11	12.67	1.60	0.041
17-SM-20	Tuff of Arc Dome	tuff	69.96	0.50	14.88	2.66	0.051
17-SM-21 A	Tuff of Clipper Gap	tuff	68.73	0.38	17.03	2.27	0.020
17-SM-21 B	Tuff of Clipper Gap	tuff	79.22	0.10	11.96	1.29	0.010
17-SM-22	Tuff of Clipper Gap	tuff	75.48	0.15	14.19	1.43	0.052
17-SM-23	Tuff of Clipper Gap	white pumice	77.28	0.07	12.95	1.11	0.084
17-SM-24	Tuff of Clipper Gap	white pumice	76.09	0.07	13.19	1.19	0.052
17-SM-25	Tuff of Clipper Gap	tuff	75.00	0.13	13.68	1.42	0.041
17-SM-26 A	Tuff of Clipper Gap	white pumice	75.14	0.11	12.69	1.67	0.040
17-SM-26 B	Tuff of Clipper Gap	tuff	76.01	0.09	12.40	1.54	0.050
17-SM-26 C	Tuff of Clipper Gap	tuff	67.68	0.30	15.49	3.10	0.092
17-SM-27	Tuff of Clipper Gap	tuff	74.37	0.17	13.45	1.78	0.022
17-SM-28	TgV2	tuff	77.49	0.08	12.41	1.19	0.030
17-SM-29	TgV2	tuff	75.31	0.15	12.70	2.20	0.020

Sample ID	MgO	CaO	Na ₂ O	K ₂ O	P ₂ O ₅	Cr ₂ O ₃	SrO	BaO	LOI	Total
16-SM-53	0.03	0.252	3.33	4.67	<0.01	<0.01	<0.01	<0.01	0.65	98.9
16-SM-55	0.07	0.224	2.09	4.66	<0.01	<0.01	<0.01	0.010	1.73	99.08
16-SM-56	0.07	0.283	3.19	4.83	<0.01	<0.01	<0.01	<0.01	1.21	100.73
17-SM-01	0.12	0.475	3.34	4.78	0.020	0.015	<0.01	0.010	1.15	101.4
17-SM-02	0.06	0.590	3.54	4.44	0.052	0.019	<0.01	0.010	3.62	101.21
17-SM-03 A	0.35	0.641	2.77	4.32	0.021	0.005	<0.01	0.011	6.86	100.56
17-SM-03 B	0.28	0.630	2.83	4.46	0.011	0.010	<0.01	0.011	6.93	101.19
17-SM-03 C	0.29	0.786	2.79	4.31	<0.01	0.010	<0.01	0.011	6.22	100.54
17-SM-06	0.90	1.608	2.32	5.76	0.032	0.009	<0.01	0.043	7.16	99.67
17-SM-07	0.09	0.703	3.35	4.47	0.041	0.006	<0.01	0.061	1.89	100.26
17-SM-08	0.78	63.486	0.60	0.62	0.055	0.005	0.027	0.041	37	99.68
17-SM-09	1.23	1.764	1.98	4.27	0.044	0.011	0.022	0.088	9.49	98.96
17-SM-10	0.11	0.568	3.44	4.68	0.020	0.008	<0.01	0.010	1.42	100.24
17-SM-11	0.21	1.903	3.69	4.66	0.041	0.009	<0.01	0.020	2.3	100.39
17-SM-12	0.11	3.215	2.99	6.28	0.041	0.004	<0.01	0.021	3.38	100.58
17-SM-13 A	0.10	0.334	3.43	4.70	0.010	0.009	<0.01	0.010	1.25	100.29
17-SM-13 B	0.20	1.211	3.43	4.77	0.102	0.007	<0.01	0.020	1.74	100.55
17-SM-14	0.21	0.827	3.68	4.71	0.010	0.018	0.010	0.091	0.82	98.42
17-SM-15 A	0.07	0.402	3.36	4.68	0.020	0.017	<0.01	0.010	0.58	98.45
17-SM-15 B	0.09	0.443	3.29	4.44	0.020	0.026	<0.01	0.020	0.64	98.44
17-SM-16 A	0.05	0.305	3.02	4.37	0.010	0.013	<0.01	0.020	1.64	99.59
17-SM-16 B	0.11	0.674	3.42	5.58	0.030	0.013	<0.01	0.070	0.52	98.98
17-SM-17 A	0.17	1.183	3.76	6.14	0.071	0.010	<0.01	0.031	1.94	99.75
17-SM-17 B	0.07	0.455	3.13	4.52	0.010	0.022	<0.01	0.010	1.07	99.14
17-SM-17 C	0.24	1.418	3.61	7.13	0.153	0.006	0.010	0.051	1.97	99.21
17-SM-18	3.42	5.064	4.31	2.16	0.225	0.017	0.133	0.133	2.26	98.22
17-SM-19	0.24	1.364	4.21	2.40	0.031	0.016	<0.01	0.021	2.61	100.94
17-SM-20	0.63	1.902	3.69	4.95	0.153	0.015	0.031	0.184	2.27	99.67
17-SM-21 A	0.08	0.968	4.71	6.69	0.081	0.009	0.010	0.030	0.79	101.02
17-SM-21 B	0.03	0.353	3.68	4.64	0.020	0.015	<0.01	0.020	0.93	101.36
17-SM-22	0.65	0.915	3.39	4.94	0.042	0.014	0.010	0.062	4.02	101.48
17-SM-23	0.18	0.734	2.67	6.06	0.021	0.009	<0.01	0.010	4.92	101.42
17-SM-24	0.15	0.544	2.22	6.30	0.010	0.012	<0.01	<0.01	4.67	100.05
17-SM-25	0.14	0.543	2.72	6.42	0.041	0.005	0.010	0.051	2.46	100.27
17-SM-26 A	0.07	0.850	3.74	5.17	0.010	0.008	<0.01	0.020	1.13	99.54
17-SM-26 B	0.10	0.383	3.70	4.98	0.020	0.009	<0.01	0.020	0.81	99.32
17-SM-26 C	0.34	0.948	4.28	6.06	0.051	0.008	0.010	0.031	1.9	98.43
17-SM-27	0.59	2.214	1.44	4.95	0.022	0.003	0.033	0.044	10.7	100.22
17-SM-28	0.12	0.504	3.32	4.96	0.010	0.023	<0.01	0.020	0.9	100.17
17-SM-29	0.13	0.577	3.30	4.84	0.020	0.020	0.010	0.051	1.21	99.34

Sample ID	Unit Name	Rock Type	SiO ₂	TiO ₂	Al ₂ O ₃	Fe ₂ O ₃	MnO	MgO
Table IV: Major Element Oxide Abundances Cont. Underdown Caldera Complex								
17-SM-30	TgV2	tuff	74.94	0.23	14.07	2.10	0.020	0.18
17-SM-31	TgV3	porphyritic pumice	69.86	0.27	15.01	1.70	0.040	0.29
Table IV: Major Element Oxide Abundances Cont. Acid washing samples								
16-SM-13Caw	Tuff of Clipper Gap	tuff	77.79	0.06	12.51	0.41	<0.01	0.05
16-SM-14aw	Tuff of Clipper Gap	white pumice	78.64	0.04	12.52	0.36	<0.01	0.03
16-SM-16aw	Tuff of Clipper Gap	porphyritic pumice	69.65	0.31	16.38	0.99	0.010	0.03
17-SM-21Aaw	Tuff of Clipper Gap	porphyritic pumice	71.55	0.29	16.58	0.72	0.010	0.03
17-SM-22aw	Tuff of Clipper Gap	whole rock	78.46	0.10	13.40	0.55	0.021	0.32
17-SM-26Aaw	Tuff of Clipper Gap	whole rock	79.02	0.06	12.52	0.47	<0.01	<0.01
17-SM-26Caw	Tuff of Clipper Gap	porphyritic pumice	73.52	0.20	15.37	1.06	0.020	0.03
17-SM-27aw	Tuff of Clipper Gap	whole rock	84.56	0.15	9.31	0.73	0.011	0.25
Table IV: Major Element Oxide Abundances Cont. Young Sierra Nevada tuffs								
H18-SN6	Young Sierra Nevada tuffs	tuff	76.63	0.11	13.14	1.73	0.01	0.06
H18-SN15	Young Sierra Nevada tuffs	tuff	76.73	0.11	13.09	1.84	0.02	0.05

Sample ID	CaO	Na ₂ O	K ₂ O	P ₂ O ₅	Cr ₂ O ₃	SrO	BaO	LOI	Total
Table IV: Major Element Oxide Abundances Cont. Underdown Caldera Complex									
17-SM-30	0.988	3.77	5.07	0.030	0.021	0.020	0.101	0.88	101.56
17-SM-31	1.577	3.98	5.68	0.051	0.015	0.020	0.142	1.09	98.67
Table IV: Major Element Oxide Abundances Cont. Acid-washed Samples									
16-SM-13Caw	0.232	3.60	5.27	0.010	<0.002	<0.01	0.010	0.89	99.95
16-SM-14aw	0.191	3.96	5.07	0.010	<0.002	<0.01	<0.01	0.57	100.83
16-SM-16aw	0.816	4.71	6.57	0.010	<0.002	<0.01	0.030	0.79	99.51
17-SM-21Aaw	0.844	4.81	6.61	0.010	0.004	<0.01	0.030	0.5	101.5
17-SM-22aw	0.590	3.42	4.84	0.010	0.006	0.010	0.052	3.57	101.91
17-SM-26Aaw	0.251	3.86	5.22	<0.01	0.004	<0.01	0.010	0.54	101.41
17-SM-26Caw	0.597	4.55	6.19	0.010	0.004	<0.01	0.020	1.14	101.58
17-SM-27aw	0.707	0.98	3.19	<0.01	0.002	0.011	0.033	10.5	101.03
Table IV: Major Element Oxide Abundances Cont. Young Sierra Nevada tuffs									
H18-SN6	0.30	3.27	4.89	0.01				1.57	101.44
H18-SN15	0.27	3.25	4.80	0.01				1.58	101.46

Table V: Precision of Major Element analyses

Element	10-LT-05	10-LT-05	10-LT-05	Average	2σ
SiO₂	48.9	49.3	47.9	48.8	1.0
TiO₂	1.43	1.44	1.44	1.45	0.06
Al₂O₃	17.8	18.25	18.4	18.18	0.46
Fe₂O₃	9.39	9.76	9.69	9.54	0.28
MnO	0.14	0.14	0.14	0.14	0.00
MgO	6.45	6.66	6.62	6.61	0.20
CaO	9.34	9.56	9.44	9.52	0.30
Na₂O	3.60	3.56	3.51	3.59	0.02
K₂O	1.02	1.03	1.03	1.02	0.04
Cr₂O₃	0.030	0.030	0.025	0.030	0.008
P₂O₅	0.36	0.38	0.38	0.38	0.02
SrO	0.11	0.11	0.11	0.11	0.00
BaO	0.06	0.06	0.06	0.06	0.00
LOI	0.53	0.67	0.71	0.73	0.30
Total	99.16	100.95	99.46	100.23	1.54

Note: The first three columns of major element data for 10-LT-05 are the results of individual runs obtained with three batches of samples submitted to ALS for geochemical analysis. Averages and standard deviation (σ) for 10-LT-05 are calculated from 31 analyses by ALS (Nov. 2013-Nov. 2019).

Table V: Precision of Major Element analyses

Element	BHVO-2	BHVO-2	BHVO-2	Average	2σ	USGS Recommended Values
SiO₂	49.7	49.2	48.5	49.4	1.4	49.9
TiO₂	2.66	2.6	2.66	2.69	0.12	2.73
Al₂O₃	13.2	13.3	13.6	13.4	0.4	13.5
Fe₂O₃	12.20	12.55	12.55	12.37	0.30	12.3
MnO	0.17	0.17	0.16	0.17	0.00	-
MgO	7.11	7.28	7.25	7.27	0.22	7.23
CaO	11.1	11.3	11.2	11.3	0.4	11.4
Na₂O	2.23	2.16	2.16	2.21	0.08	2.22
K₂O	0.51	0.52	0.51	0.51	0.02	0.52
Cr₂O₃	0.04	0.04	0.04	0.04	0.00	-
P₂O₅	0.25	0.25	0.26	0.26	0.02	0.27
SrO	0.05	0.04	0.05	0.05	0.00	-
BaO	0.01	0.01	0.01	0.01	0.00	-
LOI	-0.51	-0.57	-0.57	-0.59	0.16	-
Total	98.72	98.85	98.38	99.19	1.9	100.07

Note: The first three columns of major element data for BHVO-2 are the results of individual runs obtained with three batches of samples submitted to ALS for geochemical analysis. Averages and standard deviation (σ) for BHVO-2 are calculated from 9 analyses by ALS (Jan. 2017-Nov. 2019).

Table VI: Trace Element Concentrations

Sample ID	Unit Name	Rock Type	Ag	As	Ba	Cd	Ce	Co	Cr	Cs	Cu	Dy	Er	Eu	Ga	Gd
16-SM-02	Bonita Canyon Formation	pumice	<0.5	<5	303	<0.5	125	1	<10	114	5	8.2	4.9	0.25	26	8.95
16-SM-04	Underdown Tuff	tuff	<0.5	<5	70.6	<0.5	109	<1	<10	3.87	6	5.11	2.87	0.07	20.4	5.11
16-SM-08	Bonita Canyon Formation	tuff	<0.5	15	331	<0.5	84.4	<1	<10	9.16	4	5	2.88	0.33	18.6	5.74
16-SM-09	Mega-breccia block	tuff	<0.5	11	1245	<0.5	72	1	<10	6.4	3	3.24	1.93	0.92	17.9	3.89
16-SM-13A	Tuff of Clipper Gap	tuff	<0.5	6	573	<0.5	71.6	1	<10	5.85	5	3.32	2.06	0.41	16.5	3.86
16-SM-13B	Tuff of Clipper Gap	tuff	<0.5	13	223	<0.5	86.2	<1	10	3.68	8	5.13	2.81	0.18	18.7	5.41
16-SM-13C	Tuff of Clipper Gap	tuff	<0.5	<5	111	<0.5	92.9	1	<10	3.4	4	6.21	3.46	0.1	21.3	6.61
16-SM-14	Tuff of Clipper Gap	porphyritic pumice	<0.5	<5	32.6	<0.5	94.5	<1	<10	4.73	4	5.7	3.4	0.06	20.8	4.99
16-SM-15A	Tuff of Clipper Gap	porphyritic pumice	<0.5	12	301	<0.5	102.5	1	10	2.69	13	11.2	5.06	0.73	21.9	18
16-SM-15A	Tuff of Clipper Gap	porphyritic pumice	<0.5	12	303	<0.5	106.5	<1	<10	2.59	12	11.1	4.94	0.69	21.4	18.2
16-SM-16	Tuff of Clipper Gap	porphyritic pumice	<0.5	11	447	<0.5	74.2	<1	<10	2.02	8	10.6	4.21	0.71	20.5	19.6
16-SM-20B	Pablo Formation	andesite	<0.5	<5	419	<0.5	34.6	34	450	14.35	100	2.88	1.63	1.17	18	3.97
16-SM-20C	Pablo Formation	andesite	<0.5	6	467	<0.5	37.3	19	40	6.38	19	2.31	1.28	1.06	19.2	3.07
16-SM-21A	Bonita Canyon Formation	tuff	<0.5	<5	179	<0.5	93	1	10	5.34	8	5.99	3.19	0.2	17.7	6.65
16-SM-21B	Bonita Canyon Formation	pumice	<0.5	<5	178	<0.5	128.5	<1	10	2.99	7	6.01	2.47	0.19	12.9	9.05
16-SM-22	Bonita Canyon Formation	tuff	<0.5	6	234	<0.5	91.5	2	10	11.6	5	5.61	3.28	0.25	18.3	6.32
16-SM-26	Bonita Canyon Formation	tuff	<0.5	<5	978	<0.5	78.3	2	10	5.02	5	3.34	1.66	0.95	12.7	4.1
16-SM-29A	Underdown Tuff	porphyritic pumice	<0.5	<5	90.4	<0.5	121	1	<10	7.51	6	5.92	3.43	0.1	19.1	6.27
16-SM-29B	Underdown Tuff	white pumice	<0.5	<5	81.6	<0.5	102.5	<1	<10	6.4	7	3.88	1.96	0.05	16	5.45
16-SM-30	Bonita Canyon Formation	tuff	<0.5	7	357	<0.5	102	1	10	9.21	3	5.86	3.05	0.36	18.6	6.7
16-SM-32A	Underdown Tuff	porphyritic pumice	<0.5	<5	56.5	<0.5	114	1	<10	3.8	5	6.83	3.73	0.08	21.1	7.44
16-SM-32B	Underdown Tuff	tuff	<0.5	<5	28.7	<0.5	121	<1	<10	1.73	5	6.24	3.48	0.09	21.4	7.13
16-SM-32D	Underdown Tuff	banded pumice	<0.5	6	1170	<0.5	77.6	2	10	1.89	7	3.36	1.89	1.46	18.6	4.23

Table VI: Trace Element Concentrations Cont.

Sample ID	Hf	Ho	La	Li	Lu	Mo	Nb	Nd	Ni	Pb	Pr	Rb	Sc	Sm	Sn	Sr	Ta	Tb	Th	Tl
16-SM-02	9.4	1.64	65	30	0.7	<1	37.7	59	2	28	15.65	391	2	11	5	82.1	2.7	1.37	29.4	<10
16-SM-04	7.3	1.02	35	30	0.5	3	29	32	4	23	9.17	213	1	6.9	4	13.1	2.1	0.82	24.3	<10
16-SM-08	6.6	1.05	41	60	0.5	4	21.9	35	2	18	9.93	175	3	7.1	3	62.7	1.6	0.89	20.2	<10
16-SM-09	6.6	0.69	36	100	0.3	2	17.1	28	4	23	8.32	161	5	5.6	2	134	1.1	0.57	16.3	<10
16-SM-13A	5.8	0.7	35	40	0.3	<1	13.9	27	1	144	7.82	153	4	5.2	12	87.9	1	0.56	16.6	10
16-SM-13B	7.2	1.02	42	30	0.5	<1	26	37	3	67	10.4	191	2	7.3	13	58.7	1.8	0.79	21.9	<10
16-SM-13C	7.3	1.22	42	20	0.5	2	30.9	41	<1	35	10.7	225	1	8.3	4	22.7	2.2	1.08	23.5	<10
16-SM-14	7.5	1.18	28	20	0.5	2	30.5	26	1	32	6.62	222	1	5.6	5	22.2	2.2	0.93	22.8	<10
16-SM-15A	15.6	1.99	176	50	0.6	2	18.2	157	5	27	41.5	132	10	28	2	67.8	1.1	2.27	8.69	<10
16-SM-15A	14.8	2	161	40	0.7	2	17.7	152	6	25	42.1	130	10	29	3	68.9	1.1	2.19	9.44	<10
16-SM-16	14.3	1.9	208	40	0.5	2	15.8	130	3	22	32	102	10	21	2	84.2	0.9	2.26	8	<10
16-SM-20B	2.6	0.59	16	30	0.2	1	3.6	19	163	8	4.54	83.4	29	4.4	1	789	0.2	0.55	3.65	<10
16-SM-20C	3.3	0.47	19	30	0.2	1	7.8	18	28	13	4.52	53.9	13	3.6	1	1020	0.4	0.46	7.81	<10
16-SM-21A	7	1.2	48	30	0.5	1	25.9	42	1	21	11.1	168	2	7.9	4	59.4	1.7	1.06	20	<10
16-SM-21B	6.4	1.04	66	10	0.3	<1	32.1	55	2	34	15.15	168	1	11	2	183	1.6	1.23	19.2	<10
16-SM-22	6.6	1.17	46	50	0.5	<1	25.6	40	<1	34	10.65	214	3	7.7	4	59.2	1.7	0.98	19.3	<10
16-SM-26	5.8	0.66	42	60	0.3	1	14.6	32	1	19	8.87	123	4	5.4	1	151	1	0.6	13.5	<10
16-SM-29A	7.5	1.25	56	20	0.5	1	28.4	42	3	36	12.35	224	2	8	4	15.8	2	1	23.2	<10
16-SM-29B	5.4	0.76	50	20	0.3	1	27	42	4	15	11.75	228	1	7.8	3	13.8	1.9	0.75	21.9	<10
16-SM-30	7	1.18	53	70	0.5	1	26.4	45	1	10	11.95	150	2	8.2	4	38.2	1.7	1.07	19.9	<10
16-SM-32A	7.6	1.36	57	20	0.5	3	30.5	51	1	27	13.45	228	1	9.6	4	16	2.1	1.17	23.2	<10
16-SM-32B	7	1.24	62	10	0.5	2	27.2	48	3	20	13.8	74.4	1	8.9	3	35.4	1.9	1.06	21.9	<10
16-SM-32D	13.6	0.72	43	20	0.3	2	11.6	33	1	16	8.83	83.8	10	5.7	1	237	0.7	0.64	7.41	<10

Table VI: Trace Element Concentrations Cont.

Sample ID	Tm	U	V	W	Y	Yb	Zn	Zr
16-SM-02	0.71	9	5	1	44.1	4.85	112	284
16-SM-04	0.48	6.6	<5	7	24	2.98	72	197
16-SM-08	0.46	8.6	5	2	28.7	2.9	67	205
16-SM-09	0.3	4.3	16	4	17.7	1.83	59	245
16-SM-13A	0.31	4.3	12	2	19.6	2.29	114	186
16-SM-13B	0.45	5.9	6	2	25.5	3.01	91	208
16-SM-13C	0.51	5.5	7	3	33.5	3.28	91	209
16-SM-14	0.51	5.1	<5	4	30	3.43	77	204
16-SM-15A	0.69	5	20	3	49.9	4.55	139	805
16-SM-15A	0.73	5.2	18	3	49.5	4.65	132	749
16-SM-16	0.6	4.1	21	5	47.4	3.13	88	762
16-SM-20B	0.23	1.3	350	1	15.4	1.53	94	87
16-SM-20C	0.17	2.2	208	1	12.1	1.07	69	118
16-SM-21A	0.49	6	7	1	31.7	3.23	78	210
16-SM-21B	0.38	6	<5	2	27	2.13	42	208
16-SM-22	0.49	5.6	15	2	31.5	3.45	72	206
16-SM-26	0.26	3.6	15	5	17.7	1.77	53	231
16-SM-29A	0.51	7	<5	1	32.5	3.37	81	215
16-SM-29B	0.25	6.9	<5	1	18.1	1.77	47	162
16-SM-30	0.47	7.2	7	6	33.3	3.12	41	226
16-SM-32A	0.55	8.3	<5	1	37.6	3.62	79	229
16-SM-32B	0.52	5.4	<5	2	34.9	3.37	85	204
16-SM-32D	0.28	2.8	20	2	18.3	1.91	76	763

Table VI: Trace Element Concentrations Cont.

Sample ID	Unit Name	Rock Type	Ag	As	Ba	Cd	Ce	Co	Cr	Cs	Cu	Dy	Er	Eu	Ga	Gd
16-SM-38A	Unnamed tuff	tuff	<0.5	<5	25.9	<0.5	46.9	<1	<10	3.71	2	3.33	1.88	0.06	18.9	3.19
16-SM-38B	Unnamed tuff	pumice	<0.5	<5	82.2	<0.5	48.7	<1	10	3.29	7	2.9	1.68	0.11	17.8	3.36
16-SM-40	Unnamed pumice	pumice	<0.5	<5	202	<0.5	84.1	<1	<10	3.66	5	2.95	1.76	0.18	19	3.67
16-SM-42	Unnamed tuff	tuff	<0.5	8	498	<0.5	26.6	28	230	2.14	77	3.15	1.61	1.07	17.1	3.41
16-SM-44	Pablo Formation	andesite	<0.5	<5	52.3	<0.5	73.5	1	20	1.53	3	5.11	3.17	0.08	21.4	4.95
16-SM-45	Underdown Tuff	tuff	<0.5	<5	46.9	<0.5	103	<1	<10	2.44	4	6.45	3.63	0.08	23	7.11
16-SM-46	Underdown Tuff	tuff	<0.5	<5	41.8	<0.5	99.7	1	<10	1.87	5	7.04	3.69	0.08	21.1	7.57
16-SM-47	Underdown Tuff	tuff	<0.5	<5	68.5	<0.5	104	1	10	3.38	5	6.97	3.79	0.08	21.4	7.5
16-SM-48	Underdown Tuff	tuff	<0.5	<5	44	<0.5	103.5	<1	10	3.39	6	6.64	3.48	0.06	20.9	7.05
16-SM-49	Underdown Tuff	tuff	<0.5	<5	668	<0.5	101	<1	<10	9.62	8	6.56	3.97	1.26	24.8	7.11
16-SM-50	Underdown Tuff	tuff	<0.5	<5	55.1	<0.5	97.8	<1	<10	9.17	3	5.84	2.95	0.07	21.4	7.33
16-SM-51	Underdown Tuff	tuff	<0.5	<5	907	<0.5	80.5	1	130	3.98	2	3.65	2.06	0.73	18.1	4.36
16-SM-53	Rhyolite Intrusions	rhyolite	<0.5	16	17.9	<0.5	30.2	<1	<10	4.08	4	5.44	3.79	0.03	18.4	3.94
16-SM-55	Unnamed Tuff	tuff	<0.5	13	45	<0.5	46.2	1	<10	7.92	3	5.99	3.69	0.03	20.3	4.4
16-SM-56	Rhyolite Intrusions	rhyolite	<0.5	14	14.3	<0.5	25.9	<1	<10	4.73	3	4.7	2.76	0.03	19.7	3.27
17-SM-01	Terrill Mountains tuffs	tuff	<0.5	8	107.5	<0.5	101	1	120	6.31	5	5.36	3.18	0.13	21.9	5.4
17-SM-02	Terrill Mountains tuffs	tuff	<0.5	8	121	<0.5	122.5	1	140	8.81	4	6.61	3.72	0.12	21.2	7.34
17-SM-03 A	Terrill Mountains tuffs	white pumice	<0.5	<5	73.4	<0.5	116	<1	40	11	4	6.55	3.71	0.08	23.2	7.08
17-SM-03 B	Terrill Mountains tuffs	banded pumice	<0.5	6	45.3	<0.5	101.5	<1	70	11	5	6.56	3.51	0.05	22.4	6.8
17-SM-03 C	Terrill Mountains tuffs	tuff	<0.5	6	104	<0.5	112	<1	70	10.6	4	6.55	3.59	0.14	21.6	7.1
17-SM-06	Tuff of Clipper Gap	tuff	<0.5	13	334	<0.5	124	<1	60	9.15	4	6.29	3.49	0.3	22.2	7.1
17-SM-07	Tuff of Clipper Gap	tuff	<0.5	<5	528	<0.5	89.2	<1	40	4.74	3	4.79	2.47	0.54	18.6	5.18
17-SM-08	Tuff of Clipper Gap	tuff	<0.5	<5	233	0.5	20.6	1	30	1.81	2	1.67	1.58	0.25	3.9	1.38

Table VI: Trace Element Concentrations Cont.

Sample ID	Hf	Ho	La	Li	Lu	Mo	Nb	Nd	Ni	Pb	Pr	Rb	Sc	Sm	Sn	Sr	Ta	Tb	Th	Tl
16-SM-38A	4.9	0.67	18	70	0.3	3	25	19	1	27	5.05	266	2	4.4	4	6	2.3	0.56	26.6	<10
16-SM-38B	4.5	0.56	27	50	0.3	2	22.9	24	1	23	6.54	207	2	4.5	3	12.2	1.7	0.51	21.3	<10
16-SM-40	5.2	0.6	30	40	0.3	1	22.3	27	3	23	7.17	202	3	5.1	3	26.7	1.6	0.55	22.5	<10
16-SM-42	2.2	0.61	13	20	0.2	<1	3.5	16	58	6	3.66	39.9	34	3.7	1	665	0.2	0.51	2.36	<10
16-SM-44	7.4	1.06	36	20	0.5	2	30.5	34	1	23	8.86	224	1	6.4	4	11.7	2.2	0.8	23.6	<10
16-SM-45	7.1	1.37	48	10	0.5	3	31.4	46	3	24	11.75	236	1	9.2	5	11.3	2.2	1.13	25.5	<10
16-SM-46	7	1.42	49	10	0.5	2	30.4	47	<1	29	12.35	220	1	9.3	4	11.9	2.1	1.16	23.1	<10
16-SM-47	7.5	1.41	52	20	0.6	2	31.3	48	2	30	12.65	228	1	9.5	4	14.1	2.2	1.2	23.5	<10
16-SM-48	7.1	1.32	50	20	0.5	3	30.6	46	2	24	12.3	221	1	9.2	4	10.2	2.2	1.14	23.4	<10
16-SM-49	14.7	1.4	53	30	0.6	2	24.8	46	2	33	11.9	196	7	8.9	3	76	1.3	1.1	13.5	<10
16-SM-50	6.7	1.1	48	20	0.4	2	29.6	47	3	21	11.8	223	1	9.9	4	25.1	2.2	1.08	24.6	<10
16-SM-51	6.1	0.7	49	20	0.3	3	16.9	35	7	20	10.2	158	3	6.2	3	143	1.4	0.69	20	<10
16-SM-53	5.7	1.22	16	60	0.6	3	32.7	17	<1	37	4.29	271	2	4.2	5	5.5	2.4	0.77	26.4	<10
16-SM-55	5.5	1.31	15	410	0.6	2	35	17	<1	26	4.39	276	2	4.6	4	11.8	2.5	0.9	27.9	<10
16-SM-56	5.5	0.98	11	70	0.4	2	34.4	8.3	<1	32	2.28	295	2	2.7	5	8.5	2.6	0.7	28.5	<10
17-SM-01	7.5	1.03	51	30	0.4	3	29.9	38	7	34	11.1	221	2	6.8	5	26.6	2.1	0.81	24.5	<10
17-SM-02	7.4	1.28	62	10	0.5	5	29.8	50	8	33	13.9	228	2	9.3	5	26.2	2.1	1.07	24.2	<10
17-SM-03 A	7.9	1.25	59	10	0.5	3	28.9	48	2	26	13.3	261	2	8.9	5	58.6	2.1	1.09	24.7	<10
17-SM-03 B	7.4	1.25	53	10	0.5	4	28.7	45	<1	22	12.4	288	2	8.5	5	48.4	2.2	1.1	25	<10
17-SM-03 C	7.4	1.27	56	10	0.5	4	30.2	47	1	31	12.9	216	2	8.9	5	72.5	2.1	1.09	24	<10
17-SM-06	11.9	1.23	63	30	0.6	4	32.9	52	2	39	14.25	179	5	9.4	4	82.8	2.2	1.09	27.1	<10
17-SM-07	8.9	0.93	48	20	0.3	1	25.5	41	<1	24	10.95	144	4	7.1	3	45.9	1.7	0.77	21.6	<10
17-SM-08	1.5	0.41	13	20	0.3	<1	4.4	9.1	<1	2	2.57	15.2	2	1.6	1	209	0.3	0.26	4.25	<10

Table VI: Trace Element Concentrations Cont.

Sample ID	Tm	U	V	W	Y	Yb	Zn	Zr
16-SM-38A	0.3	4.8	<5	2	14.7	2.04	42	105
16-SM-38B	0.24	4.8	<5	2	11.8	1.95	47	108
16-SM-40	0.27	5.3	<5	1	14.8	1.71	47	144
16-SM-42	0.24	0.9	337	1	16.5	1.63	82	80
16-SM-44	0.49	7.3	<5	1	28.5	3.26	67	216
16-SM-45	0.55	6.2	<5	1	36.2	3.49	68	206
16-SM-46	0.58	7.4	<5	1	38.8	3.81	84	208
16-SM-47	0.58	8.9	<5	2	39.9	3.85	87	222
16-SM-48	0.5	9.2	<5	1	35.9	3.4	79	207
16-SM-49	0.57	13	<5	11	37.7	3.85	105	789
16-SM-50	0.4	6.3	<5	1	29.4	2.51	85	185
16-SM-51	0.29	5.5	<5	4	19.9	1.93	37	214
16-SM-53	0.57	5.6	<5	5	36.1	4.14	51	120
16-SM-55	0.56	5.8	<5	4	34.3	3.8	61	112
16-SM-56	0.43	5.7	<5	3	26.4	2.69	88	123
17-SM-01	0.45	7	8	5	25.8	2.89	86	214
17-SM-02	0.52	8.7	<5	3	35.9	3.57	85	209
17-SM-03 A	0.54	7.4	<5	3	35.7	3.42	85	224
17-SM-03 B	0.51	7.5	<5	5	34.3	3.22	86	204
17-SM-03 C	0.5	7.5	5	4	34.2	3.37	90	214
17-SM-06	0.52	8.7	17	4	33.6	3.53	95	450
17-SM-07	0.33	5.1	11	1	23.1	2.33	73	339
17-SM-08	0.25	1	16	1	18.6	1.76	29	70

Table VI: Trace Element Concentrations Cont.

Sample ID	Unit Name	Rock Type	Ag	As	Ba	Cd	Ce	Co	Cr	Cs	Cu	Dy	Er	Eu	Ga	Gd
17-SM-09	Tuff of Clipper Gap	tuff	<0.5	<5	735	<0.5	68.6	<1	80	105.5	5	3.72	2.1	0.26	18	3.86
17-SM-10	Tuff of Clipper Gap	tuff	<0.5	<5	117	<0.5	102.5	<1	70	5.05	2	5.92	3.01	0.14	20.6	6.59
17-SM-11	Tuff of Clipper Gap	tuff	<0.5	5	165.5	<0.5	112.5	<1	70	6.03	9	6.1	3.41	0.12	21.4	6.8
17-SM-12	Tuff of Clipper Gap	tuff	<0.5	17	176.5	<0.5	153	1	30	1.61	3	10.7	6.79	0.26	21.8	9.87
17-SM-13 A	Tuff of Brunton Pass	tuff	<0.5	<5	82.1	<0.5	58.7	<1	70	6.21	4	5.67	3.11	0.11	22.3	6.19
17-SM-13 B	Tuff of Brunton Pass	tuff	<0.5	<5	184	<0.5	105.5	1	50	4.73	6	7.05	3.85	0.15	21.8	8.24
17-SM-14	Tuff of Arc Dome	tuff	<0.5	8	790	<0.5	83.1	1	130	5.05	2	3.56	2.26	0.66	17.9	4.08
17-SM-15 A	Tuff of Arc Dome	tuff	<0.5	8	97.8	<0.5	66.5	<1	140	8.15	2	5.89	3.77	0.22	19.3	5.8
17-SM-15 B	Tuff of Arc Dome	tuff	<0.5	5	173	<0.5	64.2	1	200	7.88	3	4.37	2.62	0.26	17.9	4.34
17-SM-16 A	Tuff of Gabbs Valley	tuff	<0.5	<5	145.5	<0.5	92.5	<1	100	6.36	1	5.87	3.5	0.23	18.8	6.02
17-SM-16 B	Tuff of Gabbs Valley	tuff	<0.5	<5	144	<0.5	214	<1	10	5.25	7	6.19	3.64	0.21	22.2	7.55
17-SM-17 A	Underdown Tuff	porphyritic pumice	<0.5	10	626	<0.5	65.9	1	100	6.82	4	3.17	1.73	0.78	17.3	3.74
17-SM-17 B	Underdown Tuff	tuff	<0.5	<5	303	<0.5	149.5	<1	70	9.93	4	6.69	3.67	0.6	25.2	6.92
17-SM-17 C	Underdown Tuff	porphyritic pumice	<0.5	<5	93.8	<0.5	117	<1	160	11.05	3	6.64	3.82	0.19	21.1	7.43
17-SM-18	Pablo Formation	andesite	<0.5	<5	425	<0.5	74.3	2	50	13.15	4	4.45	2.8	1.42	22.4	4.9
17-SM-19	Bonita Canyon Formation	tuff	<0.5	7	1145	<0.5	27.8	14	130	8.76	68	3.07	1.99	1.05	20.7	3.07
17-SM-20	Tuff of Arc Dome	tuff	<0.5	<5	172	<0.5	98.8	<1	120	6.5	3	5.37	3.13	0.19	20.2	5.85
17-SM-21 A	Tuff of Clipper Gap	tuff	<0.5	7	1620	<0.5	103.5	4	110	5.63	3	3.75	2.19	1.09	18.9	4.27
17-SM-21 B	Tuff of Clipper Gap	tuff	<0.5	<5	235	<0.5	85.4	<1	50	2.18	3	10.2	4.87	0.75	22	12.1
17-SM-22	Tuff of Clipper Gap	tuff	<0.5	<5	184.5	<0.5	50.3	<1	90	6.01	4	3.36	1.95	0.17	19.8	4.02
17-SM-23	Tuff of Clipper Gap	white pumice	<0.5	<5	573	<0.5	77.8	1	70	6.2	2	3.56	2.02	0.42	17.6	4.22
17-SM-24	Tuff of Clipper Gap	white pumice	<0.5	6	72	<0.5	55.2	<1	60	6.6	2	3.55	2.11	0.15	18.7	3.83
17-SM-25	Tuff of Clipper Gap	tuff	<0.5	7	14.2	<0.5	67.8	1	70	6.08	2	3.78	2.2	0.16	18.9	3.96
17-SM-26 A	Tuff of Clipper Gap	white pumice	<0.5	<5	497	<0.5	43	1	30	2.57	3	3.21	1.7	0.43	16.9	4.14

Table VI: Trace Element Concentrations Cont.

Sample ID	Hf	Ho	La	Li	Lu	Mo	Nb	Nd	Ni	Pb	Pr	Rb	Sc	Sm	Sn	Sr	Ta	Tb	Th	Tl
17-SM-09	5.3	0.74	35	40	0.3	2	15.9	29	3	26	8.07	133	4	5.1	3	182	1.2	0.57	19	<10
17-SM-10	7.2	1.11	55	10	0.4	1	24.5	46	2	24	12.55	194	2	8.9	3	36	1.9	0.96	22.2	<10
17-SM-11	7.5	1.2	57	40	0.5	<1	27.1	47	3	17	12.95	215	2	8.7	2	44.2	2.1	1.04	23.3	<10
17-SM-12	7.2	2.2	66	30	0.9	1	28.9	59	<1	60	15.7	201	1	12	17	38.5	2.2	1.68	30.6	<10
17-SM-13 A	7.4	1.07	42	20	0.4	3	31.8	42	1	24	11.45	235	2	9	4	21.6	2.3	0.99	25.9	<10
17-SM-13 B	7.5	1.34	55	30	0.6	2	30.3	50	5	23	13.4	228	2	10	2	47.1	2.2	1.24	25.3	<10
17-SM-14	5.4	0.76	46	20	0.3	2	16.3	35	1	25	9.87	159	3	6.2	3	124	1.3	0.6	19.6	<10
17-SM-15 A	5	1.21	37	70	0.6	2	25.9	34	2	27	9.37	273	2	7.3	5	20.5	2.6	0.98	32.3	<10
17-SM-15 B	4.7	0.92	32	50	0.4	2	21.4	28	3	31	7.76	229	1	5.7	4	33.6	2	0.75	27.2	<10
17-SM-16 A	6.3	1.18	49	20	0.5	2	25.6	42	<1	25	10.9	184	3	7.6	3	20.4	1.8	0.94	24	<10
17-SM-16 B	8.8	1.23	121	20	0.6	2	23.8	71	4	25	22	230	3	11	4	32.7	1.7	1.03	21.7	10
17-SM-17 A	6.6	0.61	41	20	0.3	2	14.4	29	2	22	8.26	183	3	5.2	2	38.5	1.2	0.49	18.7	<10
17-SM-17 B	15.1	1.33	84	30	0.6	3	21.5	60	1	28	16.55	171	8	9.8	4	63.7	1.3	1.04	13.7	<10
17-SM-17 C	7.6	1.43	58	20	0.5	2	29.7	51	1	20	13.85	219	1	9.9	4	22.6	2.3	1.16	25.6	<10
17-SM-18	19	0.89	39	30	0.4	2	14.1	34	<1	24	8.81	171	10	6.6	2	84	0.9	0.71	7.23	<10
17-SM-19	2.7	0.68	13	30	0.3	1	3.5	15	28	6	3.54	50.3	12	3.6	1	1125	0.2	0.5	3.21	<10
17-SM-20	6.6	1.12	49	40	0.4	1	20.8	43	2	39	11.3	119	2	8.2	4	65.4	1.8	0.91	20.5	<10
17-SM-21 A	8.4	0.68	55	40	0.3	4	15.7	40	3	24	11.45	138	6	6.5	2	286	1.1	0.61	15.9	<10
17-SM-21 B	16	1.87	91	40	0.5	2	20.2	73	<1	18	19	101	6	13	2	63.7	1	1.83	9.77	<10
17-SM-22	7.4	0.62	37	30	0.3	3	28.3	33	2	21	9	193	2	6.4	2	21.4	2.1	0.62	22.7	<10
17-SM-23	5.4	0.69	38	20	0.3	2	15.6	32	2	26	8.77	139	4	6	2	85.8	1	0.57	17.5	<10
17-SM-24	4.6	0.72	26	10	0.4	3	15.4	25	<1	29	6.76	200	4	5	3	25.9	1.1	0.62	18.5	<10
17-SM-25	4.9	0.75	31	20	0.3	3	15.8	28	<1	23	7.94	212	4	5.4	2	8.3	1.2	0.65	19.3	<10
17-SM-26 A	5.3	0.6	34	20	0.3	<1	14.3	32	2	25	8.35	162	4	5.9	2	51.6	1.1	0.64	17.4	<10

Table VI: Trace Element Concentrations Cont.

Sample ID	Tm	U	V	W	Y	Yb	Zn	Zr
17-SM-09	0.33	4.9	11	3	20.4	2.13	49	145
17-SM-10	0.41	4	6	2	28.1	2.73	69	212
17-SM-11	0.48	6.2	8	6	33.6	3.26	60	227
17-SM-12	0.92	4.9	8	2	66.7	6.38	76	208
17-SM-13 A	0.45	8.1	5	2	26.7	2.88	83	201
17-SM-13 B	0.56	6.2	10	3	35.1	3.67	83	203
17-SM-14	0.3	5.8	9	2	21.3	2.25	48	189
17-SM-15 A	0.56	10	<5	3	35.8	3.83	39	107
17-SM-15 B	0.42	8.4	<5	3	25.9	2.89	45	113
17-SM-16 A	0.46	8.8	<5	2	35.9	3.03	68	191
17-SM-16 B	0.52	7.7	<5	2	33.7	3.45	93	295
17-SM-17 A	0.26	6	<5	3	17	1.67	45	253
17-SM-17 B	0.55	14	7	9	41.3	3.64	93	694
17-SM-17 C	0.52	7.1	<5	1	37.3	3.5	70	212
17-SM-18	0.38	12	6	12	28.3	2.7	91	1020
17-SM-19	0.28	1.4	235	3	18	1.94	71	97
17-SM-20	0.44	9.4	9	1	30.2	2.88	71	190
17-SM-21 A	0.29	6	31	3	20.8	2.11	81	356
17-SM-21 B	0.66	5.2	<5	3	46.5	4.11	87	794
17-SM-22	0.28	6	<5	3	15.6	1.73	63	230
17-SM-23	0.3	5.8	<5	3	19.4	2.14	55	176
17-SM-24	0.31	6.3	<5	3	19.1	2.09	54	120
17-SM-25	0.31	6.7	<5	3	20.3	2.22	49	129
17-SM-26 A	0.27	4.6	<5	1	15.9	1.57	47	166

Table VI: Trace Element Concentrations Cont.

Sample ID	Unit Name	Rock Type	Ag	As	Ba	Cd	Ce	Co	Cr	Cs	Cu	Dy	Er	Eu	Ga	Gd
17-SM-26 B	Tuff of Clipper Gap	tuff	<0.5	6	176.5	<0.5	130	<1	50	5.37	5	6.2	3.58	0.22	21	7.61
17-SM-26 C	Tuff of Clipper Gap	tuff	<0.5	<5	224	<0.5	122.5	<1	60	5.98	4	7.55	4.4	0.18	21.2	7.93
17-SM-27	Tuff of Clipper Gap	tuff	<0.5	6	321	<0.5	95.9	1	50	4.29	9	10.3	4.41	0.81	22.4	15.15
17-SM-28	TgV2	tuff	<0.5	<5	372	<0.5	102	<1	20	7.98	3	4.39	3.03	0.35	14.8	4.7
17-SM-29	TgV2	tuff	<0.5	6	156.5	<0.5	58.5	<1	140	4.71	1	4.17	2.44	0.24	16.8	4.02
17-SM-30	TgV2	tuff	<0.5	18	466	<0.5	77.5	1	130	4.94	2	4.01	2.4	0.45	17.8	4.08
17-SM-31	TgV3	porphyritic pumice	<0.5	6	1290	<0.5	113	1	90	5.35	2	2.55	1.39	0.99	16.5	3.28
Sample ID	Unit Name	Rock Type	Ag	As	Ba	Cd	Ce	Co	Cr	Cs	Cu	Dy	Er	Eu	Ga	Gd
16-SM-13Caw	Tuff of Clipper Gap	tuff	<0.5	<5	78.7	<0.5	38.4	1	<10	3.14	1	2.49	1.46	0.07	21	2.36
16-SM-14aw	Tuff of Clipper Gap	white pumice	<0.5	<5	21.3	<0.5	27.8	<1	<10	4.51	3	2.47	1.55	0.04	23.4	2.03
16-SM-16aw	Tuff of Clipper Gap	porphyritic pumice	<0.5	6	230	<0.5	27.4	1	<10	1.91	2	1.7	1.12	0.78	22	2.26
17-SM-21Aaw	Tuff of Clipper Gap	porphyritic pumice	<0.5	<5	226	<0.5	27.1	<1	30	1.94	<1	1.44	1.15	0.71	22.1	1.39
17-SM-22aw	Tuff of Clipper Gap	whole rock	<0.5	6	387	<0.5	57.8	<1	40	5.97	<1	2.31	1.32	0.31	17.9	2.96
17-SM-26Aaw	Tuff of Clipper Gap	whole rock	<0.5	5	104	<0.5	18.1	<1	40	4.95	1	1.58	1.19	0.14	22.2	1.24
17-SM-26Caw	Tuff of Clipper Gap	porphyritic pumice	<0.5	6	168.5	<0.5	50.4	1	40	4.29	1	2.79	1.75	0.27	23.6	3.11
17-SM-27aw	Tuff of Clipper Gap	whole rock	<0.5	<5	249	<0.5	40.6	<1	20	7.76	1	1.33	1.11	0.26	13.1	0.99
Sample ID	Unit Name	Rock Type	Ag	As	Ba	Cd	Ce	Co	Cr	Cs	Cu	Dy	Er	Eu	Ga	Gd
H18-SN6	Young Sierra Nevada tuffs	tuff	<0.5	5	114	<0.5	103.1	<1	<10	3.77	3	6.20	3.70	0.12	22.9	6.68
H18-SN15	Young Sierra Nevada tuffs	tuff	<0.5	<5	110	<0.5	90.5	<1	<10	6.04	2	5.71	3.31	0.12	24.2	5.56

Table VI: Trace Element Concentrations Cont.

Sample ID	Hf	Ho	La	Li	Lu	Mo	Nb	Nd	Ni	Pb	Pr	Rb	Sc	Sm	Sn	Sr	Ta	Tb	Th	Tl
17-SM-26 B	8.1	1.24	60	30	0.5	3	29.6	52	2	27	13.85	202	2	10	3	24.9	2.2	1.14	22.8	<10
17-SM-26 C	8	1.42	53	20	0.6	2	29.5	49	1	27	13	208	2	9.9	2	22.5	2.1	1.31	24.1	<10
17-SM-27	16.1	1.74	151	30	0.5	3	21.6	135	3	23	34.6	123	9	24	2	61.4	1.3	2.08	12.5	<10
17-SM-28	5.8	0.96	53	10	0.4	1	14.4	39	1	21	11.25	172	3	6.8	2	235	1	0.76	18.5	<10
17-SM-29	4.9	0.79	28	50	0.5	1	22.7	25	2	26	7.05	231	2	5.5	3	30.6	2.2	0.7	27.9	<10
17-SM-30	5.4	0.74	43	40	0.4	1	18.5	34	<1	24	9.67	185	2	6.5	3	78.3	1.7	0.71	23.4	<10
17-SM-31	6.6	0.49	69	20	0.3	3	11	38	<1	26	11.25	120	4	5	1	137	0.7	0.49	14.7	<10
Sample ID	Hf	Ho	La	Li	Lu	Mo	Nb	Nd	Ni	Pb	Pr	Rb	Sc	Sm	Sn	Sr	Ta	Tb	Th	Tl
16-SM-13Caw	7.3	0.44	24	10	0.3	1	30.7	17	1	17	4.86	240	1	3.1	2	10.7	2.5	0.37	13	<10
16-SM-14aw	7.3	0.54	17	20	0.2	1	32.8	11	1	16	2.95	251	1	2.5	2	5.1	2.6	0.35	10.2	10
16-SM-16aw	16	0.38	31	40	0.2	1	17.1	17	<1	18	4.32	114	3	2.8	1	66.1	1.1	0.29	3.8	<10
17-SM-21Aaw	17.1	0.33	22	30	0.2	1	18.4	9.7	1	17	2.66	114	2	1.9	1	64.6	1.1	0.22	4.74	<10
17-SM-22aw	5.6	0.45	32	20	0.3	2	15.1	22	1	25	6.13	160	3	4.1	2	65	1.2	0.4	14.5	<10
17-SM-26Aaw	8.1	0.33	16	30	0.3	2	31.2	6.5	<1	18	1.92	239	1	1.4	2	17.1	2.2	0.22	10	<10
17-SM-26Caw	16.5	0.62	36	30	0.4	2	22.7	23	<1	24	5.99	147	3	3.7	1	48	1.5	0.43	8.1	<10
17-SM-27aw	5.7	0.33	29	10	0.2	1	16	13	<1	9	3.95	147	1	1.5	1	86.9	1.3	0.17	6.44	<10
Sample ID	Hf	Ho	La	Li	Lu	Mo	Nb	Nd	Ni	Pb	Pr	Rb	Sc	Sm	Sn	Sr	Ta	Tb	Th	Tl
H18-SN6	8.0	1.27	48.0	30	0.55	<1	32.4	41.6	<1	25	11.26	218	2	8.29	3.00	22	2.3	1.07	25.4	<10
H18-SN15	7.3	1.12	43.4	30	0.50	1	31.1	38.3	1	25	10.21	225	2	7.62	2.00	22	2.5	0.92	26.1	<10

Table VI: Trace Element Concentrations Cont.

Sample ID	Tm	U	V	W	Y	Yb	Zn	Zr
17-SM-26 B	0.5	6.7	<5	3	33.5	3.3	79	260
17-SM-26 C	0.63	8.4	<5	5	38.9	4.05	72	220
17-SM-27	0.59	6.3	<5	4	40.1	3.71	127	707
17-SM-28	0.46	5	<5	1	27.5	2.88	43	183
17-SM-29	0.41	5.9	<5	2	21.1	2.77	42	118
17-SM-30	0.36	5.8	6	3	20.8	2.79	49	169
17-SM-31	0.24	4.8	<5	3	13	1.43	50	298
Sample ID	Tm	U	V	W	Y	Yb	Zn	Zr
16-SM-13Caw	0.25	5	<5	2	12.3	1.87	18	179
16-SM-14aw	0.25	4.2	<5	2	13.4	1.6	20	216
16-SM-16aw	0.17	2.9	<5	2	10.1	1.24	27	800
17-SM-21Aaw	0.19	3.4	21	2	9.1	1.45	18	864
17-SM-22aw	0.22	5.1	13	2	14.6	1.57	30	175
17-SM-26Aaw	0.2	4.9	<5	3	11	1.56	22	272
17-SM-26Caw	0.27	4.3	<5	3	16.5	1.87	40	768
17-SM-27aw	0.2	2.9	73	1	12.6	1.33	21	191
Sample ID	Tm	U	V	W	Y	Yb	Zn	Zr
H18-SN6	0.56	6.61	5	1	35.4	3.51	75	244
H18-SN15	0.50	7.07	5	2	31.0	3.31	78	224

Table VII: Precision of Trace Element analyses

Element	10-LT-05	10-LT-05	10-LT-05	Average	2σ
Ag	<0.5	<0.5	<0.5	<0.5	-
As	<5	<5	<5	<5	-
Ba	517	515	554	540	40
Cd	<0.5	<0.5	<0.5	0.63	0.26
Ce	49.0	45.6	48.8	48.0	3.8
Co	37	42	37	40	4
Cr	180	190	160	185	22
Cs	0.24	0.24	0.23	0.23	0.06
Cu	40	43	40	42	4
Dy	3.66	3.48	3.55	3.63	0.32
Er	1.9	1.81	1.93	1.96	0.16
Eu	1.59	1.46	1.56	1.59	0.16
Ga	19.6	18.0	19.4	19.9	1.6
Gd	4.41	4.19	4.73	4.46	0.46
Hf	3.4	3.5	3.4	3.6	0.2
Ho	0.74	0.68	0.68	0.72	0.08
La	22.6	21.2	22.3	22.4	2.0
Li	<10	10	10	10	0
Lu	0.23	0.21	0.25	0.25	0.04
Mo	2	1	1	1	0
Nb	10.8	10.5	10.7	10.9	1.0
Nd	26.9	25.2	26.7	25.6	2.0
Ni	115	120	109	116	10
Pb	2	3	3	4	4
Pr	6.32	5.96	6.24	6.21	0.62
Rb	12.2	12.1	11.6	12.5	0.8
Sc	17	15	16	17	2
Sm	5.15	4.92	5.31	5.17	0.54
Sn	1	1	1	1	0
Sr	919	864	948	935	48
Ta	0.5	0.6	0.5	0.6	0.2
Tb	0.66	0.63	0.67	0.66	0.06
Th	1.99	1.80	1.94	1.99	0.24
Tl	<10	<10	<10	10	0.00
Tm	0.27	0.24	0.25	0.27	0.04
U	0.55	0.50	0.57	0.59	0.10

Table VII: Precision of Trace Element analyses cont.

Element	10-LT-05	10-LT-05	10-LT-05	Average	2σ
V	163	165	130	164	20
W	<1	1	1	1	0
Y	18.5	18.0	18.2	18.7	1.5
Yb	1.50	1.65	1.59	1.68	0.26
Zn	91	97	88	93	8
Zr	149	151	157	151	14

Note: The first three columns of trace element data for 10-LT-05 are the results of individual runs obtained with three batches of samples submitted to ALS for geochemical analysis. Averages and standard deviation (σ) for 10-LT-05 are calculated from 31 analyses by ALS (Nov. 2013-Nov. 2019).

Table VII: Precision of Trace Element analyses cont.

Element	BHVO-2	BHVO-2	BHVO-2	Average	2 σ	USGS Recommended Values
Ag	<0.5	<0.5	<0.5	<0.5	-	-
As	<5	<5	<5	<5	-	-
Ba	126	128	138	134	14	130
Cd	<0.5	<0.5	<0.5	0.73	0.38	-
Ce	37.8	35.5	37.4	37.4	3.0	38
Co	41	45	39	44	6	45
Cr	300	310	270	304	38	280
Cs	0.1	0.1	0.04	0.09	0.04	0.1
Cu	142	134	128	136	10	127
Dy	5.07	5.02	5.3	5.28	0.52	-
Er	2.46	2.19	2.62	2.55	0.44	-
Eu	2	1.91	1.94	2.04	0.28	-
Ga	22.2	19.9	21.3	21.1	2.4	21.7
Gd	6.1	5.87	6.34	6.25	0.76	6.3
Hf	4.4	4.3	4.5	4.5	0.4	4.1
Ho	0.98	0.98	0.96	0.98	0.10	1.04
La	15.1	14.5	14.9	15.5	2.06	15
Li	<10	10	<10	10.00	0.00	-
Lu	0.26	0.25	0.28	0.28	0.04	0.28
Mo	2	4	4	3	2	-
Nb	17.6	17.1	17.9	17.7	1.8	18
Nd	25.5	24.5	24.5	24.9	2.4	25
Ni	137	124	114	126	14	119
Pb	<2	<2	<2	4.33	4.62	-
Pr	5.23	5.08	5.26	5.35	0.70	-
Rb	9.0	8.8	8.5	9.1	1.2	9.8
Sc	29	30	28	30	2	32
Sm	6.39	6.08	6.42	6.30	0.72	6.2
Sn	2	2	2	2	0	1.9
Sr	411	386	407	407	34	389
Ta	1.1	1.1	1	1.1	0.2	1.4
Tb	0.91	0.89	1	0.93	0.12	0.9
Th	1.24	1.15	1.19	1.24	0.18	1.2
Tl	<10	<10	<10	10.00	0.00	-
Tm	0.34	0.32	0.30	0.32	0.04	-
U	0.43	0.41	0.40	0.42	0.06	-
V	352	331	274	333	56	317
W	<1	1	2	1	0	-

Table VII: Precision of Trace Element analyses

Element	BHVO-2	BHVO-2	BHVO-2	Average	2 σ	USGS Recommended Values
Y	24.4	23.6	23.9	24.6	2.4	26
Yb	1.87	1.77	1.93	1.98	0.28	2
Zn	102	107	99	106	10	103
Zr	169	172	176	175	16	172

Note: The first three columns of trace element data for BHVO-2 are the results of individual runs obtained with three batches of samples submitted to ALS for geochemical analysis. Averages and standard deviation (σ) for BHVO-2 are calculated from 9 analyses by ALS (Jan. 2017-Nov. 2019).

Table VIII: Isotopic Results

Sample ID	$^{87}\text{Rb}/^{86}\text{Sr}$	$^{87}\text{Sr}/^{86}\text{Sr}$ measured	$^{87}\text{Sr}/^{86}\text{Sr}$ initial	2σ	$^{147}\text{Sm}/^{144}\text{Nd}$	$^{143}\text{Nd}/^{144}\text{Nd}$ measured	$^{143}\text{Nd}/^{144}\text{Nd}$ initial	2σ	ϵNd initial
16-SM-09	3.48909	0.70665	0.70541	0.000016	0.12113	0.512570	0.512550	0.000004	-1.09
16-SM-16	3.40854	0.70761	0.70640	0.000012	0.20535	0.512532	0.512499	0.000005	-2.09
16-SM-20C	0.15287	0.70592	0.70587	0.000011	0.12126	0.512023	0.512004	0.000010	-12.09
16-SM-21B	2.66368	0.70826	0.70731	0.000011	0.12256	0.512528	0.512508	0.000005	-1.91
16-SM-33A	1.02292	0.70617	0.70581	0.000012	0.10227	0.512535	0.512518	0.000010	-1.71
16-SM-40	49.16896	0.72343	0.70617	0.000016	0.11456	0.512515	0.512496	0.000004	-2.15
16-SM-42	21.90229	0.71328	0.70559	0.000012	0.20535	0.512523	0.512490	0.000004	-2.27
16-SM-44	0.17355	0.70438	0.70432	0.000016	0.20535	0.512699	0.512666	0.000006	1.10
16-SM-50	7.44343	0.70834	0.70571	0.000015	0.11583	0.512546	0.512527	0.000006	-1.55
17-SM-03A	15.60657	0.71005	0.70453	0.000015	0.11971	0.512529	0.512509	0.000006	-1.89
17-SM-03B	11.49824	0.71157	0.70751	0.000018	0.20535	0.512522	0.512489	0.000006	-2.28
17-SM-03C	10.66639	0.70884	0.70507	0.000017	0.20535	0.512533	0.512500	0.000007	-2.08
17-SM-07	9.04856	0.71071	0.70751	0.000015	0.10547	0.512620	0.512603	0.000005	-0.06
17-SM-09	2.12071	0.70993	0.70918	0.000012	0.10648	0.512519	0.512502	0.000010	-2.03
17-SM-14	3.70973	0.70663	0.70531	0.000012	0.10816	0.512571	0.512553	0.000006	-1.03
17-SM-17A	7.76804	0.70869	0.70556	0.000015	0.20535	0.512539	0.512506	0.000008	-1.96
17-SM-19	5.26465	0.70742	0.70595	0.000010	0.20535	0.512536	0.512503	0.000006	-2.01
17-SM-21A	4.56482	0.70734	0.70572	0.000012	0.20535	0.512537	0.512503	0.000008	-2.00
17-SM-26C	5.77320	0.70856	0.70652	0.000012	0.20535	0.512544	0.512510	0.000004	-1.87
17-SM-27	2.11770	0.70749	0.70674	0.000011	0.20535	0.512511	0.512477	0.000006	-2.51
17-SM-30	3.19658	0.70656	0.70542	0.000015	0.10645	0.512568	0.512550	0.000008	-1.08
17-SM-31	2.53275	0.70638	0.70548	0.000014	0.08056	0.512506	0.512493	0.000006	-2.21

Table VIII: Isotopic Results Cont.

Sample ID	U (ppm)	Th (ppm)	Pb (ppm)	²⁰⁸ Pb/ ²⁰⁴ Pb measured	²⁰⁷ Pb/ ²⁰⁴ Pb measured	²⁰⁶ Pb/ ²⁰⁴ Pb measured	²⁰⁸ Pb/ ²⁰⁴ Pb initial	2σ	²⁰⁷ Pb/ ²⁰⁴ Pb initial	2σ	²⁰⁶ Pb/ ²⁰⁴ Pb initial	2σ
16-SM-09	4.26	16.25	23	38.873	15.653	19.156	38.815	0.002	15.650	0.001	19.109	0.001
16-SM-16	4.62	9.54	21	38.903	15.662	19.236	38.865	0.001	15.660	0.000	19.181	0.001
16-SM-20C	2.21	7.81	13	38.706	15.619	18.935	38.657	0.001	15.617	0.000	18.893	0.001
16-SM-21B	6.01	19.2	34	38.930	15.660	19.238	38.884	0.001	15.658	0.000	19.194	0.001
16-SM-33A	2.78	7.41	16	38.903	15.661	19.210	38.865	0.001	15.659	0.000	19.166	0.001
16-SM-40	4.82	21.3	23	38.918	15.658	19.210	38.842	0.002	15.656	0.001	19.158	0.001
16-SM-42	5.34	22.5	23	38.910	15.657	19.209	38.830	0.002	15.655	0.001	19.151	0.001
16-SM-44	0.92	2.36	6	38.443	15.585	18.784	38.411	0.002	15.583	0.001	18.746	0.001
16-SM-50	13.25	13.5	33	38.896	15.661	19.265	38.863	0.002	15.657	0.001	19.165	0.001
17-SM-03A	7.37	24.7	26	38.887	15.658	19.192	38.795	0.002	15.654	0.001	19.108	0.001
17-SM-03B	7.46	25	22	38.912	15.661	19.213	38.845	0.002	15.659	0.001	19.153	0.001
17-SM-03C	7.49	24	31	38.896	15.657	19.207	38.820	0.002	15.654	0.001	19.135	0.001
17-SM-07	5.14	21.6	24	38.840	15.644	19.120	38.766	0.002	15.641	0.001	19.067	0.001
17-SM-09	4.91	19	26	38.882	15.653	19.179	38.822	0.001	15.652	0.000	19.132	0.001
17-SM-14	5.81	19.55	25	38.857	15.652	19.144	38.793	0.002	15.649	0.001	19.085	0.001
17-SM-17A	9.37	20.5	28	38.896	15.664	19.280	38.847	0.001	15.656	0.000	19.143	0.001
17-SM-19	13.5	13.7	39	38.890	15.658	19.203	38.856	0.002	15.658	0.001	19.159	0.001
17-SM-21A	5.15	9.77	18	38.899	15.661	19.230	38.854	0.002	15.658	0.001	19.159	0.002
17-SM-26C	6.25	12.5	23	38.888	15.657	19.220	38.843	0.001	15.654	0.001	19.152	0.001
17-SM-27	4.98	18.5	21	38.902	15.654	19.192	38.830	0.001	15.651	0.000	19.133	0.001
17-SM-30	5.46	20	20	38.883	15.653	19.167	38.800	0.001	15.650	0.000	19.098	0.001
17-SM-31	4.75	14.7	26	38.863	15.650	19.164	38.816	0.001	15.648	0.000	19.118	0.001

Table VIII: Isotopic Results Cont.

Sample ID	$^{87}\text{Rb}/^{86}\text{Sr}$	$^{87}\text{Sr}/^{86}\text{Sr}$ Measured	$^{87}\text{Sr}/^{86}\text{Sr}$ initial	2σ	$^{147}\text{Sm}/^{144}\text{Nd}$	$^{143}\text{Nd}/^{144}\text{Nd}$ measured	$^{143}\text{Nd}/^{144}\text{Nd}$ initial	2σ	ϵNd initial
Acid-washed Samples									
16-SM-16aw	4.96809	0.70729	0.70553	0.000012	0.09970	0.512552	0.512536	0.000008	-1.37
17-SM-21Aaw	5.10585	0.70731	0.70551	0.000011	0.11531	0.512569	0.512550	0.000018	-1.10
17-SM-26Caw	8.86186	0.70855	0.70542	0.000014	0.09838	0.512567	0.512551	0.000006	-1.07
17-SM-27aw	4.89395	0.70650	0.70477	0.000013	0.06677	0.512512	0.512502	0.000008	-2.04

Sample ID	U (ppm)	Th (ppm)	Pb (ppm)	$^{208}\text{Pb}/^{204}\text{Pb}$ measured	$^{207}\text{Pb}/^{204}\text{Pb}$ measured	$^{206}\text{Pb}/^{204}\text{Pb}$ measured	$^{208}\text{Pb}/^{204}\text{Pb}$ initial	2σ	$^{207}\text{Pb}/^{204}\text{Pb}$ initial	2σ	$^{206}\text{Pb}/^{204}\text{Pb}$ initial	2σ
Acid-washed Samples												
16-SM-16aw	2.91	3.8	18	38.896	15.661	19.229	38.879	0.003	15.659	0.001	19.188	0.001
17-SM-21Aaw	3.42	4.74	17	38.897	15.661	19.223	38.874	0.002	15.659	0.001	19.173	0.001
17-SM-26Caw	4.28	8.1	24	38.894	15.659	19.218	38.866	0.002	15.657	0.001	19.173	0.001
17-SM-27aw	2.93	6.44	9	38.904	15.654	19.182	38.845	0.002	15.650	0.001	19.101	0.001

Table IX: Sr Isotopic Precision

Sample ID	$^{87}\text{Sr}/^{86}\text{Sr}$	Average	2σ
NBS987	0.710238		
NBS987	0.710243		
NBS987	0.710237	0.710244	0.000016
NBS987	0.710237		
NBS987	0.710258		
NBS987	0.710250		
BCR-2	0.704991		
BCR-2	0.705009	0.705002	0.000018
BCR-2	0.705005		

Note:

a) Recommended value for SRM 987 is $^{87}\text{Sr}/^{86}\text{Sr} = 0.710252 \pm 13 (2\sigma)$ (Weis et al., 2006)

b) Recommended value for BCR-2 is $^{87}\text{Sr}/^{86}\text{Sr} = 0.705019 \pm 16 (2\sigma)$ (Weis et al., 2006)

Table X: Nd Isotopic Precision

Sample ID	$^{143}\text{Nd}/^{144}\text{Nd}$	Average	2σ
Nd Std	0.511814		
Nd Std	0.511825		
Nd Std	0.511808	0.511814	0.000014
Nd Std	0.511810		
Nd Std	0.511819		
Nd Std	0.511806		
BCR-2	0.512622		
BCR-2	0.512624	0.512620	0.000008
BCR-2	0.512615		
BCR-2	0.512618		

Note:

a) 38 runs of an internal Nd metal standard average $^{143}\text{Nd}/^{144}\text{Nd} = 0.511827 \pm 15 (2\sigma)$ (2010–2019), corresponding to a La Jolla value of 0.511857 based on comparative runs. Six runs of the La Jolla standard between 2012 and 2015 yield $^{143}\text{Nd}/^{144}\text{Nd} = 0.511860 \pm 9$

b) Recommended value for BCR-2 are $^{143}\text{Nd}/^{144}\text{Nd} = 0.512634 \pm 11 (2\sigma)$ (Weis et al., 2006)

Table XI: Pb Isotopic Precision

Sample ID	$^{208}\text{Pb}/^{204}\text{Pb}$	Average	2σ	$^{207}\text{Pb}/^{204}\text{Pb}$	Average	2σ	$^{206}\text{Pb}/^{204}\text{Pb}$	Average	2σ
NBS981	36.709			15.4936			16.9384		
NBS981	36.706			15.4924			16.9369		
NBS981	36.705			15.4925			16.9372		
NBS981	36.707	36.7054	0.0050	15.4931	15.4923	0.0020	16.9373	16.9367	0.0022
NBS981	36.702			15.4908			16.9349		
NBS981	36.702			15.4913			16.9358		
NBS981	36.706			15.4926			16.9365		
BCR-2	38.796			15.6207			18.7924		
BCR-2	38.793	38.7489	1.064	15.6201	15.6200	0.0020	18.7917	18.7688	0.0542
BCR-2	38.708			15.6207			18.7503		
BCR-2	38.698			15.6186			18.7407		

Note:

a) Recommended values for NBS987 are $^{206}\text{Pb}/^{204}\text{Pb} = 16.9356$, $^{207}\text{Pb}/^{204}\text{Pb} = 15.4891$, $^{208}\text{Pb}/^{204}\text{Pb} = 36.7006$ (Todt et al., 1996)

b) Recommended values for BCR-2 are $^{206}\text{Pb}/^{204}\text{Pb} = 18.7529 \pm 0.0195$, $^{207}\text{Pb}/^{204}\text{Pb} = 15.6249 \pm 0.0040$, $^{208}\text{Pb}/^{204}\text{Pb} = 38.7237 \pm 0.0405$

Table XII: Partition Coefficients

	Cs	Rb	K	Ba	Sr	Pb	Th	U	Zr	Hf	Ti	Ta	Y	Nb	Sc	Cr	Ni	Co	V
Felsic/Acidic Melts																			
Plagioclase	0.030	0.30	0.263	0.48	4.400	1.300	0.010	0.0315	0.200	0.030		0.0300	0.250	0.57	0.010	0.010	1.50	0.15	
K-Feldspar	0.025	0.40	1.490	22.0	5.900	2.545	0.022	0.0550	0.360	0.034		0.0105	0.041	0.08	0.025				
Biotite	2.800	3.20	1.010	20.8	0.410	0.850	1.135	0.8300	0.590	0.640		1.5500	1.200	6.75	12.45	19.65			
Amphibole	0.010	0.40	24.20	0.30	1.275	0.430	0.160		0.430	0.520	15.8	0.4300	9.640	4.10	14.00	40.00	7.75	37.0	19.5
Apatite						0.030		43.700	0.906	0.878			162.0						
Zircon						7.500	22.10	254.00		971.0		47.500	71.40		68.65	189.5		16.0	
Allanite		0.19				0.920	484.0	15.500	0.290	18.90		3.1500	95.50	1.70	55.85	380.0		42.5	
	Ga	P	Zn	Cu	La	Ce	Pr	Nd	Sm	Eu	Gd	Tb	Dy	Ho	Er	Tm	Yb	Lu	
Felsic/Acidic Melts																			
Plagioclase	3.200		0.480	0.245	0.300	0.220		0.190	0.120	2.000	0.129	0.165	0.13				0.100	0.100	
K-Feldspar	1.225		0.096	1.320	0.085	0.040		0.054	0.026	9.060	0.011	0.035	0.97		0.20		0.015	0.012	
Biotite	1.700		11.40		7.930	0.234		0.339	0.392	0.501	0.353	2.385	0.20		0.20		0.165	0.208	
Amphibole	1.000		2.300	0.945	0.360	0.680		1.600	2.300	3.200		2.400	11.3		7.50		1.800	1.800	
Apatite					28.20	16.60		21.00	20.70	14.50	21.70		16.9		14.0		9.400	7.900	
Zircon					1.140	1.170		1.380	2.030	0.850	6.010	37.00	44.9	74.5	107	282	516.0	689.0	
Allanite	2.900			5.800	2594.5	2279		1620	866.5	111.0		273.0	137				30.75	33.00	

References for Kd values:

Partition coefficients were aggregated from the GERM Partition Coefficient (Kd) database; specific references are listed below:

$$Kd = C_{\text{mineral element}} / C_{\text{melt element}}$$

Where $C_{\text{mineral element}}$ is the concentration of the trace element in the mineral and $C_{\text{melt element}}$ is the concentration of the trace element in the melt (both concentrations in ppm or weight percent).

	Schnetzer, C.C. and Philpotts, J.A. (1970)
	Bacon, C.R. and Druitt, T.H. (1988)
	Leeman, W.P. and Phelps, D.W. (1981)
	Philpotts, J.A. and Schnetzer, C.C. (1970)
	Ewart, A. and Griffin, W.L. (1994)
	Ewart, A. and Griffin, W.L. (1994) (Calculation from high and low)
	Nagasawa, H. and Schnetzer, C.C. (1971)
	Nash, W.P. and Crecraft, H.R. (1985) (Calculation from high and low)
	Sisson, T.W. (1994) (Calculation from high and low)
	Fujimaki, H. (1986)
	Bea et al. (1994)
	Mahood, G.A. and Hildreth, E.W. (1983) (Calculated from high and low)
	Mahood, G.A. and Hildreth, E.W. (1983)